Low-pressure resonant MEMS accelerometers for automotive applications

Eurico Esteves Moreira

UMinho | 2020

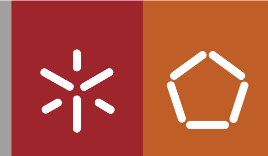

Universidade do Minho
Escola de Engenharia

Eurico Esteves Moreira

Low-pressure resonant MEMS accelerometers for automotive applications

março de 2020

REPÚBLICA PORTUGUESA
CIÊNCIA, TECNOLOGIA E ENSINO SUPERIOR
FCT Fundação para a Ciência e a Tecnologia
NORTE2020
CENTRO2020
ALENTEJO 2020
POCH
PORTUGAL 2020
UNIÃO EUROPEIA
Fundo Social Europeu

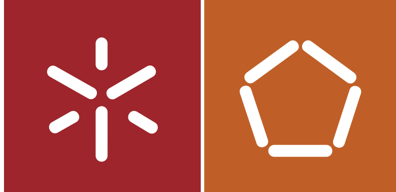

Universidade do Minho
Escola de Engenharia

Eurico Esteves Moreira

Low-pressure resonant MEMS accelerometers for automotive applications

Tese de Doutoramento
Programa Doutoral em Sistemas Avançados de Engenharia para a Indústria

Trabalho efetuado sobre a orientação de
Professor Doutor João Carlos Azevedo Gaspar
Professor Doutor Jorge Miguel Nunes dos Santos Cabral
Professor Doutor Luís Alexandre Machado da Rocha (à memória de)

março de 2020

DIREITOS DE AUTOR E CONDIÇÕES DE UTILIZAÇÃO DO TRABALHO POR TERCEIROS

Este é um trabalho académico que pode ser utilizado por terceiros desde que respeitadas as regras e boas práticas internacionalmente aceites, no que concerne aos direitos de autor e direitos conexos.

Assim, o presente trabalho pode ser utilizado nos termos previstos na licença abaixo indicada.

Caso o utilizador necessite de permissão para poder fazer um uso do trabalho em condições não previstas no licenciamento indicado, deverá contactar o autor, através do RepositóriUM da Universidade do Minho.

Licença concedida aos utilizadores deste trabalho

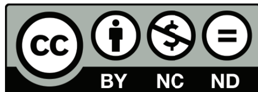

Atribuição-NãoComercial-SemDerivações

CC BY-NC-ND

https://creativecommons.org/licenses/by-nc-nd/4.0/

Acknowledgement

In the last four years, I was fortunate to learn and enlarge my knowledge, but the people I have met and the experiences I have lived made the journey unforgettable. I am genuinely grateful to those that were part of this adventure. My first acknowledgement goes to my supervisor, Professor Luis A. Rocha, without whom I wouldn't be working on MEMS. His guidance and focus inspired me throughout this work and will continue to drive me through my next challenges. Luis will not be forgotten, living through his work and the ones he taught. I would like to thank my supervisor Dr. João Gaspar for his support. He introduced me to many topics and always pushed me to do more. Thanks to his confidence in my capabilities, I had many opportunities that made me progress. I am grateful to my supervisor Professor Jorge Cabral, who first saw potential in me.

I am indebted to Burkhard Kuhlmann, who always found time to meet and discuss this project over the last years. His knowledge and support were truly helpful. I would also like to thanks his team at Bosch.

I am grateful to the Microfabrication and Exploratory Nanotechnology group at the International and Iberian Nanotechnology Laboratory (INL), and I must show my special gratitude to Rosana Dias, Filipe Alves and Helder Fonseca, for the friendship and technical help/training provided during my stay. Luckily, I started this adventure with Vasco Lima, and the companionship made this journey more enjoyable.

To my friends "The Crew", I am grateful for such friendship, and I hope it will continue to grow, despite the increasing physical distance. I also want to acknowledge everyone that helped me revising this document.

"Agradeço à minha namorada, Sara Marques, pelo o apoio e paciência, principalmente na fase dedicada à escrita deste documento. Por último, o mais profundo dos agradecimentos é para aqueles que sempre me apoiaram e que possibilitaram esta etapa da minha vida: o meu pai, Eduardo Moreira, a minha mãe, Elisabete Esteves e o meu irmão, Alexandre. Agradeço da mesma forma aos meus avós."
This thesis was supported by FCT– Fundação para a Ciência e Tecnologia through the grant PDE/BDE/114564/2016.

Eurico Esteves Moreira

June 16th, 2020

STATEMENT OF INTEGRITY

I hereby declare having conducted this academic work with integrity. I confirm that I have not used plagiarism or any form of undue use of information or falsification of results along the process leading to its elaboration.

I further declare that I have fully acknowledged the Code of Ethical Conduct of the University of Minho.

Resumo

Os acelerómetros MEMS têm um papel importante no desenvolvimento de novas soluções/funcionalidades para a indústria automóvel, nomeadamente na melhoria das condições de segurança e de condução. Não obstante, dispositivos com melhor performance, dimensões mais reduzidas e menor custo possibilitariam a implementação de mais casos de uso/funcionalidades. A encapsulação em vácuo tem sido alvo de estudo para desenvolver sensores MEMS de dimensões reduzidas e de baixo custo, uma vez que viabiliza a integração monolítica de todos os sensores que compõe uma unidade de medição inercial. Contudo, os acelerómetros MEMS tradicionais não operam corretamente nestas condições.

Esta tese foca-se no desenvolvimento de um acelerómetro MEMS ressonante baseado em ressonadores DETF (”double-ended tuning fork”). O sensor proposto é composto por dois ressonadores numa configuração diferencial para minimizar os efeitos de modo comum, ao qual foram adicionadas alavancas para aumentar a sensibilidade. Os dispositivos foram fabricados num processo standard de microfabricação na Bosch e encapsulados em vácuo. Foi desenvolvido um sistema que permite operar os ressonadores em malha aberta e malha fechada. Em malha fechada, a frequência de excitação dos DETF é constantemente atualizada, aumentando a linearidade e gama de medição. Após a caraterização exaustiva realizada é possível destacar uma alta sensibilidade (170.7 Hz/g) e boa não-linearidade (<0.63 %), em dimensões reduzidas (0.25 mm^2), uma largura de banda de 63 Hz e uma gama de medida de $\pm$5 g.

Adicionalmente, é ainda apresentado um magnetómetro MEMS diferencial e modulado em frequência, que permite provar a deteção de campo magnético com DETFs. O sensor é também composto por um transdutor de força de Lorentz, tendo sido otimizado para aumentar a sua sensibilidade. Os magnetómetros foram fabricados no INL num processo SOI e é também apresentada a sua validação experimental.

Palavras-chave: MEMS, acelerómetro ressonante, magnetómetro MEMS, vácuo.

Abstract

MEMS accelerometers are paramount in the development of the automotive industry, where many applications improved the security and driving experience. However, better, cheaper, and smaller devices would enable even further use-cases. Encapsulation in vacuum has been studied to develop more affordable and smaller devices since it would allow the monolithic integration of the sensors composing an inertial measurement unit. Nevertheless, traditional accelerometers do not operate properly at low pressures.

This work focus on the development of a resonant accelerometer based on double-ended tuning fork (DETF) resonators. The accelerometer proposed is composed of two DETF on a differential configuration to minimise common-mode effects, and a force amplification mechanism was added to increase sensitivity. The designed devices were fabricated in a Bosch standard surface micromachining process and encapsulated in vacuum. A system was implemented to validate the accelerometers, operating the resonators in open-loop and closed-loop. In closed-loop, the driving frequency of the DETF is constantly updated, increasing the sensor linearity and full-scale. An extensive characterisation was performed and a good non-linearity (<0.63% FS) and high sensitivity (170.7 Hz/g) on a small footprint (0.25 mm^2) were highlighted as the main achievements. A bandwidth of 63 Hz and a measurement range of at least $\pm 5\,g$ were also reported.

A differential frequency-modulated magnetometer was designed, implemented and characterised to prove the feasibility of magnetic field sensing using DETF resonators. A novel Lorentz force transducer was proposed and optimised to increase the device's sensitivity. The magnetometers were fabricated on an in-house two mask SOI-process, and the experimental validation of the envisioned sensor was performed.

Keywords: MEMS, resonant accelerometer, frequency-modulated magnetometer, vacuum encapsulation.

Table of Contents

List of Figures xi

List of Tables xvii

List of Acronyms xviii

1 Introduction 1

1.1 Microelectromechanical systems . . . 2

1.1.1 MEMS in the automotive industry . . . 3

1.1.2 Inertial sensors . . . 4

1.1.3 Fabrication processes . . . 5

1.1.4 Encapsulation and packaging . . . 7

1.2 MEMS accelerometers . . . 9

1.3 Resonant accelerometers . . . 11

1.3.1 Single-beam accelerometers . . . 12

1.3.2 DETF-based accelerometers . . . 13

1.4 Frequency-modulated devices . . . 14

1.5 Motivation and goals . . . 15

1.6 Organisation of this thesis . . . 17

References . . . 18

2 Resonant accelerometer 26

2.1 Resonance . . . 27

2.2 Double-ended tuning fork resonator . . . 28

2.2.1 Force measurement . . . 29

2.2.2 Actuation and sensing . . . 32

2.2.3 One-degree of freedom analysis . . . 32

2.2.4 Non-linearities . . . 37

2.2.5 Charge effects 40
2.2.6 Temperature dependence 41
2.2.7 Mechanical stress 42
2.2.8 Buckling 43
2.3 Single-axis accelerometer composed of DETF resonators 44
2.3.1 Differential operation 45
2.3.2 Force amplification mechanisms 46
2.3.3 One-degree of freedom analysis 48
2.4 Frequency-modulated device instrumentation 50
2.4.1 Resonant sensing methods 50
2.4.2 Closed-loop measurement approaches 53
2.5 Conclusion 54
References 55

3 System implementation **59**
3.1 MEMS accelerometer 60
3.1.1 Device fabrication 61
3.1.2 Sensor design 62
3.1.3 Fabricated devices 66
3.1.4 Packaging 68
3.2 Front-end electronics and phase detection 70
3.2.1 Analog front-end 70
3.2.2 Phase measurement, and resonator bias and AC driving 71
3.3 Closed-loop control components 75
3.3.1 Main finite state-machine and generic modules 76
3.3.2 Phase acquisition 80
3.3.3 Proportional-integral-derivative controller 81
3.3.4 Driving Signal generation 83
3.3.5 System configuration 85
3.4 Data acquisition and system configuration 85
3.5 Conclusion 87
References 88

4 Experimental results **90**

4.1 DETF mechanical characterisation . . . 90

4.1.1 Setup . . . 91

4.1.2 Resonant frequency and quality factor . . . 92

4.1.3 Influence of the AC driving and bias voltage signals . . . 96

4.2 Accelerometer characterisation . . . 98

4.2.1 Setup . . . 98

4.2.2 Sensitivity and linearity . . . 100

4.2.3 Sensitivity for different AC driving and bias voltages . . . 103

4.2.4 Cross-axis sensitivity . . . 105

4.2.5 Temperature dependency measurement . . . 106

4.2.6 Long-term measurement . . . 109

4.2.7 Dynamic characterisation . . . 110

4.3 Mechanical stress characterization . . . 113

4.3.1 Setup . . . 114

4.3.2 Mechanical stress dependence . . . 115

4.3.3 Comparison - soft glue/hard glue . . . 117

4.3.4 Long-term measurement of a constant force . . . 120

4.4 Conclusion . . . 121

References . . . 122

5 DETF-based magnetometer **124**

5.1 Introduction . . . 124

5.1.1 MEMS magnetometers . . . 126

5.1.2 Frequency-modulated MEMS magnetometers . . . 127

5.2 Magnetometer design . . . 128

5.2.1 Lorentz-force transducer . . . 129

5.2.2 Device operating principle . . . 129

5.3 Implementation . . . 131

5.3.1 Sensing element . . . 132

5.3.2 Fabrication process . . . 136

5.3.3 Fabricated devices . . . 137

5.3.4 Packaging . . . 139

5.4 Experimental characterization 140

5.4.1 Setup 140

5.4.2 DETF mechanical characterization 141

5.4.3 Magnetometer's sensitivity characterisation 142

5.5 Conclusions 145

References 146

6 Conclusions and future work **148**

6.1 Conclusions 148

6.2 Future work 152

6.2.1 Device design proposal 152

6.2.2 Mechanical stress decoupling at the fabrication-level 153

6.2.3 System integration 154

References 155

Appendix A Accelerometers' Masks **156**

Appendix B Magnetometer's Masks **158**

List of Publications **162**

About the Author **165**

List of Figures

1.1 Simplified schematic of an inertial sensor operating principle. 4
1.2 Process flow representing a surface micromachining process. 6
1.3 Process flow of a bulk micromachining process. 7
1.4 Schematic of a device built through bulk micromachining and encapsulated using two capping wafers. 8
1.5 Schematic of two multi-sensor measurement units composed of a gyroscope (Gyro), an accelerometer (Acc), a magnetometer (Mag), an integrated-circuit (IC) and a chip carrier. 11
1.6 Output of amplitude and frequency modulated devices when submitted to an external acceleration 12

2.1 Modes of resonance. 28
2.2 Schematic of clamped-clamped double ended-tuning fork resonators and the different features composing it 28
2.3 The behaviour of the natural frequency of DETF accordingly to the beam length and width. 30
2.4 Sensitivity of a DETF when a fixed load is applied to the extremities accordingly to the beam length and width. 31
2.5 The normalised sensitivity plotted in function of force and mass of the electrodes. 31
2.6 Schematic of the DETF basic operation when composed of driving and sensing capacitive electrodes. 33
2.7 Different forces present in a one-degree of freedom analysis. 33
2.8 Simulink model implemented to study the dynamic behaviour of the system. 37
2.9 Bode plot for devices with different quality factors. 38
2.10 Schematic of a straight beam and a buckled beam. Note, the beam can buckle to the right or to the left (bi-stable). 43
2.11 Basic operation of an accelerometer composed of a DETF. 44
2.12 Differential accelerometer architecture composed of two DETF undergoing inertial force in opposite direction. 45

2.13 Schematic of the three class of levers reproducible using standard microfabrication processes. . . . 47
2.14 Schematic of the system composed of a proof mass and the levers. . . . 48
2.15 Schematic of the model describing the behaviour of a complete frequency modulated accelerometer. . . . 50
2.16 Amplitude change sensed by driving the resonators at a constant frequency. . . . 51
2.17 Schematic of the system to detect the shift of magnitude for a fixed driving frequency. . . . 51
2.18 Sensing of natural frequency changes through phase detection. . . . 52
2.19 Schematic of the system to instrument a changing phase proportional to the natural frequency of the resonator. . . . 52
2.20 Schematic of the system composed by an oscillator to instrument the resonant sensor. . . . 53
2.21 DETF closed-loop operation based on a phase detector and a controller. . . . 54

3.1 Schematic showing the different blocks implemented in this work. . . . 60
3.2 Frequency response of a double-ended tuning fork resonator modelled using the simulink model implemented. . . . 62
3.3 Modal simulation performed using Ansys Workbench. . . . 63
3.4 Schematic of the single-axis MEMS accelerometer based on DETF resonators and force amplification mechanism. . . . 64
3.5 Features optimised using finite element method (FEM) and parametric CAD design to guarantee a maximum amplification. . . . 64
3.6 Sensitivity in function of the output lever length (La). . . . 65
3.7 scanning electron microscope (SEM) pictures of a fabricated device and highlight of the different elements composing it. . . . 67
3.8 Picture of the three devices present on the fabricated dies. . . . 68
3.9 Silicon die glued to a ceramic chip carrier and wire-bonded, as provided by Bosch. . . . 68
3.10 Response of a viscoelastic material when enduring a constant stress or strain. . . . 69
3.11 Simplified schematic of a transimpedance amplifier. . . . 71
3.12 Transimpedance amplifier and non-inverting amplification stage to convert current to voltage and amplify. . . . 72
3.13 Main blocks composing the basic operation principle of the lock-in amplifier and the connections to the resonator. . . . 73
3.14 Connections of the lock-in with the surrounding equipment and the DETF. . . . 74

3.15 Closed-loop control components and modules implemented on a FPGA. 76
3.16 Diagram showing the different stats and conditions present in the main finite state machine (MFSM). 77
3.17 Diagram of the clock signals at the output of the clock generation module. 79
3.18 Asynchronous assertion, synchronous deassertion reset scheme. 80
3.19 Block diagram showing the different blocks, constants and variables of the controller implemented. 81
3.20 Data acquisition and system configuration connection scheme. 86

4.1 Components of the setup to perform the characterisation of the accelerometers. The main parts are demonstrated, namely, the front-end electronics, the fast prototype system board with the FPGA, the DC power supply and the data acquisition board. 91
4.2 Bode plot of the right and left DETF responses for a driving and bias voltage of 325mV and 2V, respectively (sample 2-P01-S1). 92
4.3 Bode plot of the right and left DETF when the driving voltage is applied at the natural frequency (no stray capacitance decoupling). A bias and driving voltage of 2V and 25mV were used, respectively (sample 2-P01-S1). 93
4.4 Natural frequency experimentally measured and values for four different simulation conditions (Vp=2V). 94
4.5 Sample classification showing the left (L) and right (R) DETF and the devices' numbers. . 95
4.6 Quality factor experimentally measured and values for several simulation conditions (Vp=2V). 95
4.7 Frequency sweeps for an accelerometer submitted to three different accelerations (sample 5-P02-S1L, V_p=1.5V and v_a=325mV) 96
4.8 Several frequency sweeps performed with a bias voltage of 2V and different driving voltages (sample 3-P02-S1L). 97
4.9 Characterisation of the resonator for different bias voltages and a fixed driving voltage of 200mV (sample 3-P02-S1L). 98
4.10 Pictures of the setup used to perform the quasi-static characterisation. 99
4.11 Pictures of the setup used to perform the dynamic characterisation. 100
4.12 Frequency shift on the left and right DETF for accelerations going from -1g to +1g (sample 2-P02-S1). 101

4.13 Differential frequency shift measured on sample 1-P02-S1 for a gravitational acceleration incremented 10mg/step (V_p=2V, v_a= 250mV). 101
4.14 Sensitivity (S) and non-linearity (NL) experimentally measured on five samples for a full-scale (FS) of $\pm 1g$. 102
4.15 Sensor sensitivity obtained during a ten cycle experiment with the purpose of validating the response repeatibility. 103
4.16 Sensitivity experimentally measured on sample 2-P02-S1 for different bias voltages (v_a was maintained constant at 300mV). 104
4.17 Experimental results of the accelerometer sensitivity and error (relatively to the sensitivity average) for different driving voltages (V_p=2V). 105
4.18 Cross-axis sensitivity experimentally measured in the Y-axis (V_p=2V and v_a=300mV). . . 106
4.19 Simulated change in the nominal natural frequency of the DETFs over temperature and differential response. 107
4.20 Experimental measurement showing the response of the complete sensor but also of the each individual DETF for a temperature going from approximately 30°C to 70°C. 108
4.21 Highlight of the experimental frequency shift measured for different temperatures and the linear fit for the same data. 109
4.22 Differential Frequency shift measured on sample 2-P02-S1 for a time period of 12 hours (V_p=2V and v_a=300mV) 110
4.23 Allan Variance plot of the data collected during 12 hours. 110
4.24 Accelerometer (2-P02-S1) response for a sinusoidal acceleration at 20 Hz with an amplitude of $\pm 5g$. The natural frequency of the left and right DETF are also present in the figure. 111
4.25 Differential sensor response for a sinusoidal acceleration increased from $\pm 0.1g$ up to $\pm 5g$ with increments of 0.1g. 112
4.26 Bandwidth experimentally measured and comparison with the reference accelerometer. . 112
4.27 Schematic of the test setup used to measure a load applied directly on the chip carrier. . 114
4.28 Picture of the setup mounted to experimentally measure the response of the accelerometer for a load applied on the chip carrier and mapping of the testing points. 115
4.29 Frequency shift experimentally measured for a sample mounted on hard-glue (HG2-S1) undergoing a load up to 14.7 N (V_p=2.5 V, v_a=300 mV). 116

4.30 Simulated results showing the drift of natural frequency for a force with a given angle applied on the XY plane (Force=5 mN). 117
4.31 Frequency shift experimentally measured ten times for the same conditions. The average (Avg) and standard deviation (std) were calculated to retrieve information about the repeatibility. 118
4.32 Comparison of the frequency drift measured for two samples mounted on two different glues. 119
4.33 Sensitivity measured on three testing points for samples mounted on hard and soft glue. 119
4.34 Differential frequency shift measured on two samples bonded with two different glues and submitted to a constant force over 100 min. 120

5.1 Schematics a) and b) show the Lorentz-Force direction regarding the magnetic field orientation. 130
5.2 Magnetometer composed of a diamond-shaped Lorentz-force transducer coupled directly to a DETF. The Lorentz and axial forces are represented in a) and b) for magnetic field in opposite direction. 131
5.3 Differential MEMS magnetometer composed of two Lorentz-force transducers and two DETF. 132
5.4 Schematic of a diamond-like shaped Lorentz-force transducer and the different features optimised to guarantee an optimum force transfer. 133
5.5 Normalised axial force accordingly to the dimension of L1 (note that the total length is always 1mm). 134
5.6 Relation between axial force and the angle between the diagonal and vertical beam. . . . 134
5.7 Frequency response of the DETF obtained using the Simulink model. 135
5.8 Wafer cross-section showing the main steps of the SOI-based fabrication process available for microelectromechanical systems (MEMS) devices. 137
5.9 SEM pictures of the proposed magnetometer and its main features. 138
5.10 Schematic showing the cross-section and side-view of the PCB-based chip carriers. . . . 139
5.11 Picture of the PCB-based chip-carrier with a device glued and wire-bonded. 140
5.12 Setup used for the characterisation of the magnetometer's sensitivity. 141
5.13 Frequency response of the Left and Right DETF (V_p=3 V and v_a=300 mV). 142
5.14 Resonance frequency changes for the left and right resonators for a bias current of 1 mA. 143

5.15 Sensitivity of the frequency-modulated sensor for different bias currents (0.5 mA to 1.5 mA) in the range $\pm 42.5\ mT$. 143
5.16 Relation between sensitivity and bias current. 144

6.1 Design proposal composed of different improvements mainly for long-term stability improvement and cross-axis reduction. 153
6.2 Cross-section of a process allowing the decoupling of mechanical stress. 154
6.3 Proposal of a system to operate the resonators in closed-loop. This system is a more integrated version of the system used along this work. 154

A.1 Mask to pattern the device layer of the device. 156
A.2 Mask of the electrical connections coupling the devices to the pads. 157
A.3 Mask of the active layer for the three devices present on each die. 157

B.1 Mask designed to define the metal layer. 159
B.2 Mask to pattern the device layer. 160
B.3 Metal and device layers to define the proposed magnetometer. 161

List of Tables

1.1 Main research present in the literature concerning in-plane and out-of-plane resonant accelerometers based on single-beam and DETF resonators. The natural frequency, measurement range, resolution and bandwidth (BW) are some of the parameters available for comparison. 14

3.1 List of rules to design the accelerometer using the proprietary process at Bosch, Reutlingen. 61
3.2 List of the design parameters obtained through modelling of the micro-structures. 66
3.3 List of the glue properties used to bond the prototype dies to ceramic leadless chip carrier (CLCC). 69
3.4 Detailed description of the different actions performed in each state. 79
3.5 24-bit command structure to write and read from the DAC register. 84
3.6 Communication sequence to configure the FPGA with the different parameters. 86

4.1 Simulation characteristics and main results. 94

5.1 Comparison of amplitude-modulated MEMS magnetometers present in the state-of-the-art. 127
5.2 Main frequency-modulated MEMS magnetometers available in the literature. 128
5.3 Lorentz-force transducer parameters' dimensions (without considering over-etch). 135
5.4 DETF designed dimensions and properties (without considering 450 nm over-etch). . . . 136
5.5 Comparison of frequency-modulated MEMS magnetometers present in the state-of-the-art. 145

6.1 Sensitivity comparison of accelerometers based on DETF resonators. 150
6.2 Main parameters measured along the experimental characterisation. 152

List of Acronyms

2D	two-dimensional.
3D	three-dimensional.
ABS	automatic braking system.
AC	alternating current.
ADC	analog-to-digital converter.
AI	artificial intelligence.
AMR	anisotropic magneto resistance.
ASIC	application-specific integrated circuit.
BOX	buried oxide.
BW	bandwidth.
CAD	computer-aided design.
CLCC	ceramic leadless chip carrier.
CMOS	complementary metal–oxide–semiconductor.
COTS	commercial off-the-shelf.
CTE	coefficient of thermal expansion.
DAC	digital-to-analog converter.
DC	direct current.
DDS	direct digital synthesis.
DETF	double-ended tuning fork.
DRIE	deep reactive ion etching.
ESC	electronic stability control.

FEM finite element method.

FPGA field-programmable gate array.

FS full-scale.

GMR giant magneto resistance.

GPIO general-purpose input/output.

IC integrated circuit.

IMU inertial measurement unit.

INL International Iberian Nanotechnology Laboratory.

IoT internet of things.

IP intellectual property.

LiDAR light detection and ranging.

MEMS microelectromechanical systems.

MFSM main finite state machine.

MPW multi-project wafer.

NEMS nanoelectromechanical systems.

PCB printed circuit board.

PDMS polydimethylsiloxane.

PID proportional-integral-derivative.

PLL phase-locked loop.

RF radio frequency.

SEM scanning electron microscope.

SNR signal-to-noise ratio.

SOI silicon on insulator.

SPI	serial peripheral interface.
SQUID	superconducting quantum interference device.
TIA	transimpedance amplifier.
TMR	tunneling magneto resistance.
TTL	Transistor–transistor logic.
UART	universal asynchronous receiver/transmitter.
USB	Universal Serial Bus.
UV	ultraviolet.
VR	virtual reality.

Chapter 1

Introduction

Nowadays, miniaturised systems are a staple without which no one could live, but it all started back in the late 50's, when few dreamers thought about writing the Encyclopedia Brittanica on the head of a pin [1.1].

Before 1947, the electronic devices were circumscribed to large and cumbersome vacuum tubes, and the anode-cathode distance deprived high-frequency modulation [1.2]. This drawback was particularly severe in radars since they could not detect any small object. It all changed when William Shockley and his colleagues, at the Bell laboratories, presented the first transistor [1.3]. This invention proved to be more reliable, less power consuming and above all, incredibly smaller than the leading technology of that time. This technology was developed with such fierceness, that in a few years, many companies were developing and selling state of the art devices, such as: flip-flops and processors with several thousand transistors [1.4], [1.5]. First, Texas Instrument led the market with its innovations (in the field of crystal growth), but soon many other companies took over Silicon Valley to present products that shaped the world as we know it.

What started as the growth of large crystals of semiconductor materials, later evolved to what is known as the field of microfabrication, the true engine of electronic miniaturisation. Whilst the integrated circuit (IC) industry was developing new processes, the anisotropic etch of silicon by potassium hydroxide (KOH) allowed the definition of the first micromechanical device [1.6]. But more contributions from the integrated circuit industry had an impact on the new field of micromachines. The use of surface and bulk micromachining techniques, as well as the use of widely available silicon substrates, and lithography allowed the definition of 3D structures with few micrometers [1.7]. The integration of mechanical resonators was a natural evolution, and in 1967 a resonant gate transistor was presented [1.8]. Many other micromechanical devices followed, including cantilevers, membranes and nozzles [1.5]. A new concept was born, the microelectromechanical systems (MEMS).

The manufacturing capabilities of small and precise identical arrays enabled the ink-jet printers to become the first mass-market application of MEMS [1.5], [1.6], [1.9]–[1.11]. Even today, this application has an outstanding market.

In the 90's more devices emerged, pressure sensors and accelerometers became a generic use-case in the automotive industry [1.12]. However, the lack of low-power front-end electronics, the large system size due to packaging limitations, high costs for quality control and low volumes of productions were restraining their use in consumer electronics [1.6]. The innovation and rethinking of an entire industry made them available for broader use, around the year 2000, when new needs and growing volumes became very fruitful. Nowadays, MEMS are in every pocket and are used in common applications but also in demanding use-cases in the aerospace [1.13] or defence industries [1.14]. In 2018, the global MEMS market reached more than 46.2 billion US dollars (far from the modest origins), representing 11% of the integrated electronic total market [1.15].

The expansion and use of such devices is not expected to decrease any time soon, and the market is expected to reach 100 billion US dollars by 2023. New applications in navigation, internet of things (IoT), virtual reality (VR) and artificial intelligence (AI) will surely evolve conjointly with the development of new solutions based on microelectromechanical systems.

1.1 Microelectromechanical systems

Often the meaning of microelectromechanical systems is bewildered, since the micro directs to a dimensional scale, the electro to either electric or electronic parts and mechanical to movement. But the term MEMS is generally used to describe structures with dimensions going from few millimetres down to the sub-micrometres [1.16]. Additionally, thermal, magnetic, fluidic and optical devices/systems, with and without moving parts are linked to the concept [1.17]. MEMS include miniaturised systems capable of sensing, signal processing, actuation, display and control. The capability of integration with electronics (for processing and control) on the same package (with or without a specific function) promote them as true systems [1.5], [1.18].

The small scale offers advantages related to high resonance frequencies, soft springs, small overall mass and dimensions, among many others. However, some interesting physical phenomenons at the macro-scale do not scale down favourably, and others become attractive (scaling laws). A general observation is

that smaller things are less affected by some phenomenons (e.g. gravity), bringing faster speed, higher power density and efficiency to miniaturised systems [1.5].

From the MEMS technology, revolutionary sensors and actuators arose. Sensors are devices capable of converting physical or chemical quantities into something perceptive, whilst actuators transform energy to produce an action. Several methodologies are used, such as electrostatic, magnetic, thermal and piezoelectric actuation. Both sensors and actuators are referred to as transducers [1.19]. Here, the focus is on physical sensors to transform a mechanical or magnetic domain into an electrical signal.

The batch fabrication processes, developed by the microelectronics industry, are a low-cost method of making large quantities of identical devices [1.19]. The cost of production is not device dependent and manual tasks are mostly eliminated. This enlarged the adoption of MEMS in many fields since serious advantages are presented, when comparing to the fabrication of macro-scale devices.

Besides the applications already listed, many more are accessible, for instance, micro-mirrors for image acquisition [1.20] or projection [1.21], [1.22], tunable radio frequency (RF) components (switches, tunable capacitors and resonators) to reduce the number of passive components [1.6], [1.23], [1.24], microphones [1.25] and speakers [1.26] in mobile devices. Nonetheless, the pressure and inertial sensors, developed specifically for automotive applications, created almost alone the MEMS industry [1.6].

1.1.1 MEMS in the automotive industry

Automobiles use a large variety of sensors to input the control electronics, ensuring a smooth, safe and efficient performance. It was estimated that cars have between fifty to a hundred sensors, being many of them MEMS [1.15]. This success started in the ’90s, with the first manifold and barometric absolute pressure sensors [1.27]. Since then, a set of requirements were especially created for the automotive industry regarding robust systems-on-package, system interfaces, and also temperature and shock tolerances. The development of MEMS was adapted to the demanding requirements for reliability and quality control, both industries profited from this new paradigm (i.e. automotive and MEMS industries) [1.6].

The microelectromechanical accelerometers were first introduced to detect collisions and deploy the airbag system but MEMS with a higher performance enabled sophisticated chassis control systems. For instance, the automatic braking system (ABS) is an application were the skidding of the wheels is detected and pulsed braking is applied. The objective is to guarantee suitable traction, yielding a safe control of the vehicle [1.28]. Another application of MEMS inertial sensors (accelerometers and gyroscopes) in chassis systems

is the electronic stability control (ESC). With this system, the driver is assisted in case of lateral sliding and the car gets back into an aligned position [1.18]. Using the same type of sensors, roll-overs are detected, triggering an action accordingly. All these safety measures, contribute to decrease the number of accidents and fatalities registered [1.24].

The forecast for the automotive industry reports the smart automotive (further driver assistance) and the autonomous driving as instrumental in the development of new radar and ultrasonic sensors, as well as three-dimensional (3D) and light detection and ranging (LiDAR) devices. Nevertheless, the performance of inertial sensors will not cease to adapt to the new necessities (and new trends) of the industry, enabling additional applications.

1.1.2 Inertial sensors

Accelerometers and gyroscopes are denominated inertial sensors, since both measure a physical quantity resulting from a force (F) applied to a proof mass (M_{proof}). This mass is attached to a fixed frame by a spring (k) and the displacement (x) is monitored [1.16] (see Figure 1.1). Several transduction mechanisms can be used to convert the movement or the resulting force into a quantity of interest [1.29].

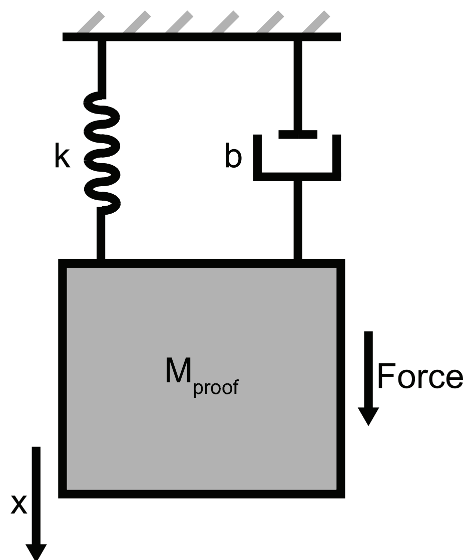

Figure 1.1: Simplified schematic of an inertial sensor operating principle.

Accelerometers measure the force that restrains the motion of the proof mass in the presence of external force, while gyroscopes measure the Coriolis force produced by a rotation rate [1.30].

When the mass starts oscillating, the movement is restrained by a damper with a damping coefficient (b). The damping is the energy dissipation caused by the interaction between a fluid or gas and a movable

part [1.19]. In MEMS, the damping is produced by air, or any other gas, inside the sensor chamber. The damping coefficient can be tuned by using gas with different viscosity or by changing the encapsulation cavity pressure.

1.1.3 Fabrication processes

The manufacture of MEMS structures consists of a sequence of material deposition, etching and patterning to incrementally shape different layers of material into a three-dimensional structure with electromechanical purposes [1.6]. Thousand of similar devices are defined on a single silicon wafer using photolithography. A photosensitive layer is defined by an ultraviolet (UV) light, defining any shaped wanted. What starts by being a two-dimensional (2D) defined shape on a planar surface, after etching of the structural layer becomes a true three-dimensional device [1.19]. In MEMS, specific fabrication challenges are reported, such as dimensional control, the process of thick structural layers and packaging of suspended and movable parts [1.19].

The MEMS manufacture is tied to the IC industry and both materials and processes are generally common. Concerning the main material used by both industries, silicon has negligible fatigue and the lack of memory makes it the material of election for structural elements [1.29]. Additionally, the material is inexpensive, abundant and available with high degrees of purity. The high purity and crystalline perfection guarantees reproducibility and reliability of the mechanical and electrical properties [1.31].

Several MEMS processes have been adapted or developed over the years to address the different manufacturing challenges. Traditionally, the processes have been categorised into surface and bulk micromachining [1.19].

Surface micromachining consists of the deposition and definition of thin films on top of a substrate wafer [1.19]. A minimum of three layers (substrate, structural and sacrificial) are needed to build a movable structure. In Figure 1.2, a simple process flow representing the different steps to build and release a membrane using surface micromachining is demonstrated. The structural layer is usually made of polycrystalline silicon, the properties are slightly different of single crystalline silicon because of deposition variations, grain-size effects and contamination [1.32]. However, surface micromachining is compatible with traditional IC fabrication and the integration of electronics and mechanical parts on the same chip is possible. This advantage represents a decrease in size, price and better performance.

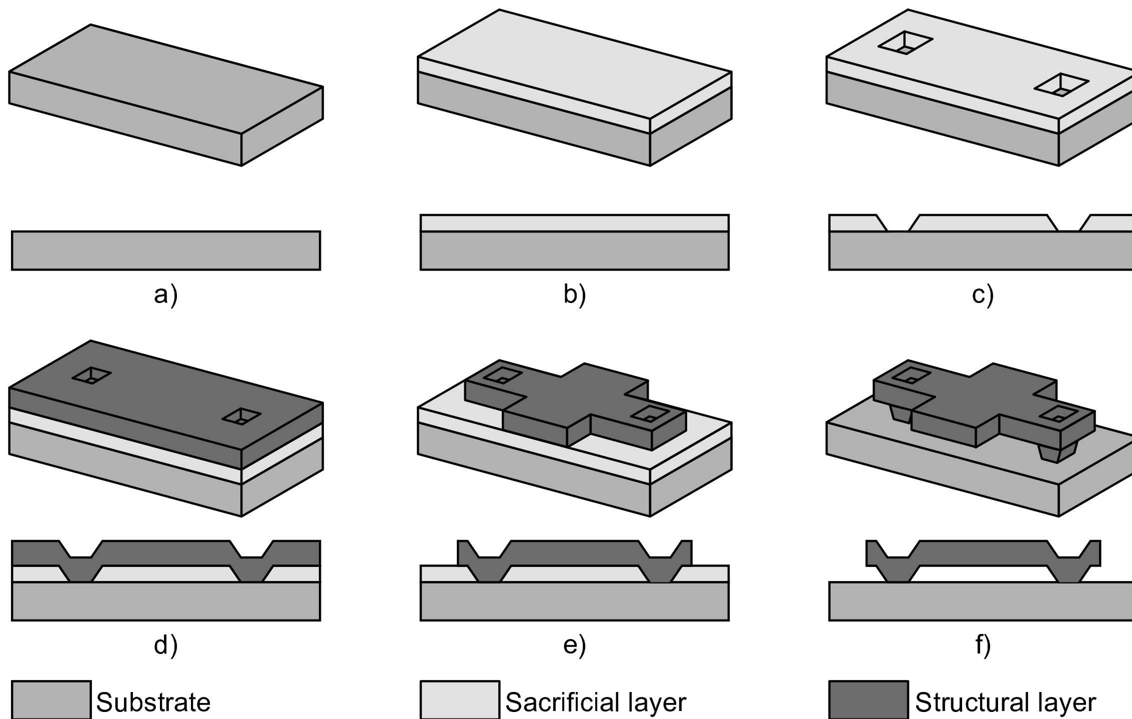

Figure 1.2: Process flow representing a surface micromachining process. a) the process starts with a substrate. b) A sacrificial layer is deposited c) The sacrificial layer is patterned and etched to create the anchors of the structure. d) A structural layer is deposited. e) The structural layer is patterned and etched to create the membrane shape. f) The sacrificial layer is removed to release the device on the structural layer.

In opposition, Bulk micromachining rests on the definition of a structure by etching the substrate wafer, resulting in thick structures (see Figure 1.3). This is especially advantageous for inertial sensors since it enables larger masses. Additionally, the bulk material can be single-crystal silicon, meaning a stable and reproducible material (ideal for mechanical structures). Two technologies are instrumental in bulk-micromachining, the use of silicon on insulator (SOI) wafers together with deep reactive ion etching (DRIE).

SOI wafers are fabricated by bonding together two silicon wafers, with an insulator layer in between [1.6]. The handle wafer (substrate) has usually a thickness around 700 μm, the buried oxide (BOX) between 1-2 μm and the active layer (SOI) is available in different thicknesses (going from thin layers of few nanometres to hundreds of micrometres). These substrates are more expensive than bare silicon, but this cost is compensated by process cost savings [1.19].

The process invented at Robert Bosch GmbH (DRIE) is mainly a junction of an intermittent etch and the deposition of a passivation layer (to protect the trench walls), yielding vertical walls (close to 90°) [1.5], [1.6], [1.33]. It enables the definition of narrow features with a high aspect ratio (i.e. ratio between the width aperture and the depth of a feature). Thicker devices layers are particularly advantageous in MEMS. This results in bigger masses in smaller areas, meaning more devices per wafer (cost reduction). But also

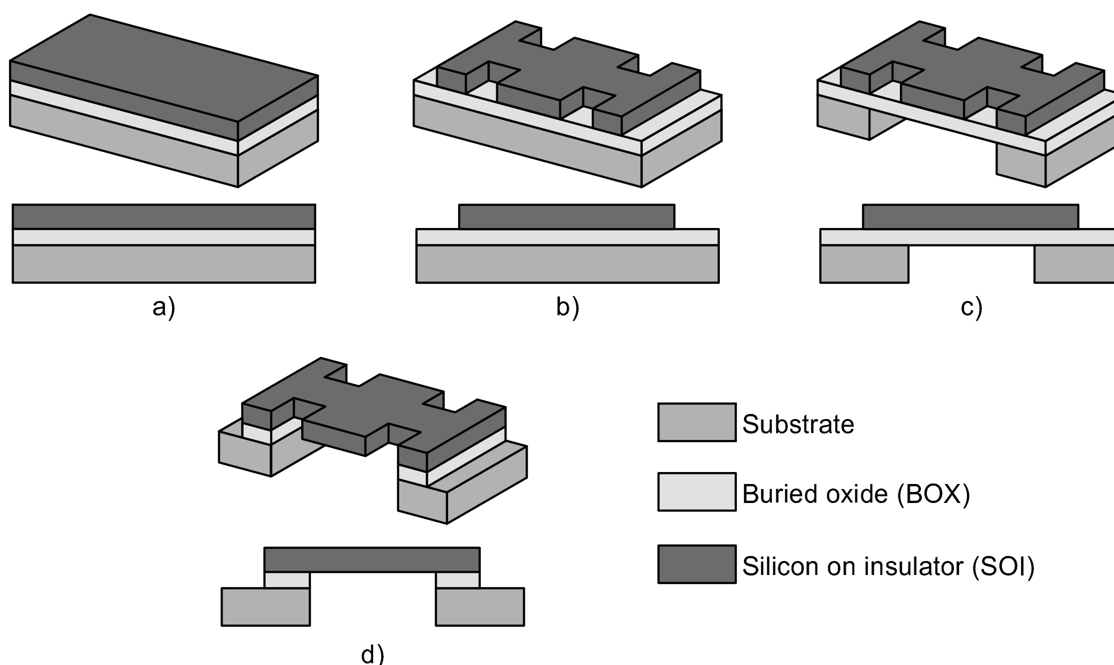

Figure 1.3: Process flow of a bulk micromachining process. a) the process starts with a SOI substrate. b) The device layer is patterned and etched, defining the device. c) The substrate is patterned and etched. d) The buried oxide is removed to release the device.

in higher areas for capacitive or electrostatic transduction and higher sensitivity.

1.1.4 Encapsulation and packaging

From the first MEMS concepts, the encapsulation of MEMS structures was recognised as particularly important to provide mechanical rigidity, protection against environmental influences and particles. Additionally, it has functional purposes in some sensors, for instance, absolute pressure sensors have a hermetically sealed cavity built by wafer bonding to maintain a stable reference pressure [1.34]. In Figure 1.4, a structure built by bulk micromachining with encapsulation is depicted.

The encapsulation of MEMS protects mechanically, electrically and chemically the thin and fragile structures. After fabrication, some processes are still needed, such as dicing to cut the wafer into single dies and packaging. The encapsulation can be seen as a first package at the wafer level to protected against fluids and mechanical forces, helping the fragile MEMS to withstand these critical processes.

Besides all the advantages regarding the protection and structural functions, the pressure and gas composition inside the cavity can be controlled. In other words, the pressure and gas can be chosen to enhance the capabilities of MEMS. Some sensors are encapsulated in vacuum, while others do best at atmospheric

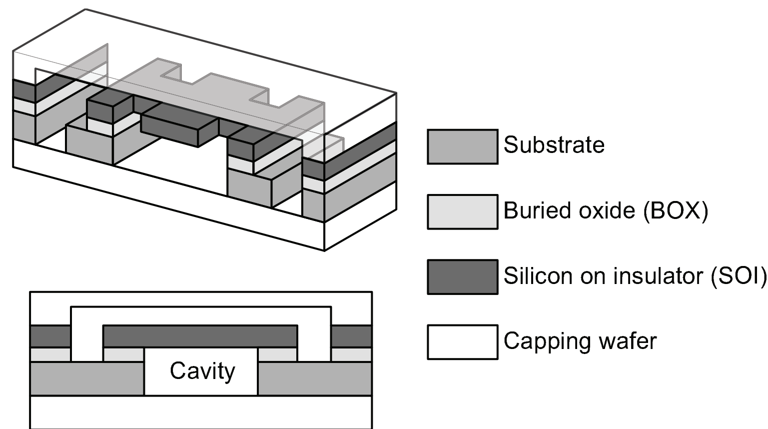

Figure 1.4: Schematic of a device built through bulk micromachining and encapsulated using two capping wafers.

or even at higher pressures. These differences are related to the damping coefficient, less pressure represents a significant damping reduction, meaning a higher quality factor. A constant pressure is also paramount since a drift in pressure represents a change on the sensor response over time, enhancing the importance of a stable encapsulation.

The encapsulation gas should be very pure otherwise stiction can occur due to dangling bonds at the surface of silicon. Additionally, moisture and changes in the MEMS material properties (e.g. corrosion) were also reported. But these issues are corrected by using noble gases, such as helium, argon, neon or krypton [1.35]. The nobles gases ensure higher response stability and helium, in particular, has been used to encapsulated oscillators since it guarantees long-term stability [1.36], [1.37].

The main techniques to encapsulate MEMS structures are wafer bonding and sealing by film deposition. Wafer bonding is accomplished through anodic bonding, silicon direct bonding and silicon-to-silicon bonding, among other techniques. It always consists of bonding a MEMS structural wafer to a capping wafer (e.g. silicon or glass) [1.6]. Sealing by film is done by depositing an additional sacrificial and structural layer (on top of the device) and then removing the sacrificial layers. The capping layer has small holes enabling a vapour etch and these are closed by the deposition of a conformal film [1.36].

The importance of MEMS packaging is often despised but it represents a complex field of research and development. Many solutions have been presented to address the different challenges of the industry and in some cases, the packaging is tailor-made for a dedicated application [1.38]. The cost of packaging can represent 20 to 80 % of the total product cost [1.19], [1.35], [1.39].

MEMS and IC are often packaged together since both are delicate and the packaging protects from hostile environments. Additionally, a micro-structure is not an autonomous device and has to be connected to

peripherals (front-end electronics, power supply, etc.). The package enables a connectivity in-package (in between an IC and MEMS in the same chip) and to the outside of the package. It can also help with the heat dissipation [1.39].

To decrease the size of ICs, many advanced packaging technologies were developed, but for the sake of simplicity, those will not be analysed. For research purposes, MEMS are usually interfaced electrically using wire-bonding and glued to a substrate. The common approach is to directly glue individual dies in a chip carrier that can be made out of plastic or ceramic [1.35].

1.2 MEMS accelerometers

Microelectromechanical systems have been largely produced to access acceleration using a wide variety of transduction mechanisms. In the literature, accelerometers are traditionally divided into two main groups: proof mass displacement or frequency shift monitoring.

Devices, where the proof mass displacement is measured, are prevalent in the scientific community and also in the market. Several techniques were used to convert displacement produced by an external acceleration into an electrical signal. Capacitive [1.40], [1.41], piezoelectric [1.42] and piezoresistive [1.43] sensors are common, but thermal [1.44], optical [1.45]–[1.47] and magnetic [1.48] transduction can also be found.

Capacitive transduction relies on a variation of distance between electrodes, resulting in a capacitance change proportional to the external acceleration. Several capacitive devices reported showed high sensitivity and resolution, proving also a good stability over-time. The drawback of this approach (when operated in open-loop) is a highly demanding electronics, since the signal values are low and parasitic capacitance should be minimised [1.40]. Closed-loop approaches were also reported, in this case, the objective is to maintain the mass at rest position by applying a restoring force to it. This approach profits from a reduced noise and an overall performance increase at the expense of an higher system complexity. The tuning of gains can be challenging, since the MEMS device has to be stable under any condition and the optimal values can change from device to device.

The principle of operation behind the thermal accelerometers is the heat convection transfer inside a confined cavity. One or more temperature sensors, a heater and a gas are required to implement this type of sensors. When no acceleration is applied, all the temperature sensors output the same temperature.

But when the device undergoes an acceleration, the gas (or fluid) temperature loses its symmetry. Those sensors do not need a proof mass to measure acceleration, benefiting from an simple fabrication process. Nevertheless, the heat convection is a slow process undermining the available bandwidth.

Piezoresistive devices are described as having simple architectures and fabrication processes. The piezoresistive material changes the resistance when deformed [1.19] and the main constraint of this approach is a strong temperature dependency. Yet, the good linearity and straight-forward electronic front-end have been endorsing these devices. Another advantage is tied to the possibility of being used in hostile environments, since the sensor can operate remotely from the electronics, but usually thermal compensation is needed [1.49].

Although, most of the pros and cons of piezoelectric and piezoresistive transduction are the same, piezoelectric devices stand-up by the self-generation (deformation is translated into a electric potential), meaning no power-supply is needed. The major drawback is the impossibility of static measurements, only strain change results in signal. The fabrication can be complex and often not compatible with other standard microfabrication processes [1.19].

The displacement of the proof mass was also successfully accessed by adding permanent magnets to the movable part and sensing the change in magnetic field using magnetic sensors (spin valves) [1.48] or pick-up coils [1.50]. These are characterised by using deposited and patterned magnets, but the achievable magnetic field is limited, reducing the sensitivity [1.48]. Moreover, the materials used in the permanent magnets are not widely used in the MEMS industry, representing a barrier to mass production.

Recently, optical MEMS accelerometers have been studied and these rely on a change of light-wave properties due to the movement of a mass. The main advantage of this approach is related to a high sensitivity. In addition, optical devices are suitable to be used in harsh environment but the packaging is complex and very expensive [1.50]. In some cases, many macro-parts are added to the system, increasing consequentially the size and weight [1.45], [1.46].

The constant need for better performance, lower production costs and higher integrability is driving the development of accelerometers capable of being encapsulated in vacuum [1.51]. The integration of several sensors in the same multi-axis inertial measurement unit (IMU), have been offered by the semiconductor leading companies [1.52]. Nonetheless, it would be advantageous to encapsulate under the same capsules at the same pressure, inertial sensors (i.e. multi-axis gyroscopes, accelerometers and inclinometers) and possibly other sensors (e.g. magnetometers). This would result in economical benefits, since all the sensors could be fabricated in the same silicon die, avoiding additional stacking of devices encapsulated at

different pressures, as shown in Figure 1.5. The area gains are also reported as beneficial and additionally the fabrication process is simplified since only one encapsulation step is necessary.

Another major advantage, arising from the encapsulation in vacuum, is related to lower thermo-mechanical Brownian noise due to mechanical damping. The Brownian noise is reduced at lower pressures [1.53].

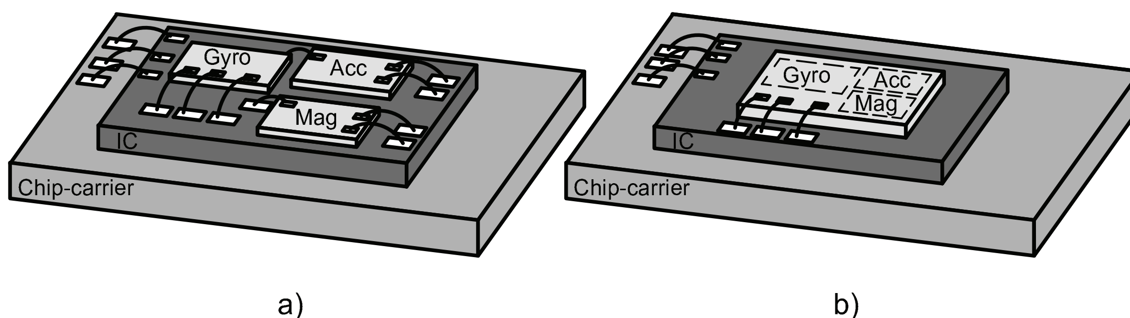

Figure 1.5: Schematic of two multi-sensor measurement units composed of a gyroscope (Gyro), an accelerometer (Acc), a magnetometer (Mag), an integrated-circuit (IC) and a chip carrier. a) Several devices encapsulated separately and fabricated in different dies. b) Three sensors fabricated on the same die and encapsulated under the same capsule.

Gyroscopes are generally encapsulated in vacuum because of the high-quality factors required, but many types of devices are not stable under such conditions and/or do not operate properly. For instance, open-loop capacitive structures suffer from the lack of vibration robustness and to operate them in closed-loop more effort is needed. Thermal transduction does not work at all in vacuum since no heat convection is possible in rarefied air. Research in this field as identified two alternatives that proved to be successful to operate accelerometers in vacuum: the use of closed-loop mechanisms to control the mass position (e.g. sigma-delta [1.54]) or devices monitoring a frequency shift, also called frequency modulated or resonant accelerometers.

1.3 Resonant accelerometers

Resonant devices experience a change of their natural frequency when exposed to a load caused by an external acceleration and these devices are along this work described as frequency modulated. Whilst, the accelerometers introduced previously are modulated in amplitude, in other words, an acceleration results on a signal with an amplitude proportional to the external stimuli. In Figure 1.6, the typical output signal of the two sorts of structures is depicted.

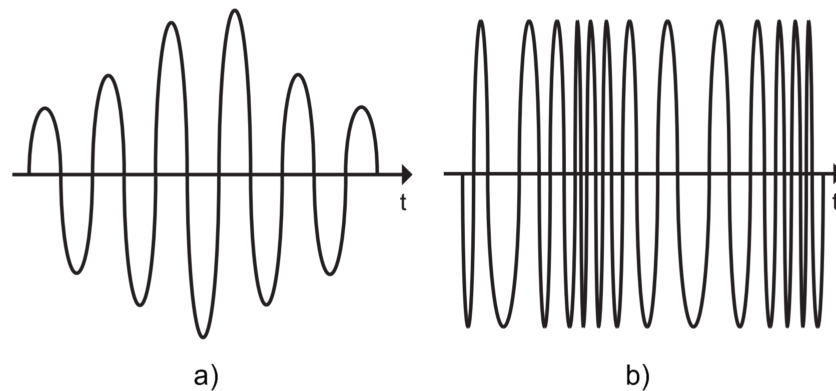

Figure 1.6: Output of an amplitude and frequency modulated devices when submitted to an external acceleration. a) Amplitude modulated sensor response. b) Frequency modulated device output.

The amplitude modulated devices are the predominant approach, yielding great resolution and noise floor as low as $0.25ng/\sqrt{Hz}$ in [1.55]. Though, scalability issues arise since the sensitivity is directly proportional to the proof mass, and has an inverse-squared relationship with the bandwidth of the accelerometer [1.56].

Frequency modulated devices offer high sensitivity, without compromising bandwidth and size, and a high dynamic range (there is no displacement limitation) [1.56], [1.57]. The fact of not having any displacement limitation is particularly important, since the accelerometers can withstand higher accelerations without damages due to collisions between the movable and fixed features. The pull-in immunity (in certain cases) and a quasi-digital output are also reported advantages [1.58].

In addition, resonant accelerometers can be implemented using different mechanisms. First, devices made out of quartz crystal were demonstrated [1.59], [1.60], but the focus shifted to microfabricated silicon devices [1.61], [1.62]. Since then, several devices with different types of resonators were presented in the state-of-the-art, for the sake of simplicity, only single-beam and double-ended tuning fork (DETF) based accelerometers will be described and compared.

1.3.1 Single-beam accelerometers

Single-beam accelerometers were presented for in-plane single [1.58] and dual-axis [1.51] measurement. These are based on a resonator composed of a straight single-beam resonating in a given mode (flexural or torsional). The single-beam accelerometers, if compared to other types of resonators, are more sensitive for their size, since a force applied to a smaller cross-sectional area (only one beam) results in higher frequency shifts. Scale-factor of MEMS resonators is an important topic of research and an outstanding

force coupling is imperative. A sensitivity of 455 Hz/g (1g=9.8m/s^2) was reported in [1.58], by using a force amplification mechanism together with two resonators on a differential configuration. This architecture was adapted for bi-axial measurement and a scale-factor of 250 Hz/g was experimentally obtained [1.51]. A device with the same type of beams with a footprint of $0.05\ mm^2$ and a sensitivity of $22 Hz/g$ was also presented [1.63]. This device was the smallest found in the state of the art, and the objective was to be one step closer to nanoelectromechanical systems (NEMS), instead of MEMS.

A device driven in the second lateral transverse mode, instead of the first mode (devices described above), and composed of a unique single-beam (not in differential configuration) reports a sensitivity of $2752\,Hz/g$. Additionally, a noise floor of $98\,ng/\sqrt{Hz}$ and a bias instability of $56\,ng$ are the best results reported for single-beam based accelerometer [1.64].

1.3.2 DETF-based accelerometers

Double-ended tuning fork (DETF) resonators are composed of two beams on a parallel arrangement. These resonators profit from a higher quality factor and zero net force at the anchors, at the expense of a lower sensitivity because of a higher cross-sectional area (in comparison to single-beam resonators) [1.19].

In the literature, most of the devices found have electrostatic actuation to drive the beams at the natural frequency and the sensing is performed through capacitive transduction. Capacitive readouts are generally employed since they offer a good noise performance and the electrodes are fabricated using standard MEMS processes [1.51]. However, piezoelectric sensing was also reported [1.65], but this transduction mechanism is inconvenient due to the lack of compatibility with standard silicon MEMS processes.

Several devices architecture and techniques to improve the sensitivity of the accelerometers were reported. More specifically, force amplification mechanisms with different configurations were studied and implemented. A Scale-factor of 1400 Hz/g with a non-linearity below 1 % and a bandwidth of $5Hz$ were experimentally measured in a device with a mass of $557.1\ \mu g$ [1.66]. The device footprint has several square millimetres, even though, a lever was used. The sensors presenting large sensitivity have generally a larger mass, and relative sensitivity (change in natural frequency per mass) comparison is useful to relate the efficiency of the sensors. A device with a smaller proof mass of $1.33\ \mu g$ and sensitivity of 17 Hz/g was also presented [1.67]. A noise figure of $4.8\ \mu g/\sqrt{Hz}$, bias stability of 55 μg for a dynamic range of $\pm 40\ g$ were experimentally measured [1.68] at a constant temperature, showing the adequate performance of this type of resonators.

Accelerometers based on torsional tuning forks resonators were developed for out-of-plane measurement (Z-axis) [1.69]. In this case, the rotational stiffness of the beam changes with the applied load. A sensitivity of $1.3\ Hz/g$, a dynamic range of $\pm 15\ g$ and a noise figure of $160\ \mu g/\sqrt{Hz}$ were also presented in the literature [1.69].

In Table 1.1, a summary of the major works reporting resonant accelerometers (single-beam and DETF based only) is demonstrated.

Resonator	Work	Axis	Natural Freq. (Hz)	Quality Factor	Scale factor (Hz/g)	Meas. Range ($\pm$g)	Res. (μg/$\sqrt{Hz}$)	BW (Hz)	Device Size (mm^2)
Single-beam	[1.58]	1	58	200	455	1*	460	100	0.25
	[1.63]	1	459	35000	22	-	5000	5	0.05
	[1.51]	2	84	-	250	1*	-	-	0.6
	[1.70]	1	549	-	61	1*	-	-	1.21*1
	[1.64]	1	352	30000	2752	1*	0.098	5	-
DETF	[1.61]	1	175	72000	2.4	20	-	-	0.12
	[1.66]	1	350	-	1399	3	309	100	7*2
	[1.67]	1	145	10000	30	1	40	1	0.55
	[1.71]	1	19.5	2.5×10^5	364	-	0.18	-	24*2
	[1.72]	2	290	-	275	1	-	-	3.61
	[1.65]	1	140.7	-	28.4	1	-	-	3.2
	[1.68]	1	22	-	250	40	-	-	110
	[1.73]	1	149.52	25000	9408	0.05	0.15	-	-
	[1.69]	1 (Z)	25	-	1.3	15	160	50	0.32

* From the data available.
*1 Proof mass size.
*2 Measured from a picture.

Table 1.1: Main research present in the literature concerning in-plane and out-of-plane resonant accelerometers based on single-beam and DETF resonators. The natural frequency, measurement range, resolution and bandwidth (BW) are some of the parameters available for comparison.

1.4 Frequency-modulated devices

The interest in MEMS devices with vacuum encapsulation and higher integration capabilities goes beyond the development of accelerometers. Several frequency-modulated devices were studied due to the integration benefits exemplified to IMU and other intrinsic properties already discussed.

In the literature, frequency modulated magnetometers [1.74], gyroscopes [1.75], inclinometers [1.76] and high resolution strain sensors [1.77], [1.78] were already presented, validating the interest in this kind of devices as a suitable alternative. The devices were adapted to sense different forces (e.g. Lorentz, Coriolis force) and encapsulated in vacuum. Gyroscopes, accelerometers and magnetometers, for instance, can be then combined in a single die (monolithic integration), resulting in 9-axis IMU. These sensors are used for absolute orientation, and the fusion of their response is applied in navigation as well as an extended number of consumer electronic devices [1.79]. The integration of additional sensors in the same silicon chip reduces costs and size and will enable even more applications in different industries.

1.5 Motivation and goals

The development of a resonant accelerometer and all the multidisciplinary components to successfully instrument and characterise it, are the main motivation of this thesis. A deep study and understanding of the transduction capabilities and the possible benefits for the automotive industry were also aimed.

The proposed approach of a MEMS accelerometer composed of DETF resonators is fairly recent in the literature and no commercial devices were found during the state-of-the-art review. The different benefits of a frequency modulated transduction have the potential of decreasing fabrication prices, making them even more accessible for the car manufacturers. Looking at the state-of-the-art, the resonant accelerometers still have large footprints to enable high-sensitivities and some drawbacks of this approach are still to be overcome. However, new designs and further developments are believed to result in a device fitting the requirements to be mass-produced.

The work developed, in this thesis, was performed in the scope of a partnership between University of Minho and Robert Bosch GmbH. This partnership resulted in a doctoral program in Advance Engineering Systems for Industry (AESI), directed by the Algoritmi Research Center. Since the research focus is on a MEMS devices for the automotive industry, a close cooperation was established with the Automotive Electronics Group at Robert Bosch GmbH, in Reutlingen, Germany. This group provided a list of different requirement to align the performance of the proposed accelerometer:

- Operation: fully resonant;
- Encapsulation pressure: 100 Pa ($1 mbar$);
- Core size: 400 μm x 400 μm ($0.16 mm^2$);

- Compatible with application-specific integrated circuit (ASIC) voltages:
  - Analog voltage: <2.5 V;
  - Digital voltage: <1.2 V;
- Temperature Range: -40 °C to 125 °C;
- Offset stability in temperature range: 20 mg;
- Measurement range: $\pm$5 g;
- Bandwidth of the sensor: 400 Hz;
- Noise figure: <100 $\mu g/\sqrt{Hz}$
- Non-linearity: <1% full-scale (FS);
- Vibrations (stable under sinusoidal accelerations in all axis):
  - 400 Hz - 5 kHz: 5g;
  - 5 kHz - 50 kHz: 2g;

These requirements target specific applications in the automotive industry and the integration with electronics implemented at the ASIC level (explaining the voltage restrictions). The stability (e.g. temperature and offset) and stable behaviour under vibrations is particularly important in this demanding industry.

To achieve the sensor envisioned, the project was divided into several milestones:

- Design, simulation and fabrication of a frequency modulated MEMS structure for acceleration measurement. The device has to comply with standard silicon MEMS processes (available at Bosch) and has to be encapsulated in vacuum.
- Development of a platform to operate the resonators in open-loop and closed-loop. The approach based on commercial off-the-shelf (COTS) equipment and discrete electronics at the printed circuit board (PCB) level has also a field-programmable gate array (FPGA) for control and interface purposes.
- Characterisation of the frequency modulated accelerometer and measurement of the main parameters.

An additional sensor was developed, as a proof of concept, to validate the feasibility of other devices based on double-ended tuning fork resonators. The intrinsic milestones of this sensor are:

- Design, simulation and implementation of a magnetometer based on DETF resonators. An in-house process on SOI wafers was used at the Iberian International Nanotechnology Laboratory to fabricate the devices.
- Optimisation of several Lorentz force transducer geometries to maximise the sensor sensitivity.
- Characterisation of the magnetometer to validate experimentally the device proposed.

1.6 Organisation of this thesis

In addition to this first chapter, where a brief introduction and the relevant state-of-the-art were covered, this document possesses five more chapters. The topics addressed in each chapter are in this section described.

In Chapter 2, the theoretical background behind the sensor design is briefly introduced. The different models are decomposed into several blocks and then joined to form the complete sensor. The instrumentation of DETF resonators is also approached.

In Chapter 3, the implementation of the frequency modulated sensor is explained in detail. The structures fabricated are shown and the design parameters listed. The different blocks composing the instrumentation system to operate the devices in open-loop and closed-loop are described.

The main characterisation results of the devices for different stimuli are shown in Chapter 4. The objective is to compare the expected behaviour of the systems (simulation results) with the experimental data, and understand the differences or limitations of the device and instrumentation system (open-loop and closed-loop). Additionally, a complete characterisation and understanding of the device behaviour, if external forces are introduced through the packaging is demonstrated. Both soft and hard glues were used to bond the silicon die to the chip carrier, and a study of the influence of these glues in the sensor response was performed.

In Chapter 5, a magnetometer composed of DETF resonators is introduced. The design and implementation steps are divided into several subsections and the theoretical background necessary to design magnetic transducers is revised. The devices are experimentally validated using the instrumentation system described in Chapter 3. This sensor brings, the state-of-the-art, one step forward to the integration of a higher number of frequency-modulated devices in the same silicon die.

In Chapter 6, the results obtained are analysed in detail. This chapter concludes this thesis and possible improvements, in terms of device and instrumentation system, are discussed.

References

[1.1] R. P. Feynman, "There's plenty of room at the bottom", Journal of Microelectromechanical Systems, vol. 1, no. 1, pp. 60–66, Mar. 1992. doi: 10.1109/84.128057.

[1.2] R. R. Schaller, "Moore's law: past, present, and future", IEEE Spectrum, vol. 34, no. 6, pp. 52–55, 57, 1997. doi: 10.1109/6.591665.

[1.3] M. Riordan, "The lost history of the transistor", IEEE Spectrum, vol. 41, no. 5, pp. 44–49, 2003. doi: 10.1109/MSPEC.2004.1296014.

[1.4] C. Lécuyer and D. C. Brock, "The Materiality of Microelectronics", History and Technology, vol. 22, no. 3, pp. 301–325, Sep. 2006. doi: 10.1080/07341510600803440.

[1.5] Chang Liu, Foundations of MEMS. New Jersey: Pearson Education, Inc., 2014, isbn: 0-13-147286-0.

[1.6] V. Lindroos, M. Tilli, A. Lehto, T. Motooka, and T. Veijola, "Handbook of silicon based MEMS materials and technologies", Micro & Nano Technologies Series, 2010. doi: 10.1016/B978-0-8155-1594-4.00014-0.

[1.7] M. Haskard, A. Hariz, and A. Marriage, "Micro engineering-a brief overview", in Proceedings Electronic Technology Directions to the Year 2000, IEEE Comput. Soc. Press, 1956, pp. 242–245. doi: 10.1109/ETD.1995.403467.

[1.8] H. C. Nathanson, W. E. Newell, R. A. Wickstrom, and J. R. Davis, "The resonant gate transistor", IEEE Transactions on Electron Devices, pp. 117–133, 1967. doi: 10.1109/9780470545263.sect1.

[1.9] E. Bassous, H. H. Taub, and L. Kuhn, "Ink jet printing nozzle arrays etched in silicon", Applied Physics Letters, vol. 31, no. 2, pp. 135–137, 1977. doi: 10.1063/1.89587.

[1.10] L. Kuhn, E. Bassous, and R. Lane, "Silicon charge electrode array for ink jet printing", IEEE Transactions on Electron Devices, vol. 25, no. 10, pp. 1257–1260, 1978. doi: 10.1109/T-ED.1978.19261.

[1.11] J. P. Baker, D. A. Johnson, V. Joshi, and S. J. Nigro, "Design and Development of a Color Thermal Inkjet Print Cartridge.", Hewlett-Packard Journal, pp. 6–15, 1988, issn: 00181153.

[1.12] D. Eddy and D. Sparks, "Application of MEMS technology in automotive sensors and actuators", Proceedings of the IEEE, vol. 86, no. 8, pp. 1747–1755, 1998. doi: 10.1109/5.704280.

[1.13] N. Tiliakos, MEMS for harsh environment sensors in aerospace applications: Selected case studies. Woodhead Publishing Limited, 2013, pp. 245–282, isbn: 9780857091185. doi: 10.1533/9780857096487.2.245.

[1.14] P. B. Ruffin, "MEMS-based sensor arrays for military applications", in Smart Structures and Materials 2002: Smart Electronics, MEMS, and Nanotechnology, V. K. Varadan, Ed., International Society for Optics and Photonics, vol. 4700, SPIE, 2002, pp. 111–121. doi: 10.1117/12.475022.

[1.15] Yole Dévelopment, From Technologies to Markets, Status of the MEMS Industry Get high for MEMS, 2018. [Online]. Available: https://www.systemplus.fr/wp-content/uploads/2018/10/YD18019_Status_of_the_MEMS_Industry_2018_sample.pdf.

[1.16] J. G. Korvink and O. Paul, MEMS: A practical guide of design, analysis, and applications. 2006, isbn: 0815514972. doi: 10.1007/978-3-540-33655-6.

[1.17] S. D. Senturia, Microsystem design, Fifth. New Delhi: Springer, 2002, p. 689, isbn: 978-0792372462.

[1.18] M. I. Lectro and E. S. Ystems, "2013 Edition International Technology Roadmap for Semiconductors", Tech. Rep., 2013, pp. 1–36.

[1.19] V. Kaajakari, Practical MEMS: Design of microsystems, accelerometers, gyroscopes, RF MEMS, optical MEMS, and microfluidic systems. Las Vegas: Small Gear Publishing, 2009, p. 496, isbn: 978-0982299104.

[1.20] J. Levinson, J. Askeland, J. Becker, J. Dolson, D. Held, S. Kammel, J. Z. Kolter, D. Langer, O. Pink, V. Pratt, M. Sokolsky, G. Stanek, D. Stavens, A. Teichman, M. Werling, and S. Thrun, "Towards fully autonomous driving: Systems and algorithms", IEEE Intelligent Vehicles Symposium, Proceedings, pp. 163–168, 2011. doi: 10.1109/IVS.2011.5940562.

[1.21] C. D. Liao and J. C. Tsai, "The evolution of MEMS displays", IEEE Transactions on Industrial Electronics, vol. 56, no. 4, pp. 1057–1065, 2009. doi: 10.1109/TIE.2008.2005684.

[1.22] L. J. Hornbeck, "Digital Light Processing for high-brightness high-resolution applications", in Projection Displays III, M. H. Wu, Ed., vol. 3013, May 1997, pp. 27–40. doi: 10.1117/12.273880.

[1.23] H. Jaafar, K. S. Beh, N. A. M. Yunus, W. Z. W. Hasan, S. Shafie, and O. Sidek, "A comprehensive study on RF MEMS switch", Microsystem Technologies, vol. 20, no. 12, pp. 2109–2121, Dec. 2014. doi: 10.1007/s00542-014-2276-7.

[1.24] G. D. Patil and N. R. Kolhare, “A Review Paper on RF MEMS Switch for Wireless Communication”, International Journal of Engineering Trends and Technology, vol. 4, no. 2, pp. 195–198, 2013, issn: 2231-5381.

[1.25] J. Weigold, T. Brosnihan, J. Bergeron, and X. Zhang, “A MEMS Condenser Microphone for Consumer Applications”, in 19th IEEE International Conference on Micro Electro Mechanical Systems, IEEE, 2006, pp. 86–89. doi: 10.1109/MEMSYS.2006.1627742.

[1.26] F. Stoppel, A. Mannchen, F. Niekiel, D. Beer, T. Giese, and B. Wagner, “New integrated full-range MEMS speaker for in-ear applications”, Proceedings of the IEEE International Conference on Micro Electro Mechanical Systems (MEMS), vol. 2018-January, no. January, pp. 1068–1071, 2018. doi: 10.1109/MEMSYS.2018.8346744.

[1.27] B. Gogoi and D. Mladenovic, “Integration technology for MEMS automotive sensors”, in IEEE 2002 28th Annual Conference of the Industrial Electronics Society. IECON 02, vol. 4, IEEE, 2002, pp. 2712–2717. doi: 10.1109/IECON.2002.1182823.

[1.28] B. Heißing and M. Ersoy, “Chassis control systems”, in Chassis Handbook: Fundamentals, Driving Dynamics, Components, Mechatronics, Perspectives. Wiesbaden: Vieweg+Teubner, 2011, pp. 493–556, isbn: 978-3-8348-0994-0. doi: 10.1007/978-3-8348-9789-3.

[1.29] B. Boser and R. Howe, “Surface micromachined accelerometers”, IEEE Journal of Solid-State Circuits, vol. 31, no. 3, pp. 366–375, Mar. 1996. doi: 10.1109/4.494198.

[1.30] N. Yazdi, F. Ayazi, and K. Najafi, “Micromachined inertial sensors”, Proceedings of the IEEE, vol. 86, no. 8, pp. 1640–1659, Aug. 1998. doi: 10.1109/5.704269.

[1.31] K. Petersen, “Silicon as a mechanical material”, Proceedings of the IEEE, vol. 70, no. 5, pp. 420–457, May 1982. doi: 10.1109/PROC.1982.12331.

[1.32] J. Bustillo, R. Howe, and R. Muller, “Surface micromachining for microelectromechanical systems”, Proceedings of the IEEE, vol. 86, no. 8, pp. 1552–1574, Jan. 1998. doi: 10.1109/5.704260.

[1.33] F. Laermer and A. Urban, “Milestones in deep reactive ion etching”, in The 13th International Conference on Solid-State Sensors, Actuators and Microsystems (TRANSDUCERS ’05)., vol. 2, IEEE, 2005, pp. 1118–1121. doi: 10.1109/SENSOR.2005.1497272.

[1.34] C. Sander, J. Knutti, and J. Meindl, “A monolithic capacitive pressure sensor with pulse-period output”, in 1980 IEEE International Solid-State Circuits Conference. Digest of Technical Papers, IEEE, 1980, pp. 78–79. doi: 10.1109/ISSCC.1980.1156130.

[1.35] Y. C. Lee, Y.-T. Cheng, and R. Ramadoss, MEMS Packaging. World Scientific, Feb. 2018, vol. 05. doi: 10.1142/10692.

[1.36] Y. Yang, E. J. Ng, Y. Chen, I. B. Flader, and T. W. Kenny, "A Unified Epi-Seal Process for Fabrication of High-Stability Microelectromechanical Devices", Journal of Microelectromechanical Systems, vol. 25, no. 3, pp. 489–497, Jun. 2016. doi: 10.1109/JMEMS.2016.2537829.

[1.37] E. J. Ng, K. L. Harrison, Y. Yang, C. H. Ahn, V. A. Hong, R. T. Howe, and T. W. Kenny, "Stable Encapsulated Charge-Biased Resonators", Journal of Microelectromechanical Systems, vol. 25, no. 1, pp. 30–37, Feb. 2016. doi: 10.1109/JMEMS.2015.2483365.

[1.38] Yole Développment, "Packaging beyond the mainstream", 3dpackaging, 2013. [Online]. Available: http://www.yole.fr/iso_upload/Mag/3D_fevrier_2013_mail.pdf.

[1.39] J. H. Lau, C. K. Lee, C. S. Premachandran, and Y. Aibin, Advanced mems packaging. McGraw-Hill Education, 2009, p. 576, isbn: 978-0071626231.

[1.40] B. V. Amini and F. Ayazi, "Micro-gravity capacitive silicon-on-insulator accelerometers", Journal of Micromechanics and Microengineering, vol. 15, no. 11, pp. 2113–2120, Nov. 2005. doi: 10.1088/0960-1317/15/11/017.

[1.41] J. Chae, H. Kulah, and K. Najafi, "An In-Plane High-Sensitivity, Low-Noise Micro-g Silicon Accelerometer With CMOS Readout Circuitry", Journal of Microelectromechanical Systems, vol. 13, no. 4, pp. 628–635, Aug. 2004. doi: 10.1109/JMEMS.2004.832653.

[1.42] TE Connectivity, 820M1 Condition monitoring accelerometer, 2019. [Online]. Available: https://www.te.com.

[1.43] M. Messina, J. Njuguna, and C. Palas, "Mechanical Structural Design of a MEMS-Based Piezoresistive Accelerometer for Head Injuries Monitoring: A Computational Analysis by Increments of the Sensor Mass Moment of Inertia", Sensors, vol. 18, no. 1, p. 289, Jan. 2018. doi: 10.3390/s18010289.

[1.44] J. Bahari and A. M. Leung, "Micromachined three-axis thermal accelerometer with a single composite heater", Journal of Micromechanics and Microengineering, vol. 21, no. 7, p. 075 025, Jul. 2011. doi: 10.1088/0960-1317/21/7/075025.

[1.45] R. P. Williams, N. A. Hall, and B. D. Avenson, "Grating-Based Acceleration Sensors with Optical Interferometric Readout and Closed-Loop Control", in 20th International Conference on Solid-State Sensors, Actuators and Microsystems & Eurosensors XXXIII (TRANSDUCERS & EUROSENSORS XXXIII), IEEE, Jun. 2019, pp. 507–510. doi: 10.1109/TRANSDUCERS.2019.8808749.

[1.46] K. Zandi, B. Wong, J. Zou, R. V. Kruzelecky, W. Jamroz, and Y.-A. Peter, “In-plane silicon-on-insulator optical MEMS accelerometer using waveguide fabry-perot microcavity with silicon/air bragg mirrors”, in IEEE 23rd International Conference on Micro Electro Mechanical Systems (MEMS), IEEE, Jan. 2010, pp. 839–842. doi: 10.1109/MEMSYS.2010.5442337.

[1.47] A. Sheikhaleh, K. Abedi, and K. Jafari, “An Optical MEMS Accelerometer Based on a Two- Dimensional Photonic Crystal Add-Drop Filter”, Journal of Lightwave Technology, vol. 35, no. 14, pp. 3029–3034, Jul. 2017. doi: 10.1109/JLT.2017.2706140.

[1.48] R. A. Dias, E. E. Moreira, I. Ribeiro, M. Costa, H. Fonseca, S. Cardoso, P. Freitas, L. A. Rocha, and J. Gaspar, “Novel magnetic readout for hybrid spintronic MEMS devices”, in 19th International Conference on Solid-State Sensors, Actuators and Microsystems (TRANSDUCERS), IEEE, Jun. 2017, pp. 818–821. doi: 10.1109/TRANSDUCERS.2017.7994174.

[1.49] S. Dalola, V. Ferrari, and D. Marioli, “Micromachined piezoresistive inclinometer with oscillator-based integrated interface circuit and temperature readout”, Measurement Science and Technology, vol. 23, no. 3, p. 035 107, Mar. 2012. doi: 10.1088/0957-0233/23/3/035107.

[1.50] O. Ergeneman, P. Eberle, M. Suter, G. Chatzipirpiridis, K. Sivaraman, S. Pané, C. Hierold, and B. Nelson, “An in-plane cobalt–nickel microresonator sensor with magnetic actuation and readout”, Sensors and Actuators A: Physical, vol. 188, pp. 120–126, Dec. 2012. doi: 10.1016/j.sna.2012.05.035.

[1.51] A. Caspani, C. Comi, A. Corigliano, G. Langfelder, and A. Tocchio, “Compact biaxial micromachined resonant accelerometer”, Journal of Micromechanics and Microengineering, vol. 23, no. 10, p. 105 012, Oct. 2013, issn: 0960-1317. doi: 10.1088/0960-1317/23/10/105012.

[1.52] A. Merdassi, M. N. Kezzo, G. Xereas, and V. P. Chodavarapu, “Wafer level vacuum encapsulated tri-axial accelerometer with low cross-axis sensitivity in a commercial MEMS Process”, Sensors and Actuators A: Physical, vol. 236, pp. 25–37, Dec. 2015. doi: 10.1016/j.sna.2015.10.014.

[1.53] Jiangfeng Wu and L. Carley, “Electromechanical /spl Delta//spl Sigma/ modulation with high-Q micromechanical accelerometers and pulse density modulated force feedback”, IEEE Transactions on Circuits and Systems I: Regular Papers, vol. 53, no. 2, pp. 274–287, Feb. 2006. doi: 10.1109/TCSI.2005.857084.

[1.54] F. Chen, X. Li, and M. Kraft, “Electromechanical Sigma–Delta Modulators ($\Sigma\Delta M$) Force Feedback Interfaces for Capacitive MEMS Inertial Sensors: A Review”, IEEE Sensors Journal, vol. 16, no. 17, pp. 6476–6495, Sep. 2016. doi: 10.1109/JSEN.2016.2582198.

[1.55] W. T. Pike, I. M. Standley, S. B. Calcutt, and A. G. Mukherjee, “A broad-band silicon microseismometer with 0.25 NG/rtHz performance”, in IEEE Micro Electro Mechanical Systems (MEMS), IEEE, Jan. 2018, pp. 113–116. doi: 10.1109/MEMSYS.2018.8346496.

[1.56] M. Pandit, C. Zhao, G. Sobreviela, X. Zou, and A. A. Seshia, “Seismic Recording Using A Mode Localized MEMS Accelerometer”, in 20th International Conference on Solid-State Sensors, Actuators and Microsystems & Eurosensors XXXIII (TRANSDUCERS & EUROSENSORS XXXIII), IEEE, Jun. 2019, pp. 2150–2153. doi: 10.1109/TRANSDUCERS.2019.8808572.

[1.57] H. Zhang, B. Li, W. Yuan, M. Kraft, and H. Chang, “An Acceleration Sensing Method Based on the Mode Localization of Weakly Coupled Resonators”, Journal of Microelectromechanical Systems, vol. 25, no. 2, pp. 286–296, Apr. 2016. doi: 10.1109/JMEMS.2015.2514092.

[1.58] C. Comi, A. Corigliano, G. Langfelder, A. Longoni, A. Tocchio, and B. Simoni, “A Resonant Microaccelerometer With High Sensitivity Operating in an Oscillating Circuit”, Journal of Microelectromechanical Systems, vol. 19, no. 5, pp. 1140–1152, Oct. 2010. doi: 10.1109/JMEMS.2010.2067437.

[1.59] M. Meldrum, “Application of vibrating beam technology to digital acceleration measurement”, Sensors and Actuators A: Physical, vol. 21, no. 1-3, pp. 377–380, Feb. 1990. doi: 10.1016/0924-4247(90)85075-F.

[1.60] B. L. Norling, “Superflex: A synergistic combination of vibrating beam and quartz flexure accelerometer technology”, Navigation, vol. 34, no. 4, pp. 337–353, 1987. doi: 10.1002/j.2161-4296.1987.tb01511.x.

[1.61] T. Roessig, R. Howe, A. Pisano, and J. Smith, “Surface-micromachined resonant accelerometer”, in Proceedings of International Solid State Sensors and Actuators Conference (Transducers ’97), vol. 2, IEEE, Nov. 1997, pp. 859–862. doi: 10.1109/SENSOR.1997.635237.

[1.62] D. Burns, R. Horning, W. Herb, J. Zook, and H. Guckel, “Sealed-cavity resonant microbeam accelerometer”, Sensors and Actuators A: Physical, vol. 53, no. 1-3, pp. 249–255, May 1996. doi: 10.1016/0924-4247(96)01135-1.

[1.63] D. Pinto, D. Mercier, C. Kharrat, E. Colinet, V. Nguyen, B. Reig, and S. Hentz, “A Small and High Sensitivity Resonant Accelerometer”, Procedia Chemistry, vol. 1, no. 1, pp. 536–539, Sep. 2009. doi: 10.1016/j.proche.2009.07.134.

[1.64] C. Zhao, M. Pandit, G. Sobreviela, P. Steinmann, A. Mustafazade, X. Zou, and A. Seshia, “A Resonant MEMS Accelerometer With 56ng Bias Stability and 98ng/Hz 1/2 Noise Floor”, Journal

of Microelectromechanical Systems, vol. 28, no. 3, pp. 324–326, Jun. 2019. doi: 10.1109/JMEMS.2019.2908931.

[1.65] Y. Wang, H. Ding, X. Le, W. Wang, and J. Xie, "A MEMS piezoelectric in-plane resonant accelerometer based on aluminum nitride with two-stage microleverage mechanism", Sensors and Actuators A: Physical, vol. 254, pp. 126–133, Feb. 2017. doi: 10.1016/j.sna.2016.12.019.

[1.66] Xudong Zou, P. Thiruvenkatanathan, and A. A. Seshia, "A Seismic-Grade Resonant MEMS Accelerometer", Journal of Microelectromechanical Systems, vol. 23, no. 4, pp. 768–770, Aug. 2014. doi: 10.1109/JMEMS.2014.2319196.

[1.67] A. Seshia, M. Palaniapan, T. Roessig, R. Howe, R. Gooch, T. Schimert, and S. Montague, "A vacuum packaged surface micromachined resonant accelerometer", Journal of Microelectromechanical Systems, vol. 11, no. 6, pp. 784–793, Dec. 2002. doi: 10.1109/JMEMS.2002.805207.

[1.68] J. Zhang, Y. Su, Q. Shi, and A.-P. Qiu, "Microelectromechanical Resonant Accelerometer Designed with a High Sensitivity", Sensors, vol. 15, no. 12, pp. 30 293–30 310, Dec. 2015. doi: 10.3390/s151229803.

[1.69] C. R. Marra, F. M. Ferrari, G. Langfelder, A. Tocchio, and F. Rizzini, "Single resonator, time-switched, low offset drift z-axis FM MEMS accelerometer", in IEEE International Symposium on Inertial Sensors and Systems (INERTIAL), vol. 2, IEEE, Mar. 2018, pp. 1–4. doi: 10.1109/ISISS.2018.8358116.

[1.70] H. Ding, W. Wang, B.-F. Ju, and J. Xie, "A MEMS resonant accelerometer with sensitivity enhancement and adjustment mechanisms", Journal of Micromechanics and Microengineering, vol. 27, no. 11, p. 115 010, Nov. 2017. doi: 10.1088/1361-6439/aa8d99.

[1.71] Y. Yin, Z. Fang, Y. Liu, and F. Han, "Temperature-Insensitive Structure Design of Micromachined Resonant Accelerometers", Sensors, vol. 19, no. 7, p. 1544, Mar. 2019. doi: 10.3390/s19071544.

[1.72] H. Ding, J. Zhao, B. Ju, and J. Xie, "A highly sensitive biaxial resonant accelerometer with two-stage microleverage mechanisms", in IEEE 29th International Conference on Micro Electro Mechanical Systems (MEMS), vol. 2016-Febru, IEEE, Jan. 2016, pp. 934–937. doi: 10.1109/MEMSYS.2016.7421785.

[1.73] X. Zou and A. A. Seshia, "A high-resolution resonant MEMS accelerometer", in 18th International Conference on Solid-State Sensors, Actuators and Microsystems (TRANSDUCERS), IEEE, Jun. 2015, pp. 1247–1250. doi: 10.1109/TRANSDUCERS.2015.7181156.

[1.74] W. Zhang and J. E.-Y. Lee, "Characterization and model validation of a micromechanical resonant magnetic field sensor", in 17th International Conference on Solid-State Sensors, Actuators and

Microsystems (TRANSDUCERS & EUROSENSORS XXVII), vol. 2, IEEE, Jun. 2013, pp. 1859–1862. doi: 10.1109/Transducers.2013.6627153.

[1.75] V. Zega, P. Minotti, G. Mussi, A. Tocchio, L. Falorni, S. Facchinetti, A. Bonfanti, A. L. Lacaita, C. Comi, G. Langfelder, and A. Corigliano, “The First Frequency-Modulated (FM) Pitch Gyroscope”, Proceedings, vol. 1, no. 4, p. 393, Aug. 2017. doi: 10.3390/proceedings1040393.

[1.76] S. Wang, X. Wei, Y. Weng, Y. Zhao, and Z. Jiang, “A Novel Single-Axis MEMS Tilt Sensor with a High Sensitivity in the Measurement Range from 0▯ to 360▯”, Sensors, vol. 18, no. 2, p. 346, Jan. 2018. doi: 10.3390/s18020346.

[1.77] L. Belsito, M. Ferri, F. Mancarella, L. Masini, J. Yan, A. A. Seshia, K. Soga, and A. Roncaglia, “Fabrication of high-resolution strain sensors based on wafer-level vacuum packaged MEMS resonators”, Sensors and Actuators A: Physical, vol. 239, pp. 90–101, Mar. 2016. doi: 10.1016/j.sna.2016.01.006.

[1.78] C. D. Do, A. Erbes, J. Yan, K. Soga, and A. A. Seshia, “Vacuum Packaged Low-Power Resonant MEMS Strain Sensor”, Journal of Microelectromechanical Systems, vol. 25, no. 5, pp. 851–858, 2016. doi: 10.1109/JMEMS.2016.2587867.

[1.79] Bosch Sensortec, BNO055 Intelligent 9-axis absolute orientation sensor, 2014.

Chapter 2

Resonant accelerometer

With the goal of designing a resonant accelerometer based on double-ended tuning fork resonators, theoretical background on the mechanics and the electromechanical coupling is necessary. This chapter is divided into three main parts, that can be considered the principal blocks to achieve the proposed device.

First, the focus of research is on the resonator (DETF) and its intrinsic characteristics. The various aspects regarding the natural frequency change when undergoing a load are studied, as well as the behaviour when coupled electromechanically through electrostatically actuated parallel-plates. A one degree-of-freedom model of the resonator composed of the different forces present in the system is critical to understand the various parameters in the oscillatory regime and design the pick-up electronics accordingly. The resonators have several physical properties that are affected by temperature dependency or charge effects, among others, which need to be accounted for when designing the device. Additionally, techniques are presented to minimise common-mode errors.

After the analysis of the pros and cons of the resonator, an accelerometer is designed to sense external acceleration. Several challenges arise, but the main focus is on increasing the sensitivity of DETF resonators since the footprint aimed is small when compared to devices reported with the same resonator type. For this reason, a differential architecture with a force amplification mechanism is introduced. A complete model of the accelerometer was developped to study the complete mechanical system.

Regarding the instrumentation of the resonators response, open-loop and closed-loop operation are described, with particular emphasis on the advantages and disadvantages of each method when applied to resonant accelerometers.

2.1 Resonance

Resonance is a property of a system resulting in a specific response at the system's natural frequency. In oscillatory systems, the resonant frequency is the frequency where the system retains the maximum input energy with the minimal loss [2.1]. This effect is observed in many systems (e.g. electronic or mechanical) composed of different elements inter-converting energy between the different domains.

In devices with movable parts, the interconversion of energy is made between kinetic and potential energy stored in the form of a compressed spring. When the spring decompresses, the mass attached to it absorbs the energy, resulting in motion [2.1]. Each cycle dissipates energy due to damping, but when the parts are vibrating at the resonance frequency, the transfer of energy is in phase, minimising losses. This results in an enhanced displacement.

Resonance is avoided in large structures, such as buildings or bridges since it can lead to critical failures. Nonetheless, the scaling laws make the effect particularly interesting in microdevices, due to a faster dimensional scaling over spring constants. At the micro-scale, resonance enhances the effect of small forces and increases device displacement. Large displacements (i.e. large oscillation amplitudes) are obtained from low-power driving (at the natural frequency). Moreover, this has several applications in MEMS sensors and actuators, because of the large motional amplitude usually desired. Gyroscopes [2.2], magnetometers [2.3] and mirrors [2.4], among other devices, largely exploit the system's characteristic at resonance.

Focusing on micromechanical resonators, many geometries are used such as beams, plates and disks, among others. Each feature shape enhances a specific mode of resonance. Commonly, resonators are categorised into the mode of operation, namely, flexural, torsional and bulk. The different modes are schematised in Figure 2.1.

The flexural mode of vibration represents transverse standing waves, meaning that the displacement is orthogonal to the bending stress in the structure [2.5]. This mode of vibration is used in single-beam and double-ended tuning fork resonators. Resonators vibrating in the torsional mode (rotational movement) are found in out-of-plane sensors [2.6]. The bulk mode of operation is identified by the longitudinal waves and devices such as wineglass gyroscopes use this vibrational modal shape [2.7].

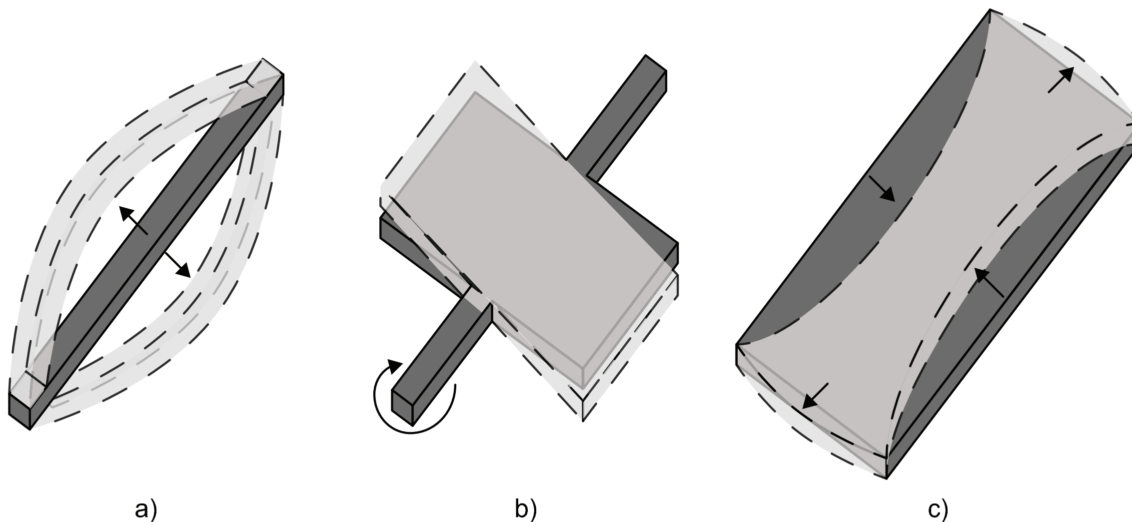

Figure 2.1: Modes of resonance: a) Flexural; b) Torsional; c) Bulk.

2.2 Double-ended tuning fork resonator

The resonating elements take many forms, but double-ended tuning fork resonators present attractive advantages that will be adressed in this section. The benefits are namely a higher quality factor and zero net force at the supporting anchors. More in detail, driving the beams in anti-phase reduces the vibration waves at the anchors, reducing the energy loss and consequently increasing the quality factor [2.8]. These resonators are composed of two parallel beams clamped on both sides and electrodes, as shown in Figure 2.2.

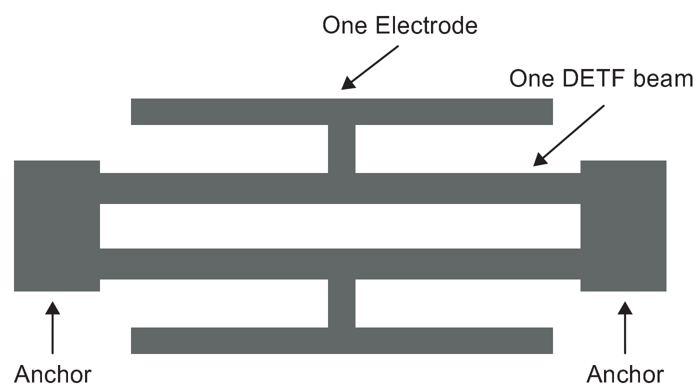

Figure 2.2: Schematic of clamped-clamped double ended-tuning fork resonators and the different features composing it

The beams are forced to vibrate when excited by an electrostatic force applied on the electrodes. The beams can be excited into any resonant mode, but here only the first flexural mode is of interest. The DETF natural frequency (f_0) is dependent on the constant of elasticity of the beams (k_b), the mass of the

electrodes (M_e - if any electrode is coupled to the beams) and the mass of the beam itself (M_b), and is given by Equation 2.1.

$$f_0 = \frac{1}{2\pi}\sqrt{\frac{k_b}{M_e + 0.38M_b}} \tag{2.1}$$

The spring constant of a single clamped-clamped beam when no force is applied to one of the extremities can be approximated by Equation 2.2, where E is the Young's modulus of the resonator's material (silicon), I_b the second moment of inertia and L_b the length of the beams.

$$k_b = \frac{192 \times E \times I_b}{L_b^3} \tag{2.2}$$

The second moment of inertia is given by Equation 2.3,

$$I_b = \frac{t \times w_b^3}{12} \tag{2.3}$$

where t is beam thickness and w_b the beam width. Analysing the equations presented, one can study the behaviour of the natural frequency of the DETF considering a constant electrode mass, see Figure 2.3. Shorter and wider beams result on higher natural frequency, note that the beam thickness does not change the natural frequency of the beams since it changes either the constant of elasticity and the mass (compensating each other).

2.2.1 Force measurement

Resonators have been used to measure several physical quantities since their natural frequency changes proportionally to an applied force. When a force is applied to an extremity of a DETF, the strain makes the spring stiffness of the beams slightly change, resulting in a change on the resonance frequency. This change is proportional, in this specific case, to the external acceleration applied to the proof mass.

The constant of elasticity of the beams (k_b) when undergoing a force (F) can be calculated using Equation 2.4 [2.9]:

$$k_b = \frac{192 \times E \times I_b}{L^3}\left(1 + \frac{L_b^2 \times F}{40 \times E \times I_b}\right) \tag{2.4}$$

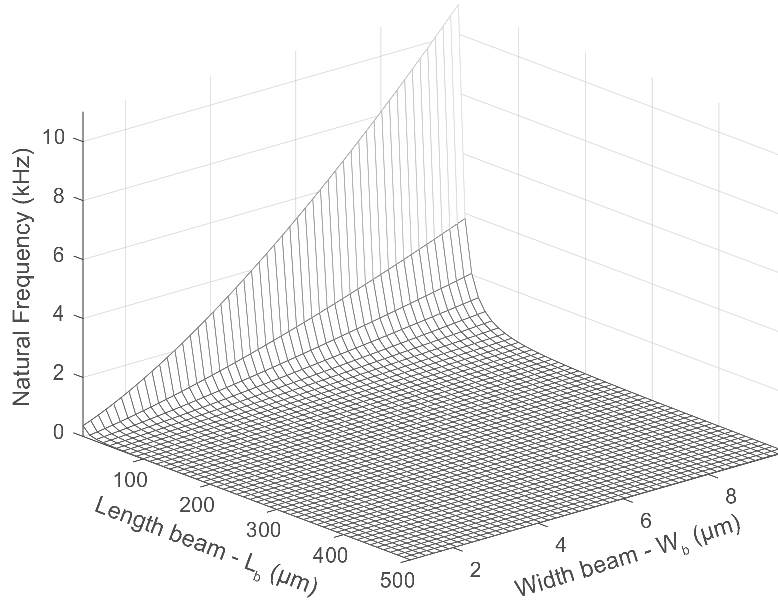

Figure 2.3: The behaviour of the natural frequency of DETF accordingly to the beam length and width.

The change in the natural frequency (Δf) of the DETF resonators is the difference between the resonance frequency (f) when submitted to force and the nominal natural frequency of the beams (f_0), it can also be presented as: $\Delta f = f - f_0$. Merging Equations 2.1 and 2.4, the drift resulting from a given force is calculated using Equation 2.5:

$$\Delta f = \frac{1}{2\pi}\left(\sqrt{\frac{\frac{192\times E\times I_b}{L_b^3}\left(1+\frac{L_b^2 * F}{40\times E\times I_b}\right)}{M_e+0.38M_b}} - \sqrt{\frac{\frac{192\times E\times I_b}{L_b^3}}{M_e+0.38M_b}}\right) \tag{2.5}$$

Using this equation, a complete study of the relation of the beams parameters (length and width) in the resonator frequency shift when undergoing a constant load was performed. Figure 2.4 shows a normalised Δf taking into account a fixed electrode weight and device thickness. Long and thin DETF beams increase the sensitivity of the resonators. In other words, the same force produces a larger frequency deviation. In addition, analysing Figures 2.3 and 2.4, resonators with lower natural frequency have a higher sensitivity.

Since the sensitivity tends to be low, usually, few Hertz per g, this parameter has to be optimised. The low frequency change is explained by the thin device layers in MEMS, yielding small proof-masses and consequently reduced forces. Another parameter that also influences the sensitivity of the DETF is the mass of the electrodes (see Equation 2.5). The scale-factor is inversely proportional to the weight of

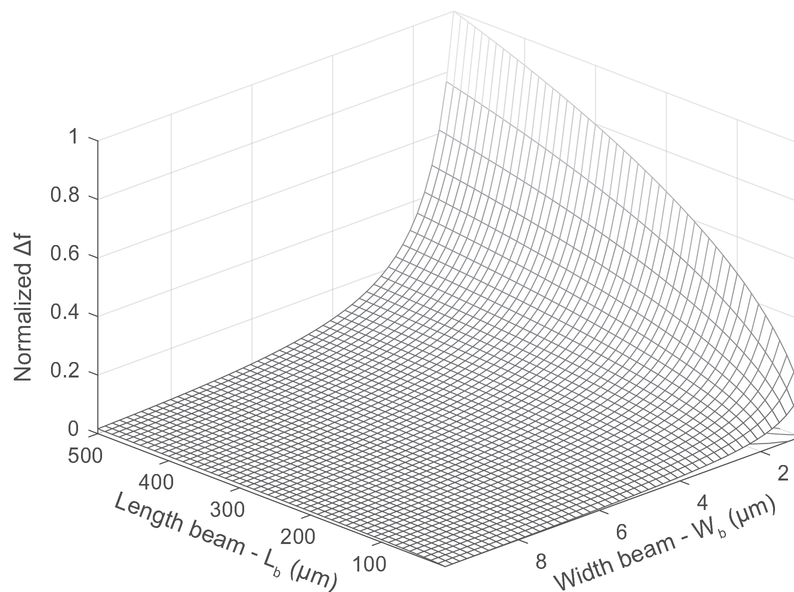

Figure 2.4: Sensitivity of a DETF when a fixed load is applied to the extremities accordingly to the beam length and width.

the electrodes, as shown in Figure 2.5. From this figure, one concludes that the highest sensitivity is obtained when no electrodes are attached to the beams. Nonetheless, coupling electrodes to the beams is advantageous for sensing and actuation proposes.

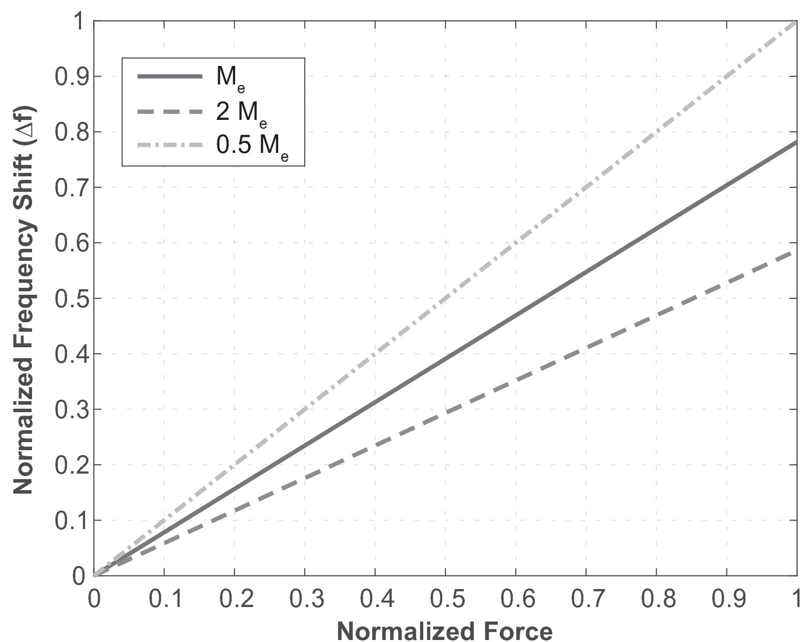

Figure 2.5: The normalised sensitivity plotted in function of force and mass of the electrodes.

2.2.2 Actuation and sensing

Actuation and sensing are part of the resonators since they enable a force to drive the beams and the means to detect the displacement. The electrodes need to be strategically placed to excite the resonance mode desired (first mode) since the beams have several resonant modes in different directions [2.10]. Additionally, the electrodes should be anchored in a way to maximise the displacement of the DETF beams. By optimising the displacement of the beams, lower excitation forces are necessary for the same amplitude of detection.

Several transduction methods are available to excite and drive the DETF, but electrostatic actuators and capacitive sensing are compatible with standard MEMS processes, being the reason for them to be here studied.

In the literature, resonators coupled to comb-drive [2.11] or parallel-plate [2.9] electrostatic actuators are reported. Comb-drives offer a good actuation linearity at the expense of lower capacity change (dC/dx) and smaller electrostatic force, when compared to parallel-plates actuators. In order to compensate the production of lower electrostatic forces generated, higher actuation voltages are required, and for beams with a high constant of elasticity, this can be problematic (in the case of resonators with high natural frequencies it leads to high driving voltages) [2.10]. But as explained in the previous section, to maximise the sensitivity, electrodes with lower mass must be used, and parallel-plates actuators offer a good dC/dx relation, and higher electrostatic forces for smaller area/mass, when compared to comb-drive actuators. A schematic of the DETF configuration with the driving and sensing electrodes is presented in Figure 2.6.

Note that some devices using single-beam or DETF resonators without any electrode are presented in [2.12]–[2.14]. Nonetheless, the increase of the scale-factor is made at the expense of lower capacity change in the sensing electrodes and higher driving voltages. Smaller signal outputs are often jeopardized by stray capacitance and higher electrostatic force yields to non-linearities, such as distortion of the output signal and instability in the resonant frequency [2.10].

2.2.3 One-degree of freedom analysis

In this section, the system composed of one of the beams of the resonator is studied. The DETF can be modelled as a simplified single-beam since the two beams are subject to the same force but moving in opposite direction to each other. Thus, recalling the driving of the beams is made in the first mode of

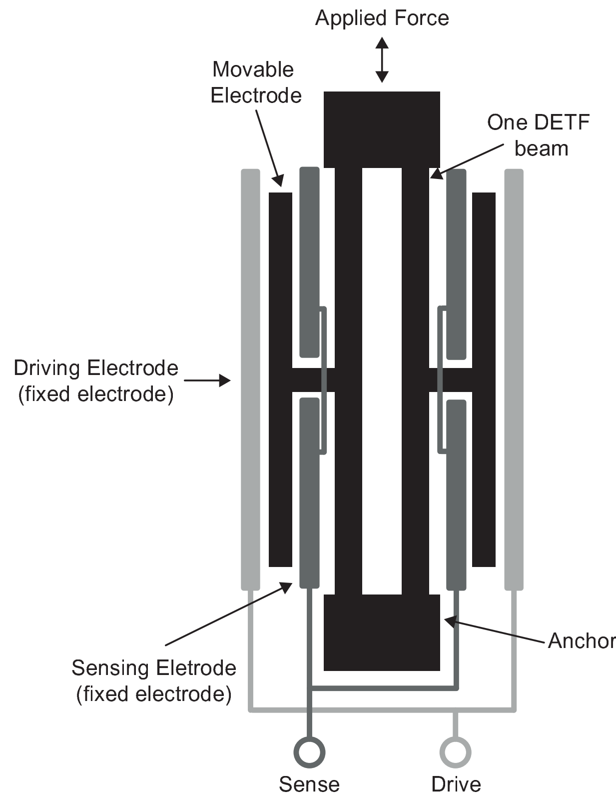

Figure 2.6: Schematic of the DETF basic operation when composed of driving and sensing capacitive electrodes.

resonance and in anti-phase. The different forces composing the system are depicted in Figure 2.7 and the movement of the beam is towards the driving and sensing electrodes.

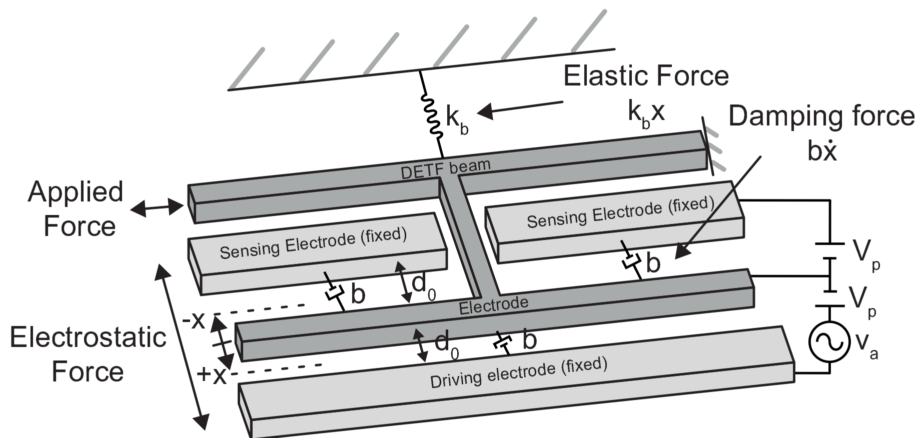

Figure 2.7: Different forces present in a one-degree of freedom analysis.

A resonator is accurately modelled as a one-degree degree of freedom damped oscillator since the vibrational behaviour, when harmonically excited, is described in terms of a time-dependent position coordinate. Additionally, the first mode of excitation is dominant and motion in other directions can be neglected, resulting in a good system accuracy [2.15].

Supposing that an excitation voltage is applied and the electrode starts oscillating, the distance between the parallel-plates changes thus producing a variation in the capacitance. The capacitance between the sensing and movable electrode (C_{0SM}) can be defined as:

$$C_{0SM} = \epsilon_0 \frac{A}{d_0 + x} \tag{2.6}$$

where ϵ_0 is the vacuum permittivity (the resonators are encapsulated in vacuum), A is the overlapping area of the parallel-plates, d_0 the initial gap in between electrodes and x the resulting displacement. If the electrode moves closer to the fixed sensing electrode, the capacitance increases. On the other hand, if the movement is in the opposite direction, the gap between the sensing electrode and the movable electrodes increases, decreasing the capacitance. The displacement of the movable electrode towards the sensing electrode or the driving electrode has different a signal, negative and positive, respectively, considering the initial gap as the reference. Therefore, The capacitance between the driving and movable electrode (C_{0DM}) is given by:

$$C_{0DM} = \epsilon_0 \frac{A}{d_0 - x} \tag{2.7}$$

If the movable electrode is biased with a DC voltage (V_p) and starts oscillating, this induces a current (i(t)) on the sensing electrodes due to the change of capacitance between electrodes (see Equation 2.8). This current is the output of the system, and since the resonators are moving in anti-phase by doubling the current amplitude value, one obtains the output of a DETF (two single-beams).

$$i(t) = V_P \frac{dC_{0SM}}{dt} \tag{2.8}$$

On the driving electrode, an AC voltage (v_a) is applied to excite the beam of the DETF. An electrostatic force is generated, forcing it to move at the same frequency. Note that the DETF beam is biased with a DC voltage (V_p), and this needs to be accounted for to calculate the force. The electrostatic force between the movable and the driving electrode is given by:

$$F_{ElectDM} = C_{0DM} \times d_0 \times \frac{(V_p \times v_a)^2}{2(d_0 - x)^2} \tag{2.9}$$

In the other hand, the electrode connected to the DETF is also attracted by the sensing electrode, considered at virtual ground potential. Resulting in an attractive force only dependent on the bias voltage:

$$F_{ElectSM} = C_{0SM} \times d_0 \times \frac{V_p^2}{2(d_0 + x)^2} \tag{2.10}$$

As a result of the movable electrode being in between two electrodes (i.e. sensing and driving electrodes), the resulting electrostatic force relation (F_{Elect}) is determined by the combination of the two forces present in the system. These are attracting in the opposite direction, restraining the motion of the beam:

$$F_{elect} = F_{ElectDM} - F_{ElectSM} \tag{2.11}$$

Another force acts in the system, the elastic force from the beams (F_{elast}=-k_bx), that opposes to the movement. The lateral constant of elasticity of the beam (k_b) changes in function of an applied force, but for now, this value is maintained constant.

At the macro-scale, the damping effects are ignored because the energy dissipation is much smaller than the energy supplied to the system. However, in MEMS, the damping defines the performance of the devices, and this effect must be studied.

The damping force ($F_b = b\frac{dx}{dt}$) depends on the motion velocity of the DETF electrode ($\frac{dx}{dt}$) and b represents the damping coefficient. The damping force, opposed to the movement of the movable plates, is mainly due to squeeze-film damping. In other words, the moving surfaces (moving electrode) squeeze the gas and cause fluid to flow towards the borders. Moreover, this effect is the strongest when the flow takes place in narrow gaps or channels [2.16]. The Bao model [2.17], with a factor of correction [2.18], is used to determine the damping coefficient:

$$b_{DM} = \frac{2.23 \times 0.96 \times (L_e + W_e) \times L_e \times t \times P_0}{4\pi} \times \sqrt{\frac{2 \times mm}{\pi \times k_B \times T}} \times \frac{N_e}{d_0 + x} \tag{2.12}$$

where L_e and W_e are the length and width of the electrode, respectively. The pressure inside the MEMS cavity (P_0), the air molar mass (mm), the Boltzmann constant (K_B) and the temperature (T) are also considered in Equation 2.12. Additionally, N_e represents the number of movable electrodes. Since the interaction of all the electrodes generates the damping force opposing to the movement, the Equation 2.12

has to be adapted to the interaction with the sensing electrodes (F_{bSM}). The total damping force (F_{btotal}) is calculated using Equation 2.13.

$$F_{btotal} = F_{bDM} + F_{bSM} \tag{2.13}$$

One other force arises from the movement of the movable electrode, the inertial force is related to the effective mass (m) and the acceleration ($\frac{d^2x}{dt^2}$): $F_i = m\frac{d^2x}{dt^2}$. The DETF and the electrode effective mass is alternatively calculated by: $m = M_e + 0.38M_b$. The inertial force opposes to the direction of movement.

All the forces considered in the system composed of a single-beam of the DETF were presented, and the equilibrium of forces is expressed by:

$$F_i + F_{btotal} + F_{elast} + F_{elect} = 0 \tag{2.14}$$

Assuming a constant linear spring (k_b), the system can be studied as a second-order mechanical model, given by Equation 2.15.

$$m\frac{d^2x}{dt^2} + b\frac{dx}{dt} + k_b x(t) = F_{exc}(t) \tag{2.15}$$

The excitation force (F_{exc}) represents the electrostatic force generated by either the driving (v_a) and bias voltages (V_p).

It is important to enhance that from this point, the system can be statically and dynamically studied. The static analysis assumes a quasi-static regime, meaning neither forces nor voltages change rapidly. This study can not be used to express the dynamic behaviour of the system since damping and inertia occur if the system undergoes motion. Thus, the dynamic behaviour can not be analytically predicted because the output of the system is time and position dependent. The equations can be analysed using simulation tools, such as Simulink™. The system here described was modelled using Simulink™, and the model is depicted in Figure 2.8.

From this model, the dynamics of the beam were extracted, namely the quality factor (Q). But all the parameters of the system are available for further study (e.g. displacement, output current and all the forces).

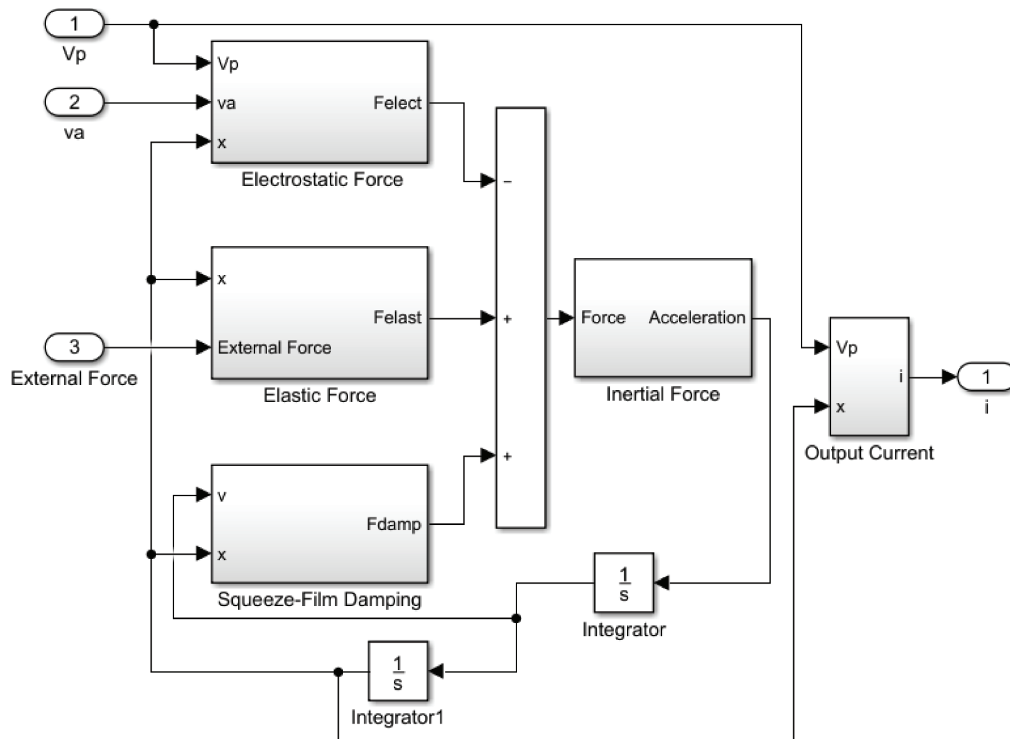

Figure 2.8: Simulink model implemented to study the dynamic behaviour of the system.

Regarding the quality factor ($Q = \frac{\sqrt{k_b \times m}}{b}$), this parameter describes the dynamic behaviour of the beams. The systems can be categorised into three groups accordingly to the value of Q:

- Q<0.5 - Overdamped system;
- Q=0.5 - Critically overdamped system;
- Q>0.5 - Underdamped system;

Underdamped systems are characterised by an oscillatory behaviour: the displacement increases at the natural frequency (losses are smaller). While overdamped and critically overdamped systems do not present this characteristic (see Figure 2.9). From this, it is possible to conclude that MEMS resonators must have a quality factor above 0.5 to possess an oscillatory behaviour at their natural frequency.

2.2.4 Non-linearities

DETF resonators are affected by physical effects that cause non-linearities. These non-linearities are divided into two categories that will be described in this section, namely mechanical and electrostatic actuation

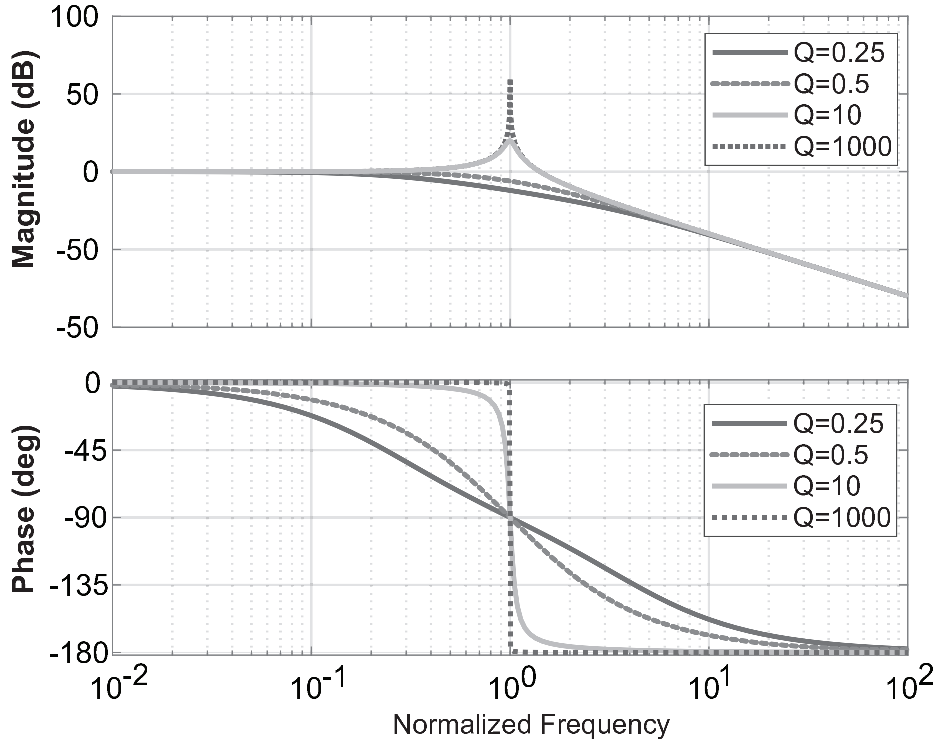

Figure 2.9: Bode plot for devices with different quality factors.

non-linearities. These affect the stability of the resonators and limit the actuation voltage (bias and driving voltage) [2.10].

Mechanical non-linearity

The predominant mechanical non-linearity is due to the hard-spring effect on the DETF beam, called amplitude stiffening. This leads to an increase of the natural frequency at large vibration amplitudes, resulting in a bending of the frequency response, which consequently influences the performance of the resonator. The driving amplitude (v_a) must be restrained to avoid large beam displacements since an axial extension cause a non-linear behaviour. If the DETF is added to an oscillatory system described by a second-order mechanical model, as the one presented in Equation 2.15, the non-linear effect of the stiffening is added through the cubic spring term ($k_{m3}x^3$) [2.19]. This results in the equation presented below:

$$m\frac{d^2x}{dt^2} + b\frac{dx}{dt} + k_b x(t) + k_{m3}x^3(t) = F_{exc}(t) \tag{2.16}$$

The cubic term is always positive and arise from an axial extension of the beams induced by large vibration amplitudes, the bending state and the structure parameters. The value of k_{m3} is not obtainable through an analytical model but by simulation or experiment [2.20]. Although, a large displacement evidences this drawback, small oscillation amplitudes induce an even lower current in the sensing electrodes, resulting in a challenging electrical detection and degradation of the signal noise floor. Concluding, a higher driving voltage results in a larger signal output but compromises the linearity of the resonator, and a trade-off must be found.

The quadratic spring constant is frequently ignored in DETF resonators, since the symmetrical geometry cancels this component [2.20].

Electrostatic actuation non-linearity

The second dominant non-linearity source is due to the non-linear actuator capacitance which induces an actuation force inversely proportional to the square of the displacement of the resonator beam. This force results on a spring softening and decreases the natural frequency of the beams. The main contribution for this force is the bias voltage (V_p), which adds an electrical spring constant. The spring constants were added to the Equation 2.16, resulting in the second-order model shown in Equation 2.17.

$$m\frac{d^2x}{dt^2} + b\frac{dx}{dt} + (k_b - k_{e1})x(t) + (k_{m3} - k_{e3})x^3(t) = F_{exc}(t) \tag{2.17}$$

where k_{e1} and k_{e3} are the linear and cubic electrical spring terms, respectively. Assuming a spring constant of a centre loaded DETF beam not dependent on the force externally applied, the constant of elasticity k_{e1} can be obtained by the Equation 2.18,

$$k_{e1} = \frac{2\epsilon_0 A_e V_p^2}{d_0^3} \tag{2.18}$$

where A_e represents the area of the electrode. The linear electric term (k_{e1}) is subtracted to the mechanical term of the constant of elasticity, in other words, the stiffness of the spring decreases with the square of the bias voltage (V_p). This effect is called spring softening, and the natural frequency of the DETF can be derived as the equation below, assuming no external force is applied to the beams.

$$f_0 = \frac{1}{2\pi}\sqrt{\frac{k_{m1} - k_{e1}}{M_e + 0.38M_b}} \tag{2.19}$$

Analysing Equation 2.19 and 2.18, one concludes higher bias voltages reduce the natural frequency of the beams. Being this beneficial for the output signal level, but it brings non-linearities explained by the introduction of electrical spring constants dependent on the voltage but also on the position of the resonator.

2.2.5 Charge effects

The capacitive electrodes of the DETF resonator are, in theory, only made of pure silicon and neither experience charging nor charge migration. Albeit, this is true in perfect conditions, the structures possess dielectric layers susceptible to charge after being fabricated using micromachining processes. The interaction of the device material with air or the different gas used during the fabrication creates these dielectric layers. Another source is the DRIE process which uses C_4F_8 (octafluorocyclobutane) to passivate the walls creating residues, namely Teflon (C_2F_4). Humidity and temperature also influence the amount of charge accumulation. Regarding humidity, this value can be expected to be constant if the resonators are encapsulated in a stable environment.

Assuming that the electrodes charge over time, the electric constant of elasticity changes, leading to a variation of the quantity to be measured (natural frequency), see Equation 2.19. This effect affects the stability of the sensor and approaches to minimise it are of interest. Additionally, since the electrical elasticity constant is affected, the sensitivity of the device is charge dependent.

Charge drift elimination is reported in MEMS resonators by using an AC bias voltage instead of a DC voltage in [2.21]. The bias of the DETF is made using an AC source to promote the discharge of the electrical insulator present in the electrode walls. In spite of that, the output of the DETF is modulated at the bias voltage frequency and further complexity is added to the system to demodulate it. A larger noise level at higher frequency was also described as one of the main drawbacks [2.21].

Another technique, to compensate the charging of the electrodes over-time, is the use of two DETF on a differential configuration and both biased with the same DC voltage (V_p). One expects that all the electrodes charge at the same rate and the electrical constant of elasticity has similar amplitudes (in both DETF). The charge effects are compensated subtracting the output of the resonators present in the configuration.

2.2.6 Temperature dependence

The temperature sensitivity of resonators is explained by three main effects: the change in Young's modulus, the thermal expansion of silicon and the mismatch of thermal expansion between silicon and the packaging materials. Additionally, the change in the non-linearity behaviour accordingly to temperature was also reported in [2.22], but for the sake of simplicity, this will not be addressed.

The Young's modulus change with temperature is called temperature coefficient (TCF), and for silicon, this value represents $-60ppm/K$ [2.23]. The stiffness of the springs decreases with an increase of the temperature, resulting as well, in a reduction of the natural frequency.

Another factor is tied to the material properties: the thermal expansion of silicon results on stress (force per unit of area) at the extremities of the resonators. This force yields a frequency change, also affecting the stability of the DETF over temperature. The linear coefficient of thermal expansion (CTE), in the thermal range 280K to 420K, was found to be $0.01 \times 10^{-6}K^{-1}$ [2.24]. In addition, the thermal expansion changes the dimension of the resonators elements, for instance, the gap between the movable and the fixed electrodes [2.25].

The CTE mismatch between the silicon die and the packaging material (e.g. chip carrier and bonding glue) also yields stress at the anchors of the DETF. The more the expansion coefficient differs, the more strain is generated in the silicon substrate. This is explained by the difference in expansion or contraction of materials that are glued together.

Therefore, the natural frequency of a DETF for a given temperature (f_{0T}) can be written as follows [2.26]:

$$f_{0T} = f_0 + (TCF + \beta) \times \Delta T \times f_0 \tag{2.20}$$

where β is the thermal stress coefficient resulting from the different CTE mismatches (e.g. glue, packaging, materials) and ΔT the temperature change.

Thermal compensation

The resonators are especially sensitive to temperature since it changes the stiffness of the beams but also stress induced in the beams produces a change in their natural frequency, affecting the long-term response. For this reason, compensation techniques are paramount to minimize the temperature dependence.

To reduce drifts because of CTE mismatch between the silicon and the packaging, the resonators can be glued to a compliant glue absorbing most of the stress resulting from the material expansion. Another technique consists on using a packaging material with a similar coefficient of thermal expansion to silicon (e.g. glass), and this material can be shaped in a way, so that thermal stress from other components does not affect the resonator [2.11]. The anchor location or number (single or multiple anchors) are also studied to minimise the strain applied to the DETF [2.11], [2.27]. Additionally, silicon dies partially glued to the substrate were reported in [2.26].

As previously mentioned, another way to remove the drift from the output of the resonator is through the use of a differential configuration. Two DETF are used, and the response is continuously subtracted. Since the two resonators are at the same temperature, the natural frequency shift is expected to be the same. Two configurations are possible: one DETF can be decoupled from the proof mass, merely measuring temperature [2.27] or both can be coupled to the central mass, being both sensitive to acceleration and temperature.

The change in Young's modulus is not easily compensated, but heaters to maintain the DETF at a constant temperature can be a possible solution [2.27]. The drawbacks are mainly the increase in power consumption and an increase of the fabrication complexity.

2.2.7 Mechanical stress

Force induced at the extremities of DETF resonators can have several origins and thermal stress resulting from CTE mismatch is the most well-studied effect. However, mechanical stress produced by external factors also influences the sensor behaviour. The external stress might be the result of forces applied to the chip carrier or the PCB during the measurement of the device, for instance. This is often neglected, but in the case of an accelerometer, the force applied to the resonators should result exclusively from the movement of a proof mass. Nonetheless, mechanical stress applied to the anchors also influences the output of the sensor (drift in resonance frequency).

Some of the techniques for temperature compensation are useful to reduce the external stress dependency. Commonly, differential architectures are employed to cancel common-mode errors, but in this case, only a configuration composed of two resonators identically coupled is effective. This is explained by the fact that both DETF have to sense the same force to eliminate it by the response subtraction. Then, the method composed of a differential configuration where one of the resonators is totally isolated from the

accelerometer structure and only senses temperature is of no interest for mechanical stress response compensation.

Typically, devices are also bonded with soft-glues for further stress decoupling or smart packaging can be used. Glass substrates with specific shapes were presented in [2.11] and are an alternative to decouple the devices from the surroundings. Although solutions using tailor-made packaging are an appealing alternative, this brings an increasing complexity and an increase in production costs.

2.2.8 Buckling

Buckling is a mechanical phenomenon occurring when the material becomes unstable and rapidly experience a deflection to one of the sides. This is not due to a material failure but to stresses developed in the structure that makes it deform randomly [2.28], as depicted in Figure 2.10.

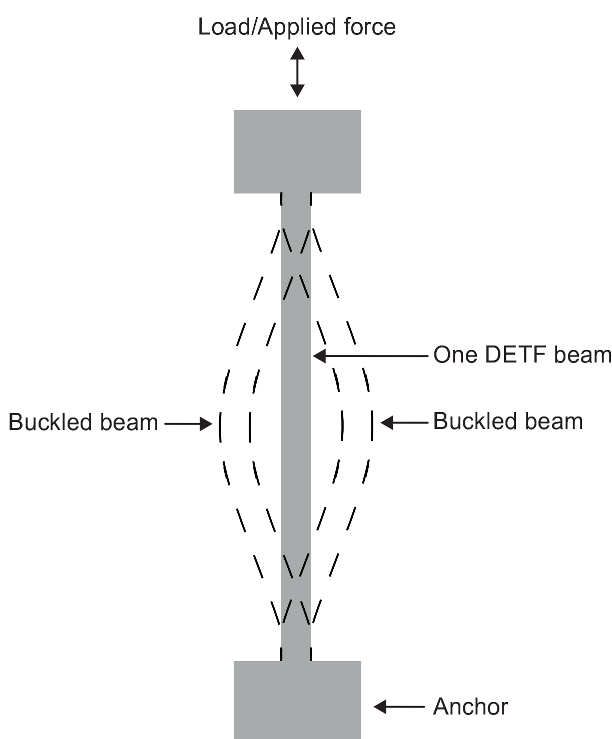

Figure 2.10: Schematic of a straight beam and a buckled beam. Note, the beam can buckle to the right or to the left (bi-stable).

This effect can damage the resonator, once the beams of the DETF undergo an irreversible deformation. Additionally, the resonator has to be axially straight (or aligned) to be sensitive to force applied at the extremities. The buckling limits the maximum force which can be applied, restraining the measurable acceleration and/or limiting the size of proof mass coupled. The study of the critical load a resonator can

endure while maintaining an aligned position is significant in MEMS, since the resonators tend to have thin and long beams.

The Euler's critical load formula is a conservative way of calculating the maximum force (F_{cr}) that can be applied to a DETF beam (see Equation 2.21, [2.28]). The model considers several assumptions, which can be accepted as true in the system composed by a single beam.

$$F_{cr} = \frac{\pi^2 EI}{(KL_b)^2} \tag{2.21}$$

Where K represents the ratio of the beam length and I the second moment of area. Considering a single-beam fixed at both ends (no lateral movement of the anchors), the constant K is equal to 0.5 (theoretical value for Euler's critical load). Being the system composed of two beams and approximating the model to a non-sway frame (no lateral motion), the maximum critical load is increased.

The higher bearable load by DETF resonators outcome a higher measurable dynamic range over single-beam resonators, being clearly a benefit. Nonetheless, for the measurement range required $\pm 5g$ and the proof-mass dimensions, no special attention is required regarding buckling, as it can be calculated using Equation 2.21.

2.3 Single-axis accelerometer composed of DETF resonators

The DETF beams and the main intrinsic characteristics were described in the previous section, but at this point, the interest is in the definition of an architecture capable of sensing acceleration. The basic principle of operation is depicted in Figure 2.11.

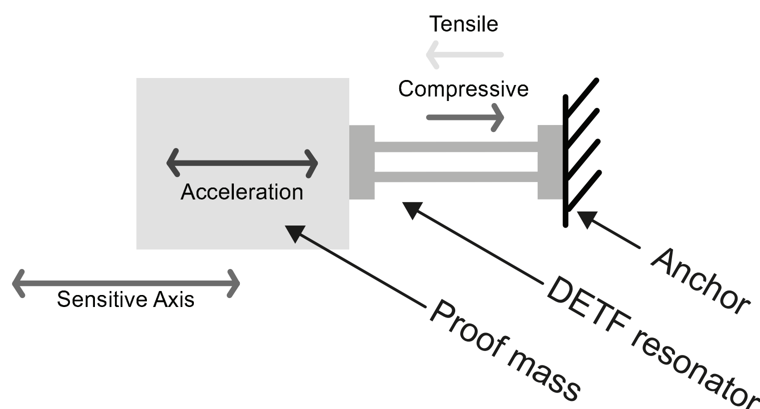

Figure 2.11: Basic operation of an accelerometer composed of a DETF.

An external acceleration (a_{ext}) produces an inertial force (F_{acc}) proportional to the mass coupled (M_{proof}) to the DETF resonators:

$$F_{acc} = M_{proof} \times a_{ext} \tag{2.22}$$

This force is considered positive or negative, accordingly to the direction of the acceleration, generating tensile or compressive strain in the DETF beams. With a single DETF, a bi-directional measurement of the physical quantity under study (acceleration) is achieved. However, this simple device architecture suffers from the different common-mode errors introduced previously and the small proof mass yielded by microfabrication results in reduced sensitivity.

2.3.1 Differential operation

In order to overcome these limitation factors, a differential operation needs the addition of one or more resonators to the architecture presented in Figure 2.11. Considering an architecture composed of two DETF, the shift of the natural frequency, resulting from an external acceleration applied to both resonators, is subtracted. In this specific case, an architecture with resonators subjected to forces in the opposite direction was studied. Since the force generated by the proof mass is applied in different directions at the extremities of the resonators, the natural frequency change is negative in one and positive in the second, which means if one undergoes tensile stress, the other sense a compressive force. In Figure 2.12, the basic architecture and working principle are depicted.

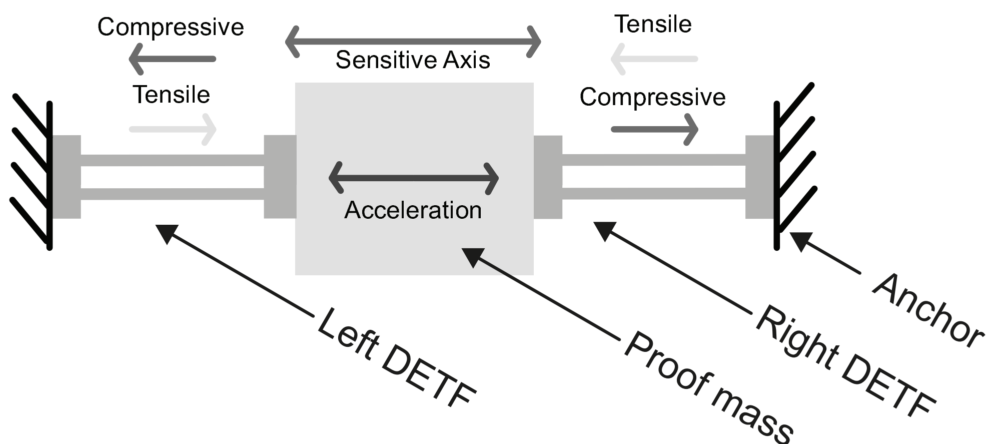

Figure 2.12: Differential accelerometer architecture composed of two DETF undergoing inertial force in opposite direction.

This architecture has numerous advantages. First, if the individual frequency shift of the left (Δf_{left}) and right (Δf_{right}) resonators are subtracted ($\Delta f = \Delta f_{right} - \Delta f_{left}$), the resulting frequency shift (Δf) has twice the amplitude, when an external acceleration is applied, representing a two-fold increase on the device sensitivity.

Additionally, as described in the sections before, several effects such as the temperature dependency, charge effects or external mechanical stress can be minimised or eliminated using this technique. This is true because the shift in frequency resulting from these common-mode effects is expected to have the same amplitude and signal on both double-ended tuning forks. The use of a differential architecture is a very good solution to avoid the higher number of issues related to common-mode effects affecting both sides (right and left) equally. Therefore, the differential DETF resonator architecture is preferred since it has a higher sensitivity and long-term stability.

2.3.2 Force amplification mechanisms

Amplification mechanisms are mechanical amplifying elements that multiply mechanical quantities, for instance, force, displacement or velocity. These elements are well-known and used in daily applications, but here, only force amplification mechanisms are described.

Force amplification mechanisms have been used in many applications where force or displacement are meant to be transferred from an input to an output with a gain factor (above or below 1) [2.29]. In micro-mechanical systems, these mechanisms have been employed to increase displacement and consequently the sensitivity of capacitive devices based on direct displacement transduction [2.30], but also to increase the force induced at the extremities of resonators [2.31]. More force applied to the DETF by lever mechanisms lead to larger frequency changes, resulting in a higher sensitivity.

The resulting inertial force (F_{acc}) from an acceleration (a_{ext}) applied to a proof mass (M_{proof}), if a force amplification mechanism (amplification factor - amp) is used, is given by:

$$F_{acc} = amp \times M_{proof} \times a_{ext} \tag{2.23}$$

A mechanical lever is constituted by four elements: the lever arm, a pivot and output and input of the system. The amplification factor is obtained, in perfect levers, by the ratio of distance (input/output) to the pivot. However, this is not true for the micro-fabricated mechanisms, since perfect pivots are not

reproducible and are replaced by rotational springs. Therefore, the force amplification results from the compliance/mobility of its elements. In this case, to obtain a value of amplification, complex analytical models or finite-element analysis (FEM) should be used (please see Chapter 3).

Concerning the geometry, levers are categorised into classes (first, second or third), that classify the placement of the pivot in relation to the input and output, see Figure 2.13. Besides, devices composed of the stacking of two levers, being the first the output system of the second, were also presented [2.14], [2.32], [2.33]. More than sixteen configurations of this compounding mechanism were studied in [2.32], but the form-factor is restrictive for devices aiming a small size (remembering an aimed device size of $0.25 mm^2$), and similar amplification factors are obtained with single-stage levers.

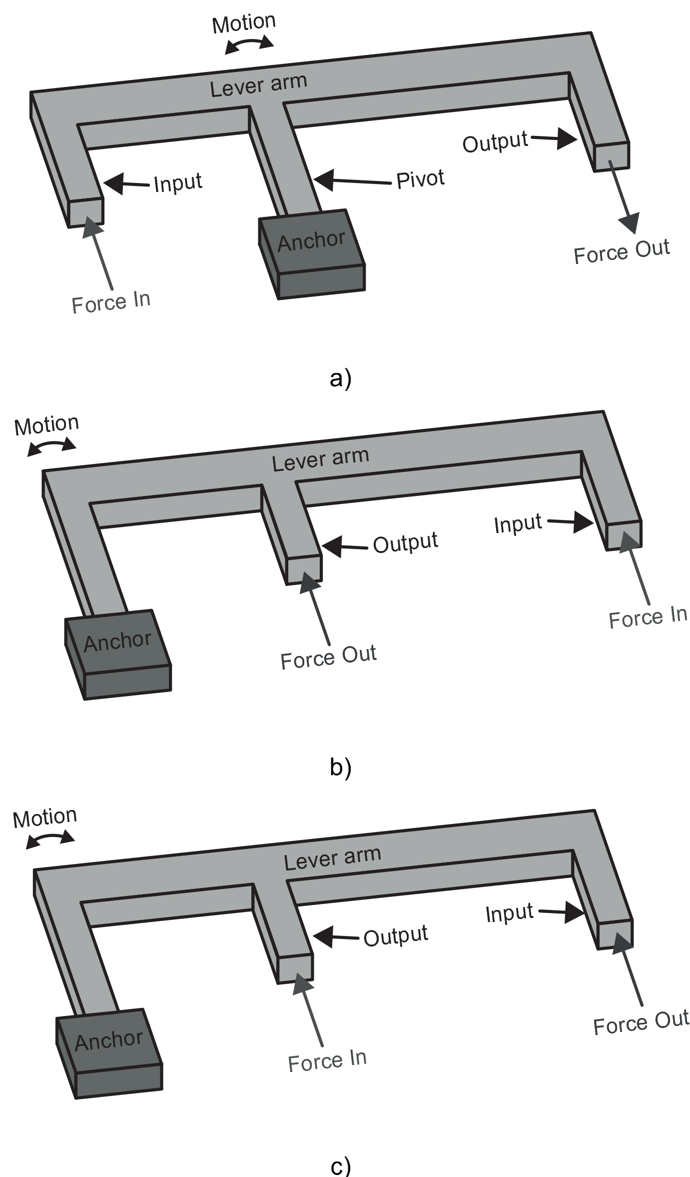

Figure 2.13: Schematic of the three-class of levers reproducible using standard microfabrication processes. a) First-class lever. b) Second-class lever. c) Third-class lever.

Sensors fabricated using surface micromachining processes (such as the Bosch proprietary process) have usually thin device layers, resulting in small proof masses, further increasing the importance of these force amplification mechanisms. To obtain highly sensitive architectures on increasingly smaller size devices based on DETF resonators such gain in force is necessary.

2.3.3 One-degree of freedom analysis

The described frequency modulated accelerometer is composed of DETF resonators on a differential configuration, force amplification mechanisms and a proof mass. The complexity to analyse such system is rather high, but it can be decomposed into three second-order models interconnected. The differential configuration has two resonators, representing two models (right DETF and left DETF), already described previously.

The third model was reduced to the system comprising a mass and the levers/springs, see Figure 2.14.

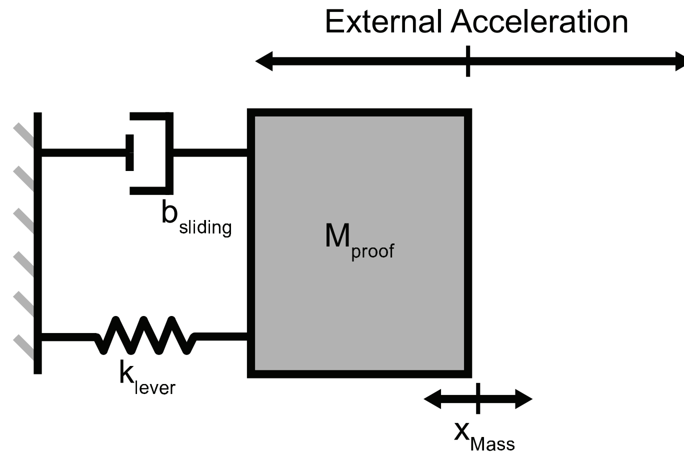

Figure 2.14: Schematic of the system composed of a proof mass and the levers.

Analysing the Figure 2.14, the equilibrium of forces acting in the system can be written as follows:

$$F_{inertialMass} + F_{elasticMass} + F_{SlideDamping} + F_{ExternalAcceleration} = 0 \tag{2.24}$$

The lever, although amplifying force transmitted to the resonators, also acts as a spring, allowing the motion of the proof mass if an external acceleration is applied. The elastic force ($F_{elasticMass}$) opposing to this movement of the central mass (M_{proof}) is calculated by:

$$F_{elasticMass} = k_{lever} \times x_{Proof} \tag{2.25}$$

where k_{lever} is the mechanical stiffness of the lever in the motion direction and x_{proof} the displacement of the mass. The stiffness of the lever cannot be easily calculated with analytical models, and finite element method (FEM) modelling is recommended. This is due to the complexity of the force amplification mechanism (composed of several features with different stiffness) and rotational motion.

The inertial force of the central mass ($F_{inertialMass}$) is also taken into consideration ($F_{inertialMass} = -M_{proof}\frac{d^2x_{Mass}}{dt^2}$).

The reduced distance between the substrate and the proof mass of microfabricated accelerometers allows the establishment of a damping mechanism, in this case, slide damping. This effect occurs when two parallel objects are moving in the same plane relative to each other. The damping force ($F_{SlideDamping} = -b_{slide}\frac{dx_{Mass}}{dt}$), in this particular case, is calculated using the Equation 2.26. The damping coefficient (b_{slide}) is influenced by the area of the proof mass (A_{mass}), the distance between the substrate and the mass (d_{SM}), the viscosity of the gas (μ) and the relative flow rate coefficient (Q_{pr}). This coefficient is a function of the Knudsen number and several approximations are available in [2.16]. Larger mass areas and a narrow distance between the two surfaces (proof mass and substrate) result in larger damping forces.

$$F_{SlideDamping} = -\frac{\mu \times A_{mass}}{Q_{PR} \times d_{SM}}\frac{dx_{Mass}}{dt} \tag{2.26}$$

This model is simplified for proof masses without release holes and a more complex model should be used to obtained a reliable damping coefficient [2.16].

In addition, the proof mass can be enforced to move by an external force ($F_{ExternalAcceleration} = M_{proof}a_{external}$), resulting from an external acceleration ($a_{external}$).

The behaviour of the system can be described as a second-order mechanical model:

$$M_{proof}\frac{d^2x}{dt^2} + b_{slide}\frac{dx}{dt} + k_{lever}x = M_{proof}a_{external} \tag{2.27}$$

From this, the dynamic behaviour of the system can be analysed statically and dynamically, returning important performance parameters of the accelerometer behaviour.

At this point, the complete accelerometer can be modelled by interconnecting the three second-order models described, see Fig 2.15.

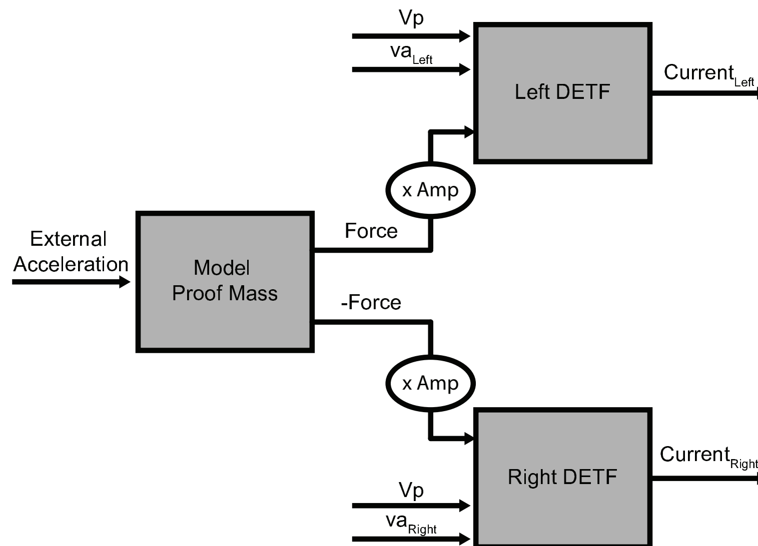

Figure 2.15: Schematic of the model describing the behaviour of a complete frequency modulated accelerometer.

By investigating the static and dynamic analysis of the complete accelerometer, the behaviour of the system for different stimuli can be studied. The interaction between the movement of the mass for external accelerations and the change in natural frequency of the DETF gives detailed information about the sensor performance. Note that the force value passed to the subsystems of the DETF is multiplied by the value of amplification of the levers, and has different signs (forces in opposite directions). The current induced on the sensing electrodes (left and right DETF sensing electrodes) gives information about the oscillatory status of the resonators.

2.4 Frequency-modulated device instrumentation

The methods to sense the natural frequency of the resonators are addressed in this section. Several methodologies are available, and the advantages and disadvantages are discussed in detail. Two main approaches regarding the excitation of the resonator either in open-loop (no changes of the driving frequency) and closed-loop (driving frequency adjusted in real-time to match the natural frequency of the DETF) are described. The two approaches are discussed in section 2.4.1 and 2.4.2, respectively.

2.4.1 Resonant sensing methods

Two methods are used to detect the change of the natural frequency of a resonator in open-loop: the difference in magnitude or the change of phase.

The magnitude change for a fixed driving voltage frequency (f_{va}), returns information about the external acceleration. This effect can be observed in Figure 2.16, where the shift in amplitude is correlated with a change in natural frequency (f_0+f). The resulting voltage output (v_{out}) can be recognised as linear only for small changes in frequency, and this is clearly a drawback. Additionally, the system has a measurement bandwidth (BW) limited by $f_0/2Q$, since the transient response of the DETF resonator does not change instantaneously [2.10]. When the resonant frequency changes, some time is required for the resonator to settle into a new steady-state. The time constant (τ) can be calculated using Equation 2.28 [2.10].

$$\tau = \frac{Q}{\pi f_0} \tag{2.28}$$

According to Equation 2.28, higher quality factors, and lower natural frequencies result in longer settling times, yielding a reduced system bandwidth.

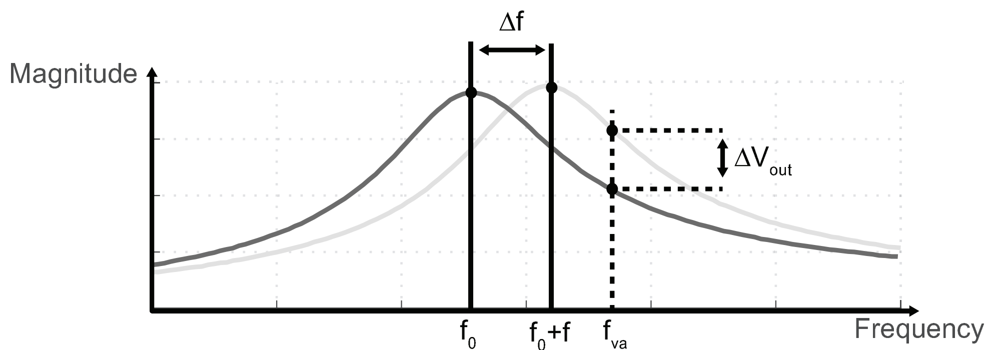

Figure 2.16: Amplitude change sensed by driving the resonators at a constant frequency.

The system based on the detection of the output magnitude is demonstrated in Figure 2.17. The output of the DETF is converted to a voltage to be read by suitable electronics.

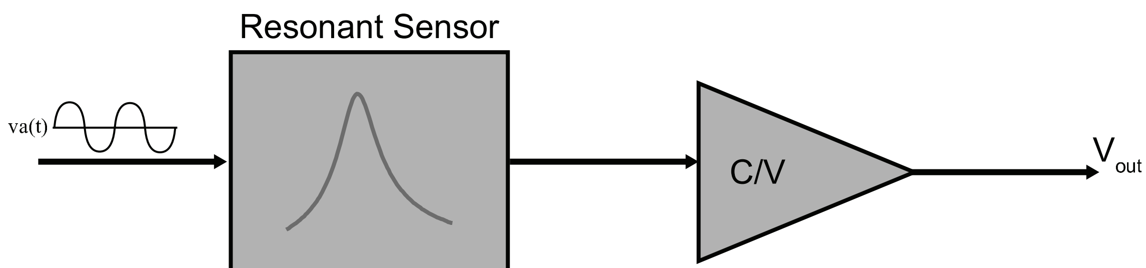

Figure 2.17: Schematic of the system to detect the shift of magnitude for a fixed driving frequency.

The second method, to sense the change in the resonant frequency in open-loop, is based on phase change detection. If the driving frequency (f_{va}) is kept constant (at a frequency near to the natural frequency of

the resonator), the phase of the output signal is expected to change if any acceleration is applied. This behaviour is depicted in Figure 2.18.

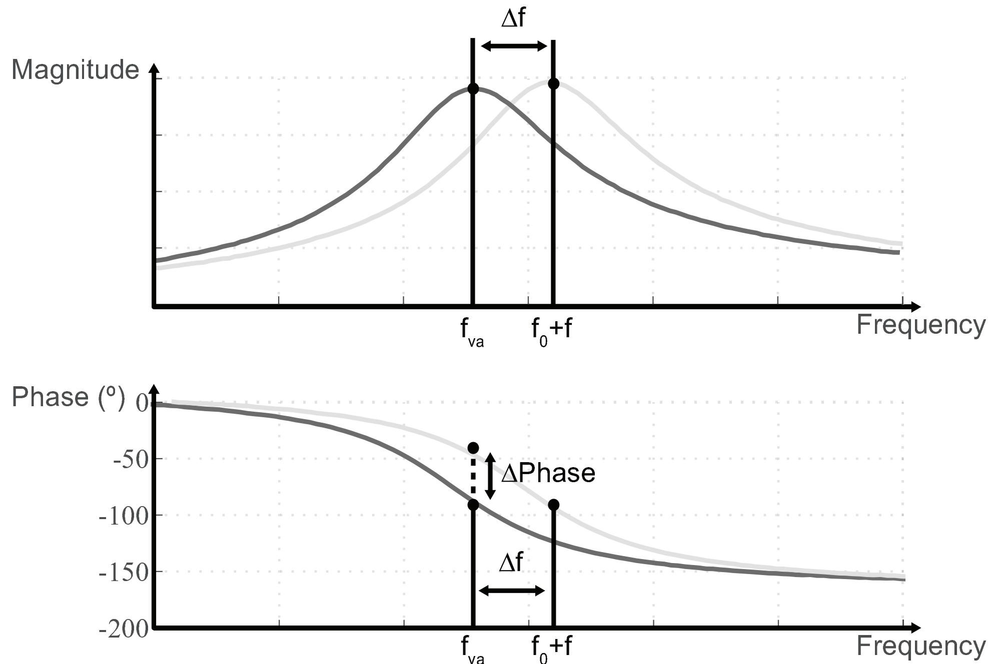

Figure 2.18: Sensing of natural frequency changes through phase detection.

By comparing the driving and output signal phases, a value of phase proportional to a shift in natural frequency can be obtained. The schematic of the system to instrument the phase is shown in Figure 2.19. The benefits of this approach are related to an increased linearity ($f_0/2Q$) and a fast-changing phase (the phase is tied to the natural frequency of the sensor). Nonetheless, the bandwidth of the system is limited by $f_0/2Q$.

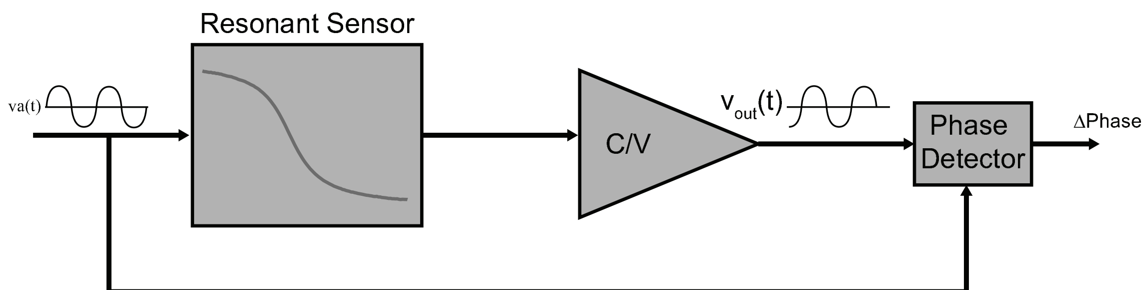

Figure 2.19: Schematic of the system to instrument a changing phase proportional to the natural frequency of the resonator.

The approaches presented are categorised as open-loop operation since the driving frequency is maintained constant during the phase or amplitude monitoring. An increased system non-linearity and reduced bandwidth are the main disadvantages reported for these two approaches.

2.4.2 Closed-loop measurement approaches

Other methods employ a driving frequency updated at the same pace as the resonant frequency changes. In this case, a feedback loop continuously forces the resonator to oscillate at its natural frequency, and this is called closed-loop operation.

The closed-loop measurement approaches presented in the state-of-the-art are usually based in an oscillatory circuitry. The oscillator automatically adjusts the driving signal frequency to guarantee a phase delay of 90 degrees in relation to the DETF output signal. By acquiring the frequency of the oscillatory circuit, one knows the natural frequency of the resonator. The schematic of this system is presented in Figure 2.20.

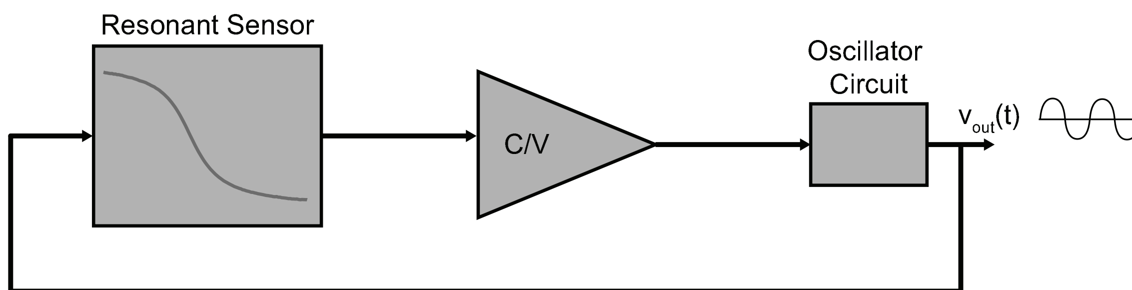

Figure 2.20: Schematic of the system composed by an oscillator to instrument the resonant sensor.

Using this method, the system bandwidth is limited by the bandwidth of the oscillator circuit. Because of this improvement, most of the sensors composed of resonators use this approach. However, the oscillatory circuit is dependent on the resonant DETF characteristics to start oscillating, and the design has to be made in parallel. For research purposes, this type of instrumentation does not present enough versatility to test, with the same system, a broad range of DETF based sensors.

In this thesis, a different approach to force the vibration of the resonator at the natural frequency is proposed. The technique is based on the open-loop phase detection, but a controller was added to it. This controller updates, at a given rate, the driving frequency of DETF beams to match the natural frequency (maintaining a phase shift of 90° between the driving and output signal), see Figure 2.21.

The linearity is strongly increased (comparing to open-loop approaches), since the phase shift is locked at 90° and any range of frequency shift can be instrumented, thus increasing the dynamic range. The implementation of this technique is further described in Chapter 3.

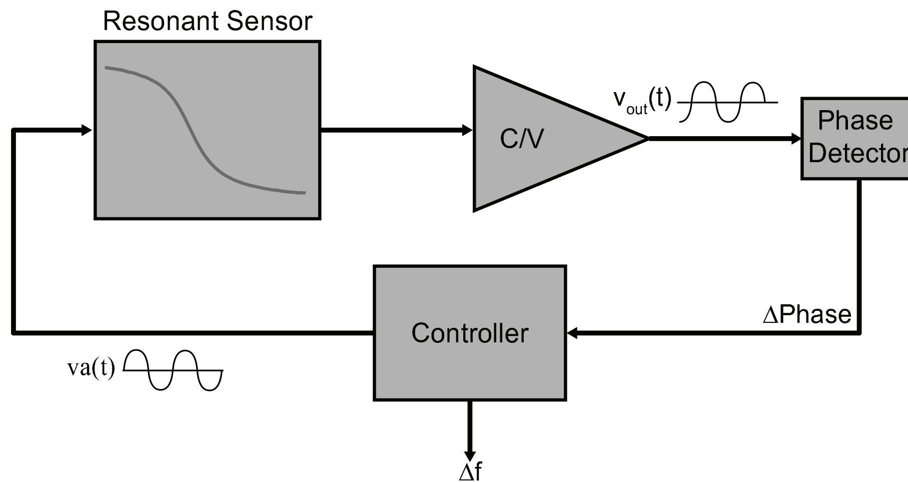

Figure 2.21: DETF closed-loop operation based on a phase detector and a controller.

2.5 Conclusion

In this chapter, the theory necessary to design and simulate a MEMS accelerometer based on double-ended tuning fork resonators was explained. First, the study of the DETF identified the necessary conditions for it to resonate and how the different forces act in the system. After, the non-linearity and other effects, such as buckling and temperature dependence were analysed, returning possible limitations of the approach. In addition, the low sensitivity issue was described as one of the main disadvantage of the chosen resonator architecture.

Finally, a differential architecture using two resonator strategically placed (never submitted to forces in the same direction) was introduced as a solution to double the sensor sensitivity, while minimising most of the common-mode effects (temperature dependency, charge effects, mechanical stress). Force amplification mechanisms are here proposed and added to the differential accelerometer to further increase the sensitivity.

To instrument the devices aimed, several methods to read the shift in natural frequency were presented and compared. The techniques were split into two groups, open-loop and closed-loop operation. Closed-loop operation profits from higher linearity, dynamic range and/or larger bandwidth, maximising the proposed resonant accelerometer performance.

References

[2.1] A. A. Seshia, “Integrated Micromechanical Resonant Sensors for Inertial Measurement Systems”, PhD thesis, University of California at Berkeley, 2002, pp. 195–221.

[2.2] M. Sharma, E. H. Sarraf, and E. Cretu, “Parametric amplification/damping in MEMS gyroscopes”, in IEEE 24th International Conference on Micro Electro Mechanical Systems, IEEE, Jan. 2011, pp. 617–620. doi: 10.1109/MEMSYS.2011.5734500.

[2.3] M. J. Thompson, “The Design and Implementation of Parametrically Amplified Lorentz Force MEMS Magnetometers”, PhD thesis, University of California Davis, 2010, pp. 1–74.

[2.4] C. Ataman and H. Urey, “Modeling and characterization of comb-actuated resonant microscanners”, Journal of Micromechanics and Microengineering, vol. 16, no. 1, pp. 9–16, Jan. 2006. doi: 10.1088/0960-1317/16/1/002.

[2.5] J. Basu and T. K. Bhattacharyya, “Microelectromechanical resonators for radio frequency communication applications”, Microsystem Technologies, vol. 17, no. 10-11, pp. 1557–1580, Oct. 2011. doi: 10.1007/s00542-011-1332-9.

[2.6] A. Caspani, C. Comi, A. Corigliano, G. Langfelder, V. Zega, and S. Zerbini, “A Differential Resonant Micro Accelerometer for Out-of-plane Measurements”, Procedia Engineering, vol. 87, pp. 640–643, 2014. doi: 10.1016/j.proeng.2014.11.569.

[2.7] D. Senkal, M. J. Ahamed, S. Askari, and A. M. Shkel, “MEMS Micro-glassblowing Paradigm for Wafer-level Fabrication of Fused Silica Wineglass Gyroscopes”, Procedia Engineering, vol. 87, pp. 1489–1492, 2014. doi: 10.1016/j.proeng.2014.11.580.

[2.8] Y. C. Lee, Y.-T. Cheng, and R. Ramadoss, MEMS Packaging. World Scientific, Feb. 2018, vol. 05. doi: 10.1142/10692.

[2.9] J. E.-Y. Lee, B. Bahreyni, and A. A. Seshia, “An axial strain modulated double-ended tuning fork electrometer”, Sensors and Actuators A: Physical, vol. 148, no. 2, pp. 395–400, Dec. 2008. doi: 10.1016/j.sna.2008.09.010.

[2.10] K. E. Wojciechowski, “Electronics for Resonant Sensors”, PhD thesis, University of California, Berkeley, 2005, p. 149.

[2.11] Y. Yin, Z. Fang, Y. Liu, and F. Han, “Temperature-Insensitive Structure Design of Micromachined Resonant Accelerometers”, Sensors, vol. 19, no. 7, p. 1544, Mar. 2019. doi: 10.3390/s19071544.

[2.12] C. Comi, A. Corigliano, G. Langfelder, A. Longoni, A. Tocchio, and B. Simoni, “A Resonant Microaccelerometer With High Sensitivity Operating in an Oscillating Circuit”, Journal of Microelectromechanical Systems, vol. 19, no. 5, pp. 1140–1152, Oct. 2010. doi: 10.1109/JMEMS.2010.2067437.

[2.13] A. Caspani, C. Comi, A. Corigliano, G. Langfelder, and A. Tocchio, “Compact biaxial micromachined resonant accelerometer”, Journal of Micromechanics and Microengineering, vol. 23, no. 10, p. 105 012, Oct. 2013, issn: 0960-1317. doi: 10.1088/0960-1317/23/10/105012.

[2.14] H. Ding, J. Zhao, B. Ju, and J. Xie, “A highly sensitive biaxial resonant accelerometer with two-stage microleverage mechanisms”, in IEEE 29th International Conference on Micro Electro Mechanical Systems (MEMS), vol. 2016-Febru, IEEE, Jan. 2016, pp. 934–937. doi: 10.1109/MEMSYS.2016.7421785.

[2.15] O. Brand, I. Dufour, S. M. Heinrich, and F. Josse, Resonant MEMS, ser. Advanced Micro and Nanosystems. Weinheim, Germany: Wiley-VCH Verlag GmbH & Co. KGaA, Apr. 2015, p. 512. doi: 10.1002/9783527676330. [Online]. Available: http://doi.wiley.com/10.1002/9783527676330.

[2.16] V. Lindroos, M. Tilli, A. Lehto, T. Motooka, and T. Veijola, “Handbook of silicon based MEMS materials and technologies”, Micro & Nano Technologies Series, 2010. doi: 10.1016/B978-0-8155-1594-4.00014-0.

[2.17] M. Bao and H. Yang, “Squeeze film air damping in MEMS”, Sensors and Actuators A: Physical, vol. 136, no. 1, pp. 3–27, May 2007. doi: 10.1016/j.sna.2007.01.008.

[2.18] L. Mol, L. A. Rocha, E. Cretu, and R. F. Wolffenbuttel, “Squeezed film damping measurements on a parallel-plate MEMS in the free molecule regime”, in International Solid-State Sensors, Actuators and Microsystems Conference (Transducers), IEEE, Jun. 2009, pp. 1425–1428. doi: 10.1109/SENSOR.2009.5285840.

[2.19] Y. P. Xu, ”MEMS silicon oscillating accelerometers and readout circuits”. Feb. 2019, isbn: 9788770220453.

[2.20] D. Chen, Y. Wang, Y. Guan, X. Chen, X. Liu, and J. Xie, “Methods for Nonlinearities Reduction in Micromechanical Beams Resonators”, Journal of Microelectromechanical Systems, vol. 27, no. 5, pp. 764–773, Oct. 2018. doi: 10.1109/JMEMS.2018.2850766.

[2.21] G. Bahl, J. C. Salvia, R. Melamud, B. Kim, R. T. Howe, and T. W. Kenny, “AC Polarization for Charge-Drift Elimination in Resonant Electrostatic MEMS and Oscillators”, Journal of Microelectromechanical Systems, vol. 20, no. 2, pp. 355–364, Apr. 2011. doi: 10.1109/JMEMS.2010.2100027.

[2.22] J. Zhang, Y. Wang, V. Zega, Y. Su, and A. Corigliano, “Nonlinear dynamics under varying temperature conditions of the resonating beams of a differential resonant accelerometer”, Journal of Micromechanics and Microengineering, vol. 28, no. 7, pp. 1–10, 2018. doi: 10.1088/1361-6439/aab7c6.

[2.23] M. A. Hopcroft, W. D. Nix, and T. W. Kenny, “What is the Young’s Modulus of Silicon?”, Journal of Microelectromechanical Systems, vol. 19, no. 2, pp. 229–238, Apr. 2010. doi: 10.1109/JMEMS.2009.2039697.

[2.24] H. Watanabe, N. Yamada, and M. Okaji, “Linear Thermal Expansion Coefficient of Silicon from 293 to 1000 K”, International Journal of Thermophysics, vol. 25, no. 1, pp. 221–236, Jan. 2004. doi: 10.1023/B:IJOT.0000022336.83719.43.

[2.25] S. L. Warma and F. Elmgren, “Micrometer Gap Distance Dependence on Temperature Changes in a Large Electrode System changes in a large electrode system”, PhD thesis, Uppsala Universitet, 2018, pp. 1–24.

[2.26] C. D. Do, A. Erbes, J. Yan, K. Soga, and A. A. Seshia, “Vacuum Packaged Low-Power Resonant MEMS Strain Sensor”, Journal of Microelectromechanical Systems, vol. 25, no. 5, pp. 851–858, 2016. doi: 10.1109/JMEMS.2016.2587867.

[2.27] D. D. Shin, Y. Chen, I. B. Flader, and T. W. Kenny, “Epitaxially encapsulated resonant accelerometer with an on-chip micro-oven”, in 2017 19th International Conference on Solid-State Sensors, Actuators and Microsystems (TRANSDUCERS), IEEE, Jun. 2017, pp. 595–598. doi: 10.1109/TRANSDUCERS.2017.7994119.

[2.28] J. M. Gere and B. J. Goodno, ”Mechanics of materials”, Seventh edition. Toronto, Canada: Cengage Learning, 2009, p. 1045, isbn: 0-534-55397-4.

[2.29] S. X.-P. Su and H. S. Yang, “Analytical modeling and FEM Simulations of single-stage microleverage mechanism”, International Journal of Mechanical Sciences, vol. 44, no. 11, pp. 2217–2238, Nov. 2002. doi: 10.1016/S0020-7403(02)00162-5.

[2.30] I. Zeimpekis, I. Sari, and M. Kraft, “Characterization of a Mechanical Motion Amplifier Applied to a MEMS Accelerometer”, Journal of Microelectromechanical Systems, vol. 21, no. 5, pp. 1032–1042, Oct. 2012. doi: 10.1109/JMEMS.2012.2196491.

[2.31] A. Seshia, M. Palaniapan, T. Roessig, R. Howe, R. Gooch, T. Schimert, and S. Montague, "A vacuum packaged surface micromachined resonant accelerometer", Journal of Microelectromechanical Systems, vol. 11, no. 6, pp. 784–793, Dec. 2002. doi: 10.1109/JMEMS.2002.805207.

[2.32] X.-p. S. Su, "Compliant Leverage Mechanism Design for MEMS Applications", PhD thesis, University of California, Berkeley, 2001, p. 219.

[2.33] Y. Wang, H. Ding, X. Le, W. Wang, and J. Xie, "A MEMS piezoelectric in-plane resonant accelerometer based on aluminum nitride with two-stage microleverage mechanism", Sensors and Actuators A: Physical, vol. 254, pp. 126–133, Feb. 2017. doi: 10.1016/j.sna.2016.12.019.

Chapter 3

System implementation

A single-axis MEMS accelerometer for in-plane measurement was designed, simulated, and implemented, to validate the chosen concept experimentally. A relevant emphasis was given to the study of several sensor features to increase the sensitivity and take maximum profit of the amplification mechanism. The fabrication of the frequency-modulated sensors was performed in a surface micromachining proprietary process at Robert Bosch GmbH and encapsulated in vacuum. Additionally, devices were packaged using two different types of glues for stress decoupling characterisation.

The implementation of the instrumentation system used along this thesis includes the interface electronics to drive and read the DETF properly. The instrumentation system was implemented using several components, discrete electronics at the PCB level, laboratory instrumentation equipment and a field-programmable gate array (FPGA). The front-end electronics converts a current signal from the MEMS to a voltage to be read by the lock-in amplifier. Then the lock-in amplifier demodulates the signal and returns paramount information, such as the signal phase and amplitude. Additionally, it enables the driving of the resonator. The FPGA was used to implement in hardware (programmable logic) the digital controller and a few more functionalities to operate the resonators in closed-loop, and this module reads a phase shift from the lock-in amplifier and returns a frequency to drive the DETF. The approach using a proportional-integral-derivative (PID) controller and a phase detector was selected since it presents a higher versatility for research purposes. In order to control and configure the entire instrumentation system but also to sample the output of the accelerometer (frequency change), an acquisition board and a computer were used. In Figure 3.1, the different blocks representing the MEMS device and the instrumentation system implemented are depicted.

This chapter is divided similarly to the different blocks introduced in Figure 3.1. The chapter starts with the MEMS accelerometer, from design to implementation, following the description of the system to read

Figure 3.1: Schematic showing the different blocks implemented in this work.

and drive the resonators (front-end electronics and phase detection). Additionally, a closed-loop controller was implemented on an FPGA, and the different subsystems will be described in the closed-loop control section. The chapter ends with the definition of the data acquisition and system configuration block. The instrumentation system, composed of these blocks, enables the characterisation of the MEMS device's prototypes developed.

3.1 MEMS accelerometer

In this section, the topics related to the implementation of the MEMS devices are reported. The device fabrication and the different rules strongly affect the design of the accelerometers, so these are addressed first. The design parameters of the single-axis frequency-modulated accelerometer follow, being the design details and choices intensely approached. The section ends with the final results regarding the fabricated devices and the packaging.

3.1.1 Device fabrication

The designed sensors were fabricated in a commercial process available at Bosch. The process provides a polycrystalline silicon layer with a thickness of 19 μm for the device and two additional layers for electrical interconnections. Such device layer thickness is achieved using the epitaxial deposition of polysilicon. The process allows high-aspect-ratio features using proprietary etching techniques yielding the formation of vertical walls ideal for MEMS sensors.

After the completion of the device, a wafer-level silicon cap bonding is performed and devices are guaranteed to benefit from a stable encapsulation in vacuum. Here, the encapsulation pressure available was 100 Pa (1 mBar). Note that the accelerometers were fabricated on an internal multi-project wafer (MPW) respecting established design rules of the process at Bosch. The set of rules is shown in Table 3.1.

Process specification	Value
Device layer thickness	19 μm
Minimum gap	1.6 μm
Minimum beam width	1.4 μm
Distance to substrate	2 μm
Young modulus (EpiPoly)	$\approx$ 169 GPa
Cavity pressure	100 Pa
Number of connection layers	2
Number of pads	25

Table 3.1: List of rules to design the accelerometer using the proprietary process at Bosch, Reutlingen.

The design of the microstructures must follow process limitations and rules, influencing the sensor behaviour and performance. The devices were designed to maximise sensitivity on a small footprint but still respecting the set of rules defined in Table 3.1. It is essential to highlight that the structure, here designed, uses the same fabrication process as the many Bosch devices present in the market, namely accelerometers and gyroscopes.

No further fabrication steps were disclosed due to company intellectual property constraints. Therefore, all the remaining layers (all but the active layer) were designed by experienced personnel at Bosch in Reutlingen.

3.1.2 Sensor design

A sensor for in-plane and single-axis measurement of acceleration was designed respecting the fabrication specification. In addition, the set of requirements (provided by our partner) was taken into account to align the device performance during the design phase.

The design of the accelerometer started by the definition of the DETF characteristics. To guarantee a high sensitivity/frequency change for a given force, the resonator beams need to be thin and long, as shown previously in Figure 2.4. Respecting the size limitations, the minimum beam width allowed by the process and the device layer, the dimensions of the DETF are restrained to $400\ \mu m$ x $1.4\ \mu m$ x $19\ \mu m$ (length x width x thickness). A single-electrode per beam was strategically coupled to ensure a maximum displacement with lower driving voltages and yielding larger capacitance changes. For that purpose, parallel-plates actuators were fixed to the centre of the beams. This type of electrodes are advantageous, comparing to comb-drives because of a smaller footprint for equal electrostatic force and capacitance change. Since the mass of the electrodes is inversely proportional to the sensitivity of the resonators (see Figure 2.5), this type of electrodes is advantageous. Implementing the dynamic model of a DETF in Simulink®(see Figure 2.8), the natural frequency of the resonator (when no force is experienced at the extremities) is expected to be about 38 kHz for a bias voltage of 2 Volts. The frequency response of the resonator is shown in Figure 3.2.

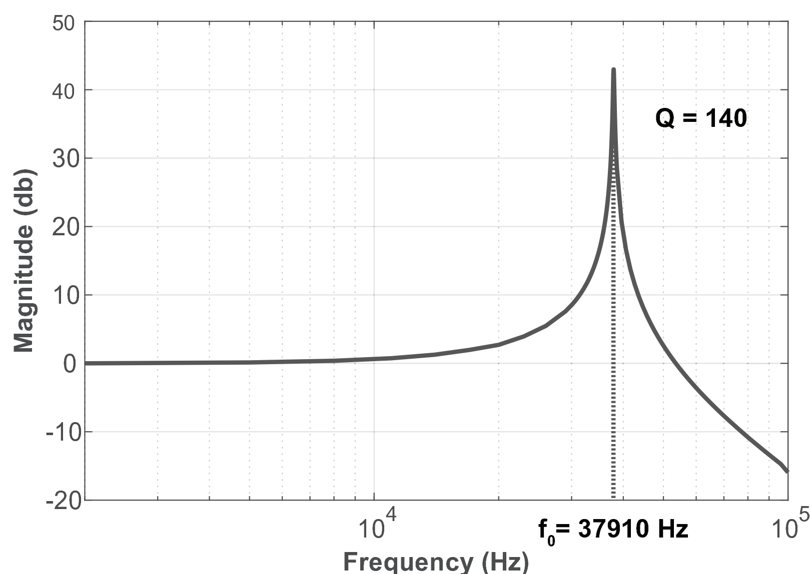

Figure 3.2: Frequency response of a double-ended tuning fork resonator modelled using the simulink model implemented.

A quality factor of 140 is expected, and this value is lower than what is typically observed on resonant devices. The main contribution for the low-quality factor is the squeeze-film damping between the movable and fixed electrodes which is significant at the encapsulation pressure considered (specific of the microfabrication process employed).

The natural frequency of the DETF was confirmed using FEM simulation, see Figure 3.3. Although the simulation performed in Ansys does not account for the excitation forces, the spring stiffness and coupling of the resonators is thoroughly examined.

Figure 3.3: Modal simulation performed using Ansys Workbench.

Two similar DETF were placed on a differential configuration, in a way, both are submitted to force but in opposite directions. Using this architecture (see Figure 3.4), the sensitivity is doubled and common-mode effects are minimised.

The accelerometer is also composed of two levers to amplify the force applied to the resonators and increase even further the sensitivity. Many lever configuration were studied and simulated, but the configuration shown in Figure 3.4 was adopted due to the several advantages presented, namely, good force multiplication and small footprint.

In Figure 3.4, it is shown that the lever used in this design is a single-stage, first-class lever with a rotational pivot, differing from the device presented in [3.1]. The levers' performance was studied and optimised using FEM modelling linked with a parametric CAD design of the complete structure since no accurate

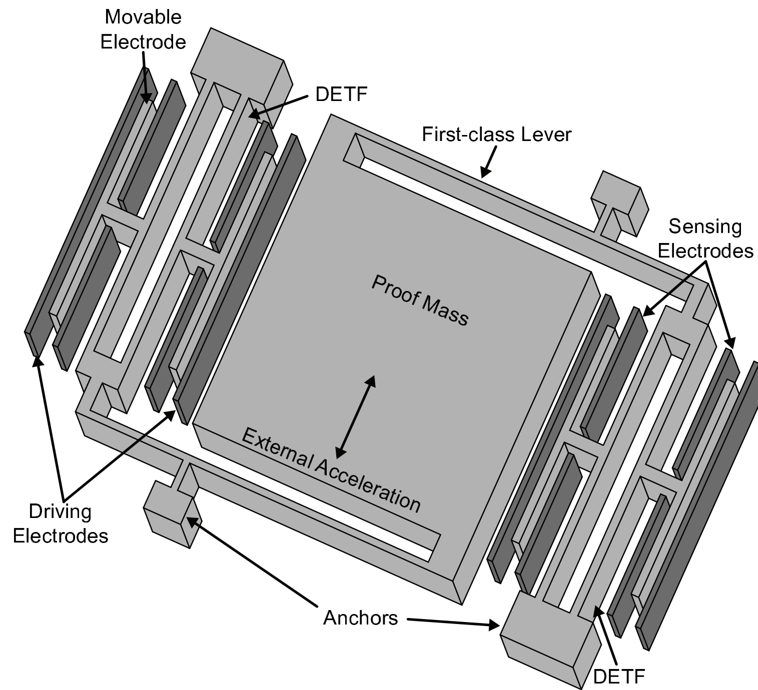

Figure 3.4: Schematic of the single-axis MEMS accelerometer based on DETF resonators and force amplification mechanism.

analytical models can be found, especially considering that perfect pivots cannot be micromachined. The lever models available in the literature are valid for a set of predefined assumptions which are design dependent and could not be considered accurate enough for the design here studied. However, the methodology used allows a straight-forward optimisation of all the features' dimensions to maximise the sensitivity obtained by the lever. In this case, the lever is acting as a spring and as a force amplification mechanism. For the sensitivity/lever gain optimisation, the features studied were the length of the output lever (La), the lever width (Wa) and the width and length of the pivot (Wp and Lp, respectively), see Figure 3.5.

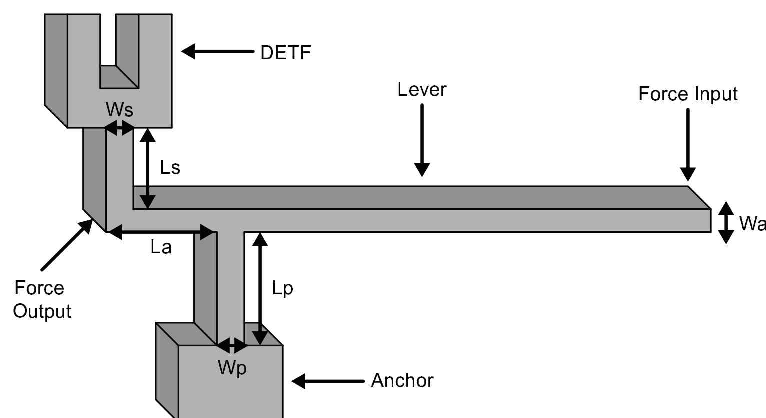

Figure 3.5: Features optimised using FEM and parametric CAD design to guarantee a maximum amplification.

Also, the width (Ws) and the length (Ls) of the DETF connector were considered. The lever length is similarly a crucial factor, but due to size restrictions, this parameter was fixed to a maximum of 430 μm. The study yielded an optimal sensitivity point dependent on the length of the output lever (La), see Fig 3.6, in accordance with published studies [3.1].

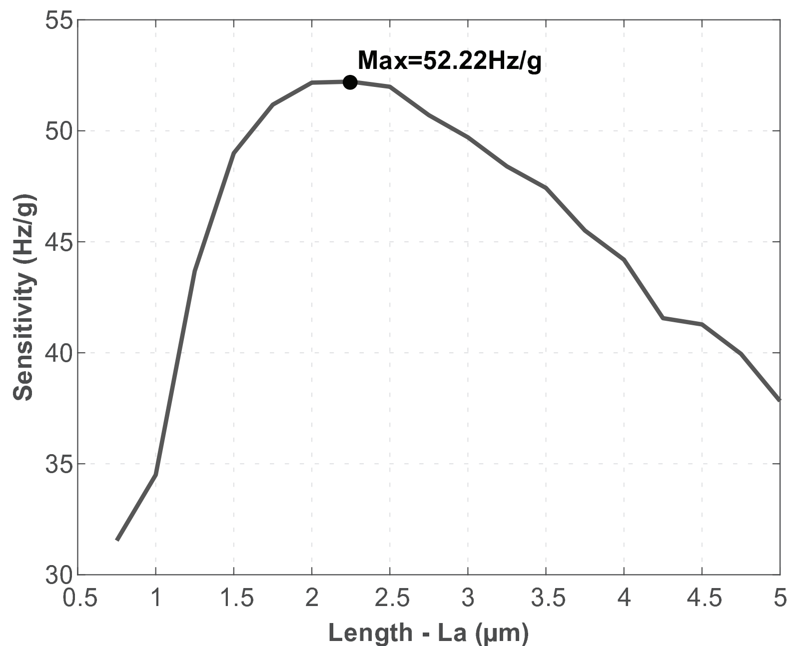

Figure 3.6: Sensitivity in function of the output lever length (La).

Similar studies were performed for each parameter, and the results in Figure 3.6 show the output lever length dependency with all other parameters already optimised. Regarding the other parameters studied here, thinner element widths (Wa, Ws and Wp) and longer features (Ls and Lp) result in a higher scale-factor. These values were then restrained by size and process limitations. The maximum sensitivity value of 52.2 Hz/g corresponds to a single DETF and lever, hence a total sensitivity of 104.4 Hz/g can theoretically be achieved with a differential configuration. This corresponds to a sensitivity improvement of around 20 times, when compared to a simple DETF without any amplification mechanism (2.5 Hz/g - for the designed mass).

The central mass (proof mass) was decided to have the maximum size allowed for the sensor core-size, 400 μm x 400 μm (0.16 mm^2). A larger mass yields a larger frequency change on the resonators for the same acceleration (more force). Nonetheless, to release the devices and allow them to move freely, many holes were added, representing a mass loss of approximately 25 %.

The entire structure was modelled using Simulink®and Ansys retrieving valuable design information. Several structure characteristics were obtained to compare with the experimental data, namely, non-linearity,

temperature dependence, among others. Table 3.2 presents the main dimensions and parameters obtained through modelling of the micro-structures.

Parameter	Parameter description	Value
Ws	DETF support width	1.4 μm
Ls	DETF support length	10 μm
La	Output lever length	2.25 μm
Wp	Pivot width	1.4 μm
Lp	Pivot length	20 μm
-	Lever length	430 μm
k_{lever}	Lever spring coefficient	0.29 N/m
L_e	Movable electrode Length	300 μm
W_e	Movable electrode width	2 μm
d_0	Rest distance (gap)	1.6 μm
L	DETF beam length	400 μm
w	DETF beam width	1.4 μm
f_0	DETF natural frequency	$\approx$ 38.7kHz
Q	Quality factor (DETF)	140
M	Proof mass	5.32$x10^{-9}$ Kg
-	Proof mass natural frequency	$\approx$ 1.2 kHz
t	Device thickness	19 μm
P_0	Encapsulation Pressure	100 Pa

Table 3.2: List of the design parameters obtained through modelling of the micro-structures.

3.1.3 Fabricated devices

After the design of the devices, the active layer mask was sent for fabrication and inclusion in a multi-project wafer (MPW) run. The masks are shown in Appendix A.

The devices were fabricated and several scanning electron microscope (SEM) images are shown in Figure 3.7. The DETF, levers, central stopper and rotational pivot were highlighted. A mechanical stopper was added to restrain the displacement of the central mass (in the X and Y axis), avoiding damage of the compliant structures when over-range accelerations are applied. The stopper was placed to allow the displacement of the mass on the sensitive axis until $\pm 25\ g$, despite the measurement range of interest being $\pm 5\ g$.

Additionally, the anchors of the structures were extended around the whole device to maintain a constant etch-environment and guarantee regular process conditions.

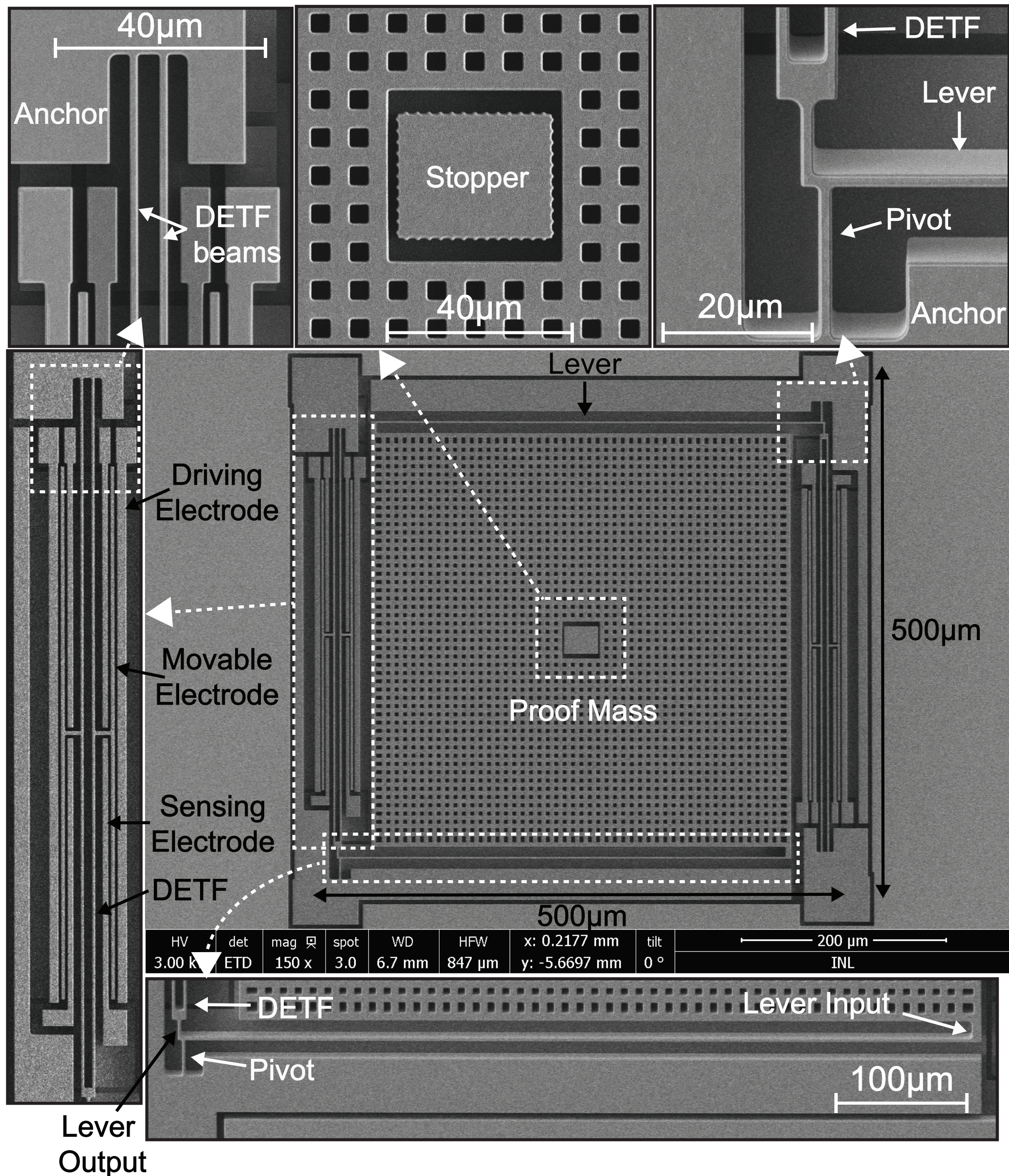

Figure 3.7: SEM pictures of a fabricated device and highlight of the different elements composing it.

Independently of the device's size, all the dies have the same dimensions due to process rules. Three devices were fabricated on each die to take maximum profit of the available area. In Figure 3.8, one notices that device 1 and 3 are sensitive in the vertical axis, while device 2 was rotated 90° to sense on the horizontal axis.

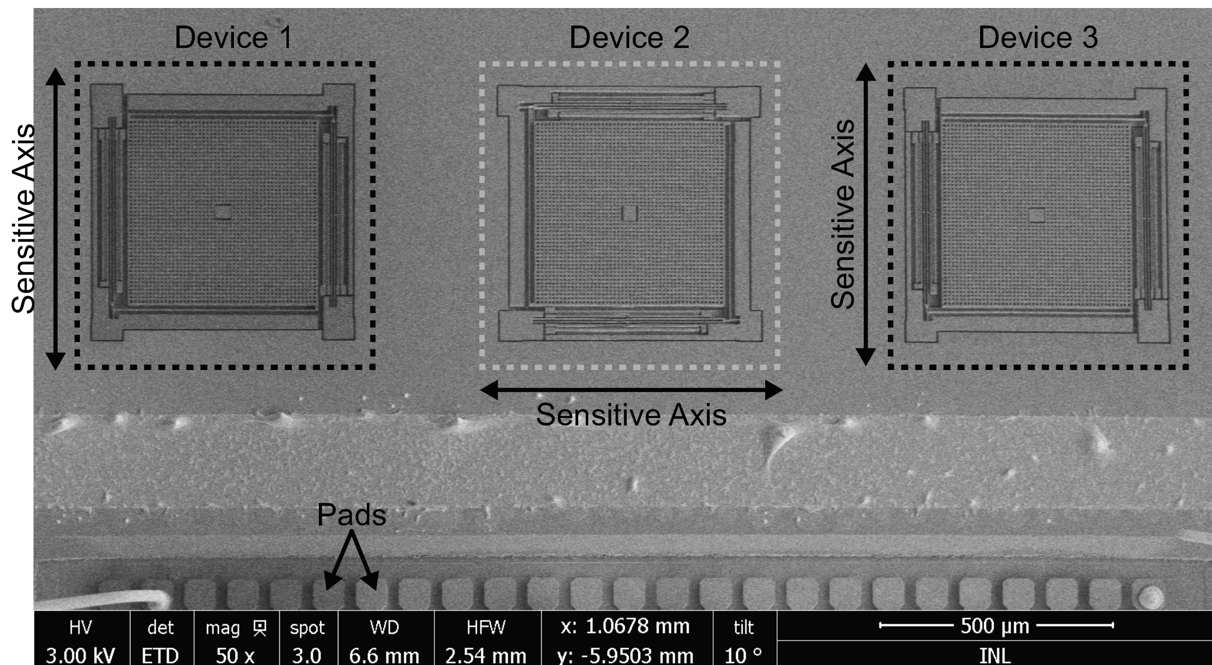

Figure 3.8: Picture of the three devices present on the fabricated dies.

3.1.4 Packaging

The dies containing the accelerometer were glued to ceramic leadless chip carrier (CLCC) with 44 pins and wire-bonded. These steps were also performed at Bosch, since the small pad footprint (65 $\mu m\,x\,65\,\mu m$) makes the wire-bonding process challenging. The final assembly is shown in Figure 3.9.

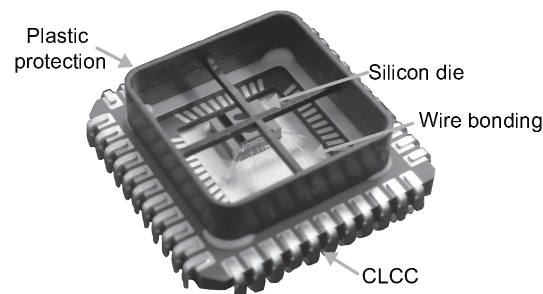

Figure 3.9: Silicon die glued to a ceramic chip carrier and wire-bonded, as provided by Bosch.

Prototypes bonded using two different types of glues with distinct properties were assembled. The adhesives are based on epoxy (hard-glue) and polydimethylsiloxane (PDMS) (soft-glue) materials, having different mechanical properties. While the epoxy-based glue is described by a high Young's modulus and a stable behaviour (no movement of the glue over-time), the PDMS-based glue presents viscoelastic characteristics. PDMS profits from stress-relaxation and creeping, mechanical properties intrinsic to viscoelastic

materials, in other words, the material exhibits viscous and elastic behaviour when undergoing a deformation [3.2]. Depending on the time scale, these materials can behave as a solid, a fluid or the combination of both.

Stress relaxation explains the reliving of induced stress (σ) when undergoing a constant strain (ε). This effect can be seen as a spring effect occurring over a long period of time. Stress relaxation occurs in viscoelastic materials because of material re-arrangement at the molecular or micro-scale. The re-arrangement is called creep and can be defined as a tendency of a material to slowly move/deform when experiencing a constant stress [3.3]. These effects are depicted in Figure 3.10.

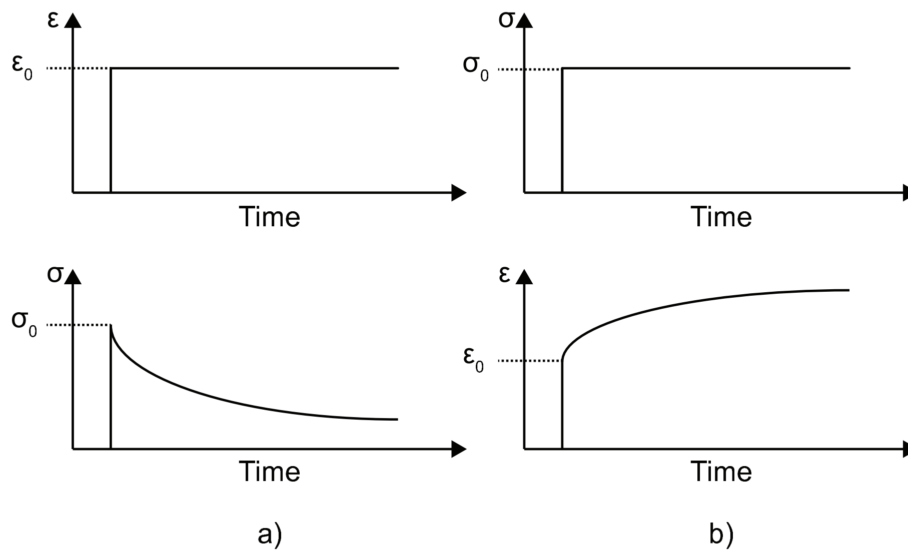

Figure 3.10: Response of a viscoelastic material when enduring a constant stress or strain. a) Stress relaxation for a constant strain. b) Creeping of the material for a constant stress.

The properties of the glues available in the technical datasheet are listed in Table 3.3 [3.4], [3.5]. Note that soft-glues are usually used in the semiconductor industry to decouple external stress from the sensors.

Manufacturer	DELO®	Wacker Chemie AG
Reference	MONOPOX MK096	SEMICOSIL®988/1K
Base	Epoxy resin	PDMS
Colour	Red	Transparent
Density (23 °C)	1.1 g/cm^3	1.1 g/cm^3
Tensile strength	60 MPa	4.5 MPa
Young's modulus	3500 MPa	0.5 MPa (at 100% elongation)
Type of cure	Thermal	Thermal
Classified as:	Hard-glue	Soft-glue

Table 3.3: List of the glue properties used to bond the prototype dies to CLCC.

A full characterisation of the sensor response when an external force is applied to the surroundings of the device was performed. The sensitivity to stress was studied for different attachment glues. In Chapter 4, the mechanical stress decoupling resulting from the epoxy and PDMS based glues is demonstrated and compared.

3.2 Front-end electronics and phase detection

The front-end electronics introduced in Figure 3.1 are described in this section. This section was divided into two main blocks, the analog front-end electronics and the phase and amplitude measurement. First, the analog circuit to convert the output current of the resonators to a voltage is addressed. Then, the lock-in amplifier, that is the element that returns the phase difference of the sensor in comparison to the AC driving voltage, is introduced. This phase shift value is later used to operate the resonator in closed-loop.

3.2.1 Analog front-end

Front-end stage

The front-end stage converts the current flowing from the sensing electrodes to a voltage to be processed. Remembering, the DETF beams when submitted to an excitation voltage start to vibrate, resulting in a capacitance change and inducing a current on the sensing electrodes (see Equation 2.8).

From the Simulink® model of the accelerometer, it is expected that the output currents at the natural frequency of the resonators are in the pico to nano ampere range (depending on the AC driving and bias voltages), and the gain of the transimpedance amplifier (TIA) should be dimensioned accordingly. The TIA configuration is ideal for this application, as it converts, with large gains, low input currents into voltage. This circuit has the advantage of not amplifying the input voltage noise and offset. The TIA was implemented using an operational amplifier and the current to voltage gain is defined by the feedback resistor (R_f), see Figure 3.11. The feedback capacitor (C_f) was added to limit the bandwidth (by introducing a zero into the system), increasing high frequency stability and avoiding oscillatory behaviour.

The circuit was designed to guarantee suitable gain but also the bandwidth necessary to read the resonator output (around 38 kHz). In addition, to implement this circuit, the low-noise (7 $nV/\sqrt{Hz}$) and low input bias current (1 pA) operational amplifier AD8066 from Analog Devices was chosen [3.6].

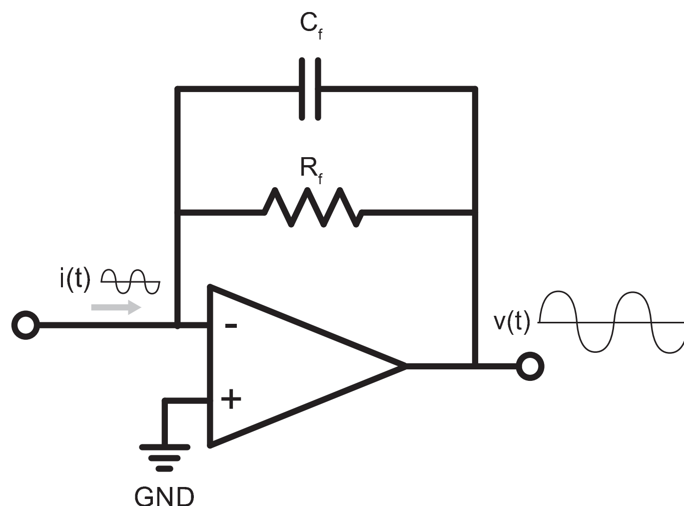

Figure 3.11: Simplified schematic of a transimpedance amplifier.

A Spice model was created in NI Multisim in order to simulate this approach. A feedback resistor and capacitor of $340\ k\Omega$ and 1 pF were used to fulfil the different requirements, namely, gain and bandwidth.

Amplification stage

The output signal from the TIA was further amplified to obtain a voltage with enough amplitude to be read by the lock-in amplifier. A non-inverting amplifier configuration was used for this effect, see Figure 3.12.

The gain of such amplifier ($A_{AmpStage}$) was calculated using the equation below, and the resistors were dimensioned to obtain a total gain (transimpedance and voltage gain) of 10 million ($R_1 = 10\ k\Omega$ and $R_2 = 294\ k\Omega$). The same integrated circuit (AD8066) was used to implement both amplification stages since each package is composed of two operational amplifiers. Additionally, the low-noise, low input offset voltage and high common-mode rejection ratio (-100 db), are advantageous for this application.

$$A_{AmpStage} = 1 + \frac{R_2}{R_1} \tag{3.1}$$

3.2.2 Phase measurement, and resonator bias and AC driving

In order to read the phase but also the amplitude of the amplified output of the resonator and drive it with an AC signal, a lock-in amplifier from Zurich Instruments was used. This laboratory equipment

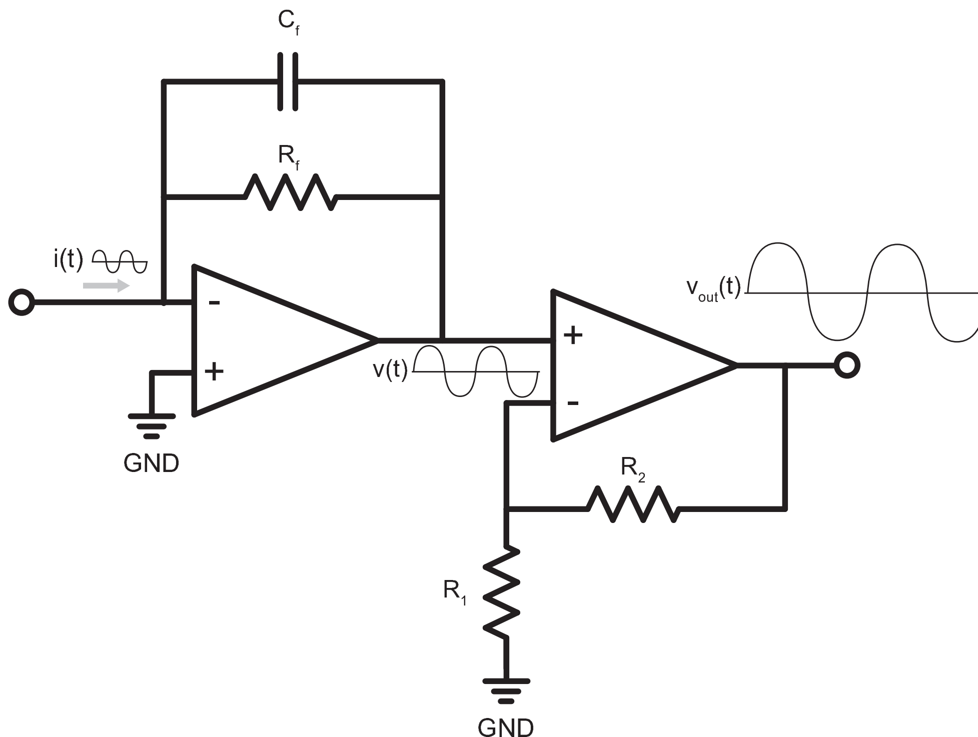

Figure 3.12: Transimpedance amplifier and non-inverting amplification stage to convert current to voltage and amplify.

possesses different functionalities, enabling the operation of the resonators in open-loop for preliminary characterisation, but also allowing the implementation of the closed-loop operation.

A lock-in amplifier is an instrument capable of extracting the amplitude and phase of an alternating current (AC) signal with a reduced amplitude even in presence of noise. Internally, a multiplication of the input and reference signal (internally generated by the lock-in) is performed, this demodulation isolates the signal of interest from all the other undesirable frequency components [3.7]. The demodulated signal passes through low-pass filters, returning two outputs, X (in-phase component) and Y (quadrature component). These values are then converted from cartesian to polar coordinates (see the schematic shown in Figure 3.13). The amplitude (R) and phase (Θ) are the output of the instrument, and additionally, the values of interest either to characterise the DETF or operate them in closed-loop.

The reference signal is usually a sinewave to allow selective demodulation of the fundamental frequency and harmonics. The equipment used can generate the reference signal, or it can be provided by an external source. Here, the demodulation reference was internally generated by the lock-in amplifier for the open-loop operation. The amplitude and frequency of the driving signal can be selected from 1 mV to 10 V and from 1 Hz to 2 MHz, respectively (suitable for the proposed resonator). In Figure 3.13, the working principle is depicted together with the connections to the DETF and the amplification stage. Using this

configuration, the phase and amplitude of the signal from the DETF are obtained. Additionally, the lock-in drives with an AC signal the DETF, allowing the adjustment of the driving frequency to match the resonance frequency of the resonators. For the sake of simplicity, the operation principle of the instrument used is not further addressed, only the functionalities of interest are described.

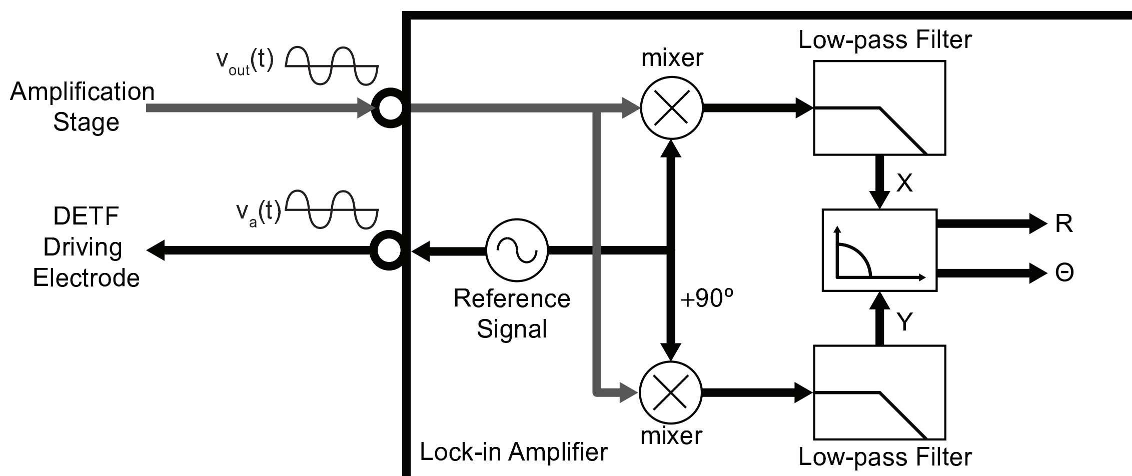

Figure 3.13: Main blocks composing the basic operation principle of the lock-in amplifier and the connections to the resonator.

The amplified output voltage (v_{out} from the amplification stage) is demodulated by a lock-in amplifier (HF2LI from Zurich Instruments), returning information about the amplitude and phase of the signal. On the other hand, the reference signal is the AC driving voltage (v_a) of the double-ended tuning fork resonators, this means, the lock-in is driving the DETF at a frequency that later is demodulated using the internal reference.

As highlighted in Chapter 2, because of the low capacitance changes resulting from the DETF displacement, even when coupled to parallel-plates actuators, stray capacitance can jeopardise the correct output signal instrumentation. Stray capacitances are unwanted capacitance resulting from the different parts of the MEMS device, connections or even the electronics, and can have amplitudes above or similar to the one resulting from the movement of the movable electrode. Therefore, the DETF output signal cannot be read or exhibits a merged response between the stray and resonator capacitance, culminating in signals with anti-resonance peaks or phase shifts at the natural frequency below 90° (contrarily to what is theoretically expected for a second-order mechanical system). Several solutions were proposed in the literature [3.8] to overcome this problem and decouple the resonator output signal from the stray capacitance. Here, the lock-in amplifier allows the driving of the resonators at half of the natural frequency, which is a great advantage since it enabled the decoupling of the stray capacitance. More in detail, the driving signal applied (v_a) is at half of the natural frequency of the resonator and the lock-in reads (demodulates) the second harmonic. The second harmonic is at the natural frequency of the DETF. This technique is used to decouple

the stray capacitance from the output signal of the resonator since the stray capacitance responds to the driving frequency while the DETF output has a component at the second harmonic (resonant frequency).

Additionally, the lock-in amplifier has several configurable analog outputs which return essential information to the surrounding equipment (i.e. FPGA and acquisition board, see Figure 3.1), enabling closed-loop operation. The phase difference between the driving signal (v_a) and the second harmonic of the output signal is passed to the digital controller using one of these outputs. The phase value should be kept at 90° (phase delay for a resonator at the natural frequency - second order system). Additionally, an analog signal corresponding to half of the driving frequency of the DETF has also information of interest, since the external acceleration is related to the resonator natural frequency. A voltage proportional to the natural frequency of the DETF is passed to the acquisition system (this is explained in section 3.4). The connection of these analog outputs (proportional to the phase and frequency) with the other surrounding subsystems can be observed in Figure 3.14.

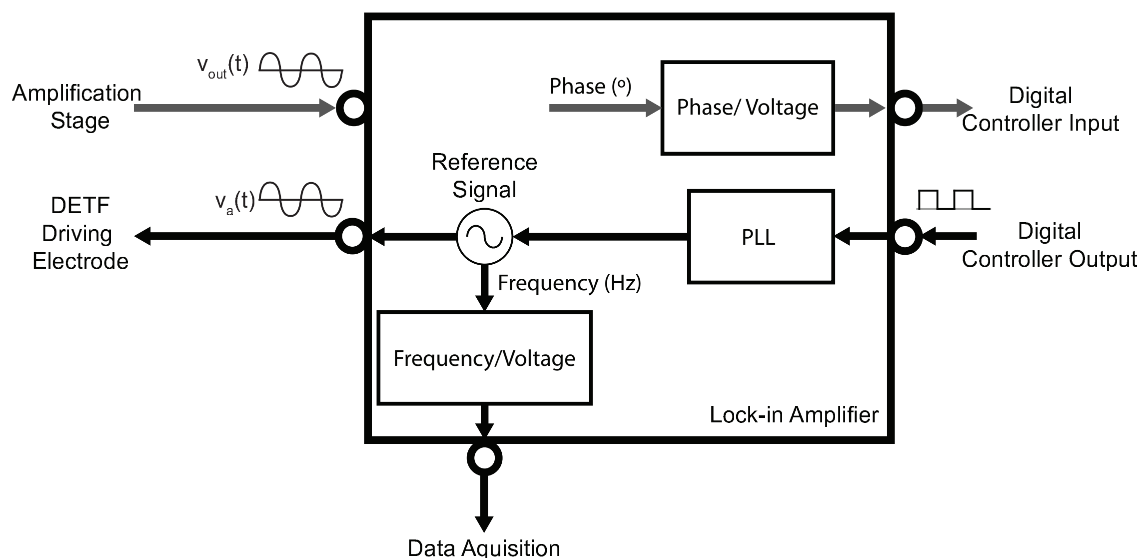

Figure 3.14: Connections of the lock-in with the surrounding equipment and the DETF.

As explained previously, the operation of the double-ended tuning fork in closed-loop consists of the continuous update of the driving frequency to match the natural frequency of the resonators. To do so, the controller outputs a signal at the frequency that has to be injected to the DETF and that serves as reference signal for the internal demodulation of the lock-in. To read the controller output signal (square-wave), the internal phase-locked loop (PLL) of the lock-in was used. Posteriorly, an AC driving signal with an amplitude v_a and at the same frequency is injected to the resonator, thus closing the loop. A sinewave is preferred to excite the resonators over a square-wave, to avoid unusual harmonics. Note that this solution was found to connect the closed-loop controller with the lock-in amplifier.

Briefly introducing a PLL working principle, a PLL is a feedback control system that automatically adjusts the phase of a locally generated signal to match the phase of an input signal. If the locked condition is true, any slight change in the input signal appears as a change in the phase between the input signal and the generated frequency. This phase shift acts as an error and the PLL oscillator compensates to match the frequency of the input signal [3.9].

In order to bias the DETF, to produce higher electrostatic forces and higher currents induced into the sensing electrodes (as referred in Chapter 2), two solutions were implemented. First, a direct current (DC) power supply available in the laboratory was used since the voltage can be tuned, enabling the characterisation of the DETF response for different amplitudes of bias. Once the bias characterisation of the devices was finished, a discrete voltage reference (REF5020) was used in the front-end electronics PCB. The REF5020 from Texas Instruments was selected due to a low-temperature drift (3 ppm/°C), high accuracy (0.05 %), low-noise and excellent long-term stability [3.10]. The selection of the bias source is made at the PCB level using electronic jumpers.

3.3 Closed-loop control components

The closed-loop control was implemented using a fast prototype system that includes a FPGA and other discrete components. The subsystems described, in this section, are responsible for updating in run-time the frequency of the AC driving signal to be injected into the DETF, maintaining them constantly resonating at their natural frequency by maintaining a 90° phase shift between the driving signal and the analog readout signal (second harmonic). An overview of the modules developed on the FPGA, together with the discrete components used to connect the controller to the lock-in amplifier, are presented in Figure 3.15. As represented in the diagram, the closed-loop system can be divided into five subsystems: phase acquisition, PID controller, main finite state machine (MFSM) and the generic modules, signal generation and system configuration. The closed-loop control components section follows a similar division into the same five subsections.

The FPGA and discrete components (analog-to-digital converter (ADC), analog switch, digital-to-analog converter (DAC)) are part of a fast prototype system developed for the operation and characterisation of MEMS time-based accelerometers [3.11] and for the study of travel extension methodologies [3.12]. This prototype system is suitable for the implementation of the closed-loop operation of the resonators, but few constraints are highlighted in this section.

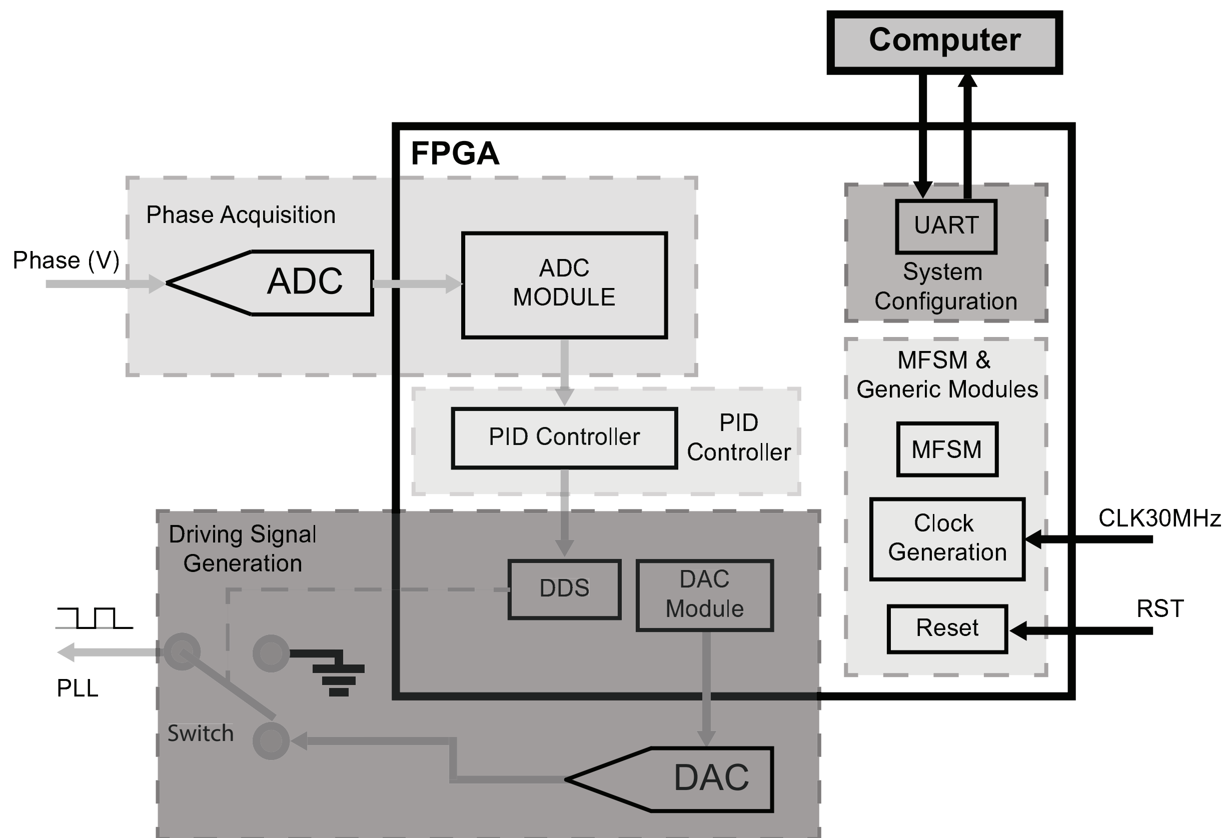

Figure 3.15: Closed-loop control components and modules implemented on a FPGA.

In what concerns the implementation of the modules on the FPGA, Verilog was used as the hardware description language, and the FPGA selected was the Altera Cyclone III (EP3C40Q240C8).

3.3.1 Main finite state-machine and generic modules

All the operations of the resonant accelerometer closed-loop (see Figure 3.15) are controlled by the main finite state-machine (MFSM). This MFSM defines the moments in which the other subsystems have to performed intrinsic tasks. In addition, two generic modules (clock generation and reset) were implemented to assist the remaining systems in the FPGA.

Main finite state-machine

The main finite state-machine is composed of five states controlling the operations to be achieved by the fast prototype system. An overview of the different states and the conditions to remain or switch state are presented in Figure 3.16. The operation of the closed-loop controller occurs in the last states, namely,

AVERAGE and UPDATE. The remaining (IDLE, CONF, INIT) are performed to guarantee a well initialised and configured system.

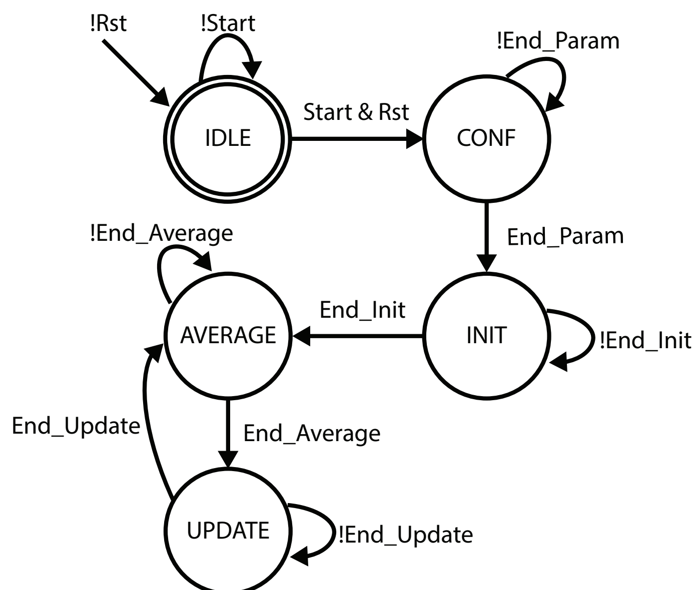

Figure 3.16: Diagram showing the different stats and conditions present in the MFSM.

The diverse actions performed on the FPGA, to implement the resonator closed-loop operation are explained in Table 3.4.

Current State	Next State	Inputs	Action
IDLE	IDLE	!Rst|!Start	This is the first state, if the reset button is pressed (!RST) and released, the MFSM returns immediately to IDLE, independently of the state running. Until the start condition is not inserted (defined by a mechanical switch), the MFSM remains in IDLE. While in IDLE, all the registers are restored to initial values.
	CONF	Start&Rst	If the start and reset conditions are satisfied, the MFSM transits to the next state.
CONF	CONF	!End_Param	The MFSM waits until all the configuration parameters are received through the communication with the computer. Additionally, the DAC configuration command is sent.

	INIT	End_Param	Once all the parameters are received, the MFSM transits to INIT. All the parameters received are loaded into the registers to guarantee the correct initialisation of the subsystems. A counter is initialised to guarantee enough time for the subsystems to start during the INIT state.
INIT	INIT	!End_Init	Until the counter does not reach the time for the correct initialisation of all the subsystems, the MFSM stays in the INIT state. In addition, a message is transmitted to the DAC with the analog voltage required.
	AVERAGE	End_Init	When the configuration time reaches the maximum value, the MFSM transits to the next state. The closed-loop starts from this moment. The generation of the signal (square-wave) starts at the natural frequency of the DETF.
AVERAGE	AVERAGE	!End_Average	The ADC starts acquiring the analog voltage proportional to the DETF phase. These values are summed and averaged until it reaches the number of samples required.
	UPDATE	End_Average	Once the right number of samples from the ADC are reached, a register of the phase average is passed to the PID controller. The average register is reset and the process restarted. The phase sampling is never stopped.
UPDATE	UPDATE	!End_Update	The new value of frequency to be injected into the DETF is calculated using the average phase value.

	AVERAGE	End_Update	Once the PID controller has stopped the calculation of the new frequency, the frequency of the generated signal is updated. This update only occurs in case of a transition (rising edge or falling edge) of the signal generated. The MFSM returns to the AVERAGE state.

Table 3.4: Detailed description of the different actions performed in each state.

Clock generation

The FPGA has an internal clock signal at 30 MHz, but some required hardware modules need a reference clock signal with a different frequency. An Altera intellectual property (IP) core implementing a PLL circuitry [3.9] was used to generate three more clock signals that are used in the different modules implemented on the FPGA. The input and outputs of the clock generation module are shown in Figure 3.17.

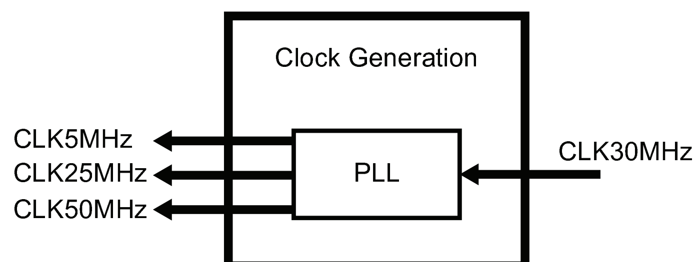

Figure 3.17: Diagram of the clock signals at the output of the clock generation module.

The 5 MHz clock regulates the sampling frequency of the ADC while the 25 MHz are used to communicate with the DAC. All the other modules use a clock frequency of 50 MHz.

Reset

Although the reset circuitry is instrumental in the correct behaviour of all the subsystems implemented on the FPGA, this aspect is often ignored during the design [3.13]. An improper reset can result in unrepeatable logical errors, yielding a malfunctioning behaviour of the hardware modules (difficult to detect).

Due to the different clock frequencies, this module has to be designed to satisfy timing constraints. A synchronous reset may outcome an initialisation of the modules working at higher frequencies while failing

on the slower. For this reason, a method for asserting all reset signals asynchronously but deasserting them synchronously was implemented (see Figure 3.18). This reset topology is more reliable than fully synchronous or fully asynchronous mechanisms [3.13]. In what concerns the working principle, the registers in the reset circuit are asynchronously reset by the external reset signal. This occurs asynchronously with the clock (the clock does not need to be running). If the external reset signal deasserts, the faster clock must toggle enough cycles to allow all the different modules to reset successfully.

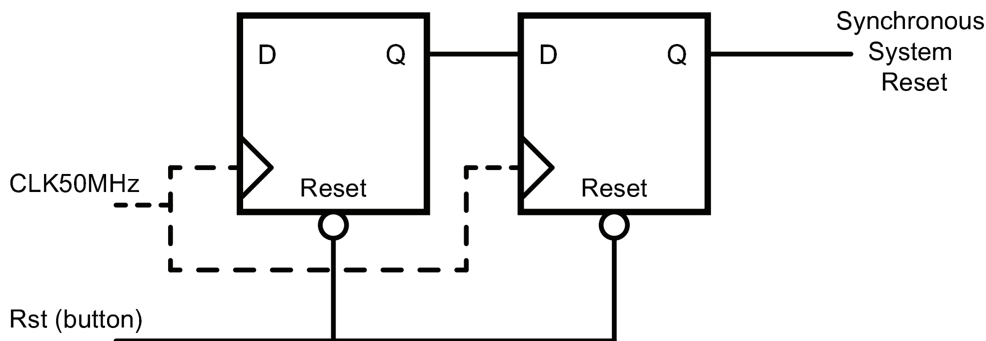

Figure 3.18: Asynchronous assertion, synchronous deassertion reset scheme.

3.3.2 Phase acquisition

The lock-in amplifier has an output that returns a voltage signal proportional to the phase difference of the amplified sensing signal from the DETF resonator (second harmonic) in comparison to the phase of the driving voltage AC signal. The phase shift has to be acquired by the FPGA since this value is the input of the controller and has to be maintained at 90°, thus implementing the closed-loop. Using the resources available in the fast prototype system used, an ADC converts this analog signal into a digital value. The ADC used is a ADS5560 from Texas Instruments [3.14], with a 16-bit resolution and a maximum sampling rate of 40 MHz.

The information from the ADC is acquired at a frequency of 5 MHz, using a parallel communication protocol. The samples are summed and averaged, resulting in a new value of phase at the input of the controller at a frequency of approximately 4.8 kHz to avoid limiting the resonant accelerometer bandwidth. A total of 1024 samples are summed, making the averaging easier (and faster) since the result is shifted to the right ten times.

The analog-to-digital converter is restrained to input voltages going from 3V to -3V and the phase value (voltage/degree) has to be configured in the lock-in amplifier to not over-range these limits.

3.3.3 Proportional-integral-derivative controller

A PID controller is a closed-loop mechanism employed in systems requiring a continuous control response. This type of controllers is widely used in industrial applications due to an increased flexibility, reliability and implementation simplicity [3.15]. In addition, a PID controller is suitable for linear systems, thus making it attractive for the application described in this thesis, namely, maintain the DETF resonators at their natural frequency.

The controller is composed of a feedback path that continuously calculates an error relative to a setpoint (see Figure 3.19). This error is essentially the difference between the setpoint and the input of the controller. The system is then corrected based on the error and three terms. As the name indicates, the controller is constituted by three elements: proportional, integral and derivative. These terms are applied to the control variable as a correction to decrease the error over time.

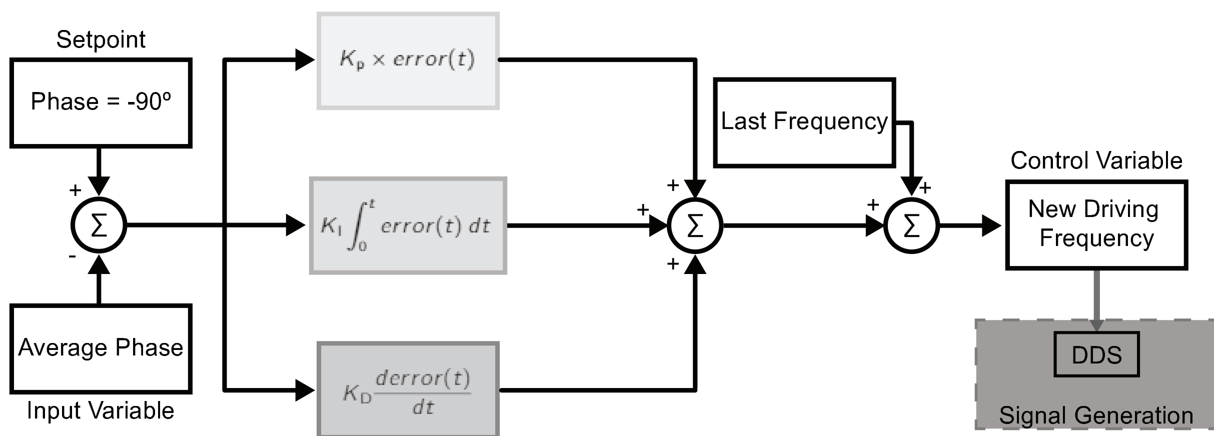

Figure 3.19: Block diagram showing the different blocks, constants and variables of the controller implemented.

The proportional term accounts for the current value of the error (error(t)) and the gain factor K_p. The response (r(t)) of a fully-proportional controller is calculated using Equation 3.2. Note that using purely this term, if no error is measured no change in the control variable occurs.

$$r(t) = K_p \times error(t) \tag{3.2}$$

Secondly, the integral term generates a response taking into account the accumulation of errors over time and the integral gain K_I (See Equation 3.3). The integration of errors reduces the controller response velocity, but zero error between the setpoint and the input variable can be reached (since the integral term contributes to the reduction of residual error).

$$r(t) = K_I \int_0^t error(t)\, dt \tag{3.3}$$

Describing the last term, the slope of the error over time, multiplied by the derivative gain (K_D), is often interpreted as a way to predict the "future" of the system to be controlled. The derivative term improves the transient response [3.15] since it generates a response based on the trend. The derivative controller response is calculated using the equation below:

$$r(t) = K_D \frac{derror(t)}{dt} \tag{3.4}$$

Applying these terms to the system implemented in this thesis, the setpoint is a fixed value of phase (ensuring the operation at the natural frequency) and the input variable is the average of the phase read by the lock-in amplifier, returning the information of the DETF resonating status. Additionally, the control variable is the driving signal frequency that needs to be injected to maintain the resonator at its natural frequency. The new value of frequency is the input of the direct digital synthesis (DDS), and this value is updated at a frequency of 4.8 kHz, thus closing the loop. The different blocks, constants and variables of the controller were demonstrated in the diagram of Figure 3.19.

In Figure 3.19, one can observe a value of frequency (last frequency) is added to the addition of the PID terms, because of the correlation between phase and frequency. Succinctly, the error of phase has to be converted into a driving frequency value to be applied back to the resonators, correcting the phase error between the output signal of the DETF and the driving AC signal. For this reason, from the phase error, a new value of frequency is added to the last frequency applied to the DETF. The frequency value can increase or decrease irrespectively to the phase error, and this value is then passed to the signal generation subsystem that was implemented to communicate with the lock-in amplifier in order to generate a AC driving signal (v_a) at a new frequency (half of the resonant frequency).

The processing of the different terms was implemented using the true parallelism capabilities granted by the FPGA. Although controllers can be implemented using diverse platforms (e.g. microcontrollers, computers), only programmable logic yields constant operation timings, increasing the controller stability and consequently, the DETF response stability. All the calculations were performed using floating point arithmetics (IEEE 754) to benefit from a higher precision. Additionally, the IP cores developed by Altera were used to carry out the operations required (e.g. calculate the PID terms).

3.3.4 Driving Signal generation

The driving signal generation module was implemented to generate a square wave signal with the same frequency to be injected by the lock-in amplifier to the driving electrodes. This was done to communicate the control variable between the FPGA and the lock-in amplifier (serving as the clock reference of the lock-in amplifier). The subsystem of the driving signal generation is divided into two main modules: the DDS and the digital-to-analog modules, as demonstrated in Figure 3.15. The DAC and analog switch could be replaced by a general-purpose input/output (GPIO) of the FPGA, since the input of the lock-in's PLL admits standard Transistor–transistor logic (TTL) values (low=0V and high=5V). However, due to limitations on the platform used and in order to avoid permanent modifications in the fast prototype system (ensuring an universal use), a DAC and a switch were used to produce a square wave.

Direct Digital Synthesis

Direct digital synthesis is used to generate periodic signals such as, sine, square and saw waves, by creating a time-varying signal in a digital form [3.16]. The main advantages of this approach are a fast output frequency switching, fine frequency resolution and an extensive spectrum of output frequency [3.17]. For this reasons, this module was implemented.

Concerning the working principle, a DDS is based on a phase accumulator generating digital states that increase linearly and represent the periodicity of the output phase waveform. The phase accumulator is a counter that has a number of states, and these are incremented at each reference clock cycle (f_{clk}). The size of the increments depends on the accumulator register bit number (n_{bits}). A larger accumulator size represents a finer phase and frequency resolution (Δf_{DDS}) [3.18]. The frequency resolution is obtained using:

$$\Delta f_{DDS} = \frac{f_{clk}}{2^{n_{bits}}} \tag{3.5}$$

The module implemented has a frequency increment resolution of 12 mHz, an accumulator of 32-bit and a fixed clock signal of 50 MHz. The incremental frequency step is important, since it can limit the resolution of the resonant accelerometer.

The output frequency of the DDS is determined by the tuning word (M) and not by the reference system frequency. By incrementing the tuning word, fewer steps per cycle (or phase accumulator total value) are

counted, resulting in a signal with higher frequency. The frequency generated (f_{va}) by the DDS algorithm depending on the tuning word is calculated using the equation below:

$$f_{va} = \frac{M \times f_{clk}}{2^{n_{bits}}} \tag{3.6}$$

Where a square-wave is necessary to transmit a frequency value to the lock-in amplifier, the tuning word is calculated to match new frequency to be injected into the driving electrodes (half of the natural frequency of the DETF). The new value of frequency is calculated by the PID controller, nonetheless, the DDS is responsible for the generation of the signal. The tuning word adjusts the square-wave frequency and a analog switch is used to commute between a value given by an external DAC and the ground, yielding a square-wave signal. The switch is also controlled by the module and the generated signal frequency is updated at a frequency of 4.8 kHz, but in signal transitions to avoid outputs with incomplete wavelengths. This mechanism was implemented to ensure the correct frequency reading on the PLL side.

Digital-to-analog converter

A digital-to-analog converter (DAC) from Analog Devices (AD5791) was used to produce a constant voltage at the input of the analog switch. The communication with this discrete component is made through serial peripheral interface (SPI) at a 25MHz clock frequency.

In the FPGA, the control of the SPI was implemented by a hardware block and the DAC operates as a slave. This SPI module was previously implemented, more details about the state-machine, required configurations and general working principle can be found in [3.19].

The input register of the DAC is composed of 1-bit to define read and write operations, and three bits to control the operation required. In addition, a word of 20-bit defines the voltage at the output. The 24-bit command structure is shown below in table 3.5.

[23]	[22:20]	[19:0]
Read/$\overline{Write}$	Register address	DAC register data

Table 3.5: 24-bit command structure to write and read from the DAC register.

The output voltage aimed at the output of the DAC (V_{DAC}) has to be converted into a 20-bit code (D) to be sent to the DAC. This value is obtained using Equation 3.7.

$$V_{DAC} = \frac{(V_{REFP} + V_{REFN}) \times D}{2^{20} - 1} - V_{REFN} \tag{3.7}$$

Where V_{REFP} and V_{REFP}, are the positive and negative DAC voltage references, 10 V and -10 V, respectively.

3.3.5 System configuration

An hardware module was created to guarantee the configurability of the different modules implemented on the FPGA. This subsystem is composed of a universal asynchronous receiver/transmitter (UART) module, allowing data exchange with a computer at a baudrate of 115200 bit/s. The different details about the UART module implementation are also available in [3.19].

The module allows a bi-directional communication, meaning that data can be received or sent from the FPGA. A total of four values are required for the configuration of two modules (DDS and PID controller) and these are sent from the data acquisition and system configuration subsystem. These configuration values are the initial frequency to be produced by the signal generation system, and the three gains (K_P, K_D and K_I) constituting the PID controller. All the parameters have a length of 32-bit and are sent using a floating-point notation (IEEE 754) during the configuration state (CONF state) of the MFSM.

To guarantee an efficient communication, other messages are exchanged, for instance, to start the communication, a computer has to send the character 'W' to the FPGA. All the communication sequence is described in Table 3.6. After all the parameters are received and loaded into the registers, the FPGA echos back all the values to ensure that the reception was successful. If this was the case, the computer sends a finalisation 'W' character to close the communication, and consequently, switches the status of the MFSM.

3.4 Data acquisition and system configuration

To acquire the voltage proportional to the driving signal frequency but also to configure the subsystems (i.e lock-in amplifier and FPGA), a computer and a data acquisition board were used. In this section, both components of this system are described. Additionally, the different blocks and connections can be observed in Figure 3.20.

Starting by the lock-in amplifier, a Universal Serial Bus (USB) connection allows the configuration of several parameters. Namely, activate/deactivate functionalities and/or channels, configuration modes, perform

Order	Sent by: Computer	FPGA
1	'W'	
2	Initial Frequency [31:0]	
3		'K'
4	K_P[31:0]	
5		'K'
6	K_I[31:0]	
7		'K'
8	K_D[31:0]	
7		'K'
8	'W'	
9		Initial Frequency [31:0]
10		K_P[31:0]
11		K_I[31:0]
12		K_D[31:0]
13	'W'	

Table 3.6: Communication sequence to configure the FPGA with the different parameters.

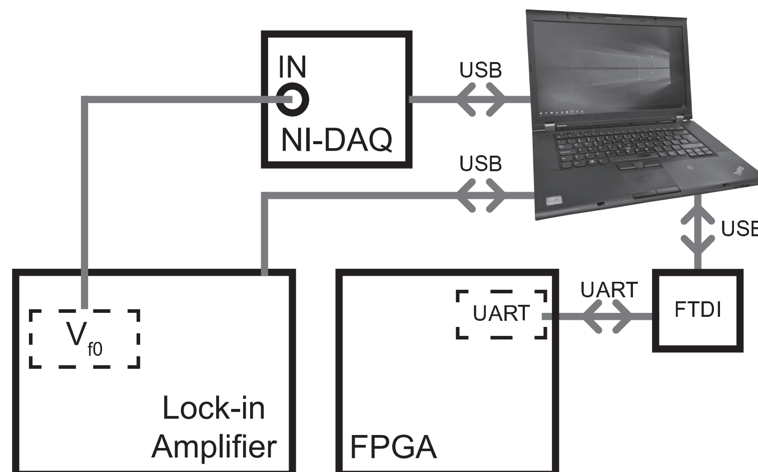

Figure 3.20: Data acquisition and system configuration connection scheme.

frequency sweeps, change gains and/or filters' parameters, among many other. A software application from Zurich Instruments enables the configuration using a graphical user interface. Nonetheless, Matlab scripts were developed to automatise tests and retrieve values of interest during the experimental proceedings. Due to a slow data debit (between the computer and the lock-in amplifier), the signal proportional to the driving frequency (V_{f0}) was configured to be available at an analog output of the lock-in amplifier (as previously shown in Figure 3.14), allowing high sampling frequencies.

An acquisition board USB-6363 from National Instruments [3.20] was used to acquire a voltage proportional to the frequency applied to the driving electrodes of the resonators (V_{f0}). The data is sent through

an USB connection to a computer and the sampling rate was defined at 1 kHz, to guarantee at least 10 samples when the accelerometer is submitted to accelerations of 100 Hz. All the configurations and data acquisition are performed using Matlab scripts to monitor and control the fast prototype system and the resonant accelerometer using a computer.

In what concerns the FPGA, as previously mentioned, a UART was implemented to configure some hardware blocks. Therefore, a connection to a computer is enabled using the FTDI chip present in the fast prototyping platform, enabling the interface via USB cable.

All the subsystems are connected to a central element (computer), enabling a fast and simple configuration. Using the advantages of scripting in Matlab and the tools to communicate with the surrounding equipment, several experimental tests were automatised. This allows an efficient and reproducible study of the device behaviour using the diverse functionalities implemented on the fast prototyping system.

3.5 Conclusion

An approach for a MEMS accelerometer based on double-ended tuning fork resonators on a differential architecture was presented. The small-size, vacuum encapsulation and ease of fabrication using standard silicon MEMS processes were enhanced as advantageous for the automotive industry. Since a standard process was used to fabricate the resonant accelerometer, the integration with numerous sensors produced at Bosch is enabled. In addition, the sensitivity of the structures was increased by the differential architecture and thorough optimisation of the different features composing the accelerometer was performed.

Besides the development of the accelerometer, the analog front-end electronics to instrument the double-ended tuning fork resonators was addressed. To operate the entire device composed of two resonators and support the differential architecture, the analog front-end electronics were duplicated as well as the digital modules implemented on the FPGA. Additionally, two inputs and two outputs of the lock-in amplifier were used, corresponding to the entire capacity of the lock-in amplifier (two inputs, two outputs, four auxiliary outputs and two PLL). The frequency change of the right and left DETF are then subtracted, producing the differential reading. This is the value of interest, and it returns information about the external acceleration sensed by the device.

References

[3.1] C. Comi, A. Corigliano, G. Langfelder, A. Longoni, A. Tocchio, and B. Simoni, “A Resonant Microaccelerometer With High Sensitivity Operating in an Oscillating Circuit”, Journal of Microelectromechanical Systems, vol. 19, no. 5, pp. 1140–1152, Oct. 2010. doi: 10.1109/JMEMS.2010.2067437.

[3.2] H. Y. Gan and Y. C. LAM, “Viscoelasticity”, in Encyclopedia of Microfluidics and Nanofluidics, D. Li, Ed. Boston, MA: Springer US, 2008, pp. 2147–2155. doi: 10.1007/978-0-387-48998-8_1666.

[3.3] F. Tavanaei, M. H. Mehranpour, and M. Moosavi, “The comparison of compression and impression relaxation tests with different diameter of indenter in salt rock”, May 2014, pp. 351–356. doi: 10.1201/b16955-57.

[3.4] DELO, MONOPOX MK096, 2011.

[3.5] Wacker Chemie AG, Semicosil ® 988/1k, 2005.

[3.6] Analog Devices, AD8065/AD8066, 2019.

[3.7] Zurich Instruments AG, Principles of lock-in detection and the state of the art, 2016.

[3.8] K. E. Wojciechowski, “Electronics for Resonant Sensors”, PhD thesis, University of California, Berkeley, 2005, p. 149.

[3.9] Altera, ALTPLL (Phase-Locked Loop) IP Core User Guide, 2017.

[3.10] Texas Instruments, REF50xx, Low-Noise, Very Low Drift, Precision Voltage Reference, 2016.

[3.11] R. A. Dias, F. S. Alves, M. Costa, H. Fonseca, J. Cabral, J. Gaspar, and L. A. Rocha, “Real-Time Operation and Characterization of a High-Performance Time-Based Accelerometer”, Journal of Microelectromechanical Systems, vol. 24, no. 6, pp. 1703–1711, Dec. 2015. doi: 10.1109/JMEMS.2015.2487686.

[3.12] E. E. Moreira, V. Lima, F. S. Alves, J. Cabral, J. Gaspar, and L. A. Rocha, “Full-gap tracking system for parallel plate electrostatic actuators using closed-loop control”, Sensors and Actuators A: Physical, vol. 244, pp. 174–183, Jun. 2016. doi: 10.1016/j.sna.2016.04.002.

[3.13] S. Kilts, ”Advanced FPGA Design”. Hoboken, NJ, USA: John Wiley & Sons, Inc., Jun. 2007, pp. 1–336. doi: 10.1002/9780470127896.

[3.14] Texas Instruments, ADS556x 16-Bit , 40 and 80 MSPS ADCs With DDR LVDS and CMOS Outputs, 2016.

[3.15] Kiam Heong Ang, G. Chong, and Yun Li, "PID control system analysis, design, and technology", IEEE Transactions on Control Systems Technology, vol. 13, no. 4, pp. 559–576, Jul. 2005. doi: 10.1109/TCST.2005.847331.

[3.16] National Instruments, Understanding Direct Digital Synthesis (DDS), 2006.

[3.17] E. Murphy and C. Slattery, "All about direct digital synthesis", Analog Dialogue, vol. 38, no. 3, pp. 8–12, 2004.

[3.18] Xilinx, DDS v5.0, 2005.

[3.19] E. E. Moreira, "Controlo de micro-atuadores eletrostáticos na zona de instabilidade", Universidade do Minho, 2014, pp. 1–117.

[3.20] National Instruments, USB-6363 - User Manual, 2018.

Chapter 4

Experimental results

In this chapter, the emphasis is on the experimental characterisation and validation of the proposed DETF resonators and whole resonant accelerometer. The main experimental results demonstrated along this chapter regard the assessment of the DETF nominal natural frequency, the sensitivity of the device for different accelerations and a long-term measurement performed over twelve hours. The change of the sensor response accordingly to temperature, and to different driving or bias voltage amplitude was experimentally measured. All the tests performed, certify the performance of the MEMS accelerometer together with the instrumentation system, being the understanding of the distinctive parameters paramount to extract the real advantages and disadvantages of the chosen approach. Therefore, the conclusions withdrawn along this chapter are instrumental in defining improvements in future architectures and comparing theoretical expectations with experimental data.

Additionally, the response of the frequency-modulated accelerometer, when in the presence of mechanical stress applied to the surroundings of the silicon die, was characterised for samples assembled using two different types of glues.

4.1 DETF mechanical characterisation

In this section, the DETFs are characterised when an external acceleration close to 0g is applied to the proof-mass of the sample, enabling the assessment of the DETF mechanical properties. Here, the main objective is to study the resonators' response in diverse conditions, namely for different electrical stimuli (driving and bias voltages).

The DETFs were operated in open-loop to evaluate their response and perform a preliminary characterisation. This characterisation consisted mainly on performing frequency sweeps to obtain the bode plot of

the devices, the nominal resonance frequencies and quality factors. The system for the validation of the resonators was previously described in Chapter 3 and is depicted in Figure 3.1. Note that the components to close the loop were not employed and that only silicon dies mounted on soft-glue were used during this characterisation steps.

4.1.1 Setup

To perform the prototypes' characterisation, the devices were introduced in a printed-circuit board composed of the front-end electronics and the bias voltage reference, as shown in Figure 4.1.

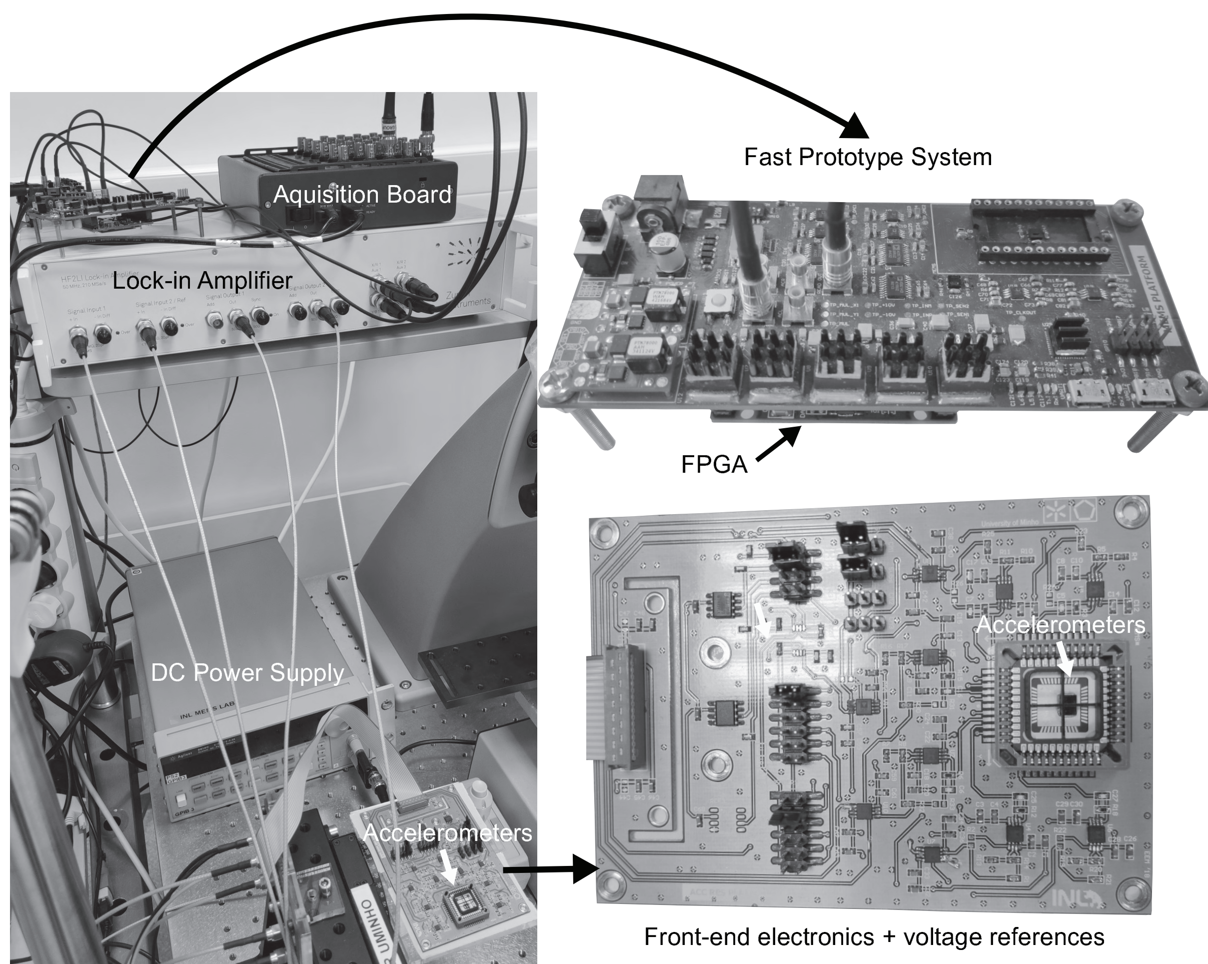

Figure 4.1: Components of the setup to perform the characterisation of the accelerometers. The main parts are demonstrated, namely, the front-end electronics, the fast prototype system board with the FPGA, the DC power supply and the data acquisition board.

As also observed in Figure 4.1, the lock-in amplifier HF2LI from Zurich Instruments was used to read and drive the resonators. The frequency sweeps enabled the evaluation of the resonators properties. Moreover,

a DC power supply was used to adjust the bias voltage applied to the resonators, allowing the study of the response for different bias voltage amplitudes.

The fast prototype system (and FPGA) used to operate the resonators in closed-loop is presented in the figure above, despite not being used during the assessment of the DETF properties.

4.1.2 Resonant frequency and quality factor

A frequency sweep using the lock-in amplifier was performed to extract the natural frequencies and quality factors of both DETFs present in the MEMS differential architecture (i.e. left and right DETF), as shown in Figure 4.2. A nominal natural frequency close to 35.8 kHz at approximately 0 g (manually placed) and quality factors of 130 were experimentally measured.

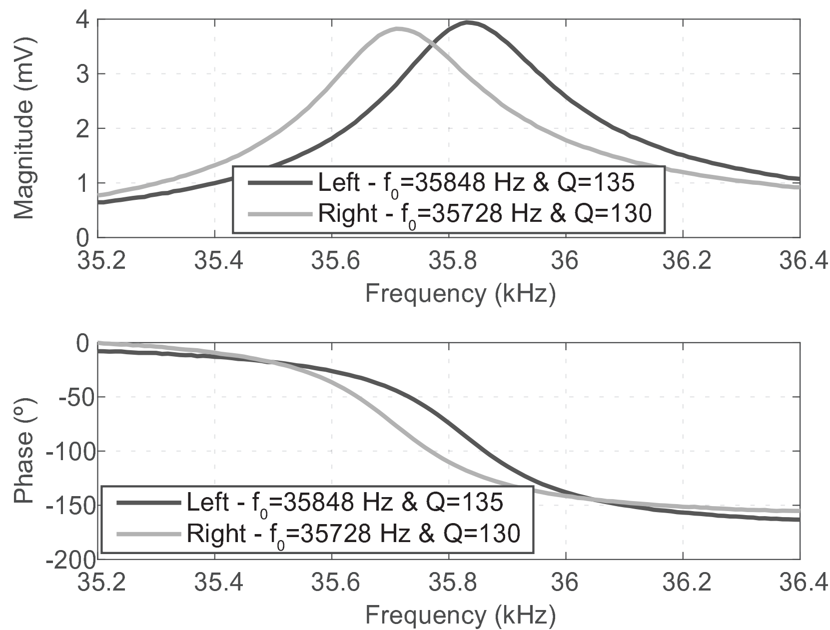

Figure 4.2: Bode plot of the right and left DETF responses for a driving and bias voltage of 325mV and 2V, respectively (sample 2-P01-S1).

The mismatch observed in natural frequency, and quality factor of the resonators can be explained by process non-uniformities which result in slight feature dimension differences on the left and right DETF. Another explanation is related to a different residual stress. The residual stress can be defined as stress that remains in the material or body, due to different thermal expansion coefficients of the materials composing the sensor (polysilicon and silicon oxide) [4.1], for instance. The fabrication process temperature changes

are the main cause of this effect, and the properties of the device can suffer modifications since tensile and compressive stress are applied to the resonators (and other features).

In Figure 4.2, the magnitude and phase curves have the expected shape for a second-order mechanical model, not presenting any anti-resonance peak on the magnitude plot neither a phase shift smaller than 180°. This is explained by the correct isolation of the signal from the stray capacitance by applying the driving voltage at half of the DETF natural frequency and demodulating at twice this frequency (second harmonic). In comparison, in Figure 4.3, one can observe the amplitude and phase of a resonator when the frequency sweep drives and reads the DETF at the same frequency (first harmonic demodulation, no stray capacitance decoupling).

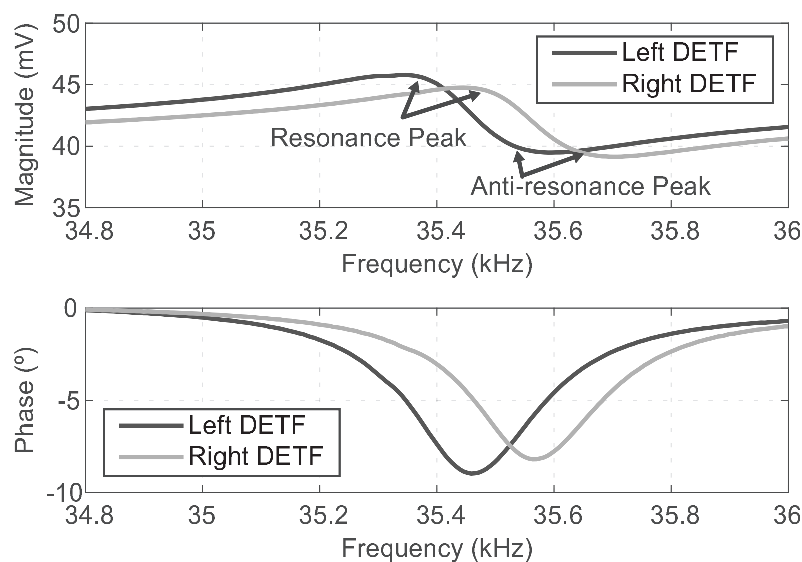

Figure 4.3: Bode plot of the right and left DETF when the driving voltage is applied at the natural frequency (no stray capacitance decoupling). A bias and driving voltage of 2V and 25mV were used, respectively (sample 2-P01-S1).

The anti-resonance peak presented in the magnitude plot (shown in the figure above) and the phase shift smaller than 180° degrees are explained by the merged response (stray capacitance and DETF) obtained using this reading methodology, hence validating the effectiveness of the approach used in this thesis.

Four different simulations were performed for distinct over-etch conditions and encapsulation pressures, enabling the comparison with experimental results. The simulation characteristics and main results are exposed in Table 4.1.

Many samples with the same accelerometer design were fabricated. Some of them were tested to compare performance and mechanical properties. In Figure 4.4, the natural frequency of resonators from different

Name	Pressure (Pa)	Over-etch	Natural Frequency (Hz)	Quality Factor
Simulation #1	150	0%	37910	99
Simulation #2	150	5%	36120	100
Simulation #3	150	10%	34280	100
Simulation #4	100	0%	37910	140

Table 4.1: Simulation characteristics and main results.

sensors is demonstrated. Also, the values obtained using the simulation model were added together with a line representing the average natural frequency experimentally measured.

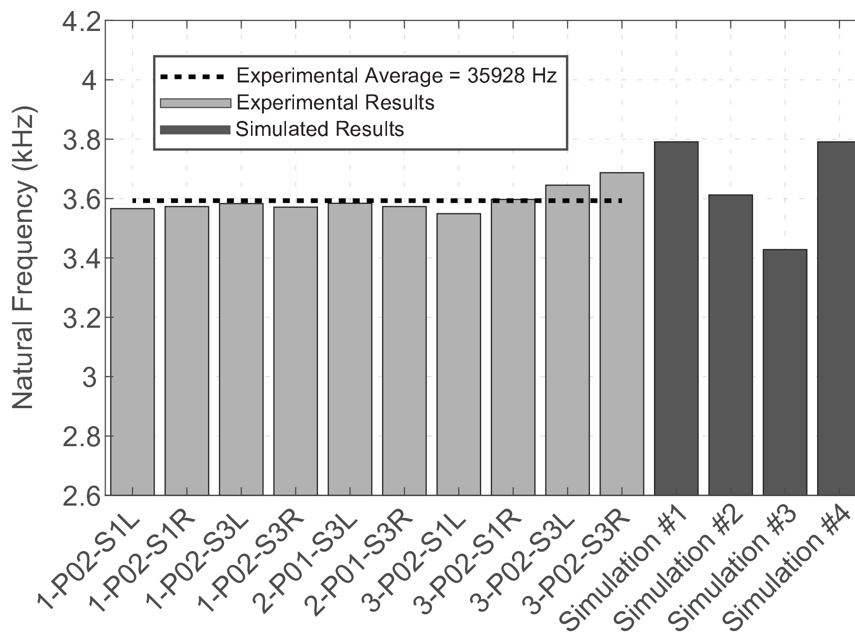

Figure 4.4: Natural frequency experimentally measured and values for four different simulation conditions (Vp=2V).

Regarding the sample names, the denomination is composed by several numbers and letters. The first number is the number of the packaged silicon die, the last number represents the accelerometer position (remembering each die has three sensors, being S1 the left accelerometer and S3 the one in the right) and finally, the last letter identifies the right (R) and left (L) DETF. As an example, a sample named 2-P01-S1L represents the sample number 2, and the left DETF of the accelerometer S1 was measured, in other words, the left sensor. This sample classification is depicted in Figure 4.5.

Looking at Figure 4.4 and Table 4.1, it can be observed that the average natural frequency is approximately 2 kHz below the theoretical value obtained from a simulation without process over-etch, representing a difference of 6%. Though adding over-etch between 5% to 10 % (decreasing the features dimensions), this difference declines. These values of over-etch are common in fabrication processes for MEMS sensors,

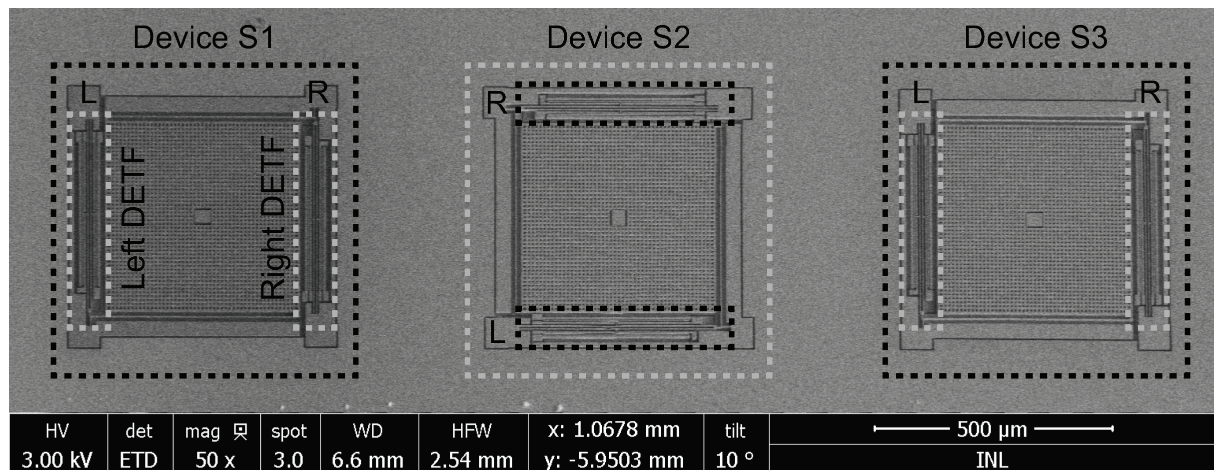

Figure 4.5: Sample classification showing the left (L) and right (R) DETF and the devices' numbers.

and the simulation model can be validated as adequate to study the resonators designed. Additionally, a natural frequency standard deviation of 417.5 Hz was experimentally measured for the ten DETF samples examined, and this represents a variation of 1.1% regarding the average resonant frequency. The resonators can be considered relatively similar, taking into account these values.

Together with the natural frequency, also the quality factor of the different samples was experimentally measured (see Figure 4.6).

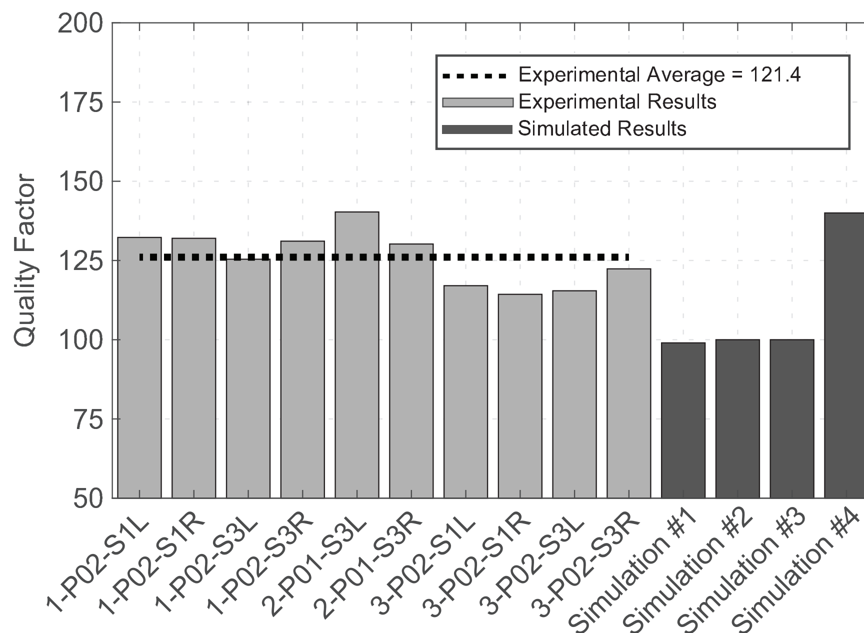

Figure 4.6: Quality factor experimentally measured and values for several simulation conditions (Vp=2V).

Although the devices were designed for an encapsulation pressure of 100 Pa, the foundry expects values

close to 150 Pa. Higher pressure results in smaller quality factors since the main dissipative component (squeeze-film damping) increases, and at this pressure range, the effect is significant. Looking at Figure 4.6, one can conclude the encapsulation pressure is expected to be between 100 Pa and 150 Pa, and this value is expected to vary on each sample.

Furthermore, three frequency sweeps were performed for an accelerometer in different positions relatively to the sensitive axis (+1g, 0g and -1g). This was done by manually rotating the printed circuit board (PCB) relatively to the sensitive axis of the accelerometer and the gravitational force component. Although, the objective is not to discuss the sensitivity of the sensor, the fact that the natural frequency of the DETF changes accordingly to an external acceleration is validated (see Figure 4.7).

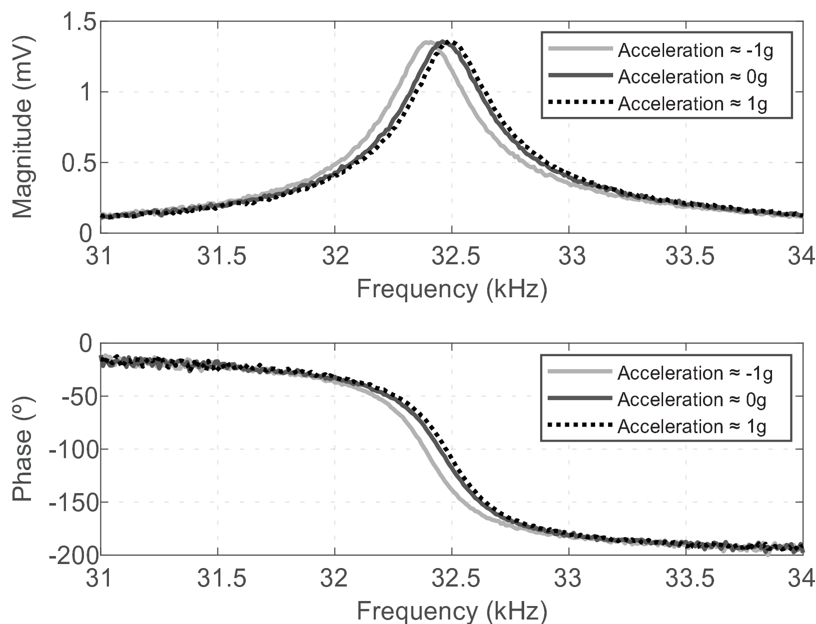

Figure 4.7: Frequency sweeps for an accelerometer submitted to three different accelerations (sample 5-P02-S1L, V_p=1.5V and v_a=325mV)

4.1.3 Influence of the AC driving and bias voltage signals

The DETFs were characterised for different driving (v_a) and bias (V_p) voltage signals, remembering v_a is an AC driving signal and V_p a DC bias signal. This study allows the perception of the influence of these voltages amplitudes on the behaviour of the resonator. As explained in section 2.2.4, non-linearities can arise from spring softening and hardening produced by greater voltage amplitudes, influencing the resonator frequency response.

Regarding the influence of the driving voltage, the amplitude of the signal was changed from 100 mV to 350 mV and frequency sweeps were performed, as observed in Figure 4.8. Experimentally, it is shown that the resonator natural frequency does not change with a higher driving voltage, but the output signal amplitude increases. The amplitude of the output signal increases since the resonator displacement amplitude is larger for a higher driving voltage, resulting in a greater capacitance change and consequently on an increased output signal.

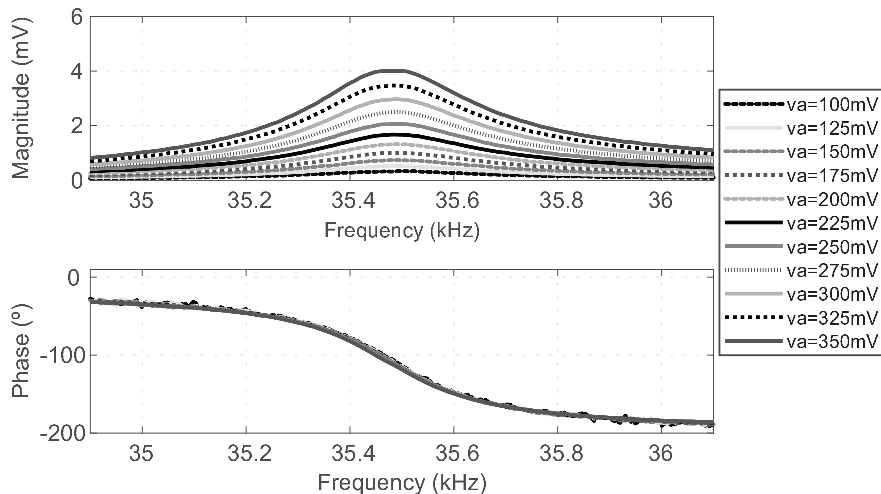

Figure 4.8: Several frequency sweeps performed with a bias voltage of 2V and different driving voltages (sample 3-P02-S1L).

Observing the last figure, no mechanical non-linearities are experimentally noticeable for the range of driving voltages tested. In other words, this range of voltages can be used to study the accelerometer behaviour, since the DETF do not present any non-linearity. Nevertheless, higher driving voltages improve the signal-to-noise ratio (SNR). This test was performed using a fixed bias voltage of 2V.

The influence of the bias voltage on the double-ended tuning fork resonators' behaviour was experimentally assessed. In this case, the driving voltage was fixed to 200mV, and frequency sweeps were performed for bias voltages ranging from 0.5V to 3V, see Figure 4.9. A rise in the bias voltage leads to a lower resonance frequency due to the negative spring effect caused by a higher electrostatic force, as theoretically expected and demonstrated in Equation 2.19. The negative spring effect reduces the total beam stiffness resulting in a lower natural frequency and a rise in the output signal magnitude since a lower stiffness yields a larger displacement.

One concludes, the nominal natural frequency is dependent on the bias voltage applied, and consequently, the stability of the resonator is tied to this voltage. Small variations of the bias reference voltage results on

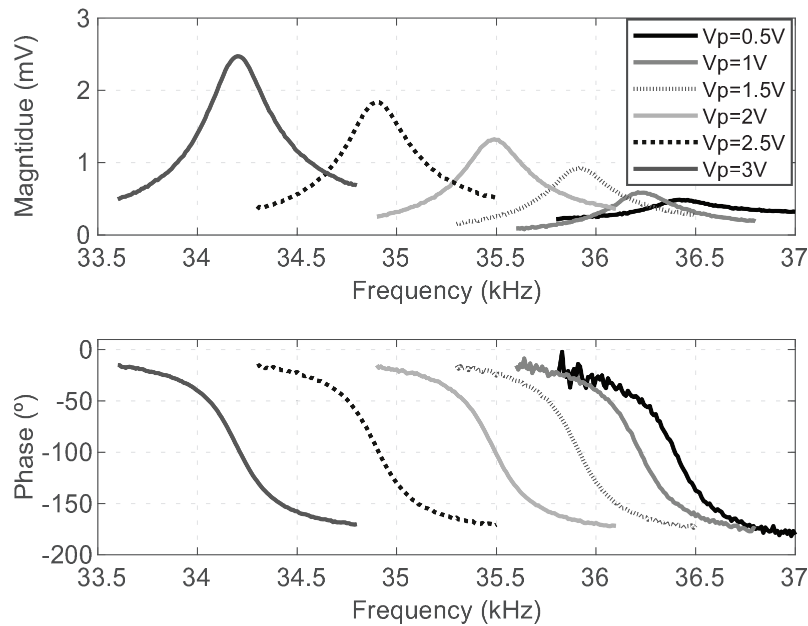

Figure 4.9: Characterisation of the resonator for different bias voltages and a fixed driving voltage of 200mV (sample 3-P02-S1L).

a natural frequency drift, and stable references should be used.

4.2 Accelerometer characterisation

The characterisation of the resonant accelerometer developed along this thesis is described in this section. Three main properties were studied: the response of the sensor to external acceleration, the stability for an extended time and the dependence to temperature. Experimental and theoretical results are shown for a better understanding and validation of the devices' performance.

At this point, the focus is no longer on the resonators but on the resonant accelerometer as a whole. The DETFs are operated in closed-loop using the instrumentation system implemented, and the setup was updated to enable the instrumentation of the physical quantities under study. Once again, the results shown along this section were obtained using samples mounted on soft-glue.

4.2.1 Setup

A setup to perform a thorough characterisation of the accelerometers' performance (e.g. sensitivity and temperature dependence) was built using COTS components. The overview of the test setup and the

different components composing it (except the elements placed outside the climate chamber) are depicted in Figure 4.10. The PCB (where the accelerometer was inserted) is coupled to a rotational motor allowing the change of the angle relative to the gravitational force (see Figure 4.10a) and consequently enabling the characterisation of the sensor in the range [-1g, +1g] (representing a rotation of 180°). The motor (CR1-Z7) and the controller (TDC001) from ThorLabs allow a controllable and stepped rotation with a precision of 7m° [4.2], [4.3]. The support connecting the PCB to the motor and other structural parts were made using 3D printing and laser cutting.

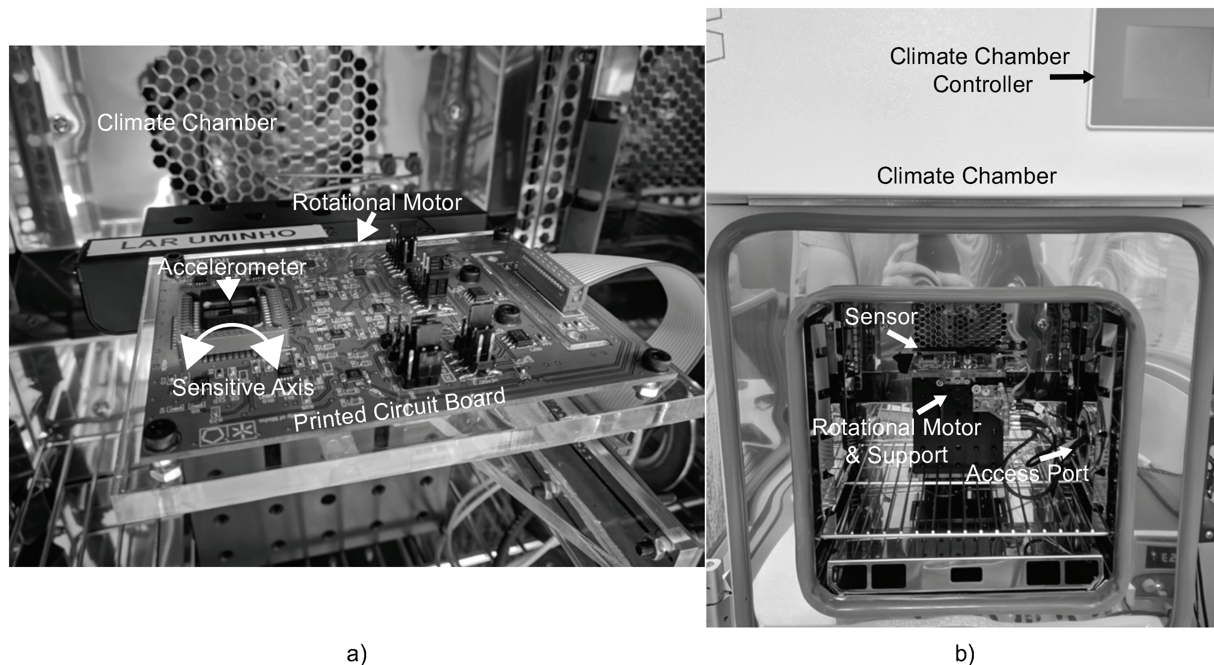

Figure 4.10: Pictures of the setup used to perform the quasi-static characterisation. a) Image of the printed circuit board and the accelerometer inside the climate chamber. b) Overview of the setup from the outside of the climate chamber.

Additionally, the PCB (with the accelerometer, the front-end electronics and the bias voltage reference) was introduced in a climate chamber Weiss WKL 34. The remaining system (lock-in amplifier, power supply, FPGA, acquisition board and computer) were placed outside. The climate chamber enables the control of humidity and temperature, from 10% to 90% and -40°C to +180°C, respectively [4.4].

Both the motor and the climate chamber are controlled by Matlab scripting, allowing test automation, yielding increased result repeatability and precise time-controlled operations.

To perform a dynamic characterisation, the devices were introduced in a test setup constituted by a shaker from Brüel & Kjaer (LDS V406 with the controller LDS COMET USB) capable of generating accelerations up to 100g in a range of frequencies starting from 5 Hz to 2 kHz (the maximum operating frequency is in theory 9 kHz, but only using other controllers) [4.5]. The proprietary software enables the control of the

vibrational platform, allowing several control modes, such as constant accelerations, frequency sweeps or acceleration ramps. The main parts of this test setup are depicted in Figure 4.11. Additionally, a reference accelerometer was also used to calibrate in real-time the vibrations produced by the shaker, and this component is shown in Figure 4.11b.

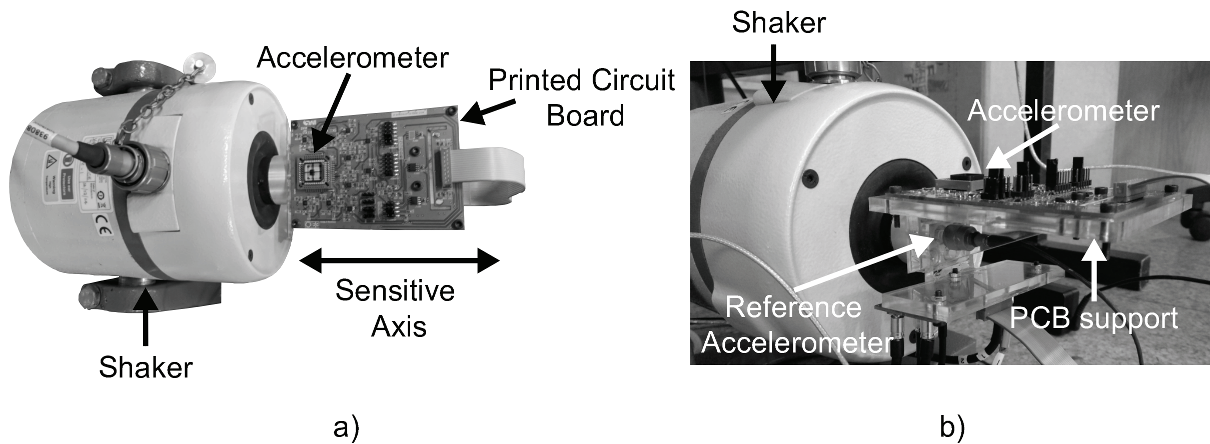

Figure 4.11: Pictures of the setup used to perform the dynamic characterisation. a) Top view of the test setup composed of the shaker. b) Side view of the setup, highlighting the use of a reference accelerometer.

The PCB was aligned with the sensitive axis of the device to be measured and once more, the mechanical parts connecting the shaker to the remaining components were made using fast prototyping tools.

4.2.2 Sensitivity and linearity

The two DETF on the differential configuration were operated in closed-loop, and the rotational motor present on the setup allowed the characterisation for gravitational accelerations in the range [-1 g, +1 g]. In Figure 4.12, the response of the left and right DETF are shown, and a frequency shift close to 80 Hz/g on each resonator is reported. Additionally, the non-linearity measured on both DETF is below 3.7% FS.

In Figure 4.12, it can be observed that the shift in natural frequency of the left and right DETF have trends going in the opposite direction. The resonators are always submitted to forces with different signs, as theoretically expected for the differential architecture designed. Although the objective is reading the differential response of resonators, the system implemented also allows the data of the individual resonators to be saved. From this point, to take maximum benefit of the sensor developed and the differential configuration, the data regarding sensitivity is presented on the differential form ($\Delta f = f_{0Right} - f_{0Left}$).

The rotational motor allows increments of gravitational acceleration in the order of few mg. The response of the sensor was experimentally validated for increments of 10 mg at a rate of 30 sec/step (1kHz sampling

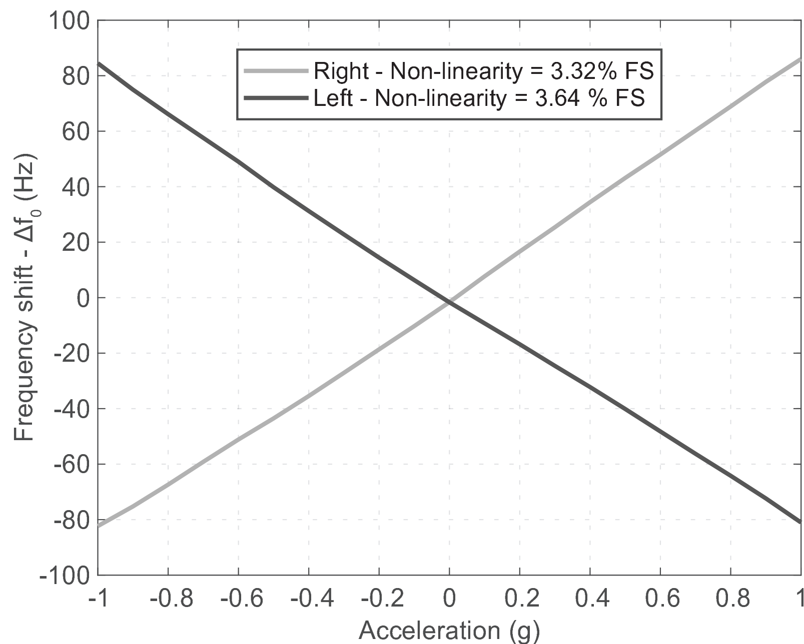

Figure 4.12: Frequency shift on the left and right DETF for accelerations going from -1g to +1g (sample 2-P02-S1).

rate, i.e. 30000 samples/10mg). The differential sensor response was continuously acquired in the specified range, as shown in Figure 4.13.

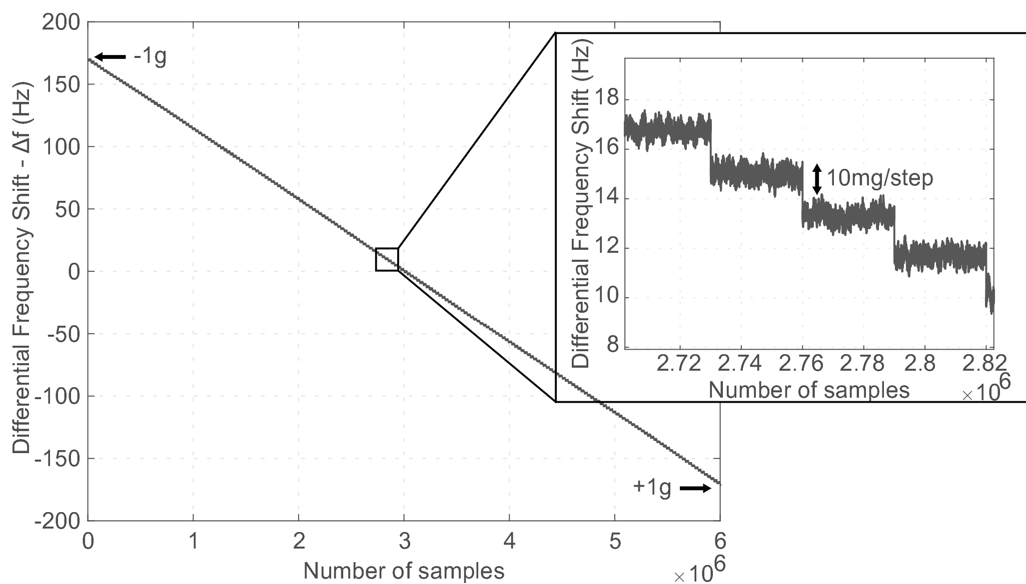

Figure 4.13: Differential frequency shift measured on sample 1-P02-S1 for a gravitational acceleration incremented 10mg/step (V_p=2V, v_a= 250mV).

The experimental sensitivity obtained is about 170.7 Hz/g, 61.4% above the designed value validated using FEM modelling (see Figure 3.6). This is due to the process over-etch during the fabrication, which positively affects the sensitivity since thinner DETF beams result in higher frequency changes, and thinner pivots

and levers increase the force amplification. Furthermore, the electrostatic stiffness was not accounted during the lever optimisation.

Several prototypes were tested for the same conditions, namely, acceleration range, bias and driving voltages of 2V and 300 mV, respectively. An average sensitivity of 163.3 Hz/g was obtained on the five samples tested, see Figure 4.14. The different sensitivities obtained are mainly explained by different process over-etch, and possibly, the alignment of the samples regarding the rotation axis can be different, for instance, the dies were manually mounted on the chip-carrier (no special attention was given to the sample alignment). The maximum sensitivity of 170.7 Hz/g will be accounted for when comparing similar devices in the state-of-the-art.

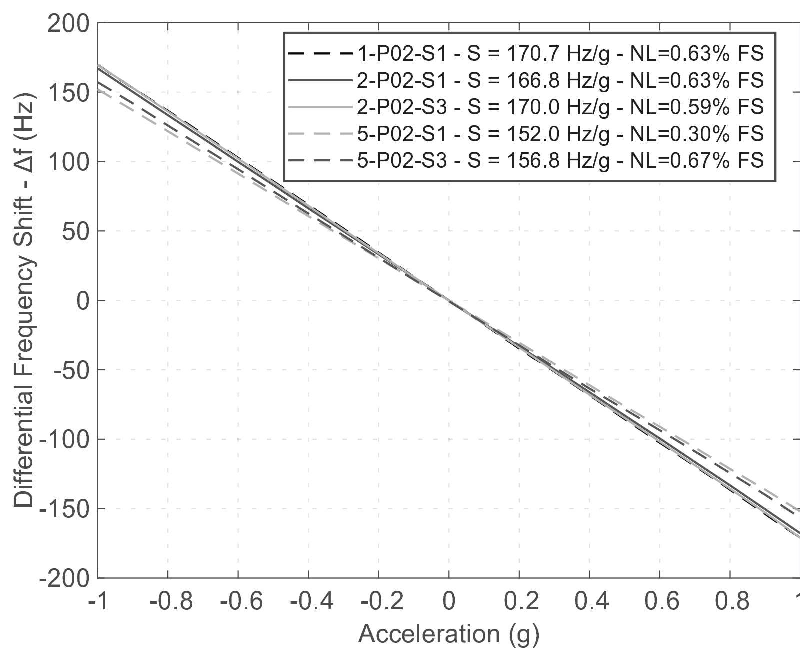

Figure 4.14: Sensitivity (S) and non-linearity (NL) experimentally measured on five samples for a full-scale (FS) of $\pm 1g$.

On the other hand, a median non-linearity of 0.56% FS was experimentally measured, differing from the theoretical value of 0.01% FS. The main reason is, once more, related to misalignments on the packaging or the measurement setup. The perfect alignment of the accelerometer sensitive axis with the parts composing the test setup (motor, PCB, PCB/motor support, among others) is difficult, and misalignment is expected.

If comparing the results shown in Figure 4.12 and 4.14, or in other words, the single DETF response and the differential measurement, one can conclude, the differential approach presents twice the sensitivity, as predicted. Additionally, the non-linearity was reduced from 3.64% FS (left DETF, sample 2-P02-S1)

to 0.63% FS (differential measurement from the same sample). The sensor linearity increased with the differential measurement, as theoretically expected. Unwanted effects such as temperature dependency or mechanical stress are also supposed to be minimised, but these are studied in section 4.2.5 and 4.3.

Furthermore, the sensitivity test was repeated ten times using one of the samples (2-P02-S3) on the same conditions (acceleration range=$\pm 1g$, bias voltage= 2V and driving voltage= 300mV). The repeatability results are presented in Figure 4.15, and the sensor demonstrated an average sensitivity of 170.18 Hz/g with a standard deviation of 0.23 Hz.

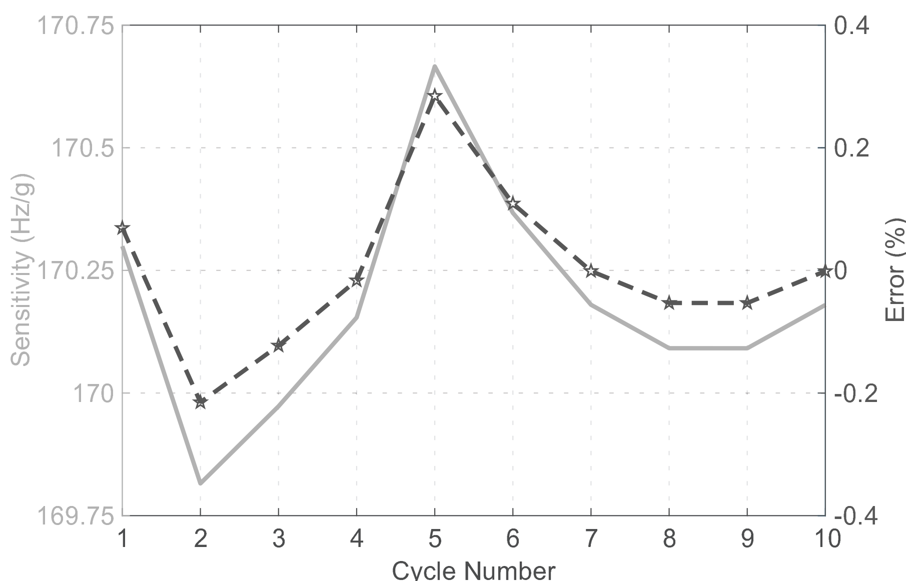

Figure 4.15: Sensor sensitivity obtained during a ten cycle experiment with the purpose of validating the response repeatibility.

The error in relation to the average sensitivity is also shown in Figure 4.15, this parameter is paramount since the same acceleration must always return the same response (or as similar as possible). A maximum error below 0.25% was here experimentally measured. This value of error is small and can be related to the rotation repeatability of the motor used (0.016°, accordingly to the datasheet) or a slight displacement of the measurement setup.

4.2.3 Sensitivity for different AC driving and bias voltages

Previously, the non-linearities originated by the driving and bias voltages, as well as the resonator response for different stimuli were presented. Therefore, since the response of the DETF can undergo a natural frequency shift related to a change in the bias voltage (due to a negative spring constant), a study of the accelerometer sensitivity for different bias is necessary. From the equations introduced in section 2.2.4,

a change in the sensitivity is expected for higher bias voltages, since the spring constant of the beams decreases. The experimental measurement of this effect is evidenced in Figure 4.16 and a quadratic increase of the sensitivity for higher value of V_p is observed. This change in sensitivity is explained in Equation 2.18, the linear electric term of the elastic constant has a square relation with the bias voltage of the DETF.

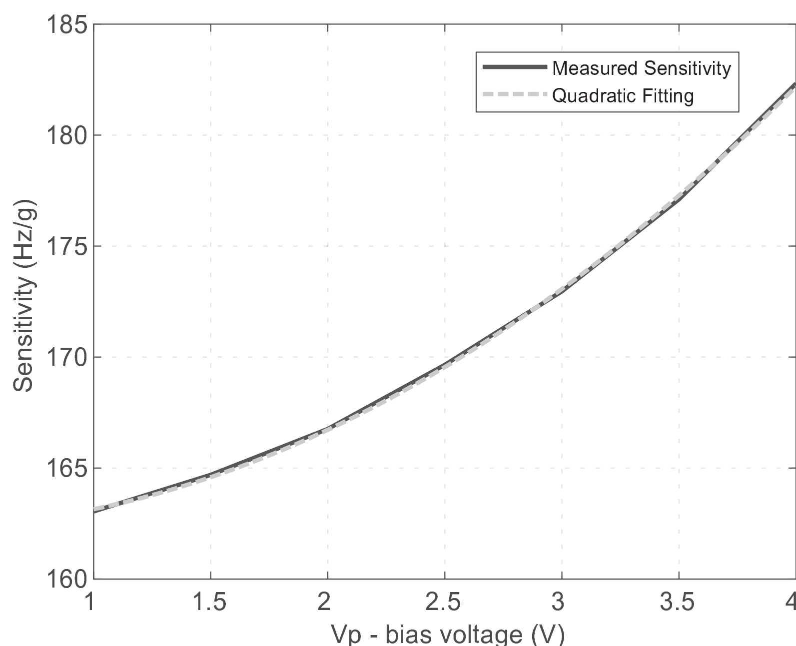

Figure 4.16: Sensitivity experimentally measured on sample 2-P02-S1 for different bias voltages (v_a was maintained constant at 300mV).

From the results obtained, the tuning of the sensor sensitivity can be achieved by applying a different bias voltage, and this can be advantageous to obtain large quantities of samples with similar performance. This tuning can also be used to compensate temperature drifts, in other words, the bias can be adjusted to maintain a constant resonator response over temperature.

The sensitivity rose from 163 to 182.3 Hz/g on the sample tested, representing a tuning capability of more than 11% for bias voltages going from 1 to 4V. Although the samples can be measured for bias voltages up to 4V, most of the characterisation was performed for Vp=2V, to avoid pull-in between the movable and fixed electrodes (damaging the resonator) and because an analog voltage below 2.5V was proposed in the requirements.

In regards to the driving voltage, if non-linearities resulting from larger displacements are observed, this can have an impact on the sensitivity. Nonetheless, as already presented in Figure 4.8, the double-ended tuning forks do not present non-linearities due to driving voltage amplitude in the range [100mV, 400mV].

No sensitivity variation is then expected, and this is confirmed by the experimental results shown in Figure 4.17 (these results were measured on sample 2-P02-S1).

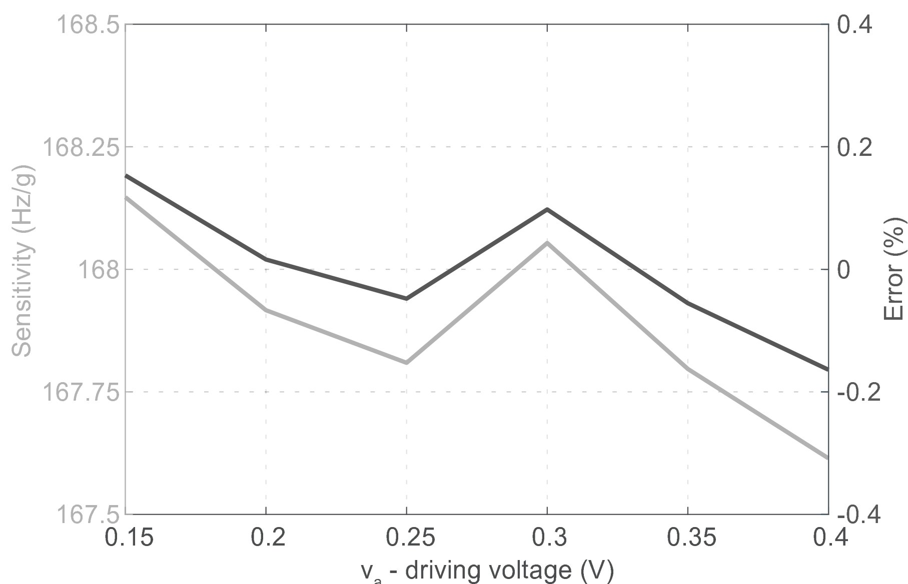

Figure 4.17: Experimental results of the accelerometer sensitivity and error (relatively to the sensitivity average) for different driving voltages (V_p=2V).

.

The slight sensitivity variation observed has a similar error compared to the sensor repeatability tests depicted in Figure 4.15. It can be concluded that the driving voltage does not introduce any sensitivity deviation within the driving voltage range tested, and the small errors are due to repeatability issues.

4.2.4 Cross-axis sensitivity

The devices were designed to be sensitive in a single-axis, and any sensitivity in the remaining axis is unwanted. Although the structures have long and thin features, such as levers, the simulations using a FEM tool retrieved an in-plane sensitivity of 5.4 Hz/g (differential reading) for the Y-axis (90° rotation relatively to the sensitive axis). This represents approximately 5% of the sensitive axis scale-factor. Experimental measurements were performed using a sample rotated 90° relatively to the in-plane sensitive axis (see Figure 3.8). An experimental scale-factor of 10.9 Hz/g was measured, representing 6.7% of the average sensitivity (on the sensitive axis) previously measured (see Figure 4.18). If comparing the cross-axis sensitivity relative to the sensitive axis, experimental and theoretical (6.7% and 5%, respectively), it is possible to conclude that these values are in close agreement.

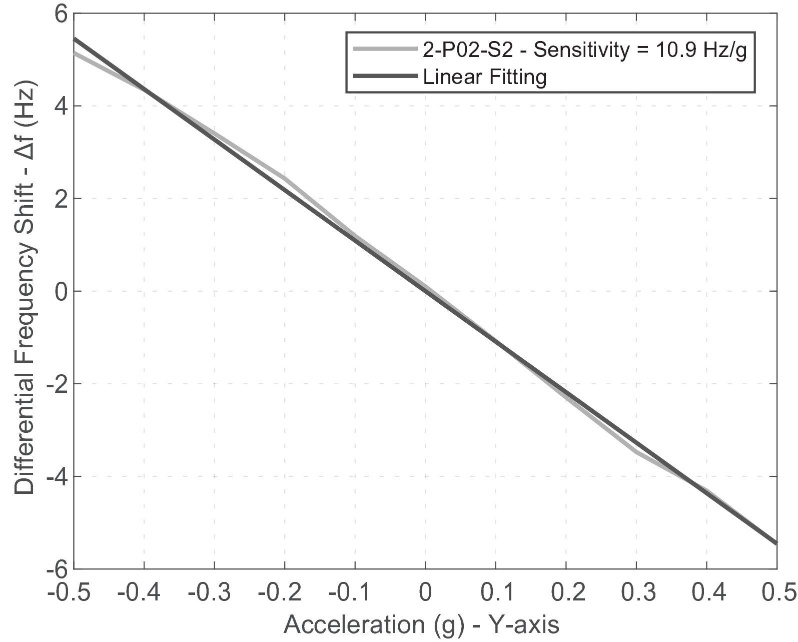

Figure 4.18: Cross-axis sensitivity experimentally measured in the Y-axis (V_p=2V and v_a=300mV).

Part of the mismatch between the theoretical and experimental values are expected to be related to over-etch and setup misalignment. Regarding the over-etch, the influence was already noted in the sensitive axis, naturally, this has also influence on the remaining axis. Regarding the setup misalignments, a small position error increases the experimental values obtained.

Additionally, the sensitivity in the Z-axis (out-of-plane) was simulated but not measured. By interpreting the FEM simulations, the sensitivity in this axis was not linear and only changed a few millihertz. The levers loose force amplification capabilities for out-of-plane movements, being this the primary explanation for this behaviour.

4.2.5 Temperature dependency measurement

Theoretically, both resonators (left and right) should have the same behaviour at different temperatures, but some differences are expected to arise from fabrication process non-uniformities. The FEM simulations demonstrated a decrease of the resonator's natural frequency of 2.53 Hz/°C, and complete elimination of this effect by subtracting the response of both DETF in the differential architecture, see Figure 4.19. This was possible because the left and right DETF have exactly the same response drift over temperature. Note

that the simulations consider the change in the Young's modulus and thermal expansion of silicon (using the values shown in section 2.2.6).

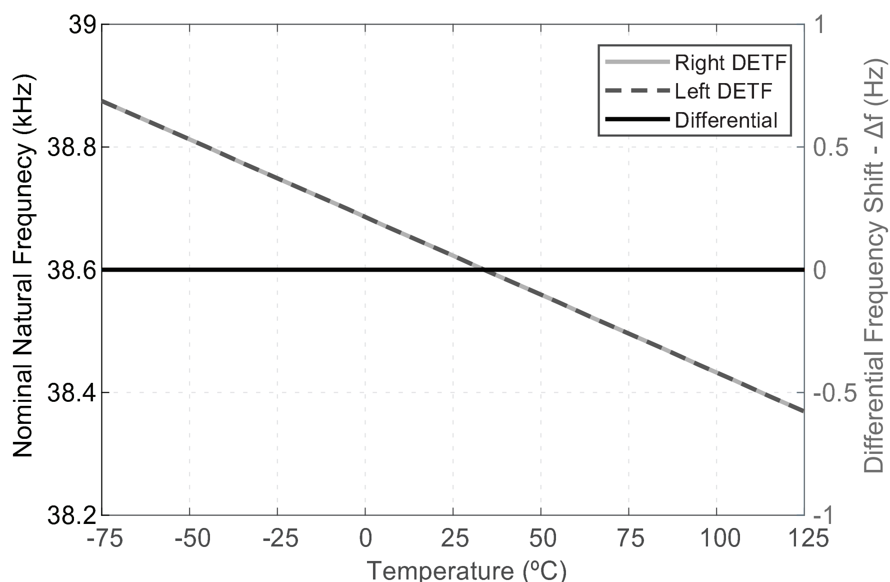

Figure 4.19: Simulated change in the nominal natural frequency of the DETFs over temperature and differential response.

A device was tested inside the climate chamber in a 0 g position and the temperature was stabilised at 70°C for 2 hours. Then the heaters were turned off, letting the temperature decrease naturally. This was done to avoid vibrations resulting from the compressors on the climate chamber, and each test ran for more than 12 hours.

The resonance frequency shift of the resonators was measured, as shown in Figure 4.20. It is shown that the resonance frequency of both DETFs increases with temperature, but at different rates. The frequency response of the resonators should decrease with temperature (Young's modulus decreases with temperature) but the effect measured was in the opposite direction. This is explained by the introduction of tensile stress on the DETF through the anchors, which results from the thermal expansion of the packaging, the main contribution for this effect. Both the magnitude of the temperature drift and the mismatch between the two DETF results were higher than expected, due to this stress coupling. Nevertheless, it is shown that the differential measurement can be used to decrease the response drift of the device from 8.7 Hz/°C (worst case) to 2 Hz/°C, representing a reduction of 77%.

Several solutions were implemented in the state-of-the-art to improve the thermal behaviour, such as the use of an improved packaging method for stress decoupling [4.6], where the die is attached to a stress-immune auxiliary structure, the use of partially glued samples [4.7] and a structure with a single anchor

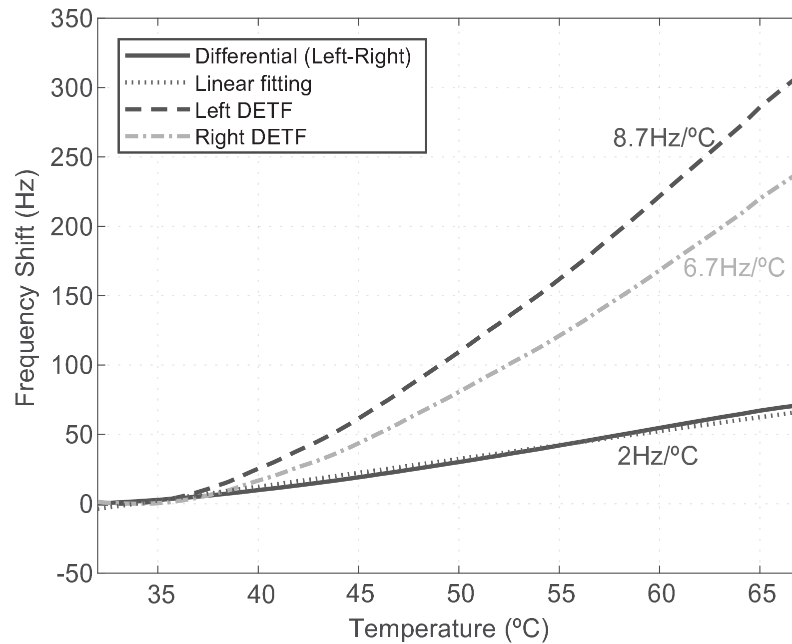

Figure 4.20: Experimental measurement showing the response of the complete sensor but also of the each individual DETF for a temperature going from approximately 30°C to 70°C.

(both DETFs share the same anchor point) [4.8]. All the solutions proposed include additional packaging processes leading to an increase in fabrication costs, being the main drawback of these approaches. The use of a heater close to the accelerometer, to maintain the device at a constant temperature was also presented in [4.8]. Therefore, the heather power consumption and the additional fabrication steps are a disadvantage, since the compensation method leads to higher energy consumption and an increase in fabrication costs. An other solution to decrease the temperature dependency is often performed by adding a temperature sensor close to the accelerometer, correcting the accelerometer response accordingly to the temperature sensed. In this case, since the differential measurement, first shown in Figure 4.20 and further highlighted in Figure 4.21, can be approximated to a linear curve, this solution can be applied. By correcting the response of the accelerometer by 2 Hz/°C, the temperature dependency should be compensated, further reducing the frequency drift and increasing the device long-term stability.

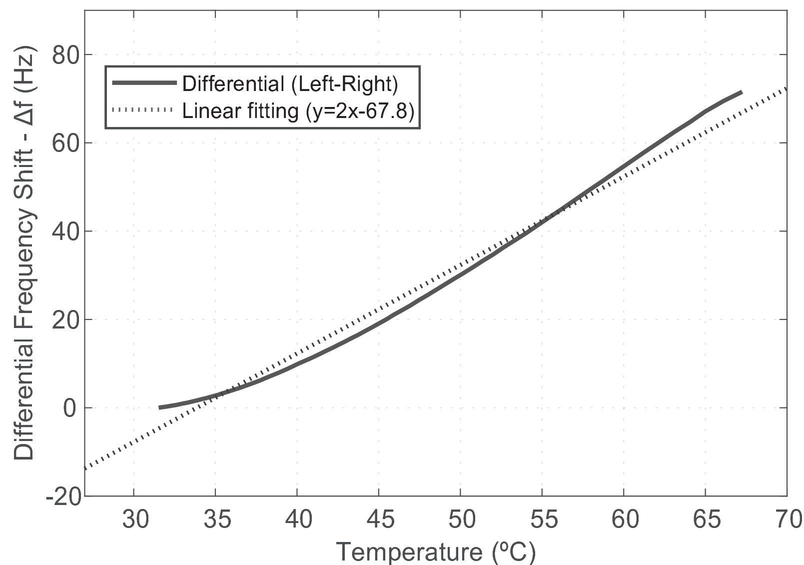

Figure 4.21: Highlight of the experimental frequency shift measured for different temperatures and the linear fit for the same data.

4.2.6 Long-term measurement

The differential frequency shift was measured over 12 hours on a low noise setup site. The temperature was controlled and stabilised around 22.6 °C (to avoid bias instability related to the poor thermal behaviour of the system), this was guaranteed by the climate chamber, and the device was kept in a position close to 0 g relatively to the sensitive axis (manually aligned). The data in Figure 4.22 shows the differential response over time in Hz and its noise floor was calculated. A value of approximately 700 $\mu g/\sqrt{Hz}$ (limit set by the electronic noise) was experimentally measured using the closed-loop approach. The standard deviation of the data measured over the 12 hours is of about 1.8 mg, and the sampling rate was 1 kHz.

The Allan variance for the measurement performed for a period of 12 hours is demonstrated in Figure 4.23. An unexpectedly elevated noise around 1 Hz is observed (away from the typical Allan Variance curves dominated at low frequencies by $1/f$ noise and by Brownian noise at high frequencies). This is believed to be due to the low level of integration of this system, which largely increases the number of possible noise sources, namely the COTS elements used and the subsystem interfaces (for instance, the interface between the FPGA and the lock-in amplifier). More work is necessary to identify the sources of noise and improve the noise performance. Namely, a higher level of integration (implementing the lock-in amplifier on a FPGA for better control) or the use of a different instrumentation topology (e.g. the use of an oscillator circuit) could be approaches to mitigate these limitations.

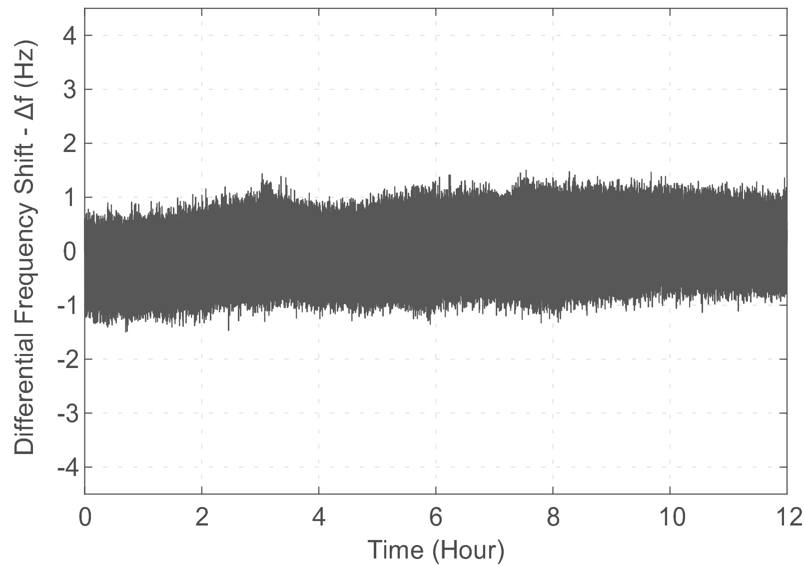

Figure 4.22: Differential Frequency shift measured on sample 2-P02-S1 for a time period of 12 hours (V_p=2V and v_a=300mV)

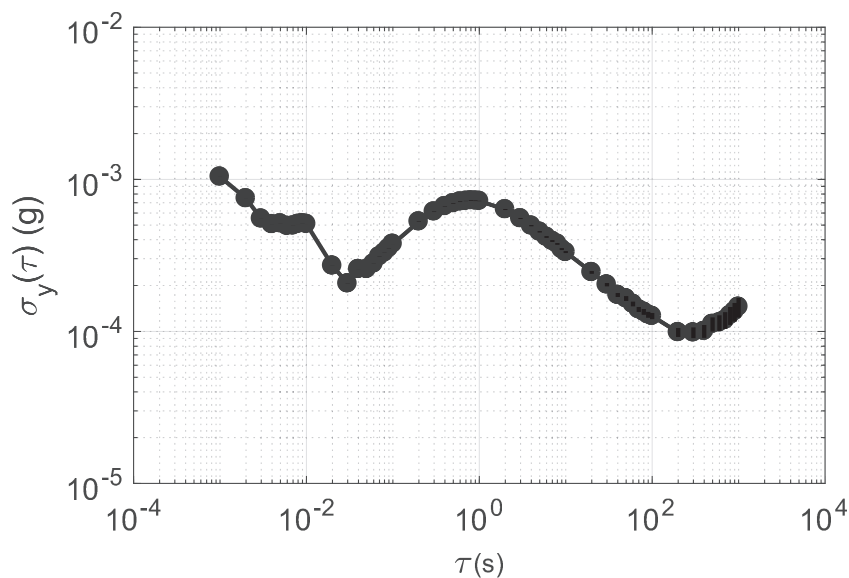

Figure 4.23: Allan Variance plot of the data collected during 12 hours.

4.2.7 Dynamic characterisation

A device was characterised on a vibrational platform, where its dynamic response was accessed. With this purpose, several types of vibration modes were tested together with different acceleration amplitudes. For instance, in Figure 4.24, the experimental measurement of acceleration with a magnitude of $\pm 5g$ at 20 Hz is demonstrated. The response of the right and left resonators were simultaneously measured, showing a behaviour in the opposite direction, as theoretically expected (remembering that both resonators

are never subjected to forces with the same signal, as a result of the device architecture). The differential response has twice the amplitude of the frequency shift of the resonators, experimentally validating the twofold sensitivity of the sensor. The resonators were operated in a closed-loop, to measure in real-time the response of both DETF at 20Hz. The system implemented is capable of preserving a phase shift of 90° between the excitation signal (v_a) and the motional current, even when sinusoidal accelerations with large amplitudes are applied.

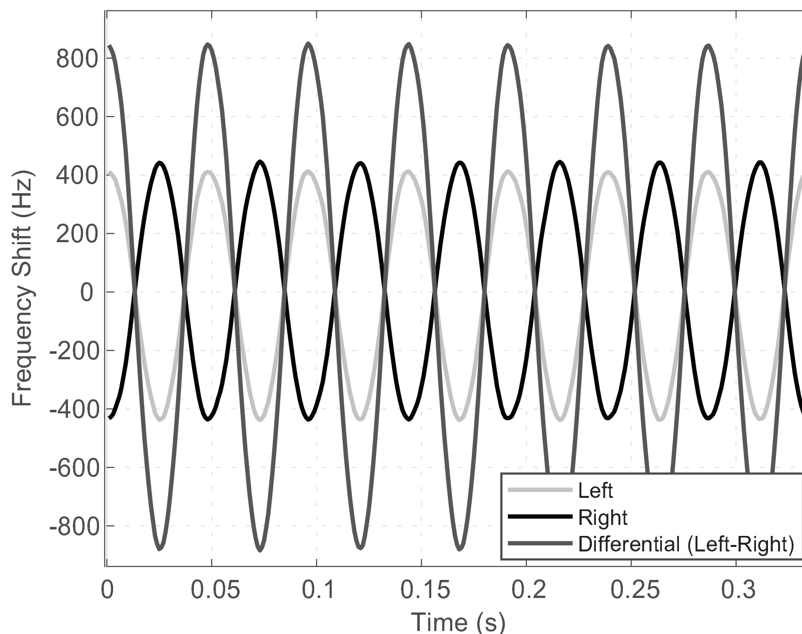

Figure 4.24: Accelerometer (2-P02-S1) response for a sinusoidal acceleration at 20 Hz with an amplitude of $\pm 5g$. The natural frequency of the left and right DETF are also present in the figure.

To evaluate the dynamic response of the accelerometer, the sinusoidal acceleration was continuously incremented from $\pm$ 0.1 g to $\pm$ 5 g with steps of 0.1 g, at 20 Hz. The differential sensor response following these steps is shown in Figure 4.25 and stable behaviour up to the maximum acceleration tested, $\pm$ 5 g is demonstrated.

An acceleration frequency sweep was performed from 20 Hz to 300 Hz with acceleration amplitudes $\pm 1g$, and a bandwidth of 63 Hz was experimentally measured (see Figure 4.26). The difference between the theoretical value of bandwidth calculated (BW=$f_0/2Q$=137 Hz) and the bandwidth experimentally measured is the result of limitations on the implemented closed-loop approach using a phase-locked loop (PLL) available on the lock-in amplifier and a PID controller. In fact, the different PLL parameters (gains and filters) were manually tuned to increase this figure. Experimentally, it was not possible to increase it further

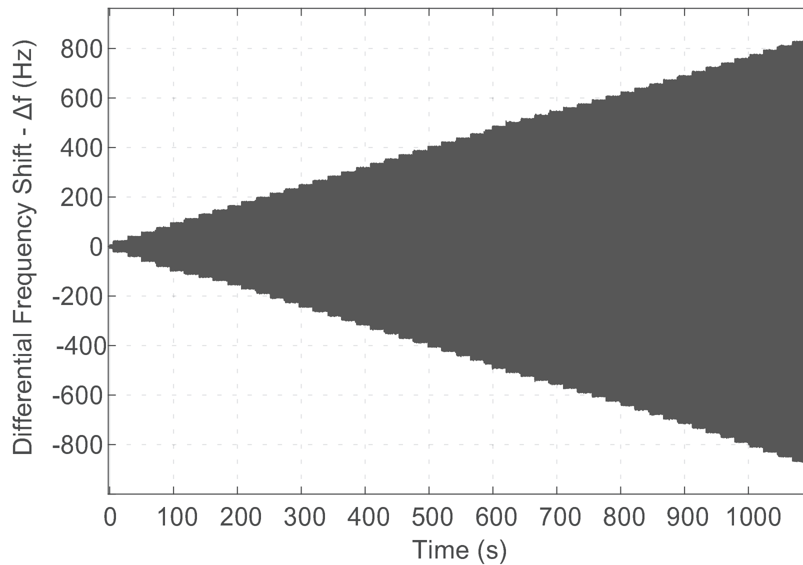

Figure 4.25: Differential sensor response for a sinusoidal acceleration increased from $\pm 0.1g$ up to $\pm 5g$ with increments of 0.1g.

than 63Hz. Additional work needs to be performed to improve this limitation, namely, integrating the lock-in amplifier on the FPGA control system. This would result in a higher control of the different subsystems composing the instrumentation of the accelerometer, and consequently a performance improvement. The proof mass and lever natural frequency is expected to be approximately 1.2 kHz. Since it is well above the bandwidth of the system, it is expected that it is not limiting the system's bandwidth.

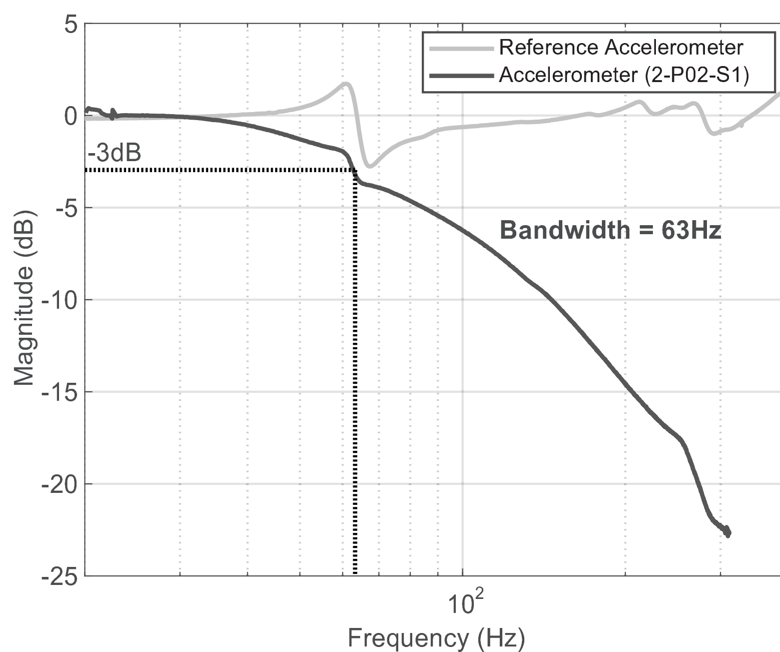

Figure 4.26: Bandwidth experimentally measured and comparison with the reference accelerometer.

The performance of the shaker used during the structure characterisation presented an artefact around 60 Hz, which was monitored by the reference and the designed accelerometer. The artefact is mainly explained by issues on the shaker controller, since the amplitude does not remain stable for the frequency range tested, contrarily to what is supposed. Peaks with several tens of g were detected for higher frequencies, depriving frequency sweeps in specific intervals. The acceleration peak at 60 Hz has different amplitudes on both accelerometers since the acceleration frequency is close to the bandwidth limit of the frequency-modulated accelerometer and the vibration amplitude was already strongly attenuated. A second factor is related to system misalignment. The two accelerometers (reference and frequency modulated) were placed next to each other but were manually mounted. A slight misalignment may have resulted in lower acceleration amplitudes applied to the accelerometer proposed.

4.3 Mechanical stress characterization

The change in the frequency response of a DETF-based resonant accelerometer when an acceleration is applied to its inertial mass was described and posteriorly validated along this thesis. Nonetheless, being a DETF a strain sensor, any force applied to the resonators results in a frequency change. Besides inertia, all the other sources must be minimized to avoid response drifts. The sensitivity to force directly applied to the surroundings of resonators is already used to measure strain, as exemplified in the literature [4.7], [4.9]. The good sensitivity of these sensors validates the high dependency on externally induced mechanical stress.

The dependency to mechanical stress of frequency-modulated accelerometers is often addressed in the literature, but most of the times the solutions to minimise the effect are directed to smart packaging techniques, or the use of soft bonding glues [4.10]. The solutions to decrease the sensor dependency to temperature due to the CTE mismatch are also pointed as useful to minimise stress issues. These are, for instance, the use of a partially glued sample [4.7] or the packaging with auxiliary stress decoupling structure [4.6]. Both rely on a more complex and/or dispendious packaging process. As already described, the accelerometer developed in this thesis was glued to a chip carrier using a soft glue, and stress decoupling trenches were added to the PCB in order to decouple stress. Additionally, it is expected that the differential architecture minimises the stress dependency since the force is likely to be applied in the same direction and amplitude in both DETF of the differential architecture.

Even though, several approaches were used to minimise the force applied to the resonator anchors through other sources than the proof mass. The change in the natural frequency, due to stress induced in the sensor, was noticed during the experimental characterisation. Firstly, the poor thermal behaviour of the device is mainly due to stress from the expansion mismatch between the materials surrounding the accelerometer. Secondly, during the tests performed, a shift in the natural frequency was measured when a force was applied to the surroundings of the accelerometer, for instance, on the PCB carrying the front-end electronics. No specific studies addressing the sensitivity to a force applied on the packaging of a frequency modulated accelerometer were found in the literature, despite the possible drawback of this transduction mechanism.

In this section, the resonant accelerometers were tested for a controlled force applied next to the silicon die. The measurements obtained more insights about the dependency to stress induced mechanically. Additionally, the behaviour of the samples mounted on soft and hard glue are compared, returning information about the effectiveness of this decoupling technique.

4.3.1 Setup

To enable a controlled and measurable force to be applied on the chip carrier containing the prototypes, a force-distance tester was used. The force-distance 925 from Tricor Systems Inc. allows accurate, fast and repeatable testing of distance and force parameters. This COTS instrument is mainly composed by a load-cell measuring the force applied to the sample and by a contact tip. In addition, the motor of the tester moves up and down, changing the load accordingly. The different components used along the testing procedures are highlighted in Figure 4.27.

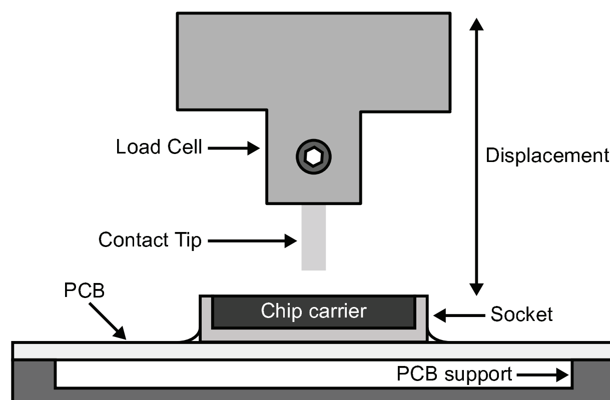

Figure 4.27: Schematic of the test setup used to measure a load applied directly on the chip carrier.

The load-cell mounted on the force-distance tester measures forces from approximately 0.98N to 35.3N. Nonetheless, the maximum load tested here was 14.7N to guarantee the integrity of the components and the repeatability of the measurements. Additionally, a PCB support, with four contact points strategically placed on the extremities, was built to allow the bending of the PCB (see Figure 4.28).

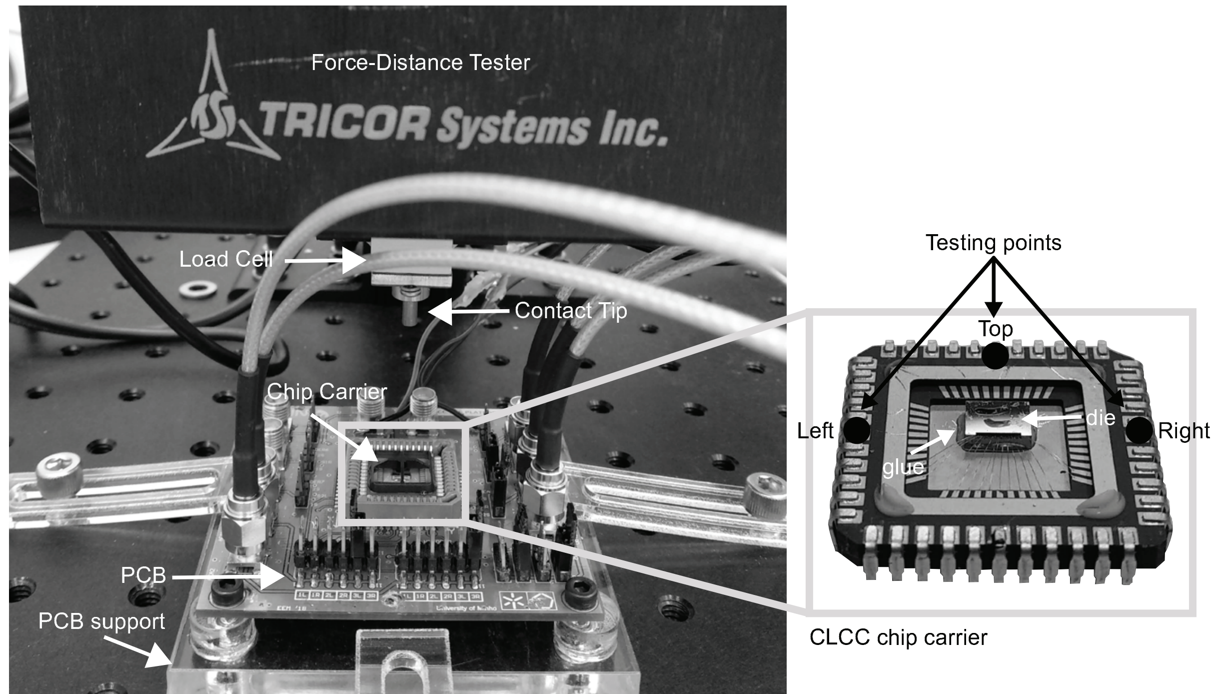

Figure 4.28: Picture of the setup mounted to experimentally measure the response of the accelerometer for a load applied on the chip carrier and mapping of the testing points.

Regarding the test points, three positions (left, right and top) were chosen to proceed with this study. Equidistant positions on different sides of the chip carrier were used to allow a comparison of the decoupling techniques for forces in different directions.

4.3.2 Mechanical stress dependence

It is crucial to mention, the load and the frequency shift experienced by the resonators are measured simultaneously. This allows a complete study of the sensitivity to a load applied on a given point of contact. In Figure 4.29, an accelerometer (HG2-S1, S1 stands for left accelerometer following the same naming convention as previously explained) mounted on hard-glue (HG) was tested for a load up to 14.7N (the glues' parameters were previously reported in Table 3.3). The natural frequency change of the left and right DETF were measured together with the load-cell present in the force-displacement station. A maximum frequency drift of 400 Hz was experimentally obtained on the right DETF (top testing point),

representing a sensitivity of 27.1 Hz/N. However, the differential measurement presents a clear decrease of the sensor drift. In fact, the response was reduced to 4.6 Hz/N, representing a decrease of 83 %. This validates the differential architecture as a suitable approach to decrease the drift due to external stress. Additionally, the sensitivity to stress was not further improved because of the different response on the left and right resonators for the same force. This can be caused by several factors: the DETFs can have different sensitivities to force due to fabrication mismatch, the DETF closer to the testing point can be affected with a higher force amplitude and the force propagation in the silicon die and surroundings can yield different loads on the DETF anchors.

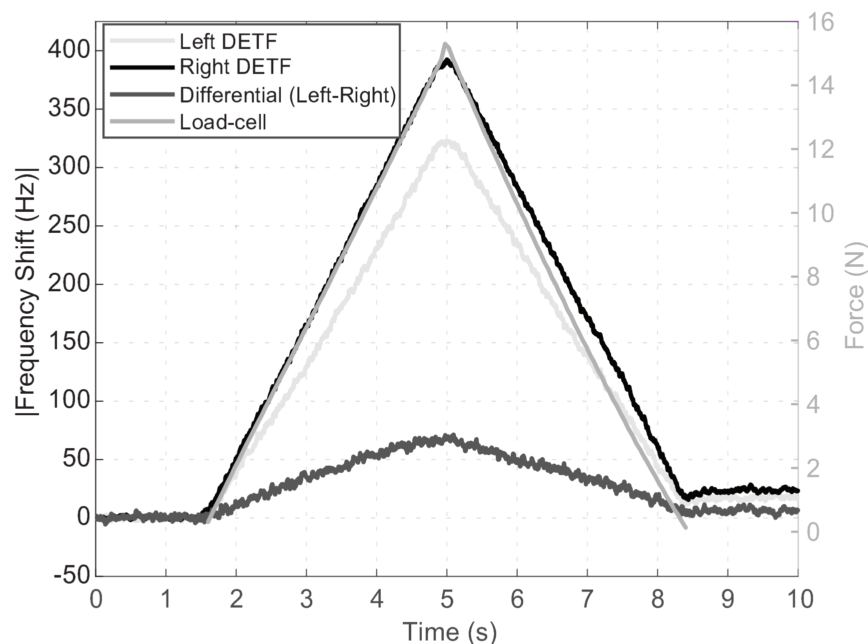

Figure 4.29: Frequency shift experimentally measured for a sample mounted on hard-glue (HG2-S1) undergoing a load up to 14.7 N (V_p=2.5 V, v_a=300 mV).

The last hypothesis was validated using a parametric modal simulation performed on a FEM tool. A force was applied to a face of a die (darker face, see Figure 4.30) containing a single accelerometer and the force angle on the plane XY was swept 360°, as shown in Figure 4.30.

The simulated results show a differential frequency shift dependent on the force angle. This is likely to happen in the die and chip carrier since the different features composing these elements force a load division or a change in the angle in which the stress is applied to the DETF. In other words, the differential reading is more effective for good stress uniformities on the die, while a reduced uniformity increases the sensitivity to stress. In the simulation, a force of 5 mN was applied, far from the 14.7 N employed on the top testing point. Although this simulation is not reflecting the experimental conditions, more rigorous simulations are extremely difficult to be made since the resulting force rely on a large number

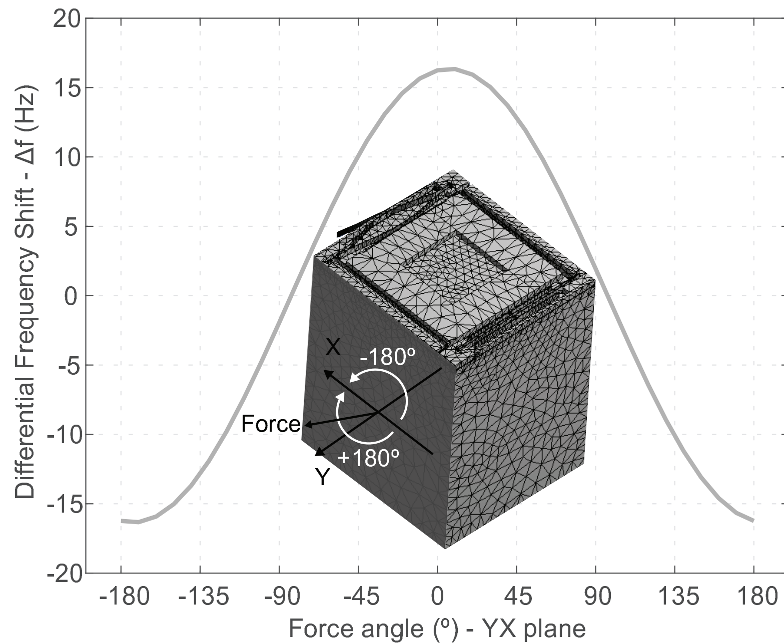

Figure 4.30: Simulated results showing the drift of natural frequency for a force with a given angle applied on the XY plane (Force=5 mN).

of parameters, namely, the Young's modulus of all the materials composing the test setup (mainly: PCB, chip carrier, socket, silicon die), the dimensions of the different parts and the thickness of the glue, among many others.

In order to validate the experiment shown in Figure 4.29, this test was repeated ten times using the same conditions (testing point, force, sample, driving and bias voltages). The standard deviation and average were calculated, showing consistent results (Figure 4.31).

Analysing the last results, a low standard deviation of 1.2 Hz (differential measurement) confirms the setup as suitable to perform these experiments. Additional studies were performed since samples bonded with two different types of glues were provided, and a comparison of the stress sensitivity was possible.

4.3.3 Comparison - soft glue/hard glue

A similar test with the same load, contact point and intrinsic voltages was performed on two samples. One sample was glue to the chip carrier using a soft glue (5-P02-S1), while the second was bonded with a hard glue (H2-S1), and the natural frequency change endured by both was measured (Figure 4.32). The improvement for a single-ended DETF measurement was of about 100 Hz, comparing the left DETF mounted on soft glue and the right DETF on hard glue. Analysing the same resonators, the sensitivity is

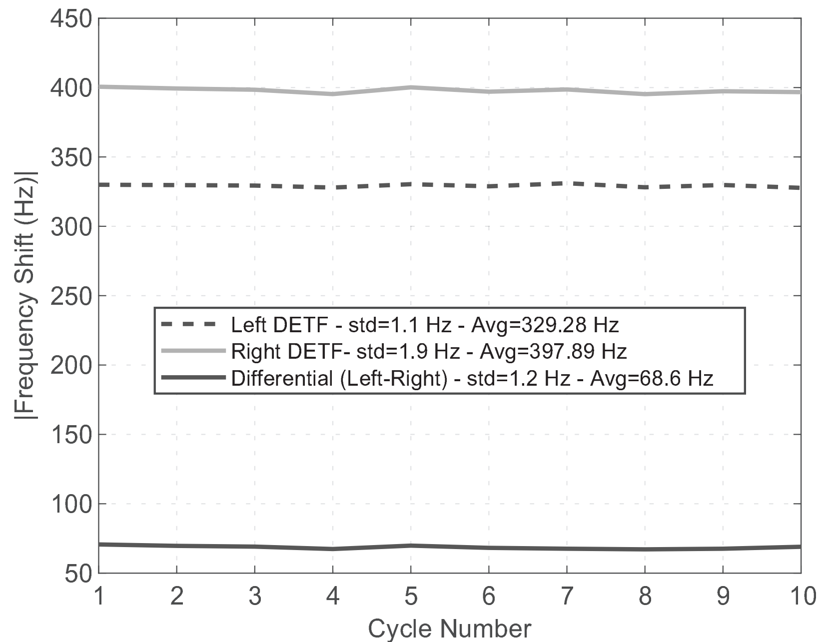

Figure 4.31: Frequency shift experimentally measured ten times for the same conditions. The average (Avg) and standard deviation (std) were calculated to retrieve information about the repeatability.

then decreased from 27.1 Hz/N (left DETF on hard glue sample) to 19.7 Hz/N (left DETF on soft glue sample), representing a decrease of around 27 %. Regarding the differential measurement, the sensitivity of the sensor on soft glue was decreased to approximately 3.6 Hz/N representing a decrease of 22 % in relation to the sensitivity measured on H2-S1. Even if a reduction of the sensor response to stress was experimentally measured and validated, the more significant contribution to this decline is due to the differential measurement and not to glue properties. The soft glue improved the decoupling, although less than expected, since it fails to completely decouple the sample from the surroundings.

Additionally, in Figure 4.32, one can observe that the sample H2-S1 takes time to return to the original response (response before a force was applied). After the force-distance station stops applying load, the sample needs more than 40 seconds to recover from the test. This is explained by the movement of the different hard materials composing the chip carrier, the socket and PCB. These take time to return to the original position (due to the low compliance), and since the accelerometer is strongly tied, it follows this movement. The main advantage of using soft-glue during the packaging is tied to a fast recovery after undergoing a load.

The tests were repeated for the same samples, but this time also on the left and right testing points, see Figure 4.33. Samples mounted on soft-glue always delivered a lower sensitivity to force for single DETF measurements, but the differential reading is related to the difference between the left and right

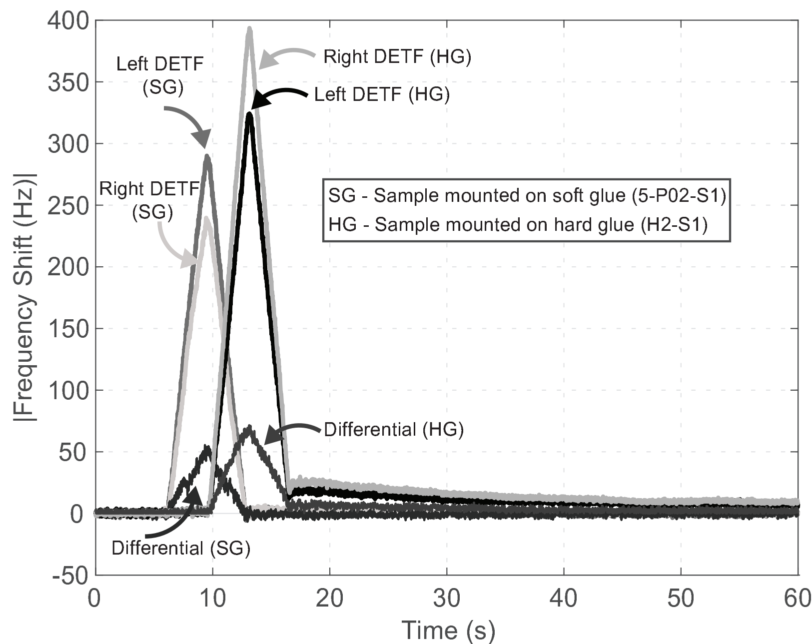

Figure 4.32: Comparison of the frequency drift measured for two samples mounted on two different glues.

resonator response. This explains a higher value of sensitivity for the sample mounted on soft glue tested on the left side, contrarily to what is expected. From this, it is possible to conclude that the differential architecture has more influence on the stress response decrease than the glue, but the effectiveness is strongly vulnerable to the stress uniformity sensed by the DETF present on both accelerometer sides.

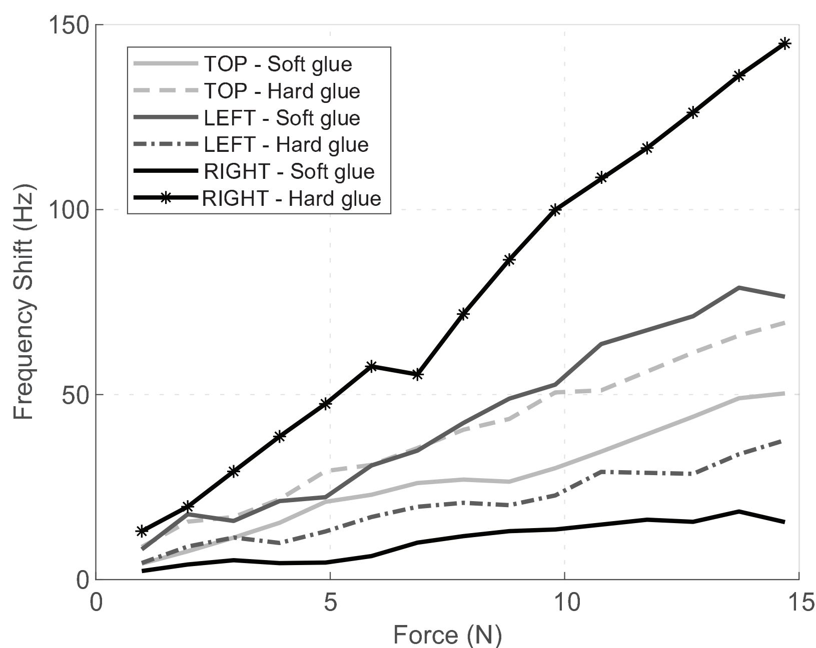

Figure 4.33: Sensitivity measured on three testing points for samples mounted on hard and soft glue.

A possible solution to improve even further the stress decoupling is related to the design of differential structures with a single anchor. In this way, it is expected that force externally applied does not provoke a change of the DETF beams response, since the stress on the die will neither result in tensile or compressive stress on the resonator. Nonetheless, the design of an accelerometer with an amplification mechanism with such restriction can be challenging.

4.3.4 Long-term measurement of a constant force

The measurements shown until this point were performed in few seconds (around 20 seconds), this was the time the force-displacement tester was taking to gradually apply force until reaching the maximum setpoint and relieve it completely (slower force/distance parameters). However, to further study the difference between the bonding glues, the response of the samples was differentially measured when a constant force was applied for more than 100 min. In Figure 4.34, this measurement can be observed, and the two samples presented a different response, mainly explained by the viscoelastic properties of the soft glue (see Table 3.3). The stress relaxation and creeping phenomenons released progressively the stress applied to the sample mounted on soft glue. After 100 minutes, the response of the sample returned to the original value, even with a constant force applied. In opposition, H2-S1 maintained a fairly constant response, since the sample is strongly bonded to the chip carrier.

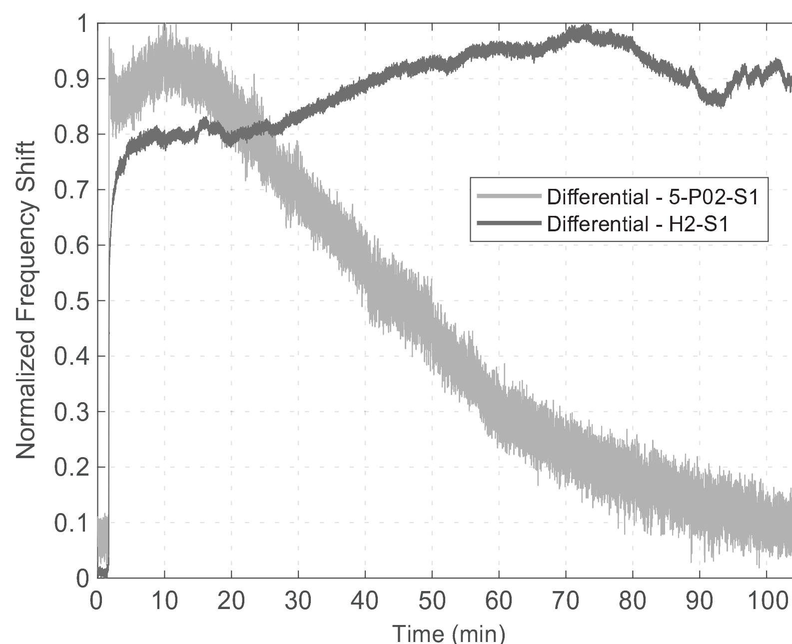

Figure 4.34: Differential frequency shift measured on two samples bonded with two different glues and submitted to a constant force over 100 min.

In fact, as explained in section 3.1.4, the soft glue is made of viscoelastic material (PDMS) and one of the intrinsic characteristics, is that it can behave like a solid or a liquid depending on the time frame. Analysing Figure 4.32 and 4.34, for a faster force change, the glue transmitted almost integrally the stress to the sample (solid behaviour) while the decoupling occurred for longer periods (liquid behaviour). With this, one concludes the use of a soft bonding is more relevant for slow-changing forces applied to the surroundings of the sensor and for fast events, the efficacity is less significant. In this last case, the differential reading was more effective.

4.4 Conclusion

In this chapter, the resonant accelerometer architecture proposed was characterised together with the developed instrumentation system. The first characterisation steps focused on the DETF mechanical properties for different stimuli. An average nominal natural frequency of 35.9 kHz and a quality factor of 121.4 were experimentally measured for ten different resonators. These values were compared with the simulated results, and the differences were mainly due to process over-etch and different encapsulation pressure. Besides, the driving of the resonators at half of the natural frequency showed a strong decoupling between the stray and sensing capacitance.

Regarding one of the major concerns during the design phase, a maximum sensitivity of 170.7 Hz/g was measured for a bias voltage of 2 V. This figure of merit validates the sensor developed as highly sensitive for the footprint dimensions (500 μm x 500 μm). On the other hand, the sensor presented poor thermal stability mainly due to stress resulting from different CTE mismatch. The stress was further studied, and two samples (one mounted on soft glue and another on hard glue) were characterised to understand the efficacity of the stress decoupling techniques implemented (differential architecture, soft glue bonding). From these tests, it is possible to conclude that the stress uniformity is instrumental for complete stress compensation through a differential measurement. In addition, packaging with soft glue proved to be effective for slow changing forces. A proper understanding of these effects was necessary for future design improvements, justifying the thorough characterisation.

Additionally, a bandwidth of 63 Hz was measured. The value is half of the theoretical DETF bandwidth and is explained by closed-loop limitations resulting from the fast prototype system and lock-in amplifier. To improve this figure of merit and the noise figure, higher integration is required. Several subsystems can not be controlled, contributing to undesirable effects. Although not mentioned in this the chapter, all

the lock-in properties, such as different gains (e.g. PLL, analog outputs), filters values, among others, were maintained constant for all the tests performed. The same is true for the PID gains used (K_p=0.25, K_i=0 and K_d=0) and these were manually tuned. A complete characterisation of the gains influence on the sensor behaviour was not performed since these are dependent on the different lock-in properties and subsystems.

The resonant accelerometer proposed along this thesis shows promising performance in several domains and integration capabilities within the same capsule with other sensors fabricated at our partner (encapsulated in vacuum). Nonetheless, further design work is necessary to improve the bias stability of the sensor, mainly influenced by the thermal behaviour and high sensitivity to mechanical stress. Additionally, the development of a more integrated instrumentation system would be beneficial.

References

[4.1] V. Lindroos, M. Tilli, A. Lehto, T. Motooka, and T. Veijola, "Handbook of silicon based MEMS materials and technologies", Micro & Nano Technologies Series, 2010. doi: 10.1016/B978-0-8155-1594-4.00014-0.

[4.2] THORLABS, PRMTZ8 - Motorized Precision Rotation Stage: User Guide, 2018.

[4.3] Thorlabs, CR1-Z7, CR1/M-Z7 - Motorized Rotation Stage: Operating Manual, 2017.

[4.4] Weiss Technik, Technical Description - Laboratory Climate Test Chamber System Weiss - Type WKL 34/70.

[4.5] Brüel & Kjær, Product Data - LDS V406 and V408 Shakers, 2012.

[4.6] Y. Yin, Z. Fang, Y. Liu, and F. Han, "Temperature-Insensitive Structure Design of Micromachined Resonant Accelerometers", Sensors, vol. 19, no. 7, p. 1544, Mar. 2019. doi: 10.3390/s19071544.

[4.7] C. D. Do, A. Erbes, J. Yan, K. Soga, and A. A. Seshia, "Vacuum Packaged Low-Power Resonant MEMS Strain Sensor", Journal of Microelectromechanical Systems, vol. 25, no. 5, pp. 851–858, 2016. doi: 10.1109/JMEMS.2016.2587867.

[4.8] D. D. Shin, Y. Chen, I. B. Flader, and T. W. Kenny, "Epitaxially encapsulated resonant accelerometer with an on-chip micro-oven", in 2017 19th International Conference on Solid-State Sensors, Actuators and Microsystems (TRANSDUCERS), IEEE, Jun. 2017, pp. 595–598. doi: 10.1109/TRANSDUCERS.2017.7994119.

[4.9] L. Belsito, M. Ferri, F. Mancarella, L. Masini, J. Yan, A. A. Seshia, K. Soga, and A. Roncaglia, "Fabrication of high-resolution strain sensors based on wafer-level vacuum packaged MEMS resonators", Sensors and Actuators A: Physical, vol. 239, pp. 90–101, Mar. 2016. doi: 10.1016/j.sna.2016.01.006.

[4.10] K. E. Wojciechowski, "Electronics for Resonant Sensors", PhD thesis, University of California, Berkeley, 2005, p. 149.

Chapter 5

DETF-based magnetometer

The measurement of the magnetic field has always been important for humanity since it enables the analysis and control of distinct operations [5.1]. The list of uses-cases is vast, and some examples include the reading of magnetic storage disks and tapes [5.1], position sensing [5.1], [5.2], mineral prospection or even brain function mapping [5.2]. Despite the different technologies available, in the past few years, MEMS magnetometers have been proposed due to several advantages, mostly related to monolithic integration with other MEMS sensors. Based on the knowledge of the DETF resonators developed and fabricated during this thesis and in the simulation tools presented in Chapter 3, a DETF-based magnetometer prototype was developed and fabricated. The monolithic integration of a MEMS magnetometer on the same silicon die of sensors composing a IMU (accelerometer and gyroscope) and encapsulated at the same pressure is advantageous to decrease fabrication costs. Additionally, the development of a DETF-based magnetic sensor validates the used of these resonators to access different physical quantities. The prototype is compatible with standard MEMS processes and was designed to sense out-of-plane (Z-axis) magnetic field.

In this chapter, the focus is on the design, implementation and characterisation of a frequency-modulated MEMS magnetometer based on DETF resonators. The chapter starts with a brief introduction and a description of the state-of-the-art regarding magnetometers, followed by a in-depth discussion of the magnetic sensor proposed.

5.1 Introduction

Nowadays, magnetic field sensors are found in different applications, namely, automotive, consumer electronics, aerospace, military, among others. Magnetometers are used to measure the rotational orientation

of an object irrespective to the Earth's magnetic field (compass), and this can be particularly useful to improve inertial navigation systems [5.3]. In the automotive industry, besides the vast interest in autonomous driving and navigation applications, magnetic sensors can be found to detect the position of the engine crankshaft [5.1] and steering wheel [5.4].

Different technologies are available to produce devices capable of magnetic field sensing, such as hall-effect, anisotropic magneto resistance (AMR), tunneling magneto resistance (TMR), giant magneto resistance (GMR), fluxgate and superconducting quantum interference device (SQUID). These have different properties, namely, range, sensitivity and cost, making them more or less suitable for a given application. Bellow, a brief description of the technologies mentioned above is given:

- **Hall effect** sensors measure the voltage difference transverse to a current-carrying electrical conductor. This effect is small in metallic conductors, while semiconductors yield a stronger effect [5.1]. Hall sensors are inexpensive, compatible with complementary metal–oxide–semiconductor (CMOS) technology and benefit from a large dynamic range, contributing for an important popularity. However, a poor resolution is described as one of the main drawbacks of this approach [5.5].
- **AMR, TMR, GMR** are all magnetoresistive sensors. In other words, the electrical resistivity variation caused by a magnetic field is exploited. These sensors are attractive because of reduced size, good resolution, compatibility with CMOS and simple operation principle (for a fixed current, the voltage changes proportionally to the external magnetic field). The drawbacks of these sensors are usually related to a high DC offset, significant temperature dependence and hysteresis [5.1], [5.6].
- **Fluxgate** sensors are composed of two coils (drive and sense) and a ferromagnetic material. The principle of magnetic induction, together with the saturation of ferromagnetic materials at high fields, is used as the transduction mechanism [5.1]. The main benefits are the capability to operate in harsh environments, while a complex construction is the main disadvantage [5.7].
- **SQUID** sensors exploit the interaction of electric current and magnetic fields in materials at very low temperatures [5.1]. These sensors were reported as very sensitive since magnetic fields down to the femtotesla range can be assessed. However, cryogenic cooling and other sophisticated equipment are required, resulting in size and complexity increase [5.8].

Many other technologies were approached in the literature to measure the magnetic field but for the sake of simplicity, these will not be further addressed. The focus here will be on MEMS magnetometers.

5.1.1 MEMS magnetometers

MEMS magnetometers have been investigated due to several advantages mainly related to the MEMS technology itself. As previously mentioned, batch fabrication of identical devices reduces fabrication costs and enables new applications. Low-weight and low-power consumption are also usually reported. But, one of the main interest in MEMS magnetometers regards monolithic integration with inertial sensors. This would result in a multi-degree of freedom IMU fabricated in the same silicon die, yielding a meaningful size and cost reduction. These benefits are mainly due to a straightforward packaging/integration process since the stacking of sensors is avoided [5.9]. In the case of a monolithic IMU, an almost a perfect alignment between accelerometers, gyroscopes and magnetometer is guaranteed at the fabrication level, avoiding alignment and calibration procedures. A better sensor alignment would also result in a precision improvement [5.10]. Apart from IMU, any system composed of several MEMS sensors can benefit from the same advantages related to integration.

To create magnetometers based on MEMS technology, several approaches can be found in the literature. An earlier design used electrodeposited ferromagnetic layers on top of a silicon structure, and the torsion of two beams was monitored [5.11]. Nevertheless, all the devices using ferromagnetic components are not compatible with standard silicon micromachining process used for MEMS. In the other hand, Lorentz-force based magnetometers are fully compatible with standard fabrication processes, and this approach is the most common in the literature. These devices measure the Lorentz force produced by a current-carrying silicon beam in the presence of an external magnetic field. The force yields the movement of a released device, and optical, capacitive and piezoresistive transduction can be employed to measure the displacement/force [5.12].

Focusing on capacitive transduction, by driving the devices at the mechanical resonance, and taking profit of high quality factors due to encapsulation at low-pressures, the displacement is increased. In capacitive MEMS magnetometers, a greater displacement represents a larger capacitance change, and consequently a higher sensitivity and resolution. A device with a sensitivity of 24.4 pF/T, a resolution of 17 $nT/\sqrt{Hz}$ and a bandwidth of 1.9 Hz was reported for out-of-plane sensing [5.13]. The sensor is encapsulated at 1Pa and has a quality factor close to 12700. The same device can measure the magnetic field in three-axis, showing a sensitivity of 17.44 pF/T and 9.28 pF/T on the X and Y axis, respectively. Higher sensitivities are obtained at the expense of lower bandwidth, because of a larger quality factor, using this principle. Off-resonance operation was presented in [5.14] and [5.15] to overcome this limitation. The off-ressonance is based on driving the devices at a frequency slightly lower than the natural frequency, and by doing this,

the bandwidth increases at the expense of lower sensitivity (quality factor decreases). Devices showing a resolution of $360\ nT/\sqrt{Hz}$ and $160\ nT.mA/\sqrt{Hz}$, and a bandwidth of 38 Hz and 200 Hz were demonstrated in [5.14] and [5.15], respectively, using off-resonance operation.

Two other principles were presented to amplify the quality factor reducing the available bandwidth, such as parametric [5.16] and thermal piezoresistive amplification [5.8]. This second approach yielded the device with the highest resolution reported in state-of-the-art ($2.76\ pT/\sqrt{Hz}$). The reported bandwidth of the device is 0.34 Hz.

In table 5.1, a summary of the most relevant research works based on amplitude-modulated MEMS magnetometers are presented. These sensors are referred, in this thesis, as amplitude-modulated since a larger displacement results in an increased voltage output proportional to the external magnetic field.

Work	Axis	Resolution (nT/Hz)	Bandwidth (Hz)	Measurement Range ($\pm mT$)	Pressure (Pa)	Device Size (mm^2)
[5.13]	3-axis	17 (Z-axis)	1.9 (Z-axis)	0.4	1	4
[5.14]	Z-axis	360	38	0.4	-	-
[5.15]	Z-axis	160*	>200	6	25	0.165
[5.16]	Z-axis	87	1	180	100000	2.1*1
[5.8]	Z-axis	0.0028	0.34	3.5×10^{-6}	100000	1.17*1

* nT.mA/$\sqrt{Hz}$.
*1 Measured from device's pictures.

Table 5.1: Comparison of amplitude-modulated MEMS magnetometers present in the state-of-the-art.

5.1.2 Frequency-modulated MEMS magnetometers

Despite being uncommon in the literature, frequency-modulated MEMS magnetometers working principle consists of measuring the change in the natural frequency of a resonator when an axial force is applied. This tension is the result of a Lorentz force, and the frequency response is proportional to the magnetic field. Several advantages were reported, such as no trade-off between quality factor and bandwidth (in opposition with amplitude modulate magnetometers), large dynamic range and a good resolution [5.17] (related to the resonator characteristics [5.5]).

A device composed of two Lorentz force transducers producing force in the opposite direction, and directly tied to beam springs to a shuttle structure was presented in [5.2]. The device natural frequency changes due to strain applied to the shuttle. A maximum sensitivity of 87.9 Hz/T, a natural frequency of 26.986 kHz

and a measurement range of $\pm 25\ mT$ were demonstrated. Additionally, a different device using a single-beam resonator coupled to a force amplification mechanism (a lever to multiply the Lorentz-force), yielded a sensitivity of 591 Hz/T (measurement range $\pm 66\ mT$) [5.17]. Once more validating the use of levers to increase the sensitivity of resonators. A DETF-based magnetometer with two Lorentz-force transducers attached directly to the extremities of the resonator was also presented [5.5]. This sensor has the smallest sensitivity (10.6 Hz/T) but the highest measurement range ($\pm 100\ mT$). Since the resolution of these sensors is still far from the one obtained on amplitude-modulated devices, the emphasis of Table 5.2 goes to the measurement range (one of the main advantages of this approach), bias current (to produce Lorentz-force) and device size.

Work	[5.2]	[5.17]	[5.5]
Axis	Z-axis	Z-axis	Z-axis
Natural Frequency (kHz)	26.986	21.9	49.3
Quality factor	17000	540	100000
Sensitivity (Hz/T)	87.9	591	10.6
Measurement Range ($\pm$mT)	25	66	100
Bias Current (mA)	10 (DC)	4 (DC)	10 (DC)
Pressure (Pa)	2	-	0.67
Device Size (mm^2)	0.21	0.82	0.36*

* Measured from device's pictures.

Table 5.2: Main frequency-modulated MEMS magnetometers available in the literature.

Analysing Table 5.1 and 5.2, the higher measurement range and smaller device size are confirmed as one of the main advantages of frequency-modulated over amplitude-modulated devices. No clear reference to sensor's bandwidth was presented for the frequency-modulated devices, depriving an accurate comparison.

5.2 Magnetometer design

The different development steps required to design a frequency-modulated MEMS magnetometer composed of DETF resonators and based on Lorentz-force transduction are described in this section. A brief theoretical introduction of the Lorentz-force is also performed.

Besides all the advantages of frequency-modulated sensors, the development of a magnetometer based on DETF resonators is related to the previous research presented since the models and instrumentation system can be reused.

5.2.1 Lorentz-force transducer

A charged particle moving on a conductive medium and exposed to a magnetic field experiences a force called Lorentz-force. In MEMS, this force is produced in current-carrying beams in the presence of an external magnetic field, and the resulting force or displacement can be monitored using different transduction mechanisms. Considering a current-carrying beam, the force ($F_{Lorentz}$) can be calculated using:

$$F_{Lorentz} = I_{bias} \times L_{beam} \times B_{magnetic} \tag{5.1}$$

where I_{bias} is the bias current, L_{beam} the length of the beam and $B_{magnetic}$ the magnetic field. From the equation above, a larger force results either from a larger current, beam length (L_{beam}) and/or magnetic field ($B_{magnetic}$). Nonetheless, high currents produce a temperature increase, large power consumption and may result in structure damages. Longer beams yield larger devices and an electrical resistivity increase (more power consumption and heat by Joule effect). To obtain a maximum force, and consequently, a higher device sensitivity on a small footprint, a trade-off must be found regarding these two parameters.

The Lorentz-force is perpendicular to the flowing current and the field direction [5.1]. Considering a current flowing always in the same direction, the Lorentz-force component changes accordingly to the magnetic field orientation, as shown in Figure 5.1. Considering only an out-of-plane magnetic-field, a bidirectional measurement is enabled since a change in the magnetic field orientation result in a different force direction.

5.2.2 Device operating principle

As previously explained, a resulting Lorentz-force induces a stiffness change in the DETF beams and thus a frequency change that is proportional to the external magnetic field. Since the force can be either positive or negative accordingly to the direction of the field and that DETF resonators measure tensile and compressive forces, bi-directional sensing is available. Nonetheless, the use of a DETF and a Lorentz force transducer is challenging because of the high axial stiffness of the DETF and the low elastic constant of the

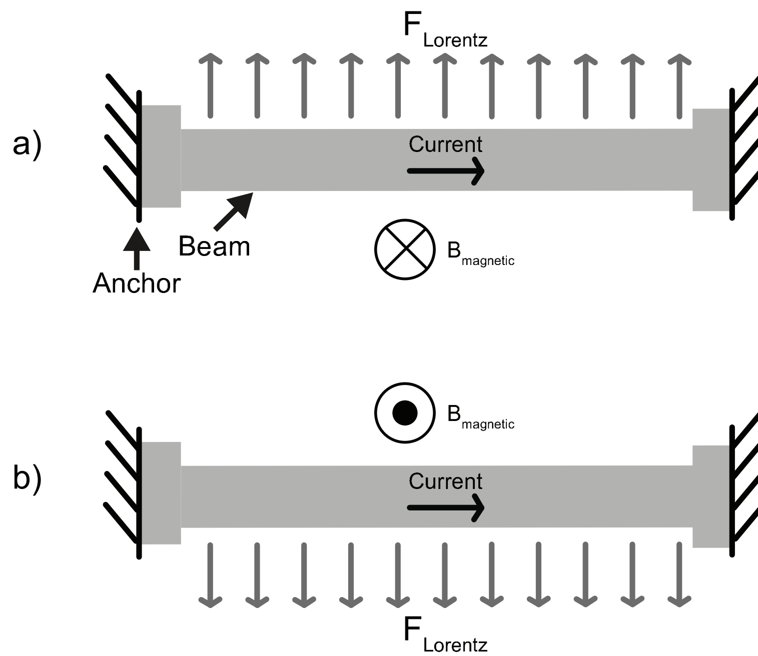

Figure 5.1: Schematics a) and b) show the Lorentz-Force direction regarding the magnetic field orientation.

Lorentz bar (these are usually thin and long to yield larger displacement). In such conditions, the different stifnesses jeopardise the force coupling between the DETF and the Lorentz-force transducer.

A study of different transducers was made to maximise the force transfer, and as a result, improve the device sensitivity. A maximum axial force must be applied to the DETF to achieve such requirement. A design composed of a vertically aligned diamond-like shaped Lorentz force transducer directly coupled to a DETF is proposed in Figure 5.2. Note that two vertical beams form each transducer.

This design transpose the distributed Lorentz force to an axial force to be applied at the extremity of the DETF. This axial force can be compressive (Figure 5.2a) or tensile (Figure 5.2b) accordingly to the magnetic field orientation. The Lorentz-bar is shaped in a diamond-like format since it was found (using FEM simulation) that this geometry resulted in a higher axial force and a higher device sensitivity, in comparison to other shapes simulated (e.g round beams, beams with several folds, levers connected to lorentz-force bars, among others). An optimisation of the Lorentz bar shape and features' dimensions was performed using parametric design linked with a FEM tool to guarantee a high sensitivity to the external magnetic field, but this will be further discussed in section 5.3.1.

Despite not presented in the schematic of Figure 5.2, the DETF configuration and electrical connections are the same as the ones previously used on the accelerometer (see Figure 2.6).

In the final design, a differential configuration was implemented to double the sensitivity and reduce

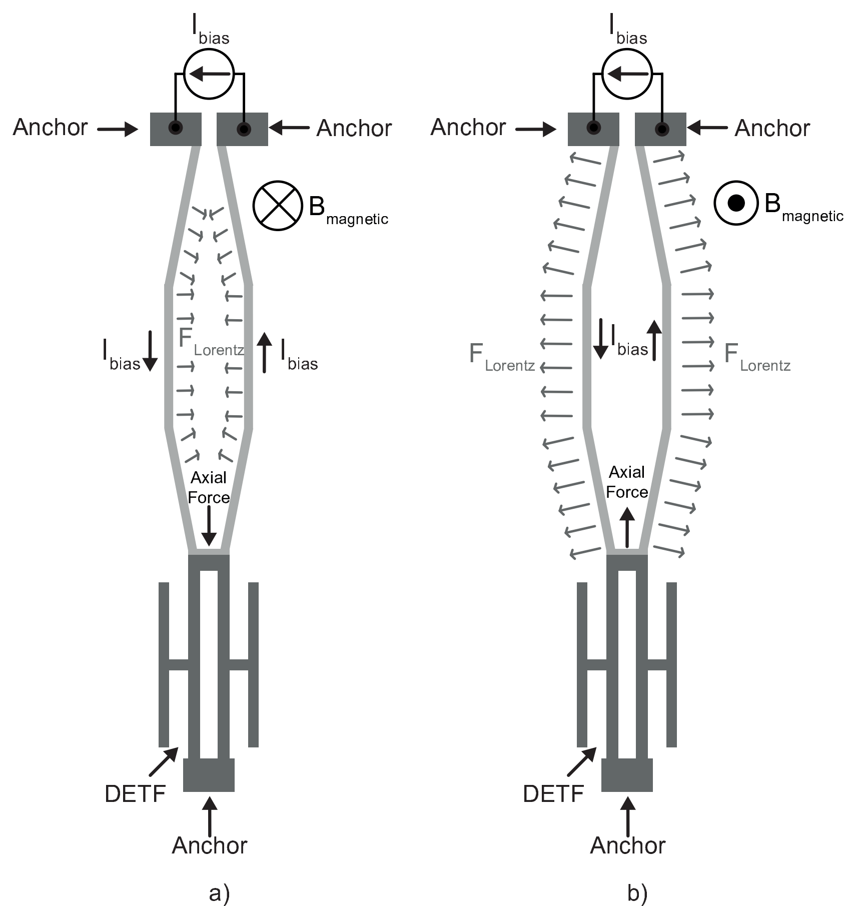

Figure 5.2: Magnetometer composed of a diamond-shaped Lorentz-force transducer coupled directly to a DETF. The Lorentz and axial forces are represented in a) and b) for magnetic field in opposite direction.

common-mode errors (i.e. temperature dependency). The differential configuration is composed of two DETF resonators and two Lorentz force transducers, as depicted in Figure 5.3.

The two diamond-shape Lorentz-force transducers are biased with current, flowing in opposite directions, as shown Figure 5.3. This leads to axial forces applied to both resonators but in different directions, enabling a differential measurement.

5.3 Implementation

The magnetometer described was designed, simulated and implemented to validate the chosen approach experimentally. Additionally, an in-house SOI process at the International Iberian Nanotechnology Laboratory was used to fabricate the sensor envisioned. All the steps to implement the single-axis MEMS magnetometer are described in this section.

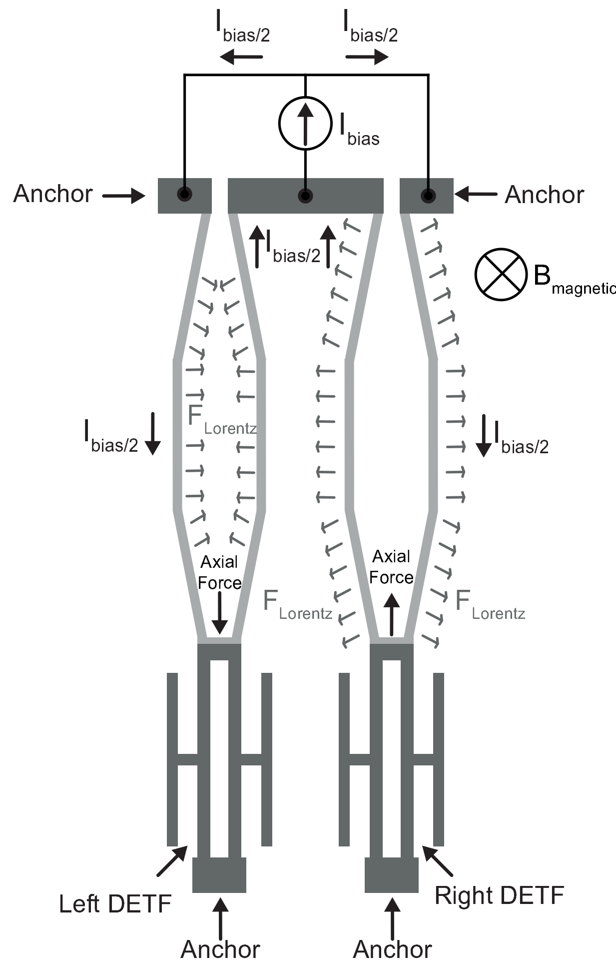

Figure 5.3: Differential MEMS magnetometer composed of two Lorentz-force transducers and two DETF.

The instrumentation system previously mentioned can be used to operate the resonators in open-loop and closed-loop, validating the versatility of the system composed of a lock-in amplifier with a PID controller. Thus, the instrumentation system used for the accelerometer is compatible with the magnetometer proposed, and consequently, the description of this system is not repeated here.

5.3.1 Sensing element

A MEMS magnetometer for out-of-plane measurement was designed and implemented following a set of constraints specific to the fabrication process. The design started with the definition of the Lorentz-force transducer dimensions and shape. Regarding the shape, as previously shown, a diamond-shaped transducer was chosen to transfer a distributed Lorentz force to a localised axial force. An optimisation of the different Lorentz-bar features' dimensions was performed to maximise the resulting strain in the DETF,

thus increasing the device sensitivity. Once more, FEM modelling together with parametric computer-aided design (CAD) was used for the optimisation since this solution is straightforward, fast and reliable. Additionally, no analytical models were available to study force transfer in this kind of transducers.

In this thesis, the diamond-shape transducer features' dimensions were divided into five variables (for optimisation purposes), namely, the length of the diagonal bar (L1), the length of the vertical bar (L2), the width of the beam (w_L), and the angle between the diagonal and vertical bars (θ). The process restricted some dimensions, such as the beam width of $4.9\,\mu m$ (metal is patterned on top and lithography deviations must be accounted for) and a device layer of $25\,\mu m$. A total Lorentz-beam length of 1 mm ($L2 + 2 \times L1$) was chosen to limit the size of the device. All the features under test during the optimisation procedures are depicted in Figure 5.4. Note that the transducer is composed of two symmetric beams.

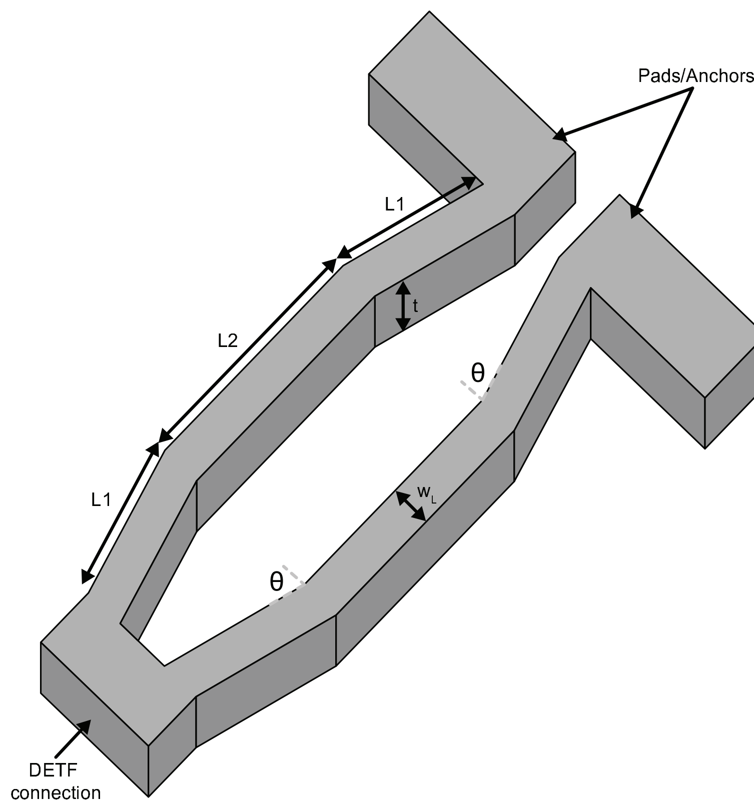

Figure 5.4: Schematic of a diamond-like shaped Lorentz-force transducer and the different features optimised to guarantee an optimum force transfer.

By studying the axial force resulting from a given bias current passing through the diamond-shape beams in presence of a magnetic field, one noticed that thinner beams resulted in more axial force. Additionally, the value of L1 and θ are instrumental in obtaining a maximum axial force, since these features have an optimal point where the force is maximised, as shown in Figure 5.5 and 5.6. These figures were obtained fixing all the dimensions but the one under study. The optimal point validates the necessity of proper optimisation.

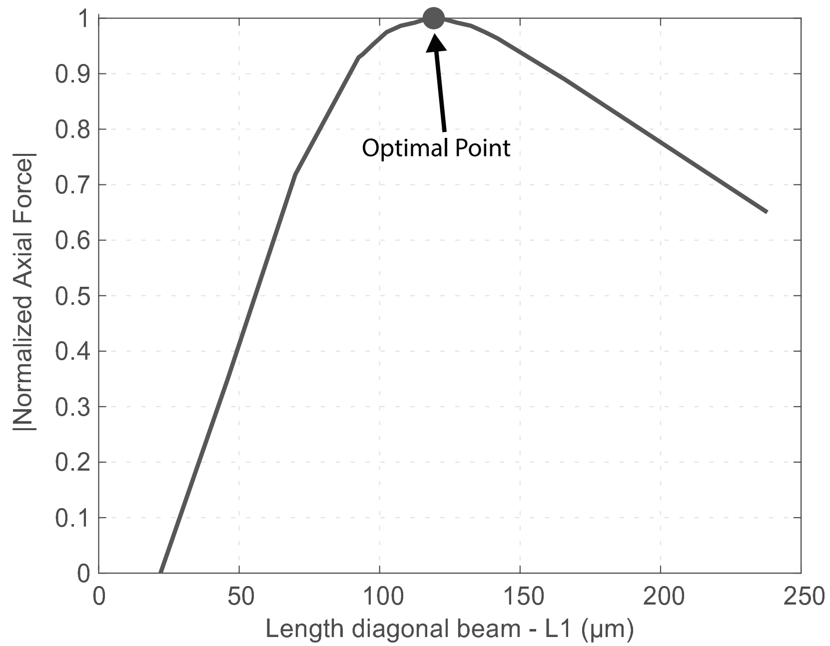

Figure 5.5: Normalised axial force accordingly to the dimension of L1 (note that the total length is always 1mm).

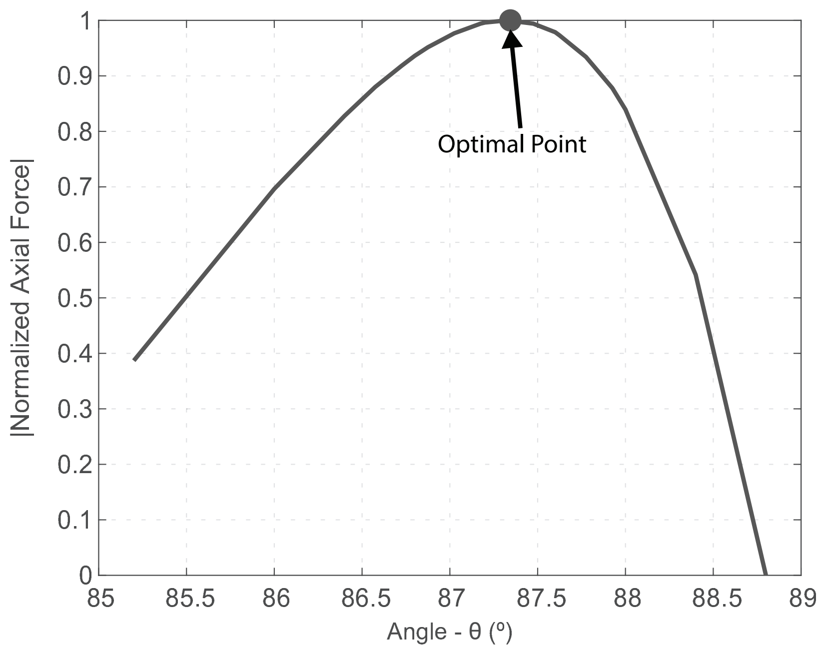

Figure 5.6: Relation between axial force and the angle between the diagonal and vertical beam.

The process was repeated, and all the parameters were studied when the Lorentz-force transducer is coupled to a DETF, in order to reach the maximum sensitivity (frequency change per unit of magnetic field). In Table 5.3, the different design dimensions are listed. During the mask design phase (for fabrication purposes), 450 nm were added (to each edge) to accommodate the over-etch of the process.

Parameter	Parameter description	Value
L1	Diagonal beam length	200 μm
L2	Vertical beam length	600 μm
Θ	Angle	88°
w_L	Lorentz-bar width	4.9 μm
t	Device thickness	25 μm

Table 5.3: Lorentz-force transducer parameters' dimensions (without considering over-etch).

Regarding the DETF, the same configuration as previously shown in the accelerometer proposed was used, but with different dimensions and a distinct encapsulation pressure. This results in new mechanical characteristics (natural frequency and quality factor). The Simulink model, previously implemented (see Figure 2.8), was used to model the DETFs present in the magnetometer. A natural frequency of 41.58 kHz and a quality factor of approximately 684 are expected, as shown in Figure 5.7.

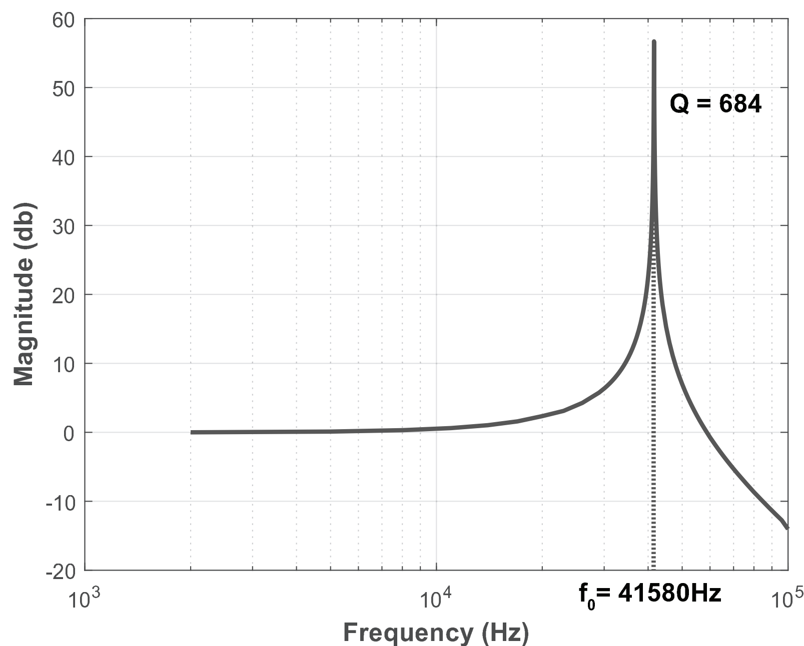

Figure 5.7: Frequency response of the DETF obtained using the Simulink model.

The dimensions and resonator characteristics are listed in Table 5.4.

After a full optimisation of the Lorentz-force diamond shaped beams, the MEMS magnetometer designed along this section, if the values defined in Table 5.3 and 5.4 are considered, has a theoretical sensitivity of 0.6 Hz/mT (for a bias current of 1 mA) considering a single-ended measurement. In the differential architecture, the sensitivity is doubled to 1.2 Hz/mT for a bias current of 1 mA on each Lorentz-force transducer.

Parameter	Parameter description	Value
L_e	Movable electrode Length	$300\ \mu m$
W_e	Movable electrode width	$1.35\ \mu m$
d_0	Rest distance (gap)	$2.25\ \mu m$
L	DETF beam length	$400\ \mu m$
w	DETF beam width	$1.35\ \mu m$
f_0	DETF natural frequency	$41.580\ kHz$
Q	Quality factor (DETF)	684
t	Device thickness	$25\ \mu m$
P_0	Encapsulation Pressure	5 mPa

Table 5.4: DETF designed dimensions and properties (without considering 450 nm over-etch).

5.3.2 Fabrication process

As previously mentioned, the devices were fabricated in an in-house two-masks SOI process at the International Iberian Nanotechnology Laboratory (INL), and the main steps are shown in Figure 5.8. These are described below in more detail:

1. **SOI wafer:** The process starts with a blank silicon-on-insulator wafer with a device layer of $25\mu m$, a BOX layer of $2\ \mu m$ and a handle layer of approximately $650\ \mu m$.
2. **Metal sputtering:** A metallic layer of AlSiCu is sputtered on the front-side of the wafer. This layer has a thickness of 330 nm.
3. **First lithography:** Photoresist ($1.035\ \mu m$) is spin-coated, exposed on a direct-write laser equipment and developed to pattern the metallic layer.
4. **Metal etching:** The metallic layer is etched by reactive ion etching, defining the contact pads and routing. The remaining photoresist is removed with an Oxygen plasma.
5. **Second lithography:** A thick layer of photoresist ($2.2\mu m$) is spin-coated, exposed and developed to define the magnetometer structure.
6. **DRIE etching:** The device layer is etched by a DRIE process, and the $2\ \mu m$ of BOX are used as a stop layer (low etching rate). The photoresist is then removed using an Oxygen plasma.
7. **Device release:** The structures are released by a dry Hydrofluoric Acid vapour etch since this selectively removes Silicon Dioxide.

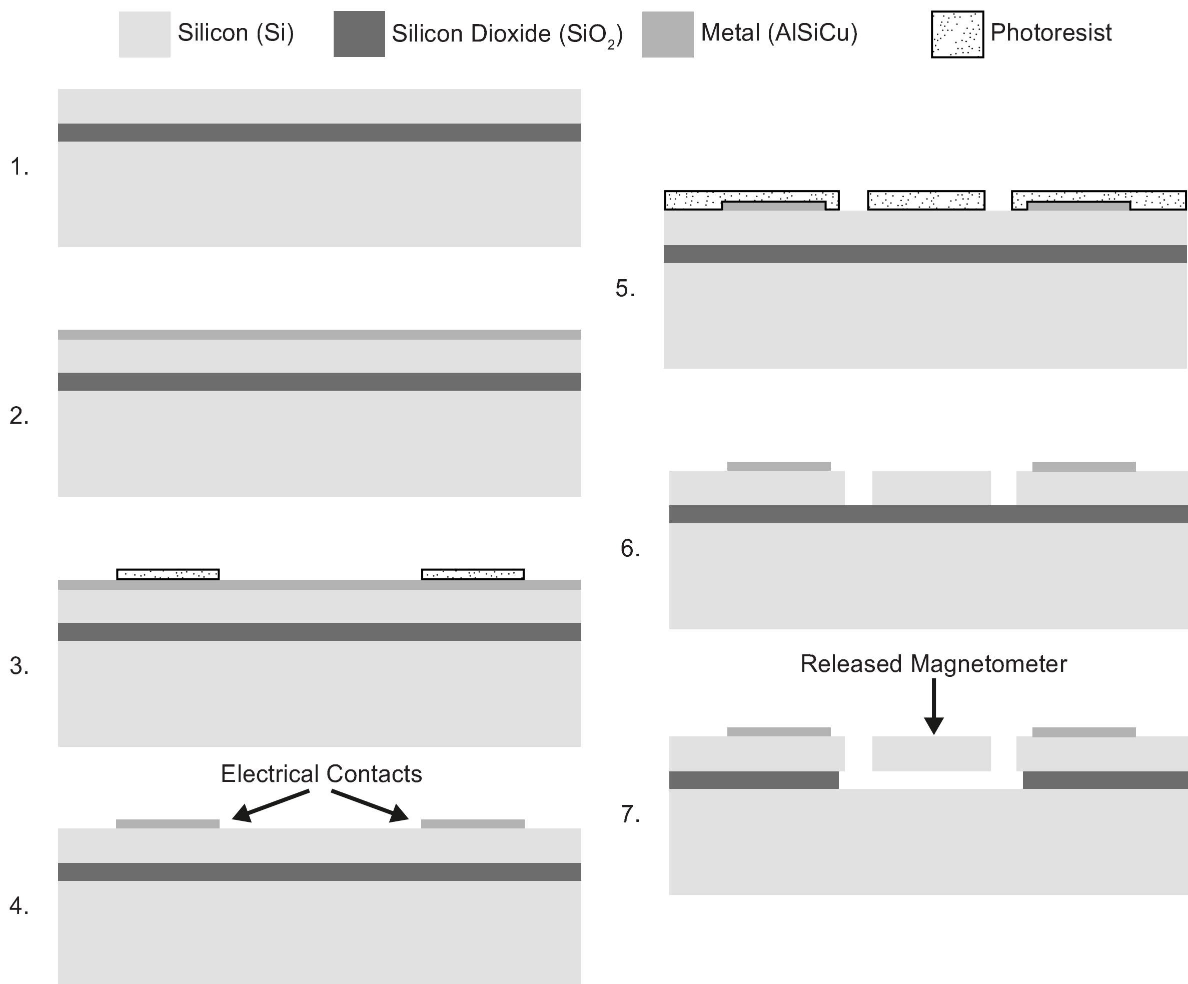

Figure 5.8: Wafer cross-section showing the main steps of the SOI-based fabrication process available for MEMS devices.

Many devices are produced on a single SOI portion and the structures were divided into dies using a dicing process. To protect the fragile components of the MEMS, before the dicing, a thick layer of photoresist (20 μm) was spin-coated.

No process for vacuum encapsulation was available, and the devices must be tested inside a vacuum chamber. Lower pressure stability is then expected compared to the devices fabricated at Bosch. Nonetheless, an appropriate device characterisation is guaranteed.

5.3.3 Fabricated devices

Masks to pattern the different layers necessary to fabricate the magnetometer were designed, as it can be seen in Appendix B. The same devices were fabricated on the two-mask SOI-based process mentioned before, and SEM pictures are shown in Figure 5.9.

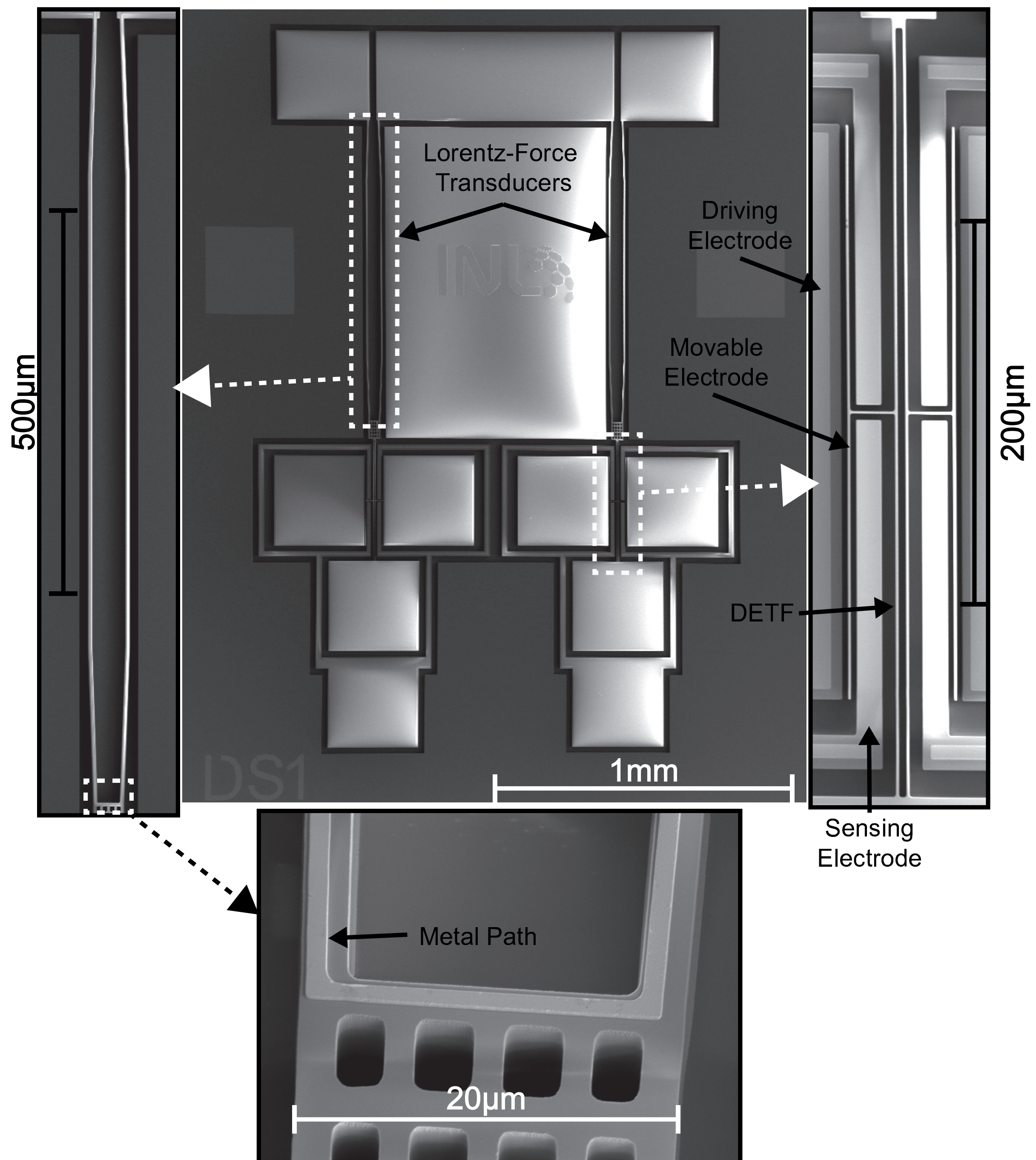

Figure 5.9: SEM pictures of the proposed magnetometer and its main features.

A metal path was defined on top of the Lorentz-force transducer to decrease the electrical resistance, yielding a lower power consumption of this component. Some applications require low-power devices, and the addition of a highly conductive layer (AlSiCu) is an appropriate solution.

Regarding the dimensions of the device, each set (DETF and Lorentz-force transducer) has a footprint of around 1.5 mm x 0.075 mm without considering the pads. The total core dimension (differential configuration) is below 0.25 mm^2, representing one of the smallest footprint of the devices analysed in

the state-of-the-art (Table 5.1 and 5.2).

5.3.4 Packaging

During the experimental characterisation of the magnetometers, it was noticed that regular ceramic chip carriers could not be used. This is explained by the ferromagnetic composition of the 24-pin CLCC available, yielding a magnetic field distortion and stress induced to the device. The last is due to the attraction between the permanent magnet (used to apply magnetic field during the experimental characterisation) and the chip carrier. Resulting in a force applied to the device and therefore, a drift of the sensor response.

To overcome this limitation, PCBs with a cavity to allocate a device were designed and developed together with Guimocircuito, Guimarães, Portugal. The main constituent of PCB (copper and glass-reinforced epoxy (FR4)) do not interact with magnetic-field, qualifying it as a proper technology for this use-case. Since a standard PCB fabrication process does not allow the tuning of the drilling height, in this case, instrumental in defining the cavity, the process was refined by our partner. The new chip carriers made out of PCB mimic standard through-hole chip carriers, as it can be observed in the schematic of Figure 5.10.

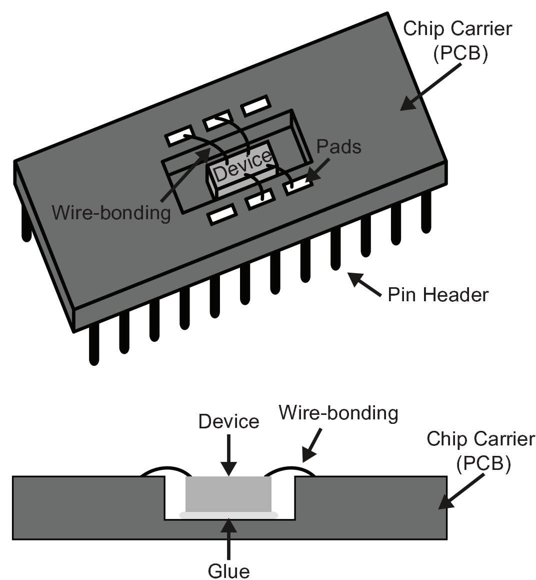

Figure 5.10: Schematic showing the cross-section and side-view of the PCB-based chip carriers.

Any shape or number of pins could be chosen, but to guarantee compatibility with the socket of the vacuum chamber, a 24-pin through-hole chip carrier was developed. The samples were glued inside the cavity using a conductive paste and wire-bonded to the PCB pads. The cavity height is approximately the same as the

total wafer thickness, shortening the wire-bonds and easing the process. A picture of the final assembly is shown in Figure 5.11.

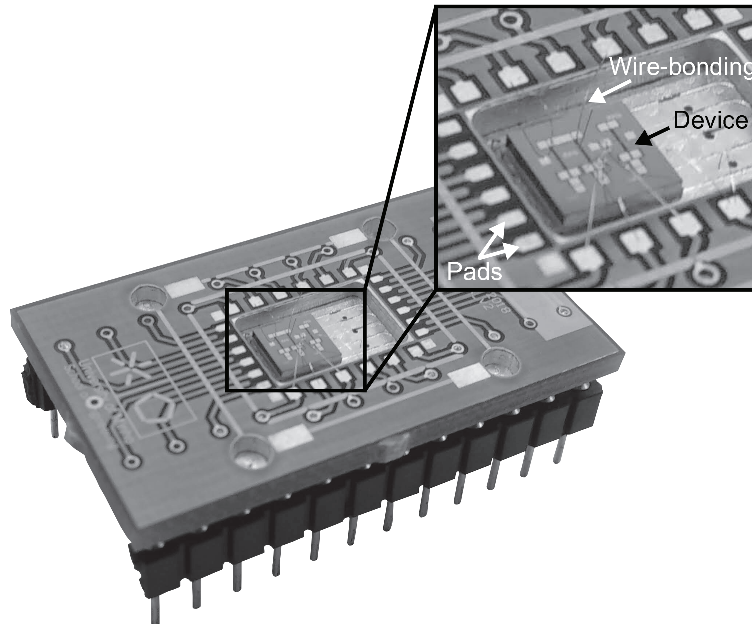

Figure 5.11: Picture of the PCB-based chip-carrier with a device glued and wire-bonded.

5.4 Experimental characterization

In this section, the focus goes to the experimental characterisation of the magnetometer proposed. Firstly, the mechanical response of the DETFs is accessed when operated in open-loop, retrieving information about the natural frequency and quality factor. After, the devices are operated in closed-loop using the fast prototype instrumentation system, and the sensitivity to the magnetic field is evaluated. Tests for different bias currents were also carried-out.

Concerning the lock-in parameters and PID controller gains, these were maintained constant along the experimental procedures. The controller gains used are: K_p=0.25, K_I=0 and K_D=0.

5.4.1 Setup

For sensitivity measurements, the devices were characterised on a setup constituted of a permanent magnet (capable of magnetic fields above 100 mT) and a linear motor LTS300 from Thorlabs to change the distance between the magnet and the sensor (see Figure 5.12). The motor has an integrated controller, and a minimum displacement increment of $0.1\ \mu m$ is achievable [5.18], representing a fine magnetic

field adjustment. Also, a reference Gaussmeter (not present in the picture) from Lakeshore (455 DSP) was strategically placed close to the device for calibration of the measurement system.

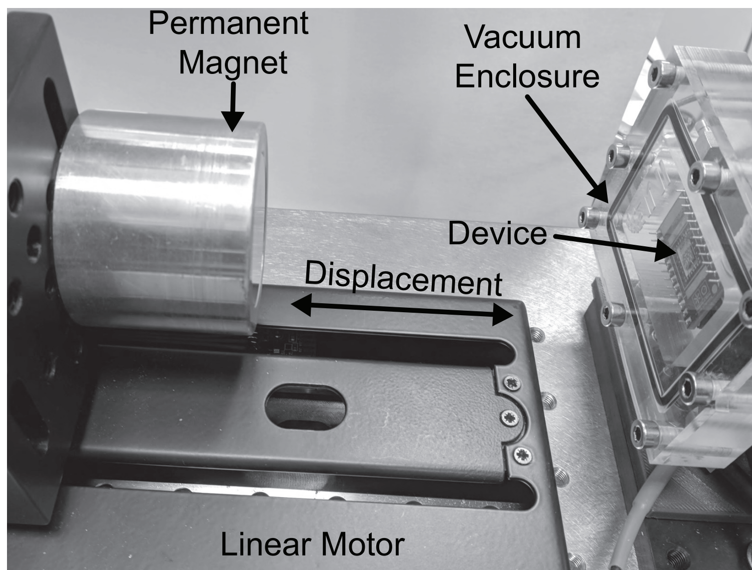

Figure 5.12: Setup used for the characterisation of the magnetometer's sensitivity.

As observed in Figure 5.12, the device was introduced in a vacuum enclosure where a low-pressure is expected. Despite not present in the picture, a turbopump was used to achieve the required pressure. All the remaining equipment to operate the devices (e.g. lock-in amplifier and FPGA) were presented before. A source meter (bench instrument) was added to bias the magnetometer's Lorentz-force transducers with a stable DC current.

5.4.2 DETF mechanical characterization

A frequency sweep was performed (using the lock-in amplifier) on the left and right DETF composing the magnetometer differential configuration. Natural frequencies of 37.7 kHz and 38.18 kHz were measured, as demonstrated in Figure 5.13. These values are about 9.3 % below the natural frequency theoretically expected (worst-case) due to additional over-etch of the DETF features. Moreover, the difference between the left and right resonators, approximately 480 Hz, are believed to be mainly the result of process mismatch.

A quality factor of around 400 was measured, representing a significant discrepancy (-41.5%) with the value expected. Nonetheless, one believes this is the result of the additional over-etch and a different pressure than the one expected inside the vacuum enclosure. A higher pressure yields lower quality factors since the main dissipative component (squeeze-film damping between the movable and fixed electrodes) is

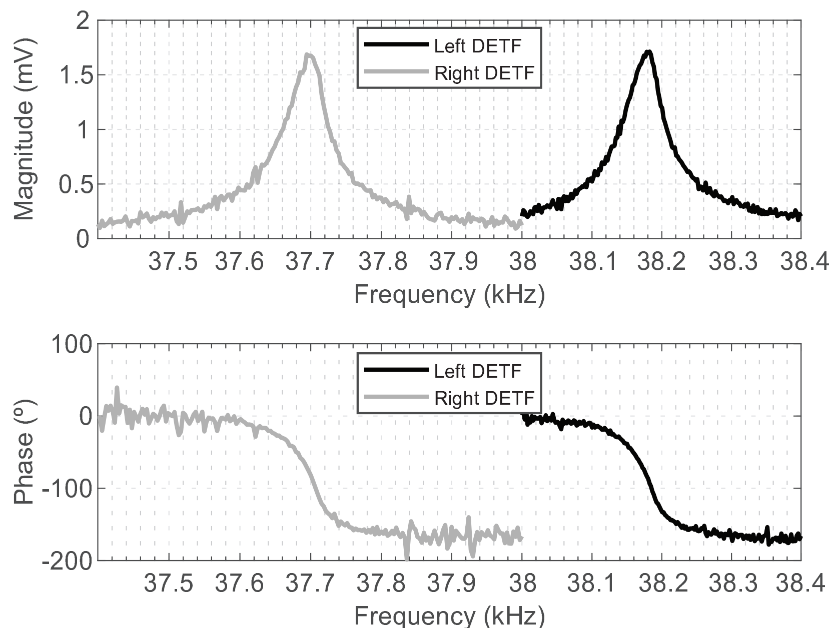

Figure 5.13: Frequency response of the Left and Right DETF (V_p=3 V and v_a=300 mV).

increased. Further work is required to measure the pressure inside the enclosure. Additionally, vacuum encapsulation at the die level, similarly to the resonant accelerometer, would be advantageous.

5.4.3 Magnetometer's sensitivity characterisation

The curves in Figure 5.14 represent the frequency change of the two resonators in the differential configuration, when an external field is applied. The magnetometer is composed of a DETF on the left and another on the right and since the current on the transducers flows on opposite directions, one resonator is subject to tensile force while the second suffers from compressive force (as demonstrated in Figure 5.3). This explains the behaviour of the curves, where the resonance frequency is increasing on the right resonator while decreasing on the left one.

The measurement range was restrained to $\pm 42.5\ mT$ because of constraints in the setup implemented. In fact, the vacuum enclosure increases the minimum distance between the permanent magnet and the device, yielding weaker magnetic fields.

Furthermore, the measurement of negative magnetic fields was reproduced by changing the current direction in the Lorentz-force transducers since fields produced by the magnet are always in the same direction. This enabled a complete sensitivity characterisation.

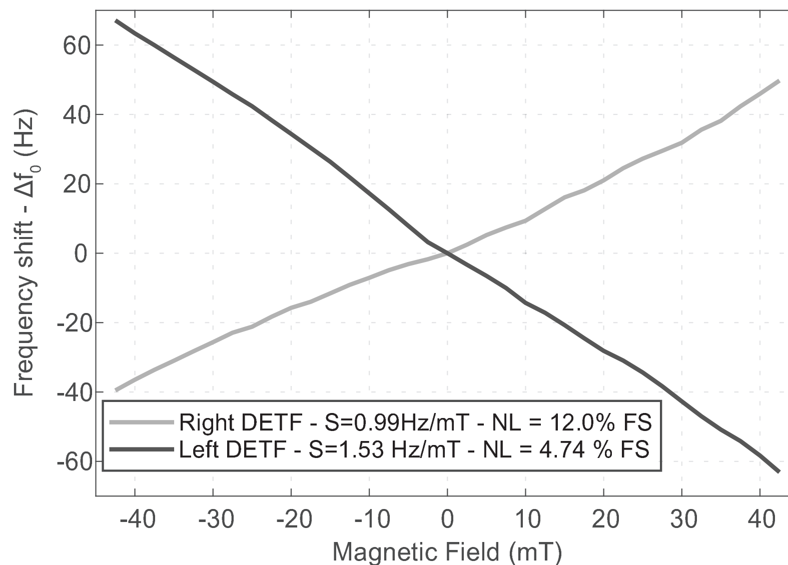

Figure 5.14: Resonance frequency changes for the left and right resonators for a bias current of 1 mA.

The sensitivity of the magnetometer for several bias currents was also assessed, and experimental results are presented in Figure 5.15. The sensitivity increases, as expected, for higher currents due to a larger force produced on the transducer. A maximum sensitivity of 4.59 Hz/mT for a bias current of 1.5 mA (on each Lorentz bar) was experimentally measured.

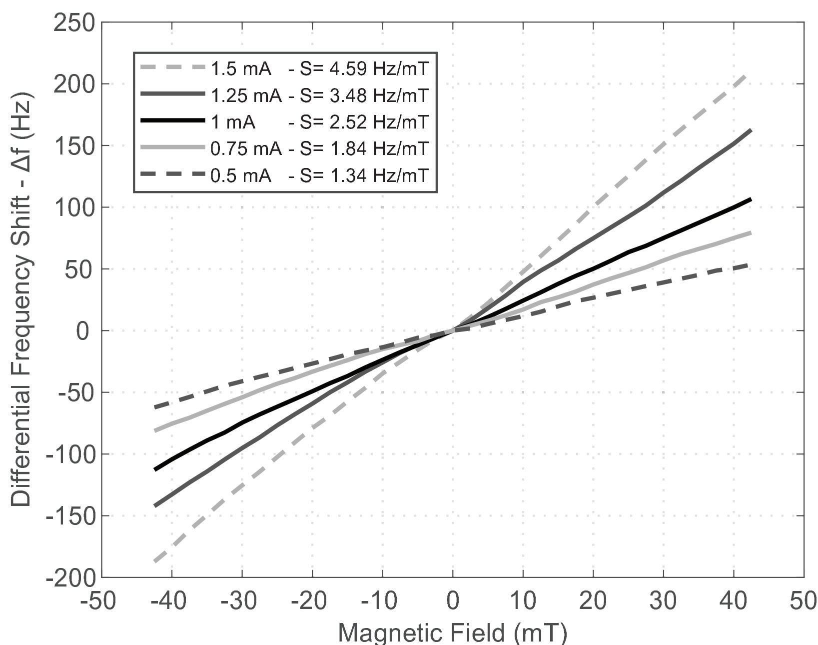

Figure 5.15: Sensitivity of the frequency-modulated sensor for different bias currents (0.5 mA to 1.5 mA) in the range $\pm 42.5\ mT$.

For a bias current of 1 mA, the sensitivity is nearly 2.5 Hz/mT, while the value expected was 1.2 Hz/mT.

This mismatch has still to be further analysed, but possibly the over-etch affects positively the natural frequency change for a given magnetic field value. Thinner Lorentz bars and DETF beams result in higher sensitivities, and a lower nominal natural frequency (experimentally measured) validates additional over-etch.

In Figure 5.15, the non-linearity was not calculated since the resonators were not measured simultaneously. The differential DETF instrumentation was not yet implemented when the magnetometers were characterised.

Moreover, the sensitivity is not increasing linearly for the higher currents as theoretically expected for Lorentz-force transducers. The sensitivity increase follows a quadratic fitting, as demonstrated in Figure 5.16.

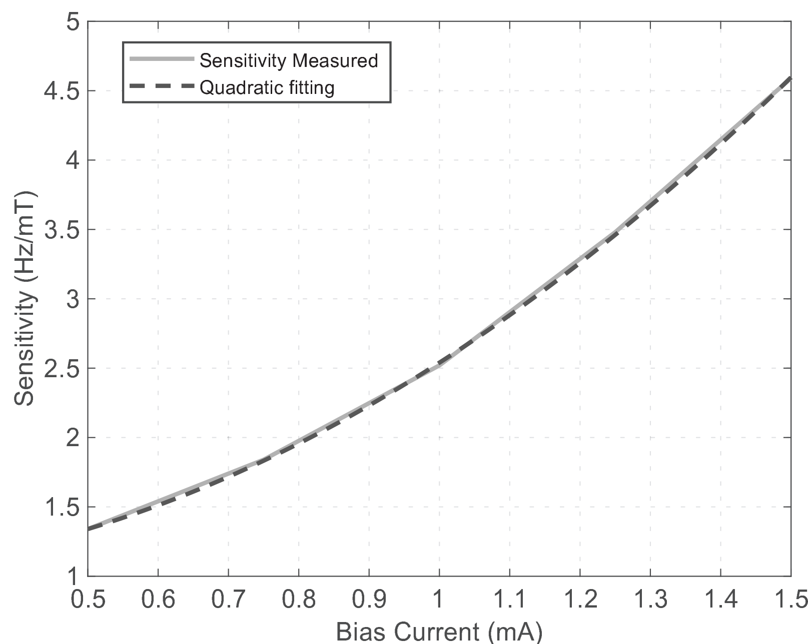

Figure 5.16: Relation between sensitivity and bias current.

Further work is required to study this phenomenon, but since the bias voltage and bias current are not isolated from each other, it is possible that the interaction of both is contributing to this effect. The quadratic sensitivity rise means that the electric stiffness of the DETF is changing relatively to the bias current. This was observed in the resonant accelerometer for different bias voltages. But the magnetometer measurement was performed for a constant bias voltage, and only the current amplitude on the transducer was changed. Probably, this phenomenon can also explain the higher sensitivity measured.

5.5 Conclusions

A differential magnetometer composed of Lorentz-force transducers and DETF resonators was proposed to further demonstrate the validity of the DETF resonators, the simulation methodology and the instrumentation system. The Lorentz-force diamond shaped beams design was optimised using a FEM software linked with a parametric CAD design to enhance the sensor sensitivity. The devices were fabricated in an in-house two-masks process on SOI wafers. A characterisation of the sensor response was performed for both resonators of the differential architecture when encapsulated in vacuum (vacuum enclosure with an expected pressure around 5 mPa). A sensitivity of 4.59 Hz/mT for a bias current of 1.5 mA (on each transducer) was experimentally measured, validating the concept. The fabricated devices' sensitivity is the highest found in the literature, and two other figures of merit are generally used for a complete comparison. The sensitivity regarding the nominal natural frequency ($\Delta f/f_0/B_{Magnetic}$) shown as $\%Hz/T$. Additionally, as found in [5.17], a figure of merit relative also to the bias current ($\Delta f/f_0/B_{Magnetic}/I_{bias}$) displayed as $\%Hz/T/mA$ is used to compare magnetometers. If analysing Table 5.5, it is possible to notice that the sensitivity and both figures of merit of the proposed magnetometer are the highest reported for frequency modulated MEMS magnetometers. Nonetheless, more devices should be measured and supplementary experimental characterisation procedures should be performed to validate the values obtained.

Work	[5.2]	[5.17]	[5.5]	This work
Natural Frequency (kHz)	26.986	21.9	49.3	38.18
Sensitivity (Hz/T)	87.9	591	10.6	4590
Measurement Range (±mT)	25	66	100	42.5
Bias Current (mA)	10 (DC)	4 (DC)	10 (DC)	3 (DC)
Device Size (mm^2)	0.21	0.82	0.36*	<0.25*1
Figure of Merit				
%Hz/T	0.33	2.7	0.02	12
%Hz/T/mA	0.033	0.675	0.002	4

* Measured from device's pictures.
*1 Only the core of the sensor is accounted.

Table 5.5: Comparison of frequency-modulated MEMS magnetometers present in the state-of-the-art.

Since this sensor was not the core of this thesis, only the mechanical properties of the DETF and the sensitivity were accessed. However, a meticulous characterisation should be performed in the future, to obtain experimentally more characteristics, such as the bandwidth, long-term stability and temperature dependency. This would further validate the magnetometer designed.

The geometry simplicity, small core size of the sensing element (below 0.25 mm^2) and the differential configuration are other main benefits of the proposed approach. Additionally, the DETF resonators proved to be suitable in an another use-case, besides the accelerometer. These resonators can be used to sense multiple physical quantities.

References

[5.1] J. Lenz and A. S. Edelstein, "Magnetic sensors and their applications", IEEE Sensors Journal, vol. 6, no. 3, pp. 631–649, Jun. 2006. doi: 10.1109/JSEN.2006.874493.

[5.2] B. Bahreyni and C. Shafai, "A Resonant Micromachined Magnetic Field Sensor", IEEE Sensors Journal, vol. 7, no. 9, pp. 1326–1334, Sep. 2007. doi: 10.1109/JSEN.2007.902945.

[5.3] D. Won, J. Ahn, S. Sung, M. Heo, S. H. Im, and Y. J. Lee, "Performance Improvement of Inertial Navigation System by Using Magnetometer with Vehicle Dynamic Constraints", Journal of Sensors, vol. 2015, 2015. doi: 10.1155/2015/435062.

[5.4] Bosch Motorsport, Steering Wheel Angle Sensor LWS, 2020. [Online]. Available: http://www.bosch-motorsport.de.

[5.5] W. Zhang and J. E. Lee, "Frequency-based magnetic field sensing using Lorentz force axial strain modulation in a double-ended tuning fork", Sensors and Actuators, A: Physical, vol. 211, pp. 145–152, 2014. doi: 10.1016/j.sna.2014.01.022.

[5.6] G. Laghi, "MEMS magnetometers: from application specifications to the development and characterization of a prototype beyond the state of-the-art", PhD thesis, Politecnico di Milano, 2017, pp. 1–126.

[5.7] A. Baschirotto, F. Borghetti, E. Dallago, P. Malcovati, M. Marchesi, E. Melissano, P. Siciliano, and G. Venchi, "Fluxgate magnetic sensor and front-end circuitry in an integrated microsystem", Sensors and Actuators A: Physical, vol. 132, no. 1, pp. 90–97, Nov. 2006. doi: 10.1016/j.sna.2006.04.043.

[5.8] V. Kumar, A. Ramezany, M. Mahdavi, and S. Pourkamali, "Amplitude modulated Lorentz force MEMS magnetometer with picotesla sensitivity", Journal of Micromechanics and Microengineering, vol. 26, no. 10, p. 105 021, Oct. 2016. doi: 10.1088/0960-1317/26/10/105021.

[5.9] M. J. Thompson, "The Design and Implementation of Parametrically Amplified Lorentz Force MEMS Magnetometers", PhD thesis, University of California Davis, 2010, pp. 1–74.

[5.10] S. Bonnet, C. Bassompierre, C. Godin, S. Lesecq, and A. Barraud, “Calibration methods for inertial and magnetic sensors”, Sensors and Actuators A: Physical, vol. 156, no. 2, pp. 302–311, Dec. 2009. doi: 10.1016/j.sna.2009.10.008.

[5.11] H. H. Yang, N. V. Myung, J. Yee, D.-Y. Park, B.-Y. Yoo, M. Schwartz, K. Nobe, and J. W. Judy, “Ferromagnetic Micromechanical Magnetometers”, in Transducers ’01 Eurosensors XV, Berlin, Heidelberg: Springer Berlin Heidelberg, 2001, pp. 164–167. doi: 10.1007/978-3-642-59497-7_38.

[5.12] H. Emmerich, M. Schofthaler, and U. Knauss, “A novel micromachined magnetic-field sensor”, in Technical Digest. IEEE International MEMS 99 Conference. Twelfth IEEE International Conference on Micro Electro Mechanical Systems (Cat. No.99CH36291), vol. 8, IEEE, 1999, pp. 94–99. doi: 10.1109/MEMSYS.1999.746759.

[5.13] M. Li, E. J. Ng, V. A. Hong, C. H. Ahn, Y. Yang, T. W. Kenny, and D. A. Horsley, “Single-structure 3-axis lorentz force magnetometer with sub-30 nT/$\sqrt{Hz}$ resolution”, in 2014 IEEE 27th International Conference on Micro Electro Mechanical Systems (MEMS), IEEE, Jan. 2014, pp. 80–83. doi: 10.1109/MEMSYS.2014.6765578.

[5.14] S. Sonmezoglu and D. A. Horsley, “Off-resonance operation of a MEMS Lorentz force magnetometer with improved thermal stability of the scale factor”, Proceedings of the IEEE International Conference on Micro Electro Mechanical Systems (MEMS), vol. 2016-February, no. January, pp. 103–106, 2016. doi: 10.1109/MEMSYS.2016.7421568.

[5.15] G. Langfelder, G. Laghi, P. Minotti, A. Tocchio, and A. Longoni, “Off-Resonance Low-Pressure Operation of Lorentz Force MEMS Magnetometers”, IEEE Transactions on Industrial Electronics, vol. 61, no. 12, pp. 7124–7130, Dec. 2014. doi: 10.1109/TIE.2014.2317153.

[5.16] M. J. Thompson and D. A. Horsley, “Parametrically Amplified Z-Axis Lorentz Force Magnetometer”, Journal of Microelectromechanical Systems, vol. 20, no. 3, pp. 702–710, Jun. 2011. doi: 10.1109/JMEMS.2011.2140355.

[5.17] M. Li, S. Nitzan, and D. A. Horsley, “Frequency-Modulated Lorentz Force Magnetometer With Enhanced Sensitivity via Mechanical Amplification”, IEEE Electron Device Letters, vol. 36, no. 1, pp. 62–64, Jan. 2015. doi: 10.1109/LED.2014.2372617.

[5.18] Thorlabs, LTS150 and LTS300 Long Travel Stages - User Guide, 2020.

Chapter 6

Conclusions and future work

The research presented in this thesis focused on the development of a frequency-modulated MEMS accelerometer, based on double-ended tuning fork resonators. The DETFs behaviour was analysed (statically and dynamically), and a high-sensitivity was identified as one of the main goals of this thesis. A differential accelerometer with a force amplification mechanism was designed, and the advantages of this architecture were discussed and presented. The sensor design respects the rules of a Bosch standard silicon micromachining process, guaranteeing higher integrability. To instrument the DETFs and read the physical quantity of interest, a read-out system was implemented to enable the resonators' operation in open-loop and closed-loop. A detailed characterisation was performed to experimentally validate the behaviour of the DETFs ,and posteriorly, the accelerometer as a whole. A comparison between these results and the theoretical expectation was made.

In this chapter, the main contributions, goals and conclusions of this thesis' research work are summarised. With the know-how gathered, future research opportunities are proposed, being mainly focused on overcoming the sensor's identified limitations.

DETF resonators have proven to be suitable to implement several devices (accelerometer and magnetometer), accessing different physical quantities and enabling the monolithic integration of various sensors. Although a frequency-modulated magnetometer was implemented and characterised, the conclusion and future work sections will focus on the accelerometer. Yet, most of the content discussed in this chapter can benefit both sensors because of the common working principle and resonator type.

6.1 Conclusions

The main conclusions drawn from the research developed along this thesis are divided as follows:

1. **Design and modelling of DETF resonators**: The natural frequency of DETFs changes with force at the extremities and this was used to sense acceleration. Besides accelerometers, other MEMS devices can benefit from this transduction mechanism (e. g. magnetometers). To maximise the DETF sensitivity, long and thin beams should be used together with force amplification mechanisms. Additionally, to drive and read the DETFs, capacitive electrodes are beneficial. However, these decrease the resonator sensitivity and a trade-off must be found.

2. **Design and optimisation of a frequency-modulated accelerometer:** A frequency-modulated accelerometer for single-axis measurement was designed, fabricated and tested. A maximum sensitivity on a small area (total of $0.25\ mm^2$) was desired, and for these dimensions, devices tend to have low sensitivities. Therefore a force amplification mechanism was used. Since perfect pivots can not be micromachined, a complete optimisation of the device was performed to take maximum advantage of all the different features. For this, FEM modelling and parametric CAD design showed significant advantages over analytical models, since these are strongly dependant on assumptions that are device dependent. A differential architecture was chosen to duplicate the accelerometer sensitivity but also to reduce common-mode errors, such as the temperature dependency and the sensitivity to mechanical stress.

3. **Device Instrumentation:** Laboratory equipment together with analog front-end electronics and a FPGA were used to implement a system capable of operating the DETF in open-loop and closed-loop. Open-loop operation suffers from reduced linearity and dynamic range. On the other hand, closed-loop operation benefits from increased linearity and dynamic range. For this reason, the accelerometer was operated in closed-loop in this thesis, while the open-loop operation was used to study the mechanical parameters of the DETF.

   The low-level of integration and the different connections between subsystems resulted in several limitations to the sensor performance. Although the system implemented allowed the characterisation of the proposed devices, this system should be improved and further integrated.

4. **Accelerometer Performance**: The proposed devices were fabricated and the performance experimentally accessed, showing a sensitivity irrespective to mass above the current state-of-the-art for MEMS accelerometers based on DETF resonators:

   (a) **Sensitivity and Linearity:** A maximum sensitivity of 170.7 Hz/g was experimentally measured operating the resonators in closed-loop. The high-sensitivity of the sensor is compared

with highly sensitive devices reported in the literature. For frequency-modulated accelerometers, the frequency shift per nominal frequency per unit of acceleration ($\Delta f/f_0/acc$), which can be expressed in %Hz/g is a commonly used figure of merit. A figure of merit in terms of $[(\Delta f/f_0)/acc]/M_{proof}$ has also been defined (in units of %Hz/g/nkg – nkg being used instead of μg to prevent misreadings), as it reflects the efficiency of the transduction mechanism irrespectively to the mass size. As shown in Table 6.1, regarding these figures of merit, or relative sensitivities, one can observe that the device developed presents the highest performance regarding the sensitivity per unit of mass. Additionally, the sensor developed has the smallest footprint of the devices present in Table 6.1. Please note that only accelerometers based on DETF resonators were compared.

Work	Proof Mass (nkg)	Natural Freq. (kHz)	Scale Factor (Hz/g)	Die area (mm^2)	Relative sensitivity	
					%Hz/g	%Hz/g/nkg
[6.1]	309	25.24	31.56	9.92	0.13	0.0004
[6.2]	23.5*1	140.7	28.4	3.2	0.02	0.0009
[6.3]	557.1	350	1400	NA	0.4	0.0007
[6.4]	32.2*1	130	158	0.46*2	0.12	0.0038
[6.5]	**1.33**	173	17	NA	0.01	0.0074
[6.6]	2444*1	149.52	**9408**	26*3	**6.29**	0.0026
This thesis	5.32	35.8	170.7	**0.25**	0.48	**0.0895**

*1 Mass calculated using a silicon density of 2350kg/m^3.
*2 Only the area of the mass is available.
*3 Only the volume of the mass is available.
NA - Not available

Table 6.1: Sensitivity comparison of accelerometers based on DETF resonators.

The only device found in the state-of-the-art presenting a higher relative sensitivity per proof mass is the one reported in [6.7] (0.22 %Hz/g/nkg), which concerns a single-beam resonator on a differential configuration using a force amplification mechanism. This highlights the benefit of using the amplification mechanisms proposed in this thesis.

A non-linearity of 0.63% FS was also experimentally measured on the same sample. This validates the use of DETF resonator on a differential configuration to measure acceleration with good linearity.

(b) **Long-term Stability:** The measurement performed showed a long-term stability affected by three main factors: temperature, mechanical stress and bias voltage stability.

In what concerns the temperature dependency, a frequency-modulated accelerometer must have a stable natural frequency over time. Nonetheless, this parameter is tied to the Young's modulus of silicon, and for the resonator designed, a drift of -2.5 Hz/°C is expected due to the material properties' change. This drift is relatively large, and a differential architecture was implemented to minimise it. Despite design diligence, a positive drift of 2 Hz/g was differentially measured. The poor thermal behaviour is explained by a CTE mismatch mainly between the packaging and the silicon die. This induces stress on the device anchors and consequently a change in the DETF natural frequency.

Additionally, the mechanical stress introduced on the silicon die through the surroundings influences the response of the sensor. Once more, stress applied at the anchor changes the natural frequency of the resonators and the differential measurement is not capable of full compensation. To decrease both mechanical stress and temperature deviations, a good stress uniformity must be ensured to maximise the differential compensation. Moreover, the influence of the bonding glue properties on the stress decoupling was studied, and a viscoelastic glue was identified as suitable for slow-changing stress, while the differential measurement was more effective for fast stimuli.

From the study of the DETF response for different bias voltages, one concludes this parameter changes the natural frequency of the device. Therefore, a stable reference voltage is required.

(c) **Bandwidth:** An experimental bandwidth of 63 Hz was experimentally measured operating the resonators in the implemented closed-loop. This value was proven to be restrained by the parameters of the lock-in PLL, and further research is required to increase the bandwidth.

(d) **Noise Figure:** A noise figure of approximately $700\ \mu g/\sqrt{Hz}$ was extracted from the Allan Variance plot at 1 Hz. The Allan Variance curve does not follow the theoretical behaviour, and this is explained by the low level of integration of the system implemented. Additionally, the interfaces between subsystems are believed to be contributing to this factor.

(e) **Accelerometer Performance Summary:** Several parameters of the devices were measured, and a summary is presented in Table 6.2. When multiple tests were performed in several devices, the average value is presented.

Device Parameters	Value
DETF natural Frequency (f_0)	35928 Hz (Average)
DETF Quality Factor (Q)	121.4 (Average)
Sensitivity	163.3 Hz/g (Average)
Non-linearity	0.56% FS (Average)
Measurement range	$\pm 5g$
Control-loop bandwidth	$63Hz$
Sensitivity Repeatability	<0.25 % (σ)
Cross-axis sensitivity (in-plane 90°)	10.9 Hz/g
Temperature Drift	2 Hz/°C
Noise Density	$700\ \mu g/\sqrt{Hz}$

Table 6.2: Main parameters measured along the experimental characterisation.

6.2 Future work

From the results of this thesis research and the expertise accumulated, several improvements were identified to overcome the actual limitations. Research challenges to improve the actual device and the instrumentation system are presented in this section.

6.2.1 Device design proposal

Analysing Table 6.2 and the conclusions drawn in the section above, one concludes that the main drawback of the proposed device is the long-term stability influenced by the temperature change and stress applied on the surroundings of the device. Several solutions were identified, but the design of a device with a single-anchor is believed to be the one with more potential. Since this represents a compensation through design and no sophisticated packaging nor additional components (e.g. heaters) are added to the sensor. Nevertheless, the design of a device composed of a single-anchor and a force amplification mechanism is challenging (because of the pivots anchors). To solve this issue, the resonators can share the same anchor, and compliant pivots (axial and rotation) can be added to the device. The compliant pivots are believed to decouple the stress from the anchors of the lever if axial compliance is guaranteed, avoiding the resonator response drift. While the rotational compliance is necessary to the lever amplification. A pivot shaped to have axial and rotational compliance, like the one demonstrated in Figure 6.1 can be beneficial to increase long-term stability.

The schematic of the proposed device is also composed of four levers, instead of two, see Figure 6.1. From this, a good force amplification is expected even for shorter levers. Additionally, increasing the number of

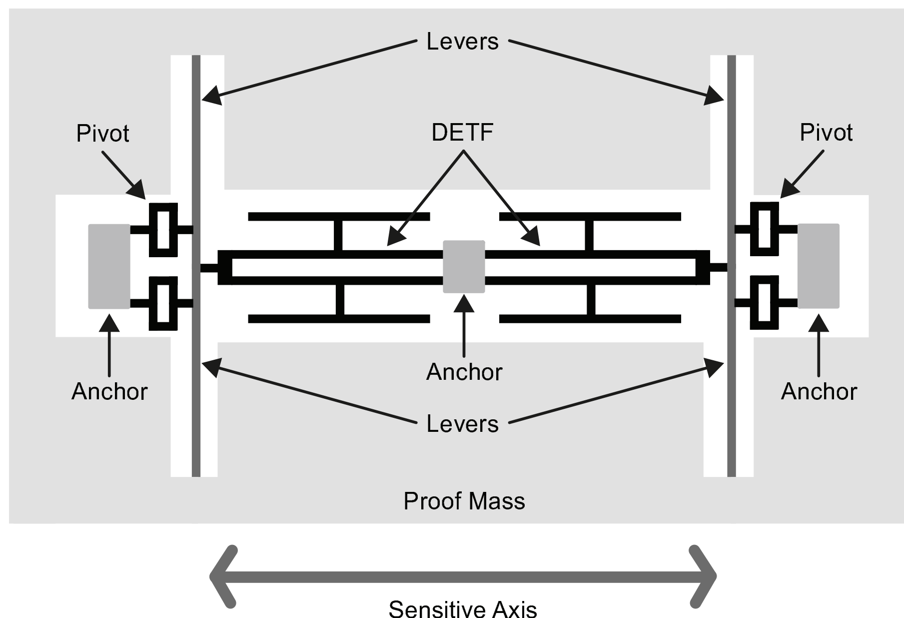

Figure 6.1: Design proposal composed of different improvements mainly for long-term stability improvement and cross-axis reduction.

connection points between the levers and the proof mass (from two on the device tested to four on the proposed device) is also expected to decrease the in-plane and out-of-plane cross-axis sensitivity. Since more connections restrain the rotation and movement of the proof-mass (increased stiffness).

Although not added to the schematic, the sensing and driving electrodes are assumed to remain in the same configuration.

6.2.2 Mechanical stress decoupling at the fabrication-level

A fabrication process presented by Bosch has the potential of decoupling the mechanical stress induced by external sources on the device. This process is part of the intellectual property of Robert Bosch GmbH, and little information can be given. Therefore, this concept is succinctly introduced.

The main advantage of the fabrication process regards the use of two active layers and a decoupling layer (see Figure 6.2). On the decoupling layer, pillars are patterned, serving as the support for the first active layer. This isolates all the layers above the pillars from external forces. The MEMS device is built on top of the first active layer that serves as a tray. A cross-section of the main layers is schematised in Figure 6.2.

Using the capabilities of this process, the MEMS devices are isolated from the stress applied to the silicon die. Therefore, this is perceived as a possible solution to decrease thermal and mechanical stress, increasing the long-term stability.

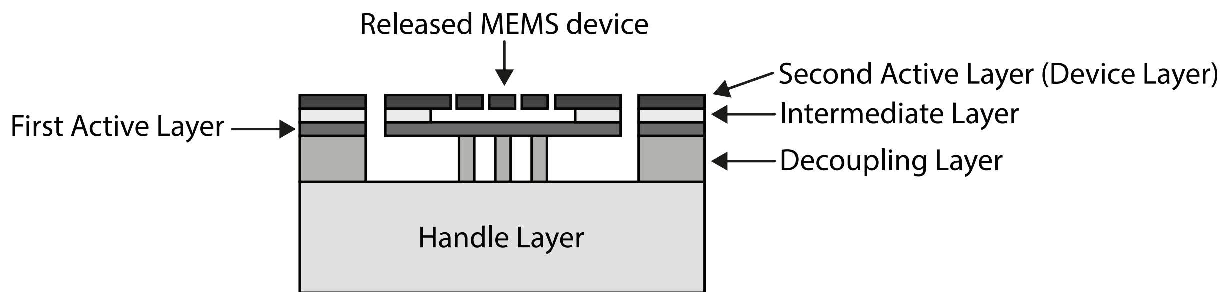

Figure 6.2: Cross-section of a process allowing the decoupling of mechanical stress.

6.2.3 System integration

The instrumentation system implemented along this thesis was used to measure the devices and was suitable for research purposes. Nonetheless, higher system integration is instrumental in overcoming some of the limitations identified but also to decrease size. It is expected that a higher integration and the control of the different subsystems can result in performance improvement. For this purpose, the lock-in amplifier should be implemented in the FPGA, to demodulate the signal from the front-end electronics and to detect the signal phase. By implementing all the elements of the closed-loop control on a FPGA, interfaces between laboratory instruments are avoided, granting a better overall performance. The DETF driving sinewave is also proposed to be generated by a DDS, serving as reference signal for the lock-in amplifier block (signal demodulation and phase shift detection) and as input for a DAC. The DAC generates the sinusoidal wave to drive the resonator at the natural frequency. The different blocks are presented in Figure 6.3.

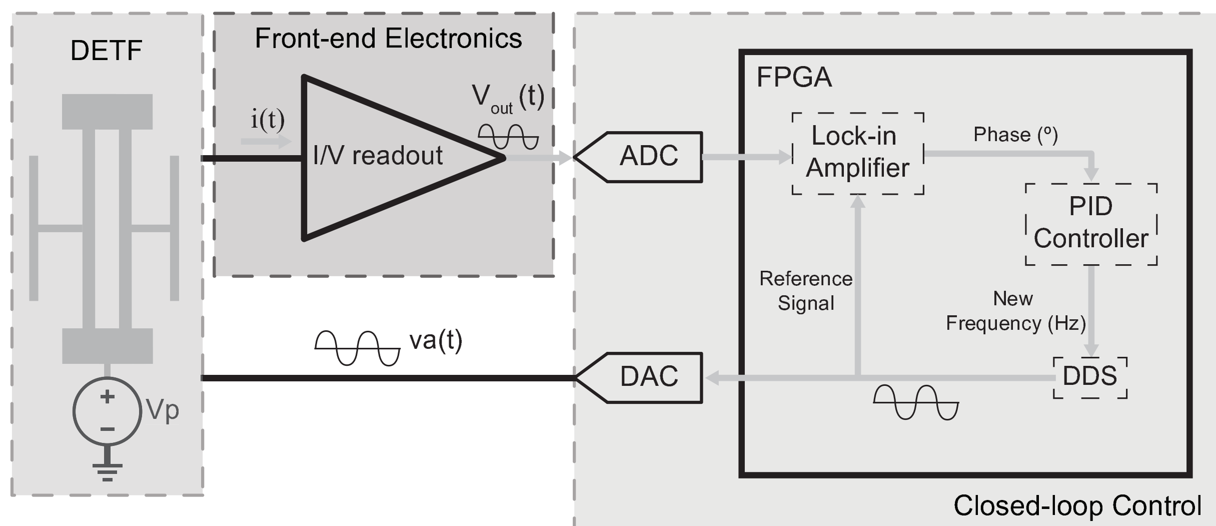

Figure 6.3: Proposal of a system to operate the resonators in closed-loop. This system is a more integrated version of the system used along this work.

The proposed closed-loop system is based on the previous instrumentation implemented in this work, and all the blocks should be duplicated to operate differentially a complete accelerometer.

References

[6.1] J. Zhang, Y. Wang, V. Zega, Y. Su, and A. Corigliano, "Nonlinear dynamics under varying temperature conditions of the resonating beams of a differential resonant accelerometer", Journal of Micromechanics and Microengineering, vol. 28, no. 7, pp. 1–10, 2018. doi: 10.1088/1361-6439/aab7c6.

[6.2] Y. Wang, H. Ding, X. Le, W. Wang, and J. Xie, "A MEMS piezoelectric in-plane resonant accelerometer based on aluminum nitride with two-stage microleverage mechanism", Sensors and Actuators A: Physical, vol. 254, pp. 126–133, Feb. 2017. doi: 10.1016/j.sna.2016.12.019.

[6.3] Xudong Zou, P. Thiruvenkatanathan, and A. A. Seshia, "A Seismic-Grade Resonant MEMS Accelerometer", Journal of Microelectromechanical Systems, vol. 23, no. 4, pp. 768–770, Aug. 2014. doi: 10.1109/JMEMS.2014.2319196.

[6.4] X.-p. S. Su, "Compliant Leverage Mechanism Design for MEMS Applications", PhD thesis, University of California, Berkeley, 2001, p. 219.

[6.5] A. Seshia, M. Palaniapan, T. Roessig, R. Howe, R. Gooch, T. Schimert, and S. Montague, "A vacuum packaged surface micromachined resonant accelerometer", Journal of Microelectromechanical Systems, vol. 11, no. 6, pp. 784–793, Dec. 2002. doi: 10.1109/JMEMS.2002.805207.

[6.6] X. Zou and A. A. Seshia, "A high-resolution resonant MEMS accelerometer", in 18th International Conference on Solid-State Sensors, Actuators and Microsystems (TRANSDUCERS), IEEE, Jun. 2015, pp. 1247–1250. doi: 10.1109/TRANSDUCERS.2015.7181156.

[6.7] C. Comi, A. Corigliano, G. Langfelder, A. Longoni, A. Tocchio, and B. Simoni, "A Resonant Microaccelerometer With High Sensitivity Operating in an Oscillating Circuit", Journal of Microelectromechanical Systems, vol. 19, no. 5, pp. 1140–1152, Oct. 2010. doi: 10.1109/JMEMS.2010.2067437.

Appendix A

Accelerometers' Masks

In this appendix, the different masks for the fabrication of the accelerometers designed along this work are shown in Figure A.1, A.2 and A.3. The first picture depicts a single device, while the remaining show the three device composing a silicon die.

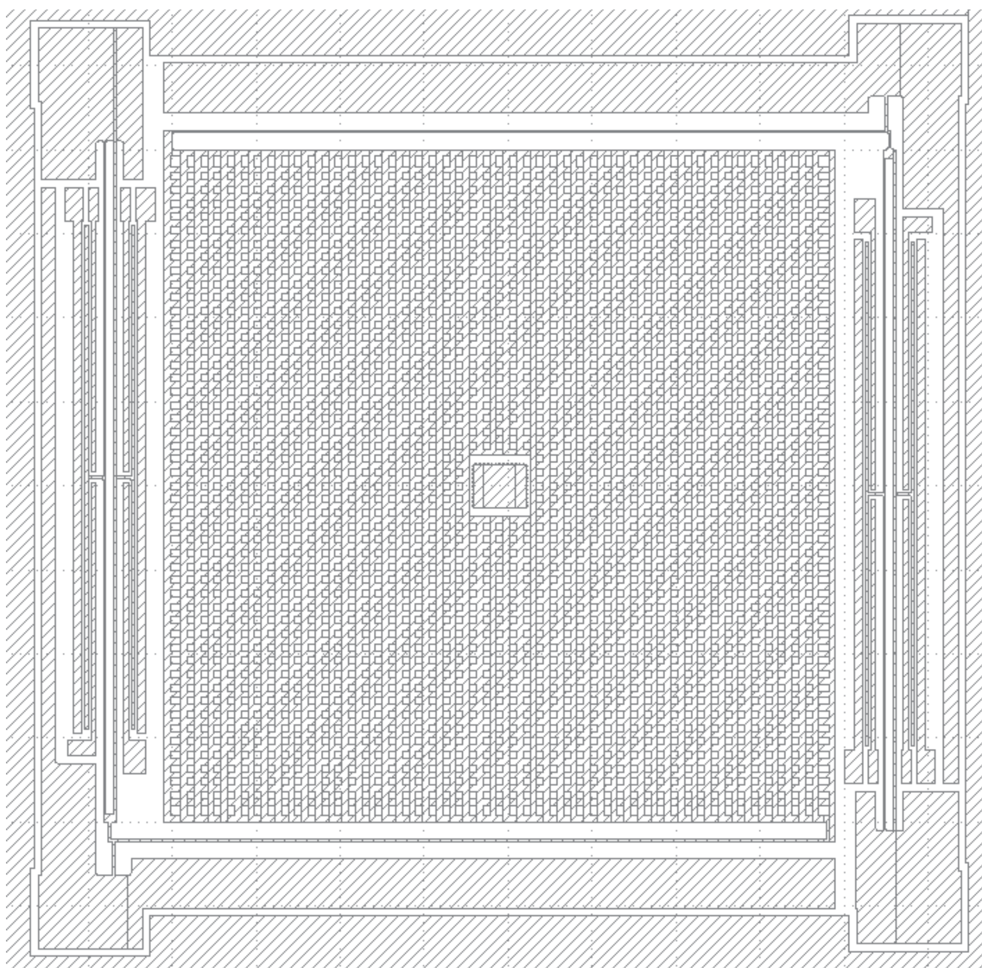

Figure A.1: Mask to pattern the device layer of the device.

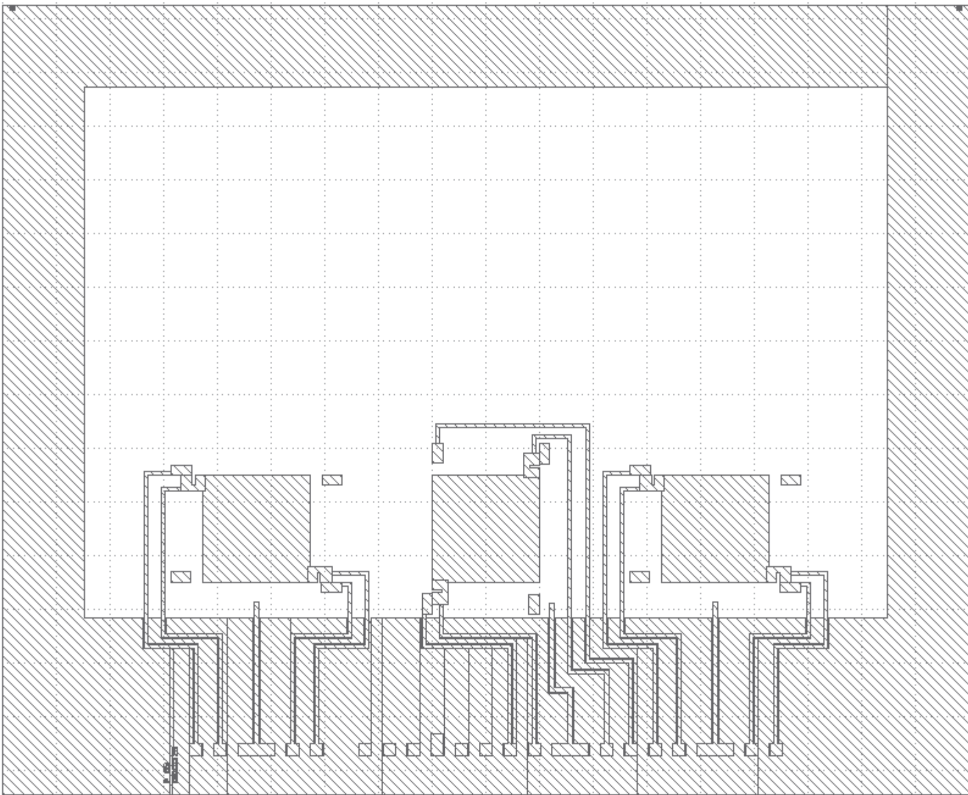

Figure A.2: Mask of the electrical connections coupling the devices to the pads.

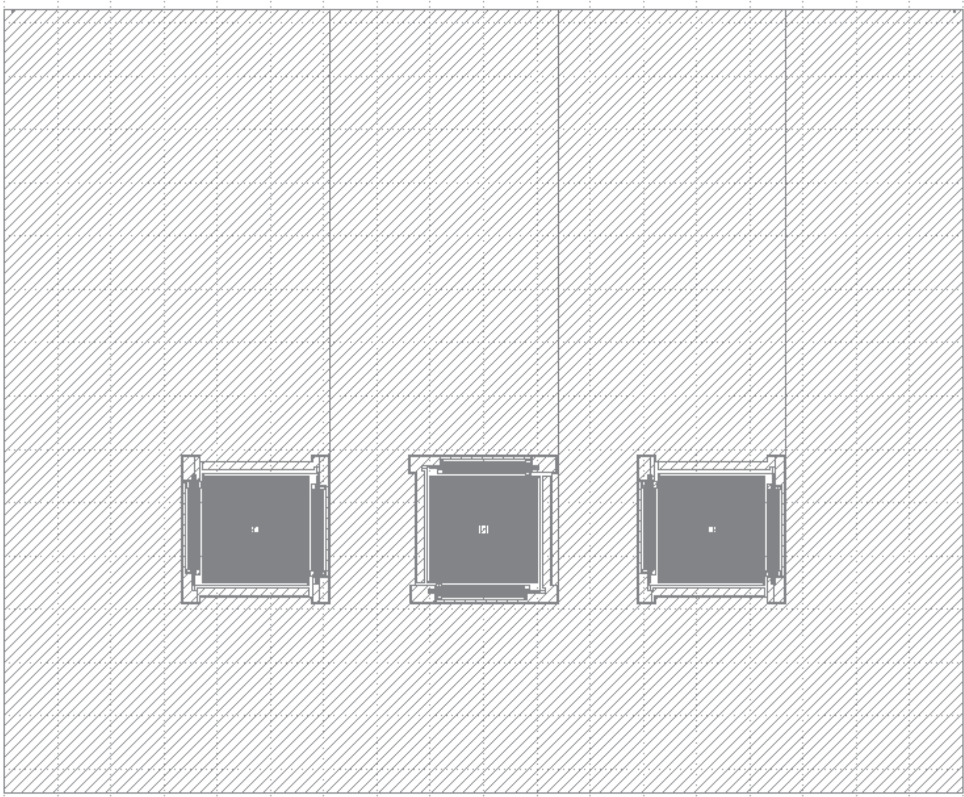

Figure A.3: Mask of the active layer for the three devices present on each die.

Appendix B

Magnetometer's Masks

The masks designed for the fabrication of a MEMS magnetometer on an in-house SOI process are shown in this appendix. The mask for the definition of the metal contacts and routing is shown in Figure B.1, while in Figure B.2, the mask to define the device layer is presented. Finally, both masks, previously described, are depicted together in Figure B.3.

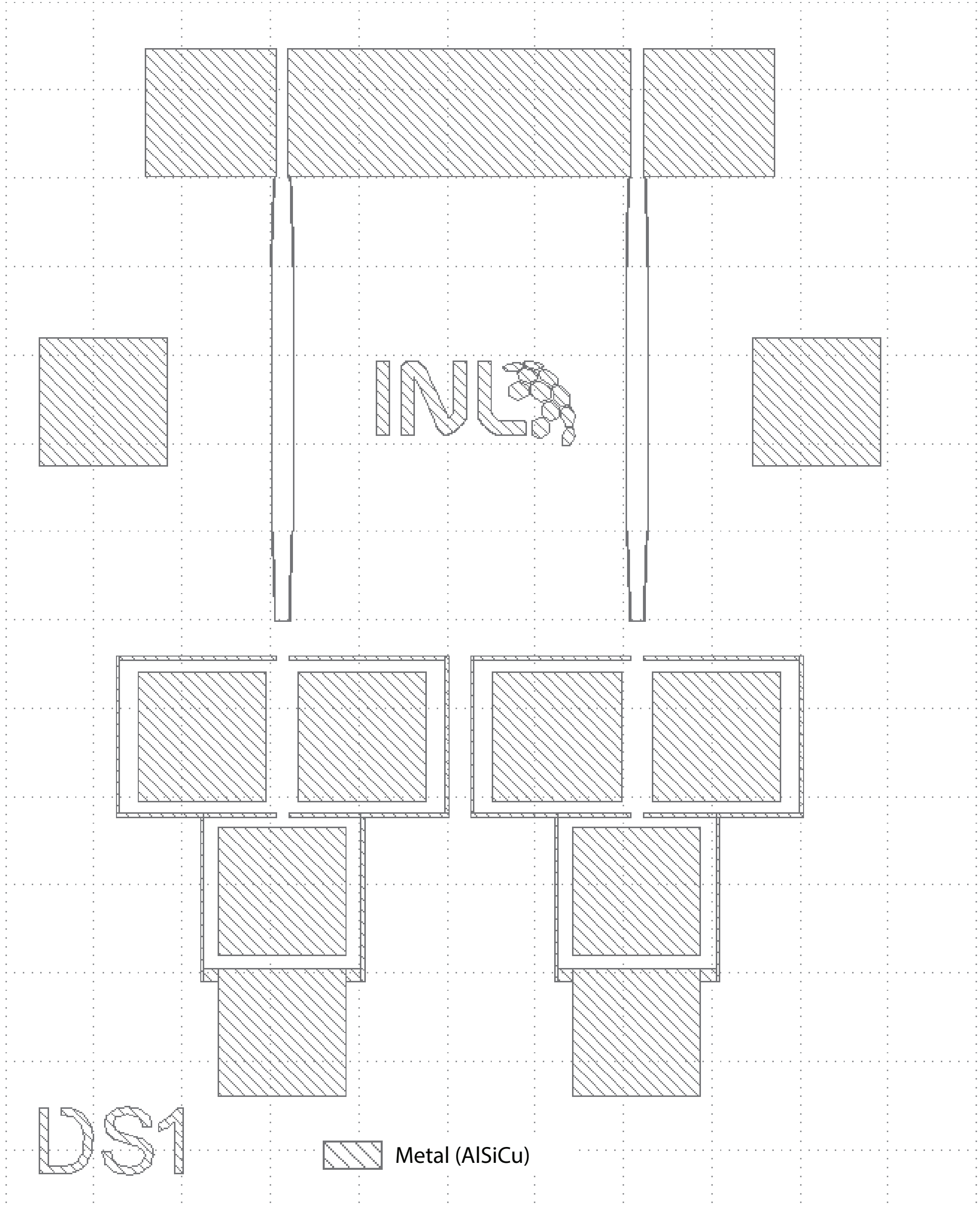

Figure B.1: Mask designed to define the metal layer.

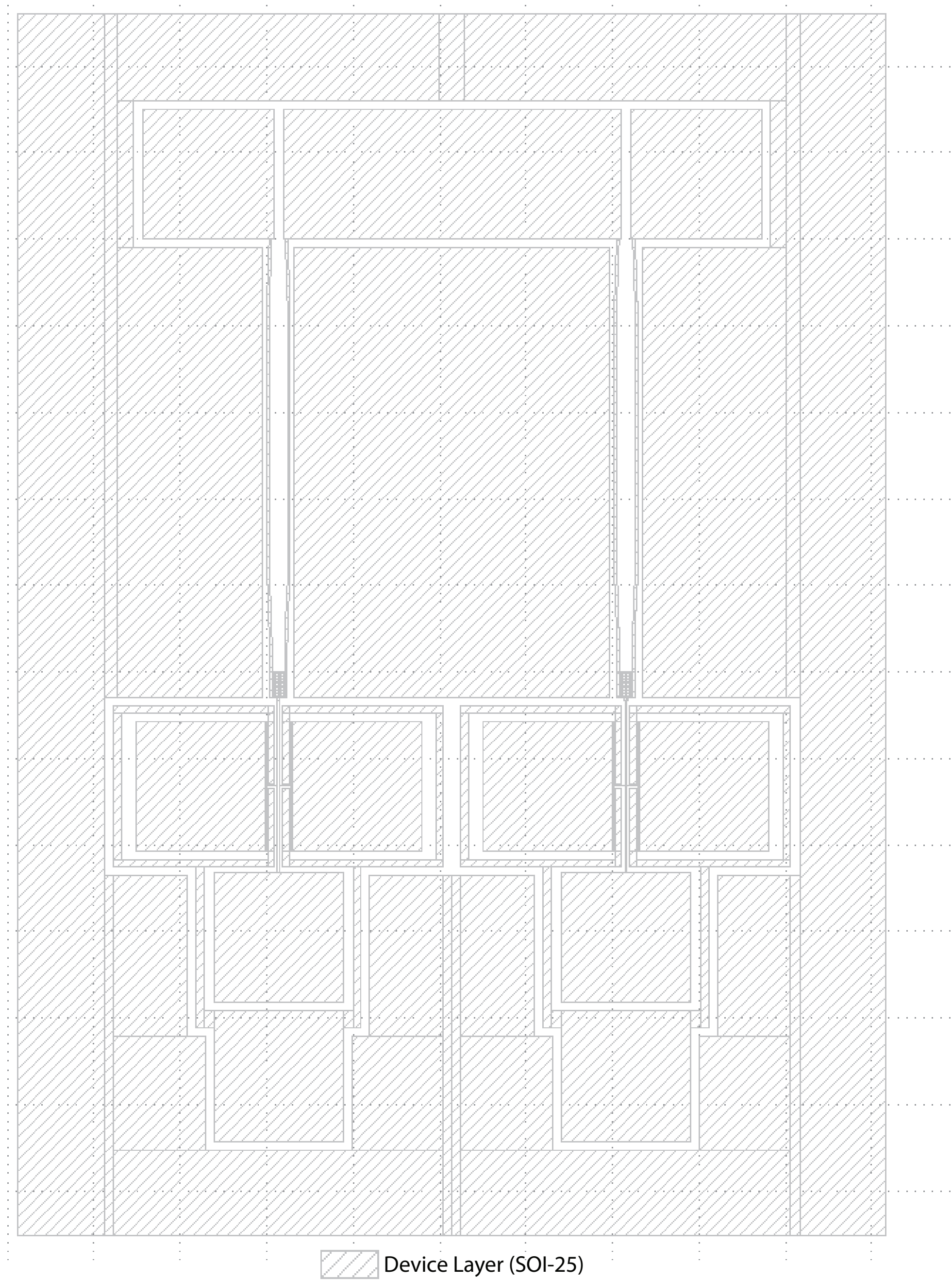

Figure B.2: Mask to pattern the device layer.

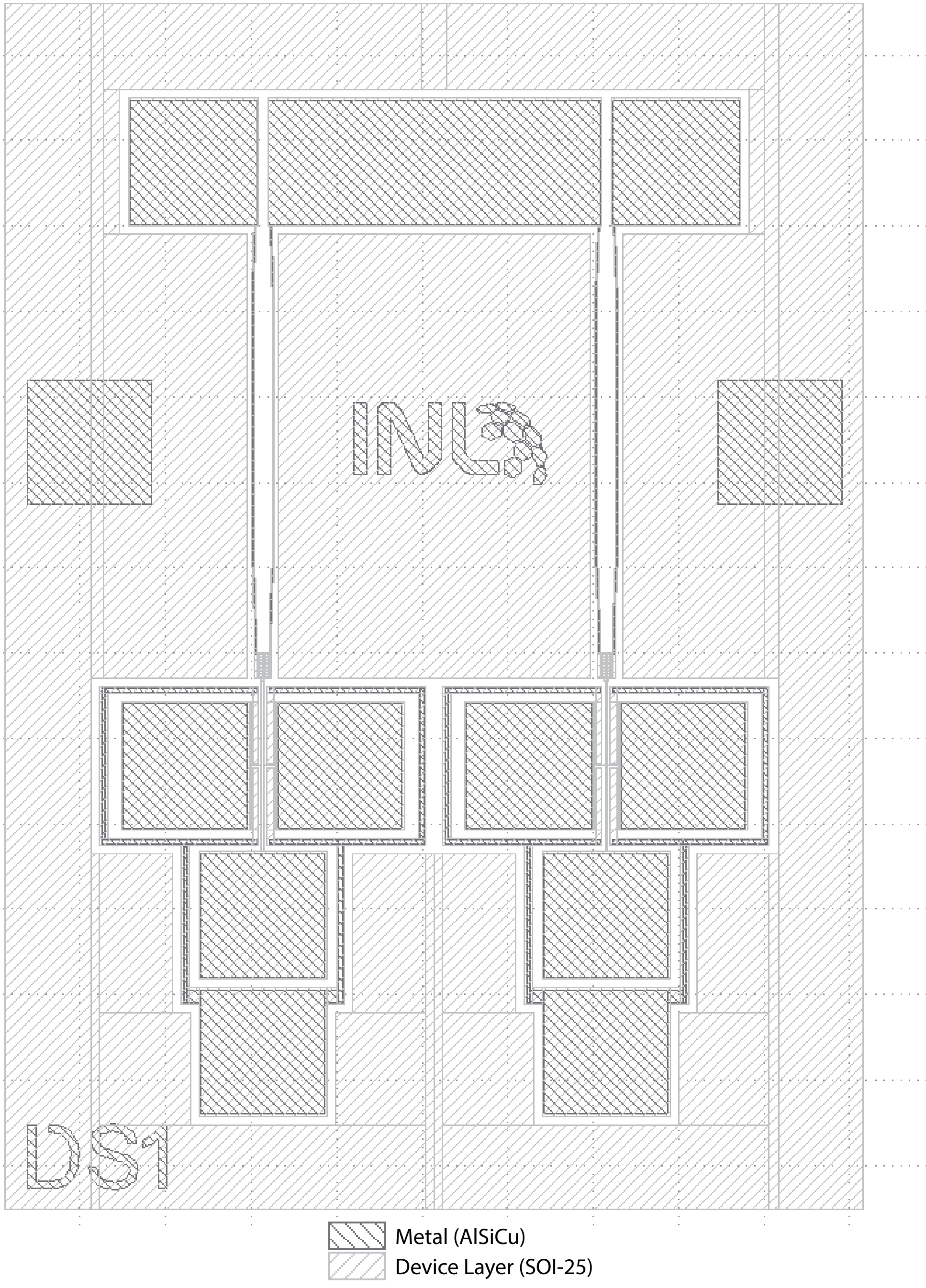

Figure B.3: Metal and device layers to define the proposed magnetometer.

List of Publications

Journal Publications

1. **E. E. Moreira**, B. Kuhlmann, F. S. Alves, R. A. Dias, J. Cabral, J. Gaspar, L. A. Rocha, ”Highly sensitive MEMS frequency modulated accelerometer with small footprint,” Sensors & Actuators A: Physical, 2020
2. F. Leitão, **E. E. Moreira**, F. S. Alves, M. Lourenço, O. Azevedo, J. Gaspar and L. A. Rocha, “High-Resolution Seismocardiogram Acquisition and Analysis System,” Sensors, vol. 18, no. 10, pp. 1–14, Oct. 2018.
3. **E. E. Moreira**, V. Lima, F. S. Alves, J. Cabral, J. Gaspar, and L. A. Rocha, “Full-gap tracking system for parallel plate electrostatic actuators using closed-loop control,” Sensors & Actuators A: Physical, vol. 244, pp. 174–183, Jun. 2016.

Conference Proceedings

1. **E. E. Moreira**, F. S. Alves, M. Martins, G. Ribeiro, A. Pina, D. E. Aguiam, E. Sotgiu, E. P. Fernandes, and J. Gaspar, ”Industry 4.0: Smart predictive maintenance on an injection tool,” in the 25th International Conference on Emerging Technologies and Factory Automation (ETFA), 2020, [Under Revision].
2. **E. E. Moreira**, B. Kuhlmann, F. S. Alves, R. A. Dias, J. Cabral, J. Gaspar, and L. A. Rocha, ”Influence of Mechanical Stress in a Packaged Frequency-Modulated MEMS Accelerometer,” in the 7th IEEE International Symposium on Inertial Sensors & Systems (INERTIAL), 2020, pp. 1-4.
3. R. A. Dias, **E. E. Moreira**, F. S. Alves, D. Mesquita, J. Gaspar, and L. A. Rocha, “Design Optimization of a Lorentz Force, Amplitude Modulated, MEMS Space Magnetometer,” in 33rd IEEE International Conference on Micro Electro Mechanical Systems (MEMS), 2020, pp. 873-876.

4. **E. E. Moreira**, B. Kuhlmann, J. Gaspar, and L. A. Rocha, "Small Size And Highly Sensitive Differential MEMS Accelerometer Based On Double-Ended Tuning Fork Resonators," in 20th International Conference on Solid-State Sensors, Actuators and Microsystems & Eurosensors XXXIII (TRANSDUCERS & EUROSENSORS XXXIII), 2019, vol. 3, no. June, pp. 602–605.

5. I. S. Garcia, **E. E. Moreira**, R. A. Dias, J. Gaspar, F. S. Alves, and L. A. Rocha, "Sub-Micron MEMS Accelerometer with Handle-Layer Patterning for Damping Enhancement Using Time Transduction," in 20th International Conference on Solid-State Sensors, Actuators and Microsystems & Eurosensors XXXIII (TRANSDUCERS & EUROSENSORS XXXIII), 2019, no. June, pp. 2045–2048.

6. **E. E. Moreira**, B. Kuhlmann, J. Gaspar, and L. A. Rocha, "Resonant Accelerometer based on Double-Ended Tuning Fork and a Force Amplification Mechanism," in Proceedings, 2018, vol. 2, no. 13, p. 1030.

7. **E. E. Moreira**, J. Gaspar, and L. A. Rocha, "Frequency Modulated Magnetometer Using a Double-Ended Tuning Fork Resonator," in Proceedings, 2018, vol. 2, no. 13, p. 1028.

8. R. A. Dias, **E. E. Moreira**, I. Ribeiro, M. Costa, H. Fonseca, S. Cardoso, P. Freitas, L. A. Rocha, J. Gaspar, "Novel magnetic readout for hybrid spintronic MEMS devices," in 19th International Conference on Solid-State Sensors, Actuators and Microsystems (TRANSDUCERS), 2017, pp. 818–821.

9. **E. E. Moreira**, J. Cabral, J. Gaspar, and L. A. Rocha, "Low-voltage, High-tuning Range MEMS Variable Capacitor Using Closed-loop Control," in Procedia Engineering, 2016, vol. 168, pp. 1551–1554.

10. M. Costa, J. Gaspar, **E. E. Moreira**, L. A. Rocha, S. Cardoso, and P. P. Freitas, "AFM Cantilevers For Scanning Magnetoresistance Applications," in Proceedings of the 13th International Workshop on Nanomechanical Sensing, 2016, vol. 3, pp. 156–157.

11. **E. E. Moreira**, F. S. Alves, R. A. Dias, M. Costa, H. Fonseca, J. Cabral, J. Gaspar and L. A. Rocha, "Bi-directional extended range parallel plate electrostatic actuator based on feedback linearization," in 28th IEEE International Conference on Micro Electro Mechanical Systems (MEMS), 2015, pp. 1036–1039.

12. **E. E. Moreira**, F. S. Alves, R. A. Dias, J. Cabral, J. Gaspar, and L. A. Rocha, "Full-gap tracking system for parallel-plate electrostatic microactuatores," in Procedia Engineering, 2014, pp. 1386–1389.

Conference Abstracts

1. I. S. Garcia, **E. E. Moreira**, R. A. Dias, J. Gaspar, F.S. Alves, L.A. Rocha, "Microfabrication of a MEMS accelerometer composed by two-thick functional layers", 45th International Conference on Micro & Nano Engineering (MNE), 2019, Rhodes, Greece. (Oral Presentation)
2. **E. E. Moreira**, J. Gaspar, L. A. Rocha, "Design and optimization of a force amplification mechanism for resonant accelerometers", 43rd International Conference on Micro & Nano Engineering (MNE), 2017, Braga, Portugal. (Poster Presentation)
3. R. A. Dias, **E. E. Moreira**, P. P. Freitas, L. A. Rocha and J. Gaspar,"Novel Magnetic Sensing Principle for MEMS Displacement Readout", 43rd International Conference on Micro & Nano Engineering (MNE), 2017, Braga, Portugal. (Oral Presentation)
4. C. Coelho, **E. E. Moreira**, R. A. Dias, J. Gaspar and L. A. Rocha,"FM accelerometer design based on thermal-piezoresistive amplification", 43rd International Conference on Micro & Nano Engineering (MNE), 2017, Braga, Portugal. (Oral Presentation)
5. R. A. Dias, **E. E. Moreira**, I. Ribeiro, H. Fonseca, S. Cardoso, P. P. Freitas, L. A. Rocha and J. Gaspar,"Novel Magnetic Sensing Principle for MEMS Displacement Readout", ChipEx2017, 2017, Tel Aviv, Israel. (Oral Presentation)
6. **E. E. Moreira**, M. Costa, H. Fonseca, J. Cabral, J. Gaspar, L. A. Rocha," Variable Capacitors using Extended MEMS Parallel-plate actuators", 42nd International Conference on Micro & Nano Engineering (MNE), 2016, Vienna, Austria. (Oral Presentation)

About the Author

Eurico Esteves Moreira was born in Morges, Switzerland in 1990. He received his BSc and M.Sc. degree in Electronic Engineering from the University of Minho, Portugal, in 2012 and 2014, respectively. After graduating, he was a researcher, for more than one year, in collaborative projects between the University of Minho and Bosch Car Multimedia, Braga. Since 2015, he has been an Associated Researcher at the International Iberian Nanotechnology Laboratory, Braga, Portugal. In 2016, he started pursuing a PhD in Advanced Engineering Systems for Industry at the same university where he graduated, in a project involving the Automotive Electronics group at Robert Bosch GmbH, in Reutlingen, Germany. His research focus has been on the design and fabrication of MEMS sensors and actuators, and embedded systems.